POLITECNICO DI MILANO

DEPARTMENT OF CIVIL AND ENVIROMNENTAL ENGINEERING

DOCTORAL PROGRAMME IN ENVIROMNENTAL AND INFRASTRUCTURE ENGINEERING

TWO-FLUID MODEL FOR SOLID-LIQUID FLOWS
IN PIPELINE SYSTEMS

Doctoral Dissertation of:
Gianandrea Vittorio Messa

Supervisor:
Prof. Stefano Malavasi

Tutor:
Prof. Francesco Ballio

The Chair of the Doctoral Program:
Prof. Alberto Guadagnini

To my grandparents

Abstract

Turbulent solid-liquid internal flows are encountered in many engineering applications, such as mining, chemical, and petroleum. The technical and economical burden of experimental tests and the lack of generalization of the many simplified physically based models made Computational Fluid Dynamics (CFD) a commonly-used approach in recent years. Among the CFD models, the *two-fluid* ones are actually the only possible way to simulate dense flows. However, even for pipe flows, the existing two-fluid models appear numerically unstable and computationally expensive; these features could complicate, and even prevent, their application to more complex flows of engineering interest.

In this thesis a new two-fluid model for the simulation of turbulent solid-liquid flows in pipeline systems is presented. The model solves a double-averaged formulation of the mass and momentum conservation equations for both phases, coupled by means of interfacial momentum transfer terms. The model is robust and numerically stable and requires rather low computer time to procure converged solution due to the peculiar way in which the key physical mechanisms governing solid-liquid flows are modeled: phase diffusion fluxes are introduced in all conservation equations to reproduce the effect of the turbulent dispersion of particles; the presence of other particles on the interfacial momentum transfer is taken into account by considering their effect on a mixture viscosity: a wall function is employed in order to model the mechanical contribution to the wall shear stress.

Three test cases are investigated. At first, the turbulent flow of solid-liquid mixtures in horizontal pipes is considered, comparing the predictions of the proposed model to both experimental data from open literature and the estimations of previous two-fluid models. Afterwards, the flow of solid-liquid slurries in a sudden expansion in a rectangular duct is simulated, evaluating the phenomenological consistency of the solution on the grounds of the theoretical background inferred from literature. At last, the model is applied to geometry of engineering interest, which is a wellhead choke valve for oil & gas applications, in order to preliminary investigate the effect of the presence of solid particles in the flow on the dissipation characteristics of the device.

Acknowledgments

Contents

List of Figures

List of Tables

Chapter 1

Introduction

This introductory chapter reports the motivations, the scopus and the methodologies of the present thesis. The chapter is divided in four sections. Section 1.1 focuses on the engineering motivations of the work. Section 1.2 introduces the possible approches to the problem considered. Section 1.3 defines the scopus of the work and the structure of the thesis. Section 1.4 provides the basic definitions and terminology concerning dispersed two-phase flows.

1.1   An engineering perspective

Turbulent flows of solid-liquid mixtures in pipeline systems are often encountered in many engineering applications. For example, *slurry pipelines* (Figure 1.1) are widely used in mining to transport mineral concentrate from a mineral processing plant near a mine. Fluidized beds, stirred tanks, and the systems for the production of hydrogen and nitrogen are very important in the chemical industry.

Among the many fields of application, this thesis is mainly addressed to the petroleum engineering. The initial consideration is that, during the extraction of oil from wells, not only oil is dragged into the pipeline, but also solid particles and gases (Figure 1.2). Actually, it is a *multiphase* mixture the one that flows into the pipelines. In particular, the presence of solid particles in the flow may have undesirable consequences, such as the erosion of steel goods and the need for separation and disposal units. Erosion is one of the most serious concerns regarding the wellhead choke valves and the fittings of the

Figure 1.1: Slurry pipelines
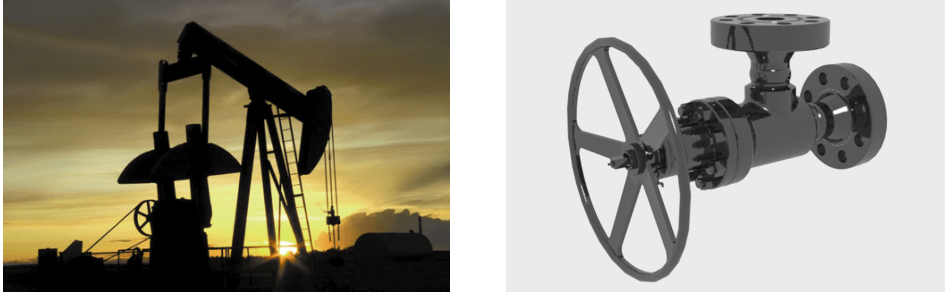
Figure 1.2: An oil well and the wellhead choke valve

Figure 1.3: Oil sands in Saskatchewan

pipelines, such as bends and the pipe joints. Erosion is typically a long-term process determined by the continous impact of particles on a surface, and it is usually related to mixtures in which the volume fraction of solids is very low. Several investigations were aimed at determining the erosion rate produced by the flow of a mixture of a fluid and particles at very low concentration. Most of them are experimental, but also numerical simulations were carried on. As far as the latter approach is concerned, the low particle loading allows using the Eulerian-Lagrangian models - described in Section 2.2 - for which the coupling with semi-empirical algebraic erosion models is straighforward. Following this approach, many authors [60, 66, 116, 151] obtained predictions of erosion rate in choke valves and pipeline fittings (bends, sudden expansions) in agreement to the experimental evidence. It is worth noticing that, for these flows, the low particle concentration is not expected to produce substantial variations in the flow regulation operated by the valve with respect to the single-phase flow case.

On the other side, the effect of the presence of solid particles on the flow control may be a serious concern when the volume fraction of particles within the mixture is high, i.e. the mixture is *dense*. Within the field of petroleum engineering, an application involving significant solids flow rates is the extraction of heavy oil from sands (Figure 1.3), which will be briefly illustrated below. A large proportion of worldwide petroleum production
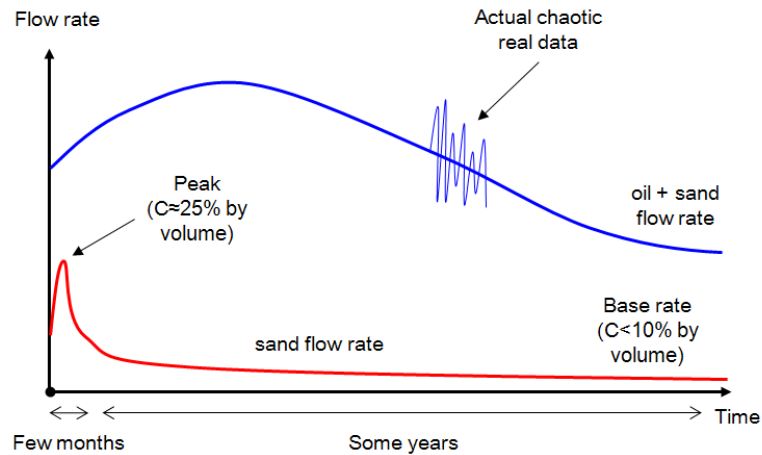
Figure 1.4: Oil and sand production history for a "typical" CHOPS well, on the basis of the work of Dusseault and co-workers [39, 40, 51]. Actual data are "noisy", curves are shoothed.

comes from regions with unconsolidated formations and high sand production potential during well life. This is the case of the oil reservoirs in Gulf of Mexico, North Sea, Middle East, Gulf of Guinea and Canada. In the past, engineers used to install sand exlcusion systems which prevents the sand particles from being dragged into the pipeline through the well, in order to avoid all the already reported negative consquences of the presence of solid particles.

Experiences in the oil sands and heavy oil fields of eastern Alberta and western Saskatchewan in Canada, showed that if sand is allowed to enter the wellbore unhindered, the oil production rate can be improved up to 40% with respect to the case in which sand exclusion technologies are used [40]. In case of heavy oil production, there is no even choice involved: without sand influx, oil rates are insufficient for economic operation [39, 40, 51]. The Canadian petroleum industry has therefore successfully developed and implemented a production approach for heavy oil in unconsolidated sandstones which involves the deliberate initiation of massive sand influx into a perforated oil well, and the continuated production of substantial quantities of sand along with the oil. This process, referred to as CHOPS (Cold Heavy Oil Production with Sand), has been slowly expanding worldwide in recent years. The physical mechanisms which determine the efficiency of CHOPS are described by Dusseault and co-workers [39, 40, 51]; they will not be discussed because they are beyond the topic of the present thesis. What really matters here is the production hystory for a "typical" CHOPS well, qualitatively sketched in Figure 1.4 on the basis of the above-mentioned references. When a new well is completed, initial sand influx is very large, resulting in a sand concentration up to 25% by volume of mixture (actually, the general chaotic nature for short-term fluctuations in oil and sand flow rate may result in even higher temporary values). Over a period that can last from several weeks to several months, the high initial sand production gradually decays towards a base rate for which the sand concentration is of the order of a few percent by volume of mixture. Therefore, the CHOPS process requires the wellhead choke valves to

control the flow in presence of sand over a wide range of volume fractions.

The CHOPS technique has marked a revolution in the design and management of oil extraction plants. The goal of finding efficent methods for preventing sand from entering the pipeline has been replaced by that of managing the flow of the sand-oil mixture, trying to limit the negative consequences of the presence of sand. With reference to the qualitative plot of Figure 1.4, in the long-lasting steady-state period the mixture is characterized by rather low solids concentration, and the protection against erosion may be a serious task. However, as previously observed, a lot of researches have been carried out about this issue. Conversely, during the first months of operation, the system experiences the flow of mixtures in which the solids concentration can reach rather high values, up to 25-30% by volume of mixture and even more for limited periods of time. This dense slurry flows through the pipeline with all its fittings through the wellhead choke valve. The proper control of the flow may be an important concern in this initial stage, since the performance of the valve is likely to be significantly affected by a high loading of sand particles. Notwithstanding, the literature available about this topic is extremely poor. Among the reasons, it is worth adding the techicnical and economic burden of experimental tests and the fact that a high particle loading doesn't allow using Eulerian-Lagrangian models due to the prohibitive computational cost, thus forcing to adopt other approaches. In perspective, the present thesis aimes at contributing to shed light on this topic.

It is worth noticing that, even if the CHOPS operations are very likely to be laminar, a turbulent flow may occur locally within the wellhead valve chamber and in correspondence to pipeline fittings. In this thesis only turbulent solid-liquid flows will be considered, shelving for future work the application to laminar flows. Doing so, whilst remaining consistent with the target field of petroleum industry, the work can take full advantage of the interdisciplinarity across the different applications mentioned at the beginning of this section. This allows disposing of more abundant literature material and experimental data and, at the same time, producing a work of more general validity, not constrained by a unique application. For the same reasons, in this stage of the work water is considered as the carrier fluid.

An overview of the possible research methodologies for addressing the investigation of turbulent solid-liquid pipeline flows is reported below.

1.2   Research approaches

The analysis of the possible research methodologies must be finalized to the objective of this thesis, which is the prediction of turbulent solid-liquid flows through pipes and pipeline fittings. In perspective, this study is addressed to the problems of flow regulation in presence of variable amounts of sand particles in the flow. The reference engineering field is the oil industry, but the willingness to provide results of more unversal validity and take advantage of more literature resources motivated the decision to address a wider range of applications. In this section only a brief description of the possible approaches

is given, as a starting point for the definition of the aims of the work. Details of each methodology will be discussed in Chapters 2 and 3.

1.2.1 Experimental tests

The turbulent flow of solid-liquid mixtures in pipeline systems have been investigated experimentally by different authors. The main advantage of this approach is that the researcher faces the *real* flow, but, as often happens, at a smaller scale. However, experimental tests are considerably expensive and require specific equipments, and significant technical difficulties arise in performing measurements, mostly for highly concentrated mixtures. Experiments on pipeline fittings are usually limited to dilute flows, and aimed at measuring the erosion rate or, less often, the velocity distribution. Experimental investigations of dense solid-liquid flows are actually limited to straigh pipes, and the experimenteres provide measurements of pressure drop, concentration distribution, and velocity distribution. Performing measurements of dense flows in pipeline fittings appears very problematic.

1.2.2 Simplified physically-based models

Simplified models are widely used by engineers dealing with two-phase flows. The models may be empirically derived but, more frequently, have a physical basis which is accompanied by simplifying assumptions about the topology of the flow and empirical closures. In most cases, the models are based on a global formulation, in the sense that they consist of an integral formulation of mass and momentum equations. These models are a powerful tool for designers, because they are economically cheap, do not require high calculation time as CFD, and are accurate enough for most applications. However, they have some limitations. First of all, the models often require the solution of several nonlinear equations, which may be difficult to perform. Moreover, their global formulation limit their use to estimate macroscopic parameters, typically head losses. At last, the need for restricting assumptions makes these models applicable only to simple flows. For solid-liquid mixtures, simplified physically-based models are essentially limited to straight pipe flows. Models for more complex flows, but indeed in simple geometries, like sudden expansions, contractions, and orifices have been developed for gas-liquid [2, 5, 23, 94, 131, 132, 137] and solid-gas [147] mixtures; however, the lack of an unquestioned validation may cast doubt on the reliability of these models.

1.2.3 Computational fluid dynamics

The latter approach to the problem consists of running numerical simulations. Compared to experimental tests, this methodology is rather cheap and, above all, versatile, as it allows simulating whatever system of whatever dimension. The main limitation is due to the fact that, even more than in single-phase flows, the huge computational burden forces to seek for approximate solutions. As it will be discussed more deeply in Section 2.2, the computational methods which are exploitable for the simulation of solid-liquid flows

of engineering interest rely either on tracking each single particle or on interpreting both phases as interpenetrating continua. The former approach requires fewer closure equations, but has a high computational cost, therefore it is currently limited to rather low solids concentration, broadly speaking below 10% by volume. The latter approch, called *two-fluid* approach, is economically cheaper, but introduces several closures which need proper modelling; actually, this is the only possible choice for simulating dense flows. However, a literature review showed that, even for pipe flows, a model of unquestioned validity has not been developed yet. Actually, almost all existing two-fluid models rely on closures based on the Kinetic Theory of Granular Flows (KTGF), and try to reproduce all the physical mechanisms governing the phenomenon. Anyway, these model shows some limitations which may prevent their application to the complex flows addressed in this thesis. A literature review revealed that, even for simple flows, the models are susceptible to numerical instabilities and require very time-consuming procedures to obtain converged solutions. Moreover, in many cases the models seem poorly validated. Another two-fluid model, which doesn't rely on KTGF, is that developed by Prof. Brian Spalding [144]; this model has the advantage of a strong numerical stability and ease to reach a converged solution, but, at the same time, appears very inaccurate except for extremely dilute flows. In conclusion, computational fluid dynamics is a very challenging approach, but the models available at present may not be directly employed for the scopus of this thesis.

1.3   Objective and dissertation outline

The present thesis deals with turbulent solid-liquid flows through pipeline systems. In future perspective, the work addresses to the specific problem of flow regulation operated by the wellhead choke valves when a certain amount of solid particles are present in the flow. Anyway, it is tried not to be constrained by a precise application, in order to take advantage of researches addressed to other engineering fields and try to provide results of more general validity. For this reason, water is considered as the carrier fluid, shelving for future work the investigation of more application-specific oil flows.

On the grounds of the considerations reported in Section 1.2, a two-fluid CFD model is used to investiate the flow. A new model was developed trying to guarantee numerical stability, ease to attain convergence, and sufficient accuracy. The two first features are really fundamental for the complex and time-consuming flows considered here. In the initial stage of development of the model, simulations concerned the flow of solid-liquid mixtures through horizontal pipes. This kind of flow, as well as being of interest for many engineering applications, allows comparing the numerical results to the many experimental data and the predictions of the existing computational models.

A more complex kind of flow, that is that through an expansion in a rectangular duct, was then simulated. This benchmark case, in addition to being an intermediate step between a pipe a choke valve, may be also of interest in itself as it may be be interpreted as a simplified version of a sudden expansion between two straight branches

of the system. The lack of experimental data for the flow conditions considered didn't allow comparing computations and measurements. A preliminar comparison to the data obtained by several experimenters in the single-phase flow case allowed setting some numerical features and revealed the good predictive capacity of the model. Afterwards, in the two-phase flow case, it was performed a sensitivity analysis to investigate the influence of all the terms which proved negligible for pipe flows but could be *potentially* significant for the backward-facing step case. This allowed establishing the robustness of the model, determining the terms which really matters. At last, the theoretical background inferred from literature served to check the phenomenological consistency of the solution.

The two-fluid model was then applied to simulate the solid-liquid flow through a wellhead choke valve. Starting from the single-phase flow case, validated with respect to experimental data reported in previous works [141], the effect of the presence of solid particles over a wide range of volume fractions on the dissipation characteristics of the device was investigated. The distribution of the phases was also analyzed in order to understand the behaviour of the mixture and provide useful considerations for the design and the management of the device.

This dissertation is divided into 6 chapters. Chapter 1 introduces the focus of this study, outlines the hypothesis, objectives and motivations, explains logical organization of the dissertation, and provides the basic concepts and terminology of two-phase flows. Chapter 2 illustrates the research approaches to the engineering problem, and reports the main features of the Eulerian two-phase flow theory applied to solid-fluid systems, on the basis of a literature review. Chapter 3 focuses on the development of the two-fluid model, with application to the horizontal pipe case. Chapter 4 describes the simulations about the expansion. Chapter 5 illustrates the application of the model to a wellhead choke valve. Chapter 6 presents the conclusions, as well as recommendations for future research.

1.4   Characterization of dispersed solid-liquid flows

The two-phase flows addressed in the present thesis are referred to as *dispersed*, because one phase (the solid) is present in the form of particles dispersed in a continous carrier phase (the liquid). The basic concepts and terminology of dispersed two-phase flows is given below.

In order to provide a hydrodynamic characterization of dispersed solid-liquid flows, it is usually made reference to integral properties. Perhaps the most important property is particle concentration, which is typically defined as the volume fraction of particles, i.e. the ratio between the volume of particles in a local volume of mixture and the volume of mixture itself. The solid particles which constitute the dispersed phase may have, in principle, different sizes. A common approach is to divide the particles into size classes (Figure 1.5). The volume fraction of the dispersed phase α_p is thus:

$$\alpha_p = \frac{\sum_i N_i V_{pi}}{V} \qquad (1.1)$$
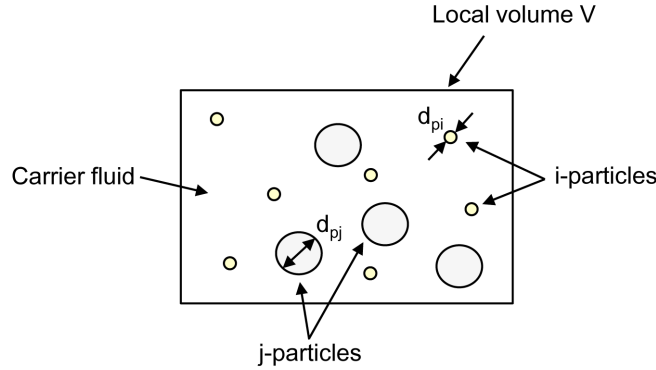
Figure 1.5: Qualitative sketch of dispersed two-phase flows

where V is the total volume and N_i is the number of particles of size i, having volume V_{pi}. Typically, $V_{pi} = \pi d_{pi}^3/6$, where d_{pi} is the particle diameter in case of spherical particles, and their volume-equivalent diameter of a sphere otherwise.

The above reported formulas become simpler if all the particles have the same size. In this case, in fact, $\alpha_p = NV_p/V$, where N is the total number of particles with volume V_p. The assumption of monodispersed particles is verified from the particle size probability distribution function, which is usually inferred from particle size measurements determined by different techniques (laser scatter analysis, analytical sieving, wall sampling). The size probability distribution function is often taken to be log-normal [77, 100]. The condition for monodispersed particles is typically $d_{90\%}/d_{10\%} < 1.2$, where $d_{q\%}$ is the size of an ideal sieve which will pass $q\%$ by volume of the material.

Since the sum of the volume fraction of the dispersed phase and the carrier phase is unity, the volume fraction of the carrier fluid is:

$$\alpha_c = 1 - \alpha_p \qquad (1.2)$$

The volume fraction of the particle α_p ranges from 0 to a maximum value $\alpha_{\max}$, often referred as *maximum packing concentration*. Such parameter depends basically on shape and size distribution of the particles. For monodispersed particles, the closest packing is about 0.74 for sperical particles and up to 1 for cubic particles. A non uniform particle size distribution may increase the maximum packing concentration, since the smallest particles occupy the interstices between the largest ones. Some characteristics of the flow may also affect the maximum packing concentration [121, 122]. For example, a high shear rate increases the maximum packing concentration of spherical particles towards the closest value of 0.74 as it changes their alignement.

The shape of the particles may affect significantly the flow of a solid-liquid mixture. In some cases, the grains are mild deviations from the spherical case and have rounded features, such as for glass beads or certain kinds of sand. In other cases, the particles often take on more complex irregular shapes. The quantitative evaluation of such characteristic is a very difficult task. Different parameters were introduced to quantify particle

shape, the most important of whom are the *sphericity* and the *roundness*. According to the traditional definition, the sphericity is the ratio of grain volume to that of the smallest circumscribing sphere; and the roundness is the ratio of the curvature of the grain edges/corners to overall grain. However, the difficulties in measuring particle volume or edge curvature and the diffusion of computer programs relying on digital image capturing for grain shape investigation led to the introduction of different parameters and to a different definition of the traditional ones. For example, starting from a two-dimensional digital image of the particles, the sphericity can be evaluated as the ratio between the radius of the inscribed circle to that of the circuscribed circle centered at the center of mass [28], or, alternatively, as the ratio between the major and minor axis of an ellipse circumscribing the grains (referred to as *axis ratio* [136]). In the same way, the roundess can be evaluated as either the ratio between the cross sectional area of the particle and that of a circle with diameter equal to the major axis of the grain [28], or the ratio between the area of the particle, multiplied by 4π, and its perimeter to the square (referred to as *circularity index* [136]).

Once particle shape has been quantified, another difficult task is how to account for it in the predictive models which all rely on the assumption of spherical particles for the sake of simplicity. Different approaches have been attempted, but the lack of a generality of the results indicate that further research is needed on this topic. Shaan and co-workers [136] accounted for particle shape via the maximum packing concentration which was experimentally determined. Sommerfeld *et al.* [142] reported a correlation for the drag coefficient in which the effect of particle shape was accounted for by empirical shape descriptors.

Alternative definitions for particle concentration have been proposed. For example, the mass loading η is the ratio beween the mass of the particles to that of the fluid in a local volume of mixture:

$$\eta = \frac{\alpha_p \rho_p}{(1 - \alpha_p)\, \rho_c} \tag{1.3}$$

being ρ_p and ρ_c the density of the particles and the fluid respectively.

A detailed classification of dispersed two-phase flows is reported by Loth [100] on the basis of the type of coupling between particle motion and that of its surroundings (Figure 1.6). Coupling include the interactions between the particles and the fluid and among the particles. The author reports that dispersed flows include four coupling sub-regimes which can be approximately ordered in terms of increasing particle concentration (α_p and η) as:

- ONE-WAY COUPLING

  The particle motion is affected by the fluid but not vice-versa. Detailed criteria for the limits of interphase transfer of mass, momentum and energy between the phases are given by Crowe *et al.* [29], who introduced specific non dimensional parameters of influence. However, it is typically assumed that regime is controlled by α_p or η, and occurs for $\alpha_p \ll 1$ or $\eta \ll 1$. Guidelines reported in literature are $\eta < 10^{-3}$ [98] and $\alpha_p < 10^{-6}$ [142].
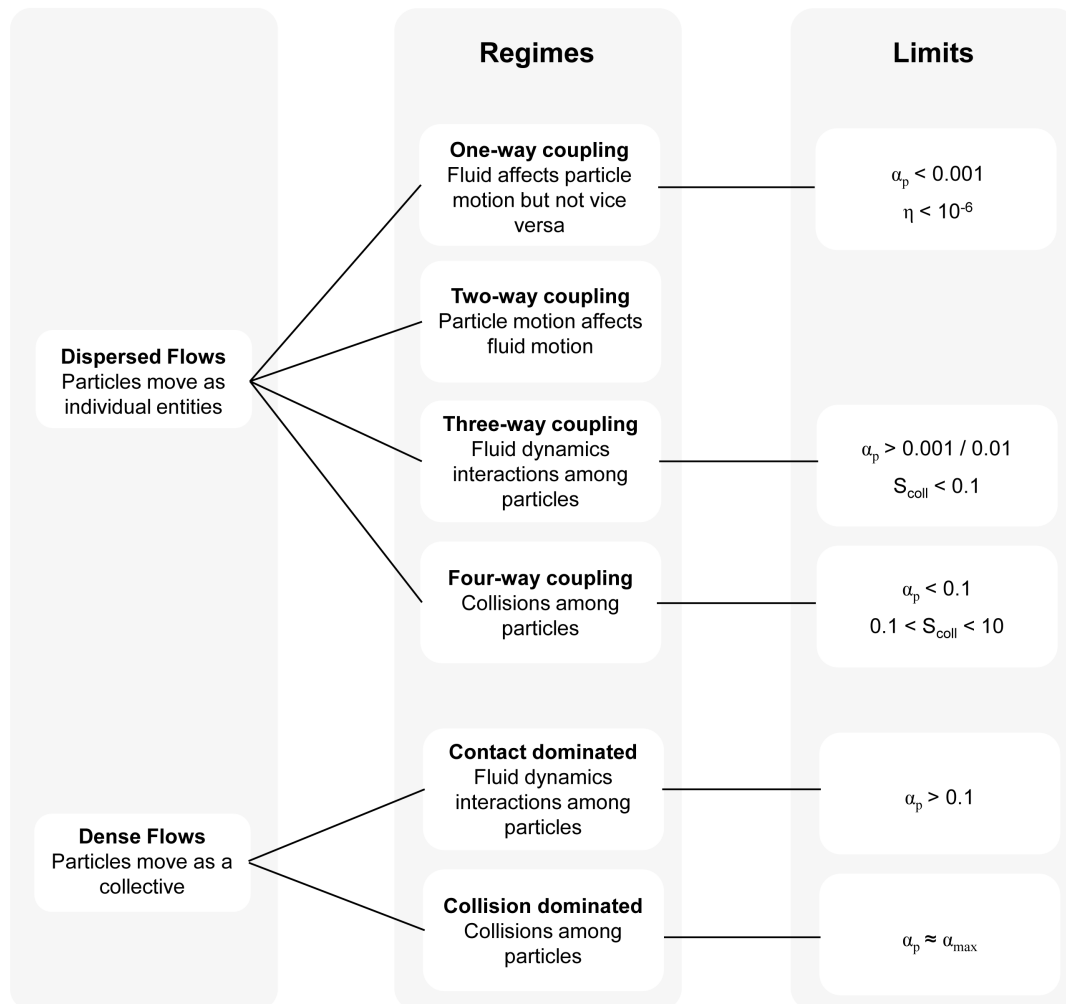
Figure 1.6: Flow regimes and limits reported in literature

- TWO-WAY COUPLING

  Particles also affect the carrier fluid motion, i.e. particle wake causes dissipation. Detailed criteria for the limits of this regime are reported by Loth [100], but, as for the previous one, it is usually assumed that two-way coupling is controlled by α_p or η.

- THREE-WAY COUPLING

  Particle disturbance of the fluid locally affects another particle's motion. Basically, the virtual volumes of two or more particles intersect so they interact in a fluid dynamic sense, although they don't come into direct contact. According to Loth [100], a rough criterion for the onset of such regime is $\alpha_p \geq 0.01$; a more rescrictive criterion ($\alpha_p \geq 10^{-3}$) is reported by Sommerfeld *et al.* [142].

- FOUR-WAY COUPLING

  Contact dynamics significantly influence overall particle motion. The non-dimensional parameter of influence is the collisional Stokes number S_{coll}, that is the product between the particle relaxation time τ_p, which will be discussed in the following, and the frequency of collisions for a single particle along its path f_{coll}. Loth [100] provides a model for estimating f_{coll}, which becomes more important as particle concentration and diameter increases. The author also suggests that four-way coupling dispersed flow occurs for $0.1 \leq S_{coll} < 10$ and $\alpha_p \leq 0.10$.

Dispersed flows in which collisions and fluid dynamics interactions between particles are negligible, that is one-way and two-way coupling flows, are often referred as *dilute* flows. Conversely, as the volume fraction of the dispersed phase α_p increases above 0.10, particle motion is dominated by the interactions between particles, so they tend to move as a collective. Unlike other references [142] whose terminology is followed in this thesis, Loth claims that these flows cannot be referred to as *dispersed*, but must be called *dense*. The same author proposed a classification of dense flows in the following sub-regimes:

- COLLISION-DOMINATED

  The particles are in contact with other particles for short periods, so that their free-flight motion is controlled by rebound velocities.

- CONTACT-DOMINATED

  The time of contact between particles increases and the particles spend a significant portion of the time rolling and rubbing against each other. This regime occurs for $\alpha_p \approx \alpha_{max}$, being α_{max} the maximum packing concentration already defined in the present Section.

Another important feature of dispersed two-phase flows is the influence of the fluid on the particle motion. The reference non-dimensional parameter is the Stokes number S, which is the ratio of the particle relaxation time τ_p, also called particle's fluid dynamics

Large eddies   Intermediate eddies   Small eddies
  (τ_Λ)   (τ_λ)
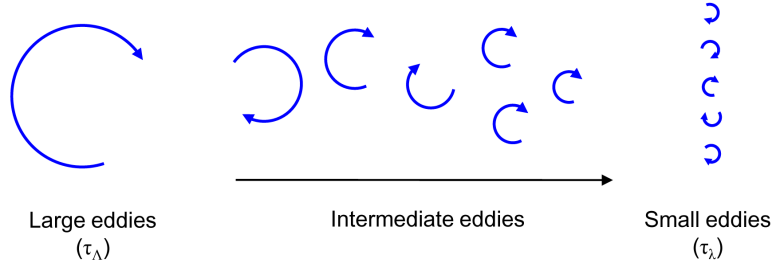
Figure 1.7: Scales of turbulence

response time, to a characteristic time scale of the fluid τ. The particle relaxation time τ_p represents a typical timescale of the particle's reaction to changes in the fluid phase velocity. τ_p is usually associated with drag, since this force typically represents the largest continous phase effect on particle motion [100] and, for a spherical particle, it is given by:

$$\tau_p = \frac{4}{3}\frac{(\rho_p + C_{vm}\rho_c)\,d_p}{\rho_c C_{d,s}|u_{\mathrm{r}}|} \tag{1.4}$$

in which: C_{vm} is the virtual mass coefficient, discussed on page 35 and approximately equal to 0.5; $C_{d,s}$ is the drag coefficient of a single sphere in an infinite medium; and u_{r} is the relative velocity between the particle and the fluid. The estimation of $C_{d,s}$ is discussed in Appendix A.

Different Stokes numbers are introduced according to the characteristic time scale τ with respect to which the particle relaxation time is normalized. Since turbulcence is characterized by many time scales (Figure 1.7), reference is often made to the integral scale Stokes number S_Λ and the micro-scale Stokes number S_λ. The former is defined with respect to the characteristic time of the largest (and more energetic) eddies τ_Λ, whose evaluation is typically problem-dependent [46, 109]. According to Loth [100], the condition $\mathrm{S}_\Lambda \ll 1$ means that particle motion approximately follows the macroscopic flow, and, conversely, $\mathrm{S}_\Lambda \gg 1$ stands for negligible influence of the macroscopic flow on particle motion. The intermediate situation $\mathrm{S}_\Lambda \approx 1$, which is typically the case considered in this work, indicates that particle motion is substantially modified by the macroscopic flow. The microscale Stokes number S_λ is defined with respect to the characteristic time of the smallest scales of the turbulence, which are basically the Kolmogorov scales. The condition $\mathrm{S}_\lambda \ll 1$ means that the particles are in local equilibrium with respect to the turbulent motion, therefore that the behavior of the particles is similar to that of a passive scalar. Conversely, $\mathrm{S}_\lambda \gg 1$ (which is the case of the flow conditions considered in this thesis) indicates that the particles are weakly affected by the small-scale turbulence, though they may be affected by integral-scale turbulence. At last, particles with $\mathrm{S}_\Lambda \approx 1$ will not be close to equilibrium, but will be significantly influenced by the micro-scales.

Chapter 2

Research methodologies for the investigation of solid-liquid dispersed flows

This chapter illustrates the possible methodologies for the investigation of solid-liquid flows, extending the brief overview given in Section 1.2. Section 2.1 illustrates the technologies available for performing measurements of solid-liquid flows, and focuses on their reliability and limitations. This is useful for guaranteeing the consistency of the comparison between numerical predictions and experimental data available in literature. Section 2.2 describes the different CFD methods, while Section 2.3 concentrates on the *two-fluid* model, reporting the main features of the Eulerian two-phase flow theory applied to solid-fluid systems. At last, in section 2.4 the two-fluid model of Spalding [144] is presented.

2.1   Experimental investigation of solid-liquid flows

As already mentioned in section 1.2, the investigation of solid-liquid flows by means of experimental tests shows considerable technical and economic difficulties, especially for dense mixtures and complex flows. The most important fluid dynamic properties of interest are solids concentration, velocity, and pressure. A review of the experimental techniques available for each quantity is given below. Actually, it is often hard to separate the description of the method to the specific flow measured, which is typically that through a straight pipe. Therefore, in the present section reference will be often made to the straight pipe case, trying not to mine the generality of the discussion. It is worth noticing that the limitations reported even for such simple geometry suggest the extreme difficulty of performing experimental tests in case of more complex ones.

2.1.1   Solids concentration

As already noticed, the concentration of the dispersed phase can be defined in different ways, on the basis of either volume or mass. It appears rather easy to switch from
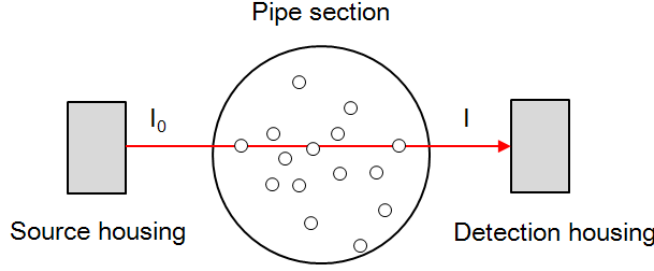
Figure 2.1: Basic principle of the absorption method

one to another. Hereafter, the words "concentration" and "volume fraction" will be used indifferently. The concentration of solids in solid-liquid flows can be characterized by either mean or local values. The mean solids concentration is a global quantity referring to the whole mixture. In some works concerning solid-liquid flows through straigh pipes [53, 136], reference is made to the *in-situ* concentration, which is evalated by adding a certain amount of solids in a water tank whose volume is known before recirculating the mixture in the loop. The in-situ concentration is rather easy to measure but may not be representative of the volume fraction of particles which are actually flowing into the system, the so called *delivered* concentration. This is not only due to that fact the particles may accumulate somewhere in the rig, but also because thay may have a different velocity from that of the surrounding fluid. From the paper of Gillies *et al.* [55] it appears clear that the in-situ concentration equals the delivered one only if the relative velocity between the particles and the fluid is zero, which typically happens when the Stokes number of the particles is sufficiently small. To overcome this problem, most experimenters provide values of the mean delivered concentration, which is either measured directly with expensive counter flow meters [103, 104, 140] or inferred from the local values obtained with the techniques described below.

In the *absorbtion method*, it is the attenuation of ratiation (X-rays or γ-rays) that serves as the basis for the measurements of concentration. This technique rely on the phical principle that the intensity of a monocromatic beam of radiation passing through a medium is attenuated according to the Beer-Lambert law:

$$I = I_0 e^{-\rho \tilde{\mu}_j l} \tag{2.1}$$

where: I is the intensity of radiation detected after the beam has travelled a distance l through the medium; I_0 is the initial intensity; and ρ and $\tilde{\mu}_j$ the density and the mass absorption coefficient of the medium. For a beam passing through a mixture of two substances, say solids particles and a liquid with an attenuation coefficient $\tilde{\mu}_p$ and $\tilde{\mu}_c$ and density ρ_p and ρ_c respectively, the corresponding relation becomes:

$$I = I_0 e^{-\rho_p \tilde{\mu}_p l_p - \rho_c \tilde{\mu}_c l_c} \tag{2.2}$$

where l_p and l_c are the path lengths within the particles and the liquid, respectively.
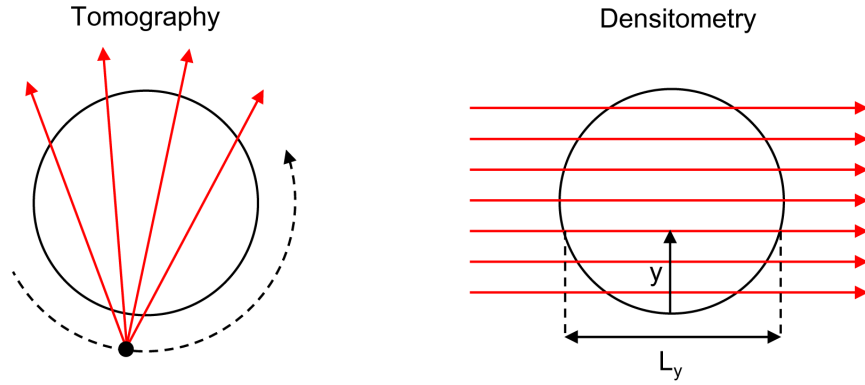
Figure 2.2: Scanning procedures in the absorption method

Equation 2.2 allows therefore evaluating chord-averaged values of solids concentration by measuring two values of radiation intensity (Figure 2.1). Therefore, the absorption method doesn't provide local values of solids concentration, but something in between them and the mean values [87]. Despite being expensive, the absorbtion method is the most commonly-used tecnique to investigate the flow of solid-liquid slurries in horizontal pipes. The method, in fact, provides accurate measurements with uncertainties around a few percentage points also in case of highly concentrated mixtures [104].

The process of reconstruction of the distribution of the solids concentration across a given cross section from the chord-averaged values is referred to as tomography, and requires a lot of measurements at different angular orientation (Figure 2.2). Simplified techniques can be used only under specific assumptions about the topology of the distribution. In horizontal pipe flows, for example, the concentration of particles was proved to be symmetric with respect to the vertical diameter [77, 126], therefore a less expensive process of densitometry, in which the scanning beam moves vertically while remaining horizontal, is usually followed. As depicted on the right side of Figure 2.2, densitometry allows measuring the chord-averaged concentration at different vertical positions y. The average of the measurements weighted by the chord length L_y [52] is used to evaluate the mean solids concentration.

In order to measure local values of the concentration of particles flowing in a system, *L-shaped probes* (Figure 2.3a) can be used. This techniques evaluates the local concentration of the undisturbed flow at the edge of the probe by measuring the concentration of the mixture flowing within the nozzle. This value can be obtain in different ways. In a first investigation, Nasr-El-Din and co-workers [112] collected samples of the mixture over very short time intervals then evaluated the concentration from their weight and volume. Later, the same authors developed a conductivity probe in which the volume fraction of solids is inferred from the resistance encountered by an electric current between two electrodes. Their probe, described in many references [27, 52, 87], is currently used in most investigations performed with L-shaped probes. A similar instrument, based on measurements of capacity rather then conductivity, is cited in Kumar *et al.* [87].
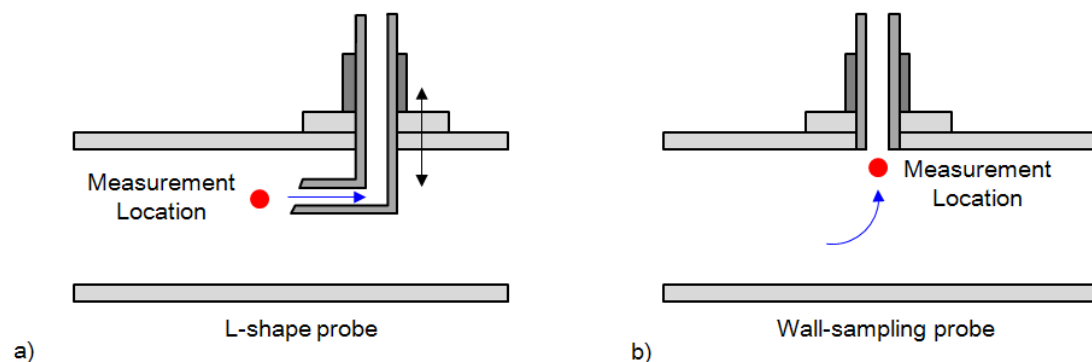
Figure 2.3: Probes for measuring local values of solids concentration: a) L-shape probe b) wall-sampling probe

Measurements with L-shaped probes are cheap but often unaccurate, due to the disturbances caused by the probe on the flow. Although it is established that the absorbtion method provides the most precise measurements, it is not totally clear under which conditions also L-shape probes can be reliable. Colwell and Shook [27] checked the capability of this technique to measure the concentration profile of mixtures of water and either sand or polystyrene particles flowing in a horizontal pipe. The size of the particles was between 190 μm and 1.4 mm. Measurements were reported to be reliable near the pipe wall, but subjected to significant errors in the center of the pipe, the data being strongly dependent on the direction of insertion of the probe within the pipe (either upward from the bottom of the pipe or downward from its top). Kaushal and Tomita [79] compared the concentration distribution of slurry flows in horizontal pipes measured by the absorption method and an L-shaped probe. The solid phase consisted of spherical glass beads with diameter of either 125 μm or 440 μm. A substancial coincidence was obtained only for the smaller particles. On the other side, the two set of data about the bigger particles were significantly different. In particular, the authors observed that the L-shape probe didn't allow evaluating correctly the solids concentration close to the bottom wall. Nasr-el-Din *et al.* [112] tested the capability of the L-shape probe for the case of sand-water slurries with particle diameter between 165 μm or 720 μm and mean delivered concentration up to 0.25 in a vertical pipe. The authors claimed satisfactory predictions of the concentration profiles, but it is worth noticing that the concentration distribution in a vertical pipe is almost uniform and not characterized by a high gradients like that in a horizontal pipe. Moreover, no measurements have been reported near the pipe wall.

Since the L-shaped probes provide measurements of the solids concentration at pointwise locations, the evaluation of the mean delivered solids concentration is performed by averaging the measured values weighted by the area associated to each position probe, as described in Gillies [52] and depicted in Figure 2.4(a). Simplified procedures can be applied under certain hypothesis on the solids concentration distribution. For example, Kaushal and co-workers [77, 79] evaluated the mean delivered solids concentration in a
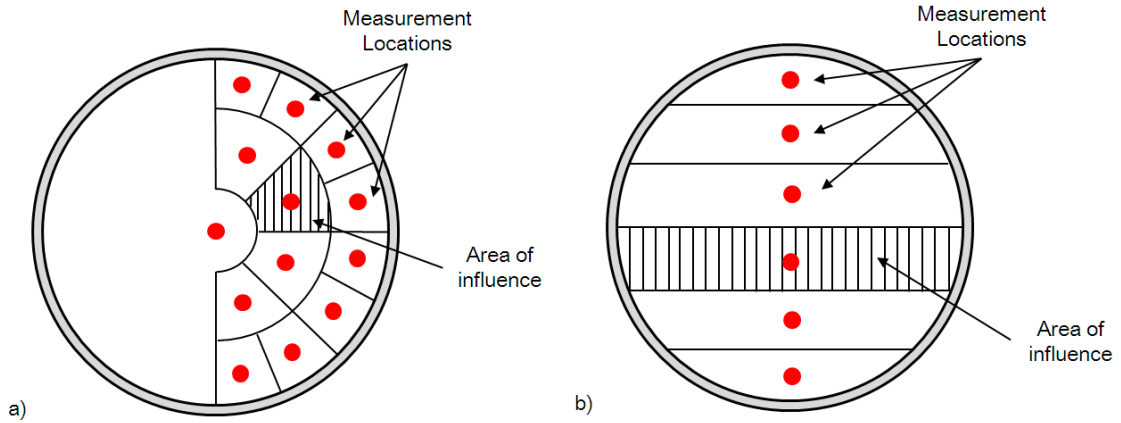
Figure 2.4: Sampling procedures for measurements with L-shape probes as reported by: a) Gillies [52] b) Kaushal and Tomita [79] for horizontal pipe flows

horizontal pipe by making the assumption that the concentration is uniform along each horizontal chord. Such hypothesis allowed them to computed the mean concentration by area-averaging the measurements along the vertical diameter (Figure 2.4(b)).

Wall-sampling probes (Figure 2.3(b)) allow measuring the concentration at a certain location in correspondence to the pipe wall. This technique, described by Nasr-et-Din *et al.* [113], is rather similar to the L-shape probe, and evaluates the local concentration of the undisturbed flow near the pipe wall at the edge of the probe from the concentration of the mixture flowing laterally within the nozzle. As in a previous work concerning the L-shape probe, Nasr-et-Din and co-workers evaluated the concentration within the nozzle by collecting samples of the mixture over very short time intervals and measuring their weight and volume. The use of the wall sampling probe is substantially limited to flow through vertical pipes, in which the solids concentration distribution is almost uniform, and therefore a local value close to the wall is representative of the mean delivered solids concentration. However, Nasr-et-Din *et al.* [113] applied the technique to sand-water with particle size between 165 μm or 720 μm and mean delivered concentration up to 0.28, and concluded that side wall sampling causes serious errors in concentration measurements. The errors were found to increase as the Stokes number and the mean delivered concentration increases. This technique doesn't seem frequently adopted in recent investigations.

Another way to measure dynamically the local solids concentration at the pipe wall is the *wall conductivity probe* developed by Klausner *et al.* [85] (Fig. 2.5). Unlike wall-sampling probes, this technique is not intrusive, using a series of electrodes placed outside the pipe all around the wall. The local concentration at the wall is inferred from conductance (impedance) measurements between adjacent elecrodes. The wall conductivity probe is used for slurries flowing in horizontal pipes with large diameter. The solids concentration distribution and the mean solids concentration are calculated from the local values at the wall by assuming that, due to gravitational stratification, the slurry
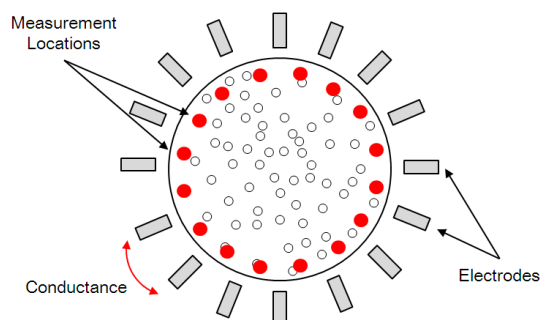
Figure 2.5: The wall conductivity probe developed by Klausner et al. [85]
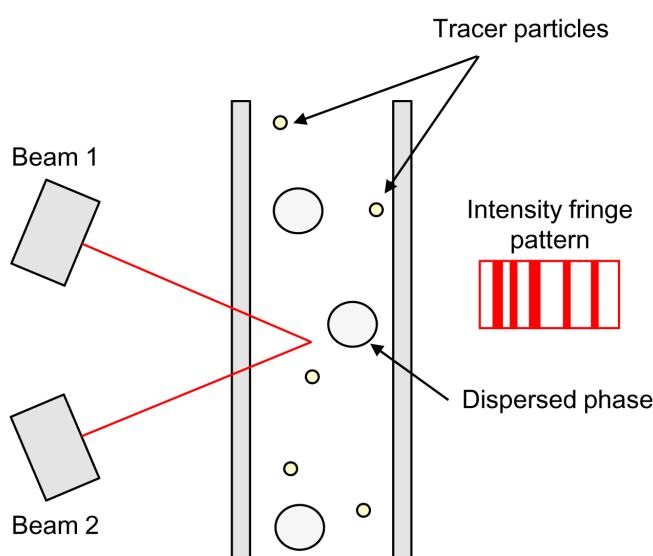
Figure 2.6: Basic principle of Laser Doppler Velocimetry

concentration is uniform in a horizontal plane.

2.1.2   Velocity

The velocity fields of solid liquid flows, like the solids concentration, can be characterized in terms of either mean or local parameter. A global characterization is given by the volumetric flow rate of the mixture, which is tipically measured using electomagnetic flow meters as in single phase flows [52, 79].

Laser Doppler Velocimetry (LDV) is commonly used for determining local values of the velocity of both phases. This technique, considered an accurate and reliable method of measuring flow velocities in single phase flows, requires two laser beams of equal intensity which are focused to cross at a point of interest in the flow field (Figure 2.6). The fluid is seeded with minute tracer particles which follow the motion of the fluid. When one of such particles passes through the measuring point, light from each of the
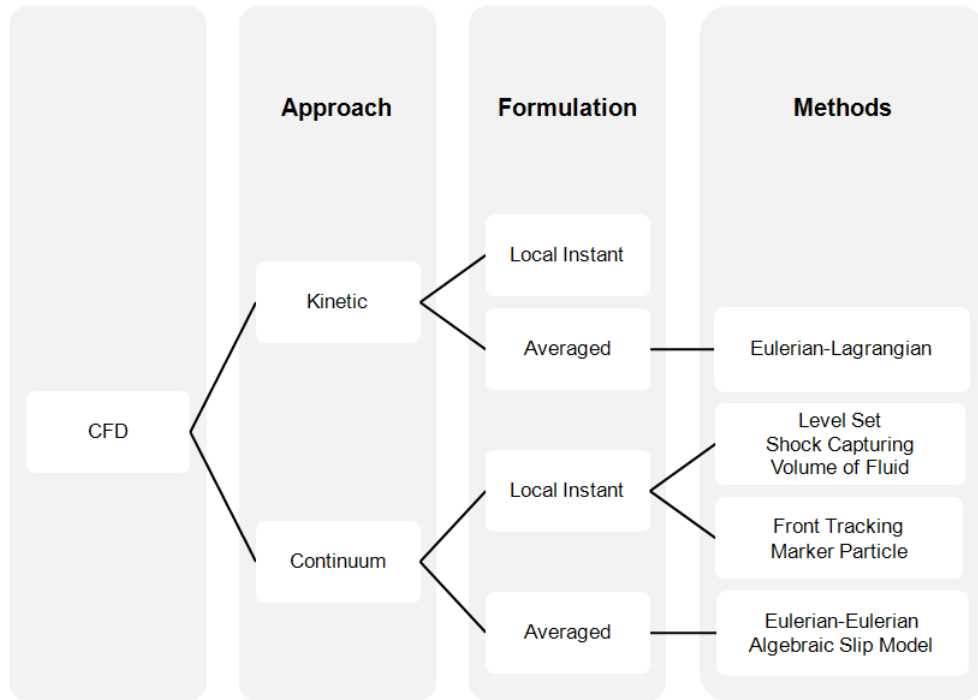
Figure 2.7: Overview of the methods

beams get scattered and interfere in space. This is seen as a varying intensity fringe patterns by a detector, and can be related to the velocity of the tracer particle, a good approximation of that of the fluid. When one of the bigger particles which consitute the dispersed phase passes through the beam, a different amount of light is scattered. Specific tecniques were developed for discriminating the two velocities, making the LDV processor able not to interpret the light scattered by a dispersed phase particle as the liquid phase velocity. A lot of examples of use of LDV for solid-liquid flows are reported in literature [18], but such technique is claimed not reliable for concentrated mixtures (mean solids concentration above 15-20%) except for homogeneous flows, when the difference in velocity between the phases is small [87].

When using the L-shaped probe developed by Nasr-el-Din and co-workers, local values of particle velocities were obtained by specific cross-correlations procedures [27, 52, 53, 126].

2.1.3 Pressure

The pressure of a solid-liquid mixture is commonly measured by means of pressure transducers as in single-phase flows. Separation chambers are often provided in order to assure that only water can enter into the transducers and their tubings [79].
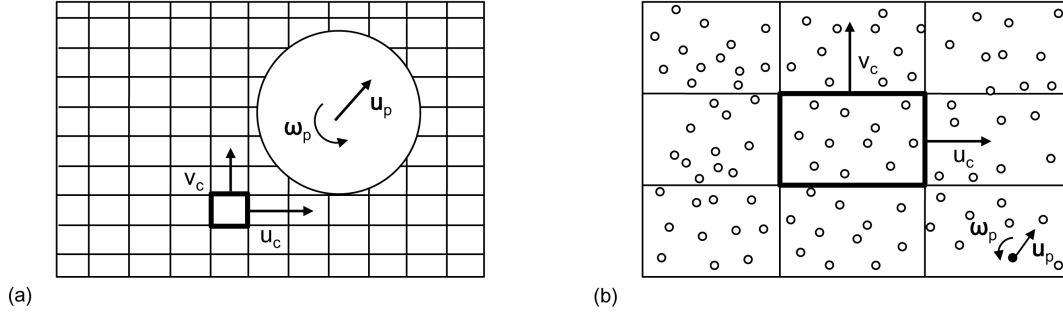
Figure 2.8: The *kinetic* approach without (a) and with (b) the *point-particle* approximation

2.2   Computational methods for dispersed two-phase flows

Basically, all computational methods for dispersed two-phase flows consider the carrier fluid phase as a continuum. A classification of the methods is usually performed according to the manner in which the dispersed phase is treated (Fig. 2.7). In the former approach, referred as *kinetic* [134], the individual particles are tracked in the computational domain. The dispersed phase field is represented by particle trajectories obtained from integrating the particle motion equation; the particle mass and velocity are calculated along the trajectories. The standard differential balance equations describe the behaviour of the carrier fluid. In the latter approach, called *continuum* [134], the dispersed phase is considered as a continuum; therefore, the two-phase flow field is subdivided into single-phase regions with moving boundaries between the phases. The standard differential balance equations hold for every subregion occupied by the same phase. In both approaches, appropriate jump conditions must be set to model the interactions between the phases at the interface. Details of the two approaches are given below.

2.2.1   Methods based on kinetic approach

Methods based on the kinetic approach can be used only for dispersed flows, in which the dispersed phase consists of particles, droplets or bubbles. Since the present thesis focuses on solid-liquid flows, the unit mass of the dispersed phase is indicated as *particle*. No mass exchange is admitted at the particle surface.

Each particle is tracked through the calculated flow field by solving a set of ordinary differential equations for particle location $\mathbf{x}_p$, particle velocity $\mathbf{u}_p$, and particle angular velocity $\boldsymbol{\omega}_p$ [90]:

$$\frac{\mathrm{d}\mathbf{x}_p}{\mathrm{d}t} = \mathbf{u}_p \tag{2.3}$$

$$m_p \frac{\mathrm{d}\mathbf{u}_p}{\mathrm{d}t} = \mathbf{F}_p \tag{2.4}$$

$$I_p \frac{\mathrm{d}\boldsymbol{\omega}_p}{\mathrm{d}t} = \mathbf{T}_p \tag{2.5}$$

where m_p is the particle mass, I_p the moment of inertia of a particle, $\mathbf{F}_p$ and $\mathbf{T}_p$ the net force and the torque acting on a particle respectively. The force acting on a particle is given as the sum of different contributions, among which the drag, Saffman lift, Mangus lift, virtual mass, Basset force, pressure force and gravity, which will be analyzed in detail in Section 2.3.

The carrier fluid phase, referred to as c, is considered a continuum, whose description is carried out in an Eulerian framework. The standard differential balance equations hold for every region occupied by the fluid, and sticky boundary conditions are imposed at the particle surface (Figure 2.8(a)). If the particles are sufficiently small, a common solution strategy is to treat particles as mass points with zero dimension. This is the so called *point-particle* approximation [125, 142] (Figure 2.8(b)). Doing so, the fluid is solved over the whole domain, and its balance equations in *local instant formulation* are:

$$\frac{\partial \rho_c}{\partial t} + \nabla \cdot (\rho_c \mathbf{u}_c) = 0 \tag{2.6}$$

$$\frac{\partial}{\partial t} (\rho_c \mathbf{u}_c) + \nabla \cdot (\rho_c \mathbf{u}_c \mathbf{u}_c) = \nabla \cdot \boldsymbol{T}_c + \rho_c \mathbf{g} + \sum_{n=1}^{N_p} \mathbf{F}^n \left(\mathbf{x}_p^n \right) \delta \left(\mathbf{x} - \mathbf{x}_p^n \right) \tag{2.7}$$

where: ρ_c is the density; $\mathbf{u}_c$ the local velocity field; $\boldsymbol{T}_c$ the stress tensor; and $\mathbf{g}$ the gravitational acceleration. The last term in Eq. 2.7 represents the force per unit volume exterted by the N_p particles on the fluid, approximated by a superimposition of Dirac's delta functions centered at the location $\mathbf{x}_p^n$ of each particle. Conservation of angular momentum becomes $\boldsymbol{T}_c = \boldsymbol{T}_c^+$, where the superscript '+' indicates that the transpose of the dyadic is taken.

Equations 2.6 and 2.7 can be solved directly [124, 142]. As in single phase flow, the need to resolve all the scales of the phenomena implies that the grid size must be smaller than the Kolmogorov scales. Moreover, the point-particle approximation requires the particles to be small compared to the grid size. Therefore, DNS of the equations in local instant formulation cannot be performed except for extremely small particles.

An averaged form of Eq. 2.6 and 2.7 is more often solved. In some cases [4, 124, 162] it is made use of a Large Eddy Simulation (LES) approach, in which a spatial filter is applied to the local instantaneous equations, and a sub-grid scale stress tensor reproducing the effect of the sub-grid scales on the resolved eddies is modeled. The *filtered* pressure and velocity fields are obtained. The consistent amount of computing time required by LES led most Authors [1, 48, 49, 90, 118] to solve a Reynolds averaged (RANS) formulation of the local instantaneous equations, obtained performing a Reynolds decomposition of the flow variables and then time averaging. A proper turbulence model is introduced to close the system of equations, whose unknowns are the *mean* pressure and velocity fields. Methods based on the latter approach are usually referred to as *Eulerian-Lagrangian*.

Whatever the formulation - either local instant or averaged - of the balance equations for the carrier fluid phase is, the fluid properties are evaluated at fixed mesh points. The solution of the equations of motion for the particles (Eq. 2.3-2.5) requires the values of
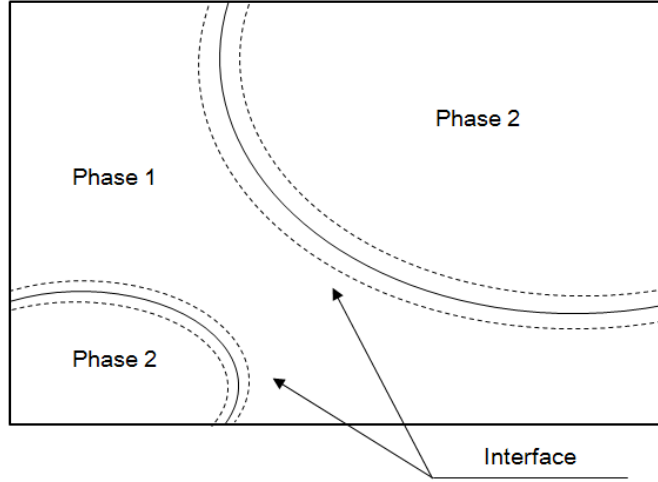
Figure 2.9: The *continuum* approach

fluid properties at the particle position. Therefore, interpolation of the flow field at the particle position is to be performed. Interpolation methods are described by Prosperetti and Tryggvason [125], who discussed also the possible errors associated to this process.

The effect of turbulence on particle trajectories is an important feature of methods based on the kinetic approach. When solving an averaged formulation - either LES or RANS - of the balance equations for the fluid phase, the instantaneous turbulent fluctuations are not solved but modeled. Several models have been proposed in literature; an overview is reported by Crowe *et al.* [30] and Shirolkar *et al.* [138]. The uncertainty associated to the modeling of the instantaneous turbulent fluctuations of the fluid is one of the main source of errors of the Eulerian-Lagrangian methods.

2.2.2   Methods based on continuum approach

The continuum approach assume that the whole two-phase flow field can be subdivided into single-phase regions with moving boundaries (Fig. 2.9). The standard differential balance equations hold for every subregion occupied by the same phase. Appropriate local istantaneous jump conditions must be set to model the interactions between the phases at the interface.

The standard differential balance equations of motion of phase k, valid in the interior of each phase, are the conservation of mass and linear momentum:

$$\frac{\partial \rho_k}{\partial t} + \nabla \cdot (\rho_k \mathbf{u}_k) = 0 \tag{2.8}$$

$$\frac{\partial}{\partial t} (\rho_k \mathbf{u}_k) + \nabla \cdot (\rho_k \mathbf{u}_k \mathbf{u}_k) = \nabla \cdot \boldsymbol{T}_k + \rho_k \mathbf{g} \tag{2.9}$$

where: ρ_k is the density of pure phase k; $\mathbf{u}_k$ the local velocity field; and $\boldsymbol{T}_k$ the stress tensor. As already observed, conservation of angular momentum for both phases implies the simmetry of the dyadic $\boldsymbol{T}_k$, therefore $\boldsymbol{T}_k = \boldsymbol{T}_k^+$.

The local istantaneous jump conditions are particular forms of the balance equations applied at the interface between two phases to specify the exchange of mass and momentum through the interface and stand as matching conditions between the two phases. A rigorous derivation of the local istantaneous jump conditions is reported by Ishii [70]. Their final expressions are:

$$\sum_{k=1}^{2} \dot{m}_k = \sum_{k=1}^{2} \rho_k \mathbf{n}_k \left(\mathbf{u}_k - \mathbf{u}_i \right) = 0 \tag{2.10}$$

$$\sum_{k=1}^{2} \left(\dot{m}_k \mathbf{u}_k - \boldsymbol{T}_k \cdot \mathbf{n}_k \right) = \sigma \kappa \mathbf{n} \tag{2.11}$$

where: $\dot{m}_k$ is the mass transfer of phase k per unit area of interface and unit time; $\mathbf{u}_i$ the velocity of the interface; $\mathbf{n}_k$ the unit outward normal vector of phase k; σ the surface tension; κ the mean curvature of the interface; and $\mathbf{n}$ the unit interface curvature radius vector.

The balance equations (Eq. 2.8-2.9) and the jump conditions (Eq. 2.10-2.11) in local instant formulation can be solved directly. Pressure and velocity of each phase as well as the position of the interface are the unknowns. Besides the high computational time required all the scales of the phenomenon up to the Kolmogorov ones, the main difficulty is to track the interface, where density and viscosity change abruptly. In most cases, a *one fluid* approach [125] is adopted, introducing a marker function H which is 1 where a particular fluid is located and 0 elsewhere, and solving a transport equation for H. According to the definition of H, different methods are have been developed, such as *Level Set*, *Shock Capturing* and *Volume of Fluid* (VOF). In both methods, the sharpness of H is likely to result in an inaccurate determination of the interface location. Other methods, like *Front Tracking* and *Marker Particle* are more accurate, but even more time consuming. As for the kinetic approach, the direct solution of the local instantaneous equations is mostly limited to very simple flows of academic interest.

It is worth noticing that the application of Eq. 2.8-2.11 are not fully unquestionable for solid-liquid flows, because the solid particles are more like to be described by the balance laws of solid continuum mechanics. However, an averaged formulation of the above mentioned equations is more likely to be accepted, since a group of solid particles is more easily regarded as a sort of "fluid". Such an approach, which have also the advantage of reducing the computational burden of the simulations, is commonly followed in most numerical investigations concerning solid-liquid flows.

Methods relying on an averaged version of Eq. 2.8-2.11 are the two-fluid model, already mentioned in section 1.2, and the the Algebraic Slip Model (ASM). In the former, the full set of averaged equations is solved for both phases. In the latter, the averaged equations are added to get the averaged balance equations for the mixture, which are solved together with the averaged continuity equation for the dispersed phase and an approximate algebraic balance equation to account for the velocity difference between the phases. The ASM, often referred as Mixture Model [101] or Diffusion Model [70],

allows reducing the computational effort considerably, and has been frequently used for
the simulation of solid-liquid flows [62–64, 78, 93, 95, 120, 156–159]. The ASM assumes
that a local inter-phase equlibrium is reached over short spatial lenght scales, i.e. that
dispersed phase is rapidly accelerated to the terminal velocity. Therefore, its application
is limited to very low value of the Stokes number and moderate concentrations [78].
Even in these cases, however, the predictions of the model are often not very accurate.
Consequently, the ASM is not used in the present work.

2.3   The two-fluid model

The two-fluid model solves an averaged version of the balance equations (Eq. 2.8-2.9) and
the jump conditions (Eq. 2.10-2.11) in local instant formulation. The present Section
describes the basic features of the model, focusing on its application to solid-liquid
flows. In particular, Sub-section 2.3.1 reports the derivation of the averaged equations,
Sub-section 2.3.2 illustrates the laws needed to close the system of equations, and Sub-
section 2.3.3 discusses the way in which the two-fluid model accounts for turbulence.

2.3.1   Averaged equations

In order to obtain the averaged equations, an average operator is applied to the balance
equations and jump conditions in local instant formulations (Eq. 2.8-2.11). Different
operators have been considered [14, 36, 61, 70, 149], and their consistent application
require the fulfillment of specific conditions [44]. Commonly-used averages of property
$\phi(\mathbf{x}, t)$ are:

- TIME AVERAGE:
$$< \phi(\mathbf{x}, t) >= \frac{1}{T} \int_{t-T/2}^{t+T/2} \phi(\mathbf{x}, t) \, dt \tag{2.12}$$

  The time interval T chosen for averaging must be chosen in such a way that the
  time scale of the turbulent fluctuations is $\ll T$, in turn $\ll$ than the time scale of
  the mean flow fluctuations.

- VOLUME AVERAGE:
$$< \phi(\mathbf{x}, t) >= \frac{1}{V} \int_{V} \phi(\mathbf{x}, t) \, dV \tag{2.13}$$

  The volume V chosen for averaging must be chosen in such a way that the charac-
  teristic dimension of phases is $\ll V$, in turn $\ll$ than the characteristic dimension
  of physical system.

- ENSEMBLE AVERAGE:
$$< \phi(\mathbf{x}, t) >= \int_{\Omega} \phi(\mathbf{x}, t; \omega) \, d\mu(\omega) \tag{2.14}$$

where $\phi(\mathbf{x}, t; \omega)$ is a realization of the quantity ϕ over a set of possible "equivalent" realizations Ω.

Derivations of the average equations are reported by many authors. Ishii [70] applied time average (Eq. 2.12) to the local istantaneous equations. Volume average (Eq. 2.13) was considered by Drew [36], Enwald *et al.* [44], Brennen [14], and Hiltunen *et al.* [61]. The derivation of the equations using ensemble average (Eq. 2.14) is reported by Hiltunen *et al.* [61]. Whatever the kind of average considered is, the final formulation of the Eulerian Two-Fluid model is formally identical. Hereafter, the general averaging operator $\langle \ldots \rangle$ denotes any of the specific operators defined above.

To obtain the averaged equations a phase indicator function $X_k(\mathbf{x}, t)$ is first introduced:

$$X_k(\mathbf{x}, t) = \begin{cases} 1 & \text{if } \mathbf{x} \text{ is in phase } k \text{ at time } t \\ 0 & \text{otherwise} \end{cases} \tag{2.15}$$

whose average $\alpha_k(\mathbf{x}, t) = \langle X_k(\mathbf{x}, t) \rangle$ if from time to time the relative residence time, the volume fraction, or the probability of occurrence of phase k at $(\mathbf{x}, t)$ according to the specific average operator considered. Hereafter, α_k will be denoted as "volume fraction", being a sort of differential generalization of the parameter already introduced in Section 1.4.

The local istantanous balance equations (2.8-2.9) are then multiplied by $X_k(\mathbf{x}, t)$ and then the averaged operator $\langle \ldots \rangle$ is appied. This yelds:

$$\frac{\partial}{\partial t} \langle X_k \rho_k \rangle + \nabla \cdot \langle X_k \rho_k \mathbf{u}_k \rangle = \Gamma_k \tag{2.16}$$

$$\frac{\partial}{\partial t} \langle X_k \rho_k \mathbf{u}_k \rangle + \nabla \cdot \langle X_k \rho_k \mathbf{u}_k \mathbf{u}_k \rangle = \nabla \cdot \langle X_k \boldsymbol{T}_k \rangle + \langle X_k \rho_k \mathbf{g} \rangle + \mathbf{M}_k \tag{2.17}$$

where Γ_k and $\mathbf{M}_k$ are the interfacial transfer terms, defined as:

$$\Gamma_k = \langle \rho_k \left(\mathbf{u}_k - \mathbf{u}_i \right) \cdot \nabla X_k \rangle \tag{2.18}$$

$$\mathbf{M}_k = \langle [\rho_k \mathbf{u}_k \left(\mathbf{u}_k - \mathbf{u}_i \right) - \boldsymbol{T}_k] \cdot \nabla X_k \rangle \tag{2.19}$$

The same procedure is applied to the jump conditions in local instant formulation (2.10-2.11), resulting in the averaged jump conditions:

$$\sum_{k=1}^{2} \langle \rho_k \left(\mathbf{u}_k - \mathbf{u}_i \right) \cdot \nabla X_k \rangle = \sum_{k=1}^{2} \Gamma_k = 0 \tag{2.20}$$

$$\sum_{k=1}^{2} \langle [\rho_k \mathbf{u}_k \left(\mathbf{u}_k - \mathbf{u}_i \right) - \boldsymbol{T}_k] \cdot \nabla X_k \rangle = \sum_{k=1}^{2} \mathbf{M}_k = \sigma \langle \kappa \nabla X_k \rangle = \mathbf{M}_m \tag{2.21}$$

Eq 2.16 and 2.17 are then rewritten into expressions containing the products of averages instead of the averages of product. This is done by employing the Reynolds decomposi-

tion and a weighting procedure to the general variable ϕ:

$$\phi = \langle\phi\rangle^W + \phi' = \frac{\langle W\phi\rangle}{\langle W\rangle} + \phi' \tag{2.22}$$

The variables are either weighted with the phase indicator function (*phasic average*) or with the phase indicator function times the density (*Favre average*):

$$\overline{\phi} = \langle\phi\rangle^{X_k} = \frac{\langle X_k\phi\rangle}{\langle X_k\rangle} = \frac{\langle X_k\phi\rangle}{\alpha_k} \tag{2.23}$$

$$\hat{\phi} = \langle\phi\rangle^{\rho_k X_k} = \frac{\langle\rho_k X_k\phi\rangle}{\langle\rho_k X_k\rangle} = \langle\phi\rangle^{\rho_k X_k} = \frac{\langle\rho_k X_k\phi\rangle}{\overline{\rho}_k\alpha_k} \tag{2.24}$$

For each variables, the appropriate weight for averaging depends on its appearence in the momentum equation. As remarked by Ishii [70], phasic average is appropriate for quantities defined per unit volume while the Favre average is used for those defined per unit mass. Consequently, the decomposed form of the averaged balance equations is:

$$\frac{\partial}{\partial t}\left(\alpha_k\overline{\rho}_k\right) + \nabla\cdot\left(\alpha_k\overline{\rho}_k\hat{\mathbf{u}}_k\right) = \Gamma_k \tag{2.25}$$

$$\frac{\partial}{\partial t}\left(\alpha_k\overline{\rho}_k\hat{\mathbf{u}}_k\right) + \nabla\cdot\left(\alpha_k\overline{\rho}_k\hat{\mathbf{u}}_k\hat{\mathbf{u}}_k\right) = \nabla\cdot\left[\alpha_k\left(\overline{\boldsymbol{T}}_k + \overline{\boldsymbol{T}}_k^T\right)\right] + \alpha_k\overline{\rho}_k\mathbf{g} + \mathbf{M}_k \tag{2.26}$$

where $\boldsymbol{T}_k^T$ is the fluctuating stress tensor:

$$\overline{\boldsymbol{T}}_k^T = -\frac{\langle X_k\rho_k\mathbf{u}_k'\mathbf{u}_k'\rangle}{\alpha_k} \tag{2.27}$$

often referred as *pseudo-turbulent stress tensor* in analogy with the usual Reynolds stress tensor in turbulent single-phase flow. However, as noticed by Hiltunen *et al.* [61], this terms contains momentum fluxes arising from both the turbulent fluctuations within each phase and the fluctuations of the velocity of phase k due to the presence of the other phase, therefore it may not be zero even for laminar flow.

It is usually convenient to express the averaged stress tensor $\overline{\boldsymbol{T}}_k$ as the sum of pressure and deviatoric stresses:

$$\overline{\boldsymbol{T}}_k = -\overline{p}_k\boldsymbol{I} + \overline{\tau}_k \tag{2.28}$$

and to express the interfacial momentum transfer $\mathbf{M}_k$ in a form involving the interfacially averaged pressure and shear stress. This is done by defining the weighted averaged interfacial pressure and shear stress as:

$$p_{k,I} = \frac{\langle p_k\nabla X_k\cdot\mathbf{n}_k\rangle}{\langle\nabla X_k\cdot\mathbf{n}_k\rangle} \tag{2.29}$$

$$\tau_{k,I} = \frac{\langle\tau_k\left(\nabla X_k\cdot\mathbf{n}_k\right)\rangle}{\langle\nabla X_k\cdot\mathbf{n}_k\rangle} \tag{2.30}$$

and rewriting $\mathbf{M}_k$ as:

$$\mathbf{M}_k = \Gamma_k \mathbf{u}_{k,I} + p_{k,I}\nabla\alpha_k - \tau_{k,I}\nabla\alpha_k + \mathbf{M}_k^d \tag{2.31}$$

where: $\Gamma_k \mathbf{u}_{k,I}$ is the interfacial velocity of phase k, accounting for phase change through the interface:

$$\Gamma_k \mathbf{u}_{k,I} = \langle[\rho_k \mathbf{u}_k (\mathbf{u}_k - \mathbf{u}_i)]\cdot\nabla X_k\rangle \tag{2.32}$$

and $\mathbf{M}_k^d$ is the generalized drag force acting on phase k, given by:

$$\mathbf{M}_k^d = -(p_k - p_{k,I})\,\boldsymbol{I} + (\tau_k - \tau_{k,I}) \tag{2.33}$$

Substitution of Eq. 2.28 and Eq. 2.31 into Eq. 2.17 yelds:

$$\begin{aligned}
\frac{\partial}{\partial t}(\alpha_k \bar{\rho}_k \hat{\mathbf{u}}_k) + \nabla\cdot(\alpha_k \bar{\rho}_k \hat{\mathbf{u}}_k \hat{\mathbf{u}}_k) &= -\alpha_k \nabla \bar{p}_k + \nabla\cdot\left[\alpha_k\left(\bar{\tau}_k + \overline{\boldsymbol{T}}_k^T\right)\right] \\
&+ \Gamma_k \mathbf{u}_{k,I} + (p_{k,I} - \bar{p}_k)\nabla\alpha_k - \tau_{k,I}\nabla\alpha_k + \mathbf{M}_k^d + \alpha_k \bar{\rho}_k \mathbf{g}
\end{aligned} \tag{2.34}$$

Using Eq. 2.31, the averaged jump conditions for momentum (Eq. 2.21) expressed in terms of the generalized drag $\mathbf{M}_k^d$ becomes:

$$\sum_{k=1}^{2}\left(\Gamma_k \mathbf{u}_{k,I} + p_{k,I}\nabla\alpha_k + \tau_{k,I}\nabla\alpha_k + \mathbf{M}_k^d\right) = \sigma\langle\kappa\nabla X_k\rangle = \mathbf{M}_m \tag{2.35}$$

In the two-Fluid model the averaged balance equations (Eq. 2.25 and 2.34) are solved for each phase k. The averaged jump conditions (Eq. 2.20 and 2.35) provide the coupling between the phases. Closure laws are needed to close the system of equations.

If the two-phase system consists of solid particles ($k = p$) in a liquid ($k = c$), the following assumptions can be made:

- The density of both phases is constant: $\bar{\rho}_k = \rho_k = \text{const}$

- No phase change occurs: $\Gamma_k = 0$

- The interfacial pressure difference $(p_{k,I} - \bar{p}_k)\nabla\alpha_k$ and the combined interfacial shear and void fraction effects $\tau_{k,I}\nabla\alpha_k$ are negligible [44]

- The surface tension between solid and liquid is negligible [61, 70]

In this case, the formulation of the Eulerian Two-Fluid model becomes:

$$\frac{\partial}{\partial t}(\alpha_k \rho_k) + \nabla\cdot(\alpha_k \rho_k \hat{\mathbf{u}}_k) = 0 \tag{2.36}$$

$$\begin{aligned}
\frac{\partial}{\partial t}(\alpha_k \rho_k \hat{\mathbf{u}}_k) + \nabla\cdot(\alpha_k \rho_k \hat{\mathbf{u}}_k \hat{\mathbf{u}}_k) &= \\
&- \alpha_k \nabla\bar{p}_k + \nabla\cdot\left[\alpha_k\left(\bar{\tau}_k + \overline{\boldsymbol{T}}_k^T\right)\right] + \mathbf{M}_k^d + \alpha_k \rho_k \mathbf{g}
\end{aligned} \tag{2.37}$$

$$\mathbf{M}_p^d + \mathbf{M}_c^d = 0 \tag{2.38}$$

2.3.2   Closure laws

Extra equations are required to close the system of Eq. 2.36-2.38. They include the constitutive laws, relating physical properties using axioms and experimental data; and the transfer laws, describing the interactions between the phases occurring at the interface. An overview of the closure laws is reported below. Actually, closured for the pseudo-turbulent stress tensor $\overline{\boldsymbol{T}}_k^T$ are needed too, but this feature will be discussed when dealing with turbulent two-phase flows (Sub-section 2.3.3).

Constitutive Laws

The constitutive laws specify how the physical parameters of one phase interact with each other, providing expressions for the deviatoric stresses $\overline{\tau}_k$ and the pressure p_k. For the carrier fluid phase, the Newtonian strain-stress relation is usually-assumed:

$$\overline{\tau}_c = \xi_c \left(\nabla \cdot \hat{\mathbf{u}}_c \right) \boldsymbol{I} + 2\mu_c \left[\overline{\boldsymbol{S}}_c - \frac{1}{3} \left(\nabla \cdot \hat{\mathbf{u}}_c \right) \boldsymbol{I} \right] \tag{2.39}$$

where $\overline{\boldsymbol{S}}_c$ is the strain-rate tensor, defined as:

$$\overline{\mathbf{S}}_c = \frac{1}{2} \left[\nabla \hat{\mathbf{u}}_c + \left(\nabla \hat{\mathbf{u}}_c \right)^+ \right] \tag{2.40}$$

Starting from Eq. 2.39, Ishii [70] derived the following model:

$$\overline{\tau}_c = 2\mu_c \overline{\boldsymbol{S}}_c + b\mu_c \left[\nabla \alpha_p \left(\hat{\mathbf{u}}_p - \hat{\mathbf{u}}_c \right) + \left(\hat{\mathbf{u}}_p - \hat{\mathbf{u}}_c \right) \nabla \alpha_p \right] \tag{2.41}$$

where b is a free parameter, called *mobility* of the dispersed phase, which acquires values between 0 and 1. According to Drew [36], no experimental evidence has been offered to verify Eq. 2.41. In simulating solid-liquid flows, it is often assumed $b = 0$ [19, 78]; such approximation is consistent with the model of Ishii when the slip velocity $\hat{\mathbf{u}}_p - \hat{\mathbf{u}}_c$ is small. The resulting expression can also be obtain from Eq. 2.39 with $\xi_c = 0$ and $\nabla \cdot \hat{\mathbf{u}}_c = 0$, as in single-phase incompressible flow.

The proper constitutive relations for the deviatoric stresses in the dispersed phase are less clear. Drew [36] purposes to set $\overline{\tau}_p = 0$ for solid particles, and such assumption is made by different authors [19, 49]. However, a more common choice [17, 41, 78] is to make use of a Newtonian-like constitutive equation:

$$\overline{\tau}_p = \xi_p \left(\nabla \cdot \hat{\mathbf{u}}_p \right) \boldsymbol{I} + 2\mu_p \left[\overline{\boldsymbol{S}}_p - \frac{1}{3} \left(\nabla \cdot \hat{\mathbf{u}}_p \right) \boldsymbol{I} \right] \tag{2.42}$$

in which the strain-rate tensor $\overline{\boldsymbol{S}}_p$ is defined as in Eq 2.40. The meaning of Eq. 2.42 may not be totally clear as it relies on parameters like the dynamic viscosity μ_p and bulk viscosity ξ_p typically related to fluids and not to solid particles. Those parameters may be evaluated from empirical or semi-empirical models based on the particle properties and the local solids volume fraction. For example, Chen and co-workers [20] set $\xi_p = 0$

and used the following formula developed by Ahilan and Sleath for μ_p:

$$\mu_p = 1.2\mu_c \left[\left(\frac{\alpha_{\max}}{\alpha_p} \right)^{1/3} - 1 \right]^{-2} \tag{2.43}$$

where $\alpha_{\max}$ is the maximum packing concentration of solids, already introduced in Section 1.4. Alternatively, a theoretical characterization of μ_p and ξ_p can be obtained from the Kinetic Theory of Granular Flow (KTGF); such approach, well-established for solid-gas flow but frequently applied also to solid-liquid flows, introduces an additional PDE to the system of equations, increasing the computational effort. The KTGF is very complex and, relying on a strong physical basis, tries to reproduce all the mechanisms governing the behaviour of the mixture. However, as it will be discussed in Section 3.2.3, the existing two-fluid models based on KTGF appear unstable numerically and time consuming even for simple flows [41, 89]. These features make them not easily applicable to complex flows, which primarily require a very robust model. For these reasons, closures obtained from the KTGF are not considered at this stage of the work. Future developments of this thesis may concern the integration between the proposed two-fluid model and the KTGF.

Unlike that of the continous phase $\bar{p}_c = \bar{p}$, particle pressure is more difficult to characterize [44, 56]. As for the particle viscosities μ_p and ξ_p, a thoretical interpretation of this parameter is given by the KTGF. Alternative, the tradition approach based on the particle properties and the local solids fraction can be used. According to the latter, the particle pressure term is given as the sum of three contributions:

$$\nabla \left(\alpha_p \bar{p}_p \right) = \nabla \left(\alpha_p \bar{p}_{p,\mathrm{kin}} \right) + \nabla \left(\alpha_p \bar{p}_{p,\mathrm{coll}} \right) + \nabla \left(\alpha_p \bar{p} \right) \tag{2.44}$$

corresponding to the momentum transfer caused by particle velocity fluctuation correlations $\left(\bar{p}_{p,\mathrm{kin}} \right)$ and by particle interactions $\left(\bar{p}_{p,\mathrm{coll}} \right)$, and a contribution from the continouous phase pressure. Enwald *et al.* [44] claim the first term on the right-hand side of Eq. 2.44 to be usually negligible. Several models for the collisional pressure term are available in the literature about gas-solid fluidized beds. Most of them are based on the following formulation:

$$\nabla \left(\alpha_p \bar{p}_{p,\mathrm{coll}} \right) = -G \left(\alpha_c \right) \nabla \alpha_c \tag{2.45}$$

where $G \left(\alpha_c \right)$ is the solid phase elasticity modulus, a parameter which is modeled empirically. The models available for G are of two types:

$$G \left(\alpha_c \right) = 10^{B_1 \alpha_c + B_2} \tag{2.46}$$

$$G \left(\alpha_c \right) = G_0 \mathrm{e}^{-C(\alpha_c - \alpha^*)} \tag{2.47}$$

The empirical constants $B_1, B_2, G_0, C, \alpha^*$ depend mainly on material and shape of the particles, and are often treated as tuning parameters in CFD simulations. The constants considered by different, collected by Enwald *et al.* [44] and Gomez and Milioli [56], are reported in Table 2.1, and produce very different values of the collisional pressure

Table 2.1: Empirical constants for Eq. 2.46

Source	B_1	B_2
Jayaswal	-8.76	5.43
Gidaspow and Ettehadieh	-8.76	5.43
Ettehadieh *et al.*	-10.46	6.577
Gidaspow *et al.*	-10.5	9.0

Table 2.2: Empirical constants for Eq. 2.47

Source	G_0	C	α^*
Bouillard *et al.*	1.0	600	0.376
Gidaspow and Syamlal	1.0	500	0.422
Gidaspow and Ettehadieh	1.0	20	0.62
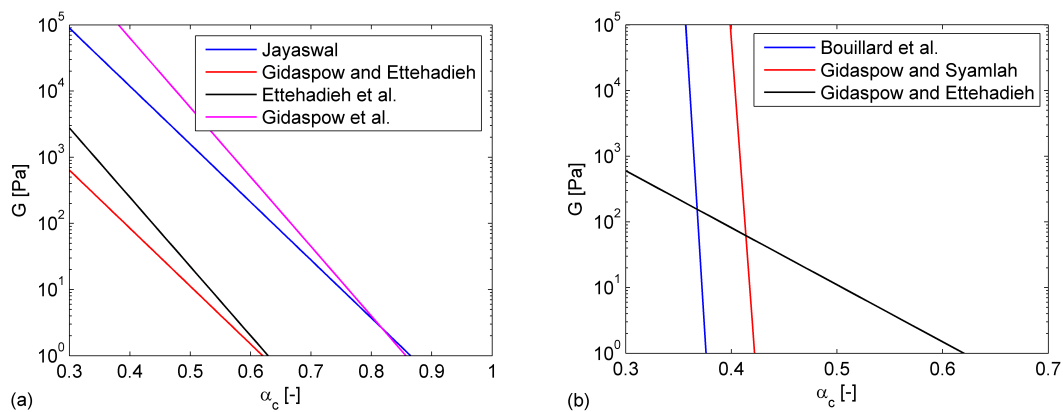
Figure 2.10: Modulus of elasticity obtained from (a) Eq. 2.46 (b) Eq. 2.47 according to the values of the empirical constants reported by different authors

(Figure 2.10). A physical interpretation of Eq. 2.47 is given by Gamwo *et al.* [50]. According to the authors, the motivation for an expression in form of Eq. 2.47 is the experimental observation that plotting the logarithm of consolidating pressure versus volume yelds a substantially straight line for both metallic and non metallic powders under compaction. The constant C, called compaction modulus, is the slope of $\ln G$ versus α_c; and α^* is the compaction fluid volume fraction. For $\alpha_c < \alpha^*$, the elasticity modulus becomes larger as α_c decreases, preventing the particle concentration to exceed its maximum possible concentration.

Trasfer laws

The transfer laws describe the interactions between the phases occurring at the interface, providing closures for the generalized drag $\mathbf{M}_k^d$, representing the force per unit of volume acting on a suspension of particles. If the dispersed phase consist of spherical particles with mean diameter d_p, $\mathbf{M}_p^d$ is usually modeled as [44, 71]:

$$\mathbf{M}_p^d = n_d \left(\mathbf{F}_d + \mathbf{F}_t + \mathbf{F}_{vm} + \mathbf{F}_{hi} \right) \tag{2.48}$$

where $\mathbf{F}_d, \mathbf{F}_t, \mathbf{F}_{vm}, \mathbf{F}_{hi}$ are the forces acting on a particle in the suspension, which will be described below, and n_p is the number of particles per unit volume, given by:

$$n_p = \frac{6\alpha_p}{\pi d_p^3} \tag{2.49}$$

The forces in Eq. 2.48 are:

- *Standard drag force.* This force includes friction and form drag. For a single solid sphere in a liquid, it is modeled as:

$$\mathbf{F}_d = \frac{1}{2} C_{d,s} \rho_c \mathbf{u}_r |\mathbf{u}_r| A_p \tag{2.50}$$

  where: $C_{d,s}$ is the drag coefficient for a single sphere in an infinite medium $\mathbf{u}_r = \mathbf{u}_c - \mathbf{u}_p$ is the relative velocity between the fluid and the particle and $A_p = \pi/4 \cdot d_p^2$ is the projected area of a particle. $C_{d,s}$ is in turn evaluated from the particle Reynolds number $\mathrm{Re}_p = \rho_c \mathbf{u}_r d_p / \mu_c$ through any of the correlations reported in Appendix A. Typically, the two-fluid models introduce Eq. 2.50 in Eq. 2.48 to evaluate the generalized drag $\mathbf{M}_k^d$. However, the procedure is not straightforward. Firstly, the term $\mathbf{u}_r$ in Eq. 2.50 is the local instantaneous relative velocity between fluid and particle, but the unknowns of the two-fluid model are the Favre averaged velocities $\hat{\mathbf{u}}_c, \hat{\mathbf{u}}_p$. Evaluation of Eq. 2.50 in terms of $\hat{\mathbf{u}}_r$ may give rise to errors, especially for turbulent flows, therefore most two-fluid models account for the effect of the fluctuating relative velocity by means of either an additional turbulent dispersion force or phase diffusion fluxes. The two approaches will be discussed in Subsection 2.3.3.

  Moreover, Eq. 2.48 holds for a single particle in an infinite medium, but, in a two-

phase mixture, the influence of the distortion of the flow field caused by the presence of other particles must be considered. With an increasing particle concentration, a particle feels an increase in the flow resistance which in turn leads to a higher drag coefficient. Therefore, in Eq. 2.50 the drag coefficient of for a single sphere in an infinite medium $C_{d,s}$ is replaced by that of a particle in a suspension C_d. Different approaches, summarized by Rusche and Issa [129], have been developed to estimate C_d from $C_{d,s}$.

A very simple method is to calculate C_d from the correlations developed for $C_{d,s}$ (reported in A), but defining the particle Reynolds number Re_p with respect to the viscosity of the mixture μ_m instead of that of the continuous phase μ_c. Different expressions, almost all empirical and dependent on tuning parameters, have been developed to estimate the viscosity of the mixture starting from the volume fraction α_p. An overview of the most commonly-used ones is listed in Appendix B.

Alternatively, C_d can be evaluated as the product by $C_{d,s}$ and a multiplier f, depending on the solids volume fraction α_p. The following expressions for f are available in literature:

1. RUSHE and ISSA [129]

$$f = \exp\left(2.68\alpha_p\right) + \alpha_p^{0.43} \tag{2.51}$$

2. WEN and YU [32, 44]

$$f = (1 - \alpha_p)^{-1.65} \tag{2.52}$$

3. DI FELICE [32, 44]

$$f = (1 - \alpha_p)^{2-\beta}$$
$$\beta = 3.7 - 0.65\exp\left[-\frac{(1.5 - \log \text{Re}_\text{p})^2}{2}\right] \tag{2.53}$$

Other authors developed specific correlations for C_d without starting from those for $C_{d,s}$. In most cases, those formulas were further modified following any of the above mentioned approaches (mixture viscosity and drag coefficient multiplier). Ishii and Mishima [71] evaluated the drag coefficient as:

$$
C_d = \begin{cases}
\dfrac{24}{\text{Re}_p}\left(1 + 0.15\text{Re}_p^{0.687}\right) & \text{if } \text{Re}_p \leq 1000 \\[3mm]
0.45\left[\dfrac{1 + 17.67 f\left(\alpha_p\right)^{6/7}}{18.67 f\left(\alpha_p\right)}\right] & \text{if } \text{Re}_p > 1000
\end{cases}
$$
$$f(\alpha_p) = \sqrt{1 - \alpha_p}\left(\frac{\mu_c}{\mu_m}\right)$$
$$\text{Re}_p = \frac{\rho_c |\mathbf{u}_r| d_p}{\mu_m} \tag{2.54}$$

with the viscosity of the mixture μ_m given by Eq. B.5. Syamlal and O'Brien [44]

made use of a correlation for the drag coefficient derived from that of Dellavalle (Eq. A.5):

$$C_d = \left(0.63 + 4.8\sqrt{\frac{R_t}{\text{Re}_p}} \right)^2 \tag{2.55}$$

in which R_t is the ratio of Richardson and Zaki, i.e. the ratio between the falling velocity of a particle in a suspension and the terminal velocity of a single particle, estimated as follows:

$$2R_t = C_1 - 0.06\text{Re}_p + \sqrt{(0.06\text{Re}_p)^2 + 0.12\text{Re}_p\,(2C_2 - C_1) + C_1^2} \tag{2.56}$$

where C_1 and C_2 are functions of α_p:

$$
\begin{aligned}
C_1 &= (1 - \alpha_p)^{4.14} \\
C_2 &= \begin{cases} (1 - \alpha_p)^{2.65} & \text{if } \alpha_p \leq 0.15 \\ 0.8(1 - \alpha_p)^{1.28} & \text{if } \alpha_p > 0.15 \end{cases}
\end{aligned}
\tag{2.57}
$$

- *Transverse forces* A particle moving in a fluid experience a transverse force if the flow is non uniform (i.e. in the presence of a velocity gradient), if the particle is rotating or if the particle moves in the vicinity of a wall.

  The lift force is a hydrodinamic force acting on particle dispersed in a shear flow due to the particle rotation. The rotation of the particle can be caused by a velocity gradient or may be imposed from some other source. Different models for the lift force have been developed in literature [161].

  Saffman derived analitycally the following expression for a small rigid sphere in a linear shear flow in the limit of small particle Reynolds number and high shear:

$$\mathbf{F}_l = 1.615\rho_c \left(\frac{\mu_c}{\rho_c} \right)^{0.5} d_p^2 \,(\mathbf{u}_c - \mathbf{u}_p) \left| \frac{\mathrm{d}\mathbf{u}_c}{\mathrm{d}y} \right|^{0.5} \text{sign}\left(\frac{\mathrm{d}\mathbf{u}_c}{\mathrm{d}y} \right) \tag{2.58}$$

  This correlation requires the particle Reynolds number Re_p to be much smaller than the shear Reynolds number $\text{Re}_s = \rho_c d_p |\nabla \times \mathbf{u}_c| / \mu_c$, and both Reynolds numbers to be smaller than one. Due to its limiting constrains, the expression of Saffman is not usually implemented in the two-fluid model, even if extensions have been proposed [142, 161].

  A more common alternative is the following model, derived analitically by Drew and Lahey [37] for inviscid flows:

$$\mathbf{F}_l = C_l \rho_c d_p^3 \,(\mathbf{u}_c - \mathbf{u}_p) \times (\nabla \times \mathbf{u}_c) \tag{2.59}$$

  where C_l is a lift coefficient, accepted to be constant as 0.5 for inviscid flow of an incompressible fluid. For real flows, C_l is usually treated as a calibration parameter. Experimental investigations however showed that the lift coefficient values are variable and significantly less than the inviscid value of 0.5, and even negative in
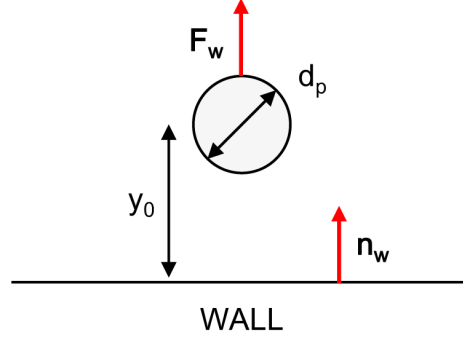
Figure 2.11: The wall lubrication force

some cases [117].

Particles which are not freely rotating may experience a lift force due to their rotation, called Magnus force. The Magnus force acting on a particle rotating with angular velocity ω_p is reported by Crowe *et al.* [29]:

$$\mathbf{F}_l = \frac{\pi}{8} d_p^3 \rho_c C_{lr} |\mathbf{u}_c - \mathbf{u}_p| \frac{\mathbf{\Omega} \times (\mathbf{u}_c - \mathbf{u}_p)}{|\mathbf{\Omega}|} \qquad (2.60)$$

where $\mathbf{\Omega}$ is the particle rotation relative to the fluid:

$$\mathbf{\Omega} = \frac{1}{2} (\nabla \times \mathbf{u}_c) - \omega_p \qquad (2.61)$$

and C_{lr} is a Magnus lift coefficient depending on the particle Reynolds number and $\mathbf{\Omega}$. For small particle Reynolds number, Eq. 2.60 reduces to the analytical model of Rubinow and Keller [29, 142].

To account for the repulsion of particles from the walls observed in some experiments concerning pipe flows, some authors argued for the existance of a transverse force which acts on the particles coming in close proximity to a wall and drives the particles away from it. This force is referred to as either *wall lubrication*, *off-wall lift*, or *hydrodynamic lift force*.

The origin of this force is rather obscure. A theoretical derivation is performed by Antal *et al.* [3] for a two-dimensional inviscid flow between a cylinder and a wall. A generalization of their model to the case of spherical particles yelds:

$$\mathbf{F}_w = \frac{\pi}{3} \rho_c d_p^2 \max\left[C_{w1} + C_{w2} \left(\frac{d_p}{2y_0} \right), 0 \right] \left[\mathbf{u}_r - (\mathbf{u}_r \cdot \mathbf{n}_w) \mathbf{n}_w \right] \qquad (2.62)$$

where: y_0 is the distance between the particle and the wall; $\mathbf{n}_w$ is the unit outward normal vector on the surface of the wall (Figure 2.11); C_{w1} and C_{w2} are given by $-0.104 - 0.06|\mathbf{u}_r|$ and 0.147 respectively (as previously mentioned, $\mathbf{u}_r$ is the relative velocity between the fluid and the particle). Due to its local formulation, Eq. 2.62 - or any of the alternative models available in literature [73] - can easily

be included in a two-fluid model. Eq. 2.62 is usually applied to gas-liquid bubbly flows [3, 42], but proved ineffective for solid-liquid flows [41]. This may be because of the inadequate values of the calibration costants, but, more probably, because of the different origin of the mechanisms which tends to push the particles away from the walls in the two cases.

A semi-theoretical model for the lubrication force in solid-liquid pipe flows is developed by Wilson and Sellgren [155], who applied the Kutta-Zhukovski theorem in the near-wall region using the logarithmic velocity profile and estimated the maximum lubrication force as:

$$(\mathbf{F}_w)_{\max} = \frac{1}{8} C_{L0} f_c V^2 d_p^2 \tag{2.63}$$

where: f_c is the friction factor of the fluid; and C_{L0} is a lift coefficient, which is dependent on the shear Reynolds number $\mathrm{Re}^* = \rho_c U^* d_p / \mu_c$ (U^* is the shear velocity), but can be considered substantially equal to 0.27 for sand particles. Strickly speaking, the lubrication force given by Eq. 2.63 requires the center of the particles to be in the logarithmic region of the boundary layer ($30 \leq Y^+ \leq 130$), even if the maximum force is predicted at $Y^+ \approx 15$. In practice, the particle size range in which the lift force is effective is found to be $0.15 \div 0.40$ mm for sand-water slurries. Later, Wilson *et al.* [154] provide an expression for K to account for the effect of particle size, concentration, and pipe diameter (Sub-section 3.2.2). On the basis of the data reported in their paper, such expression seems to procure rather good agreement to the experimental evidence. Anyway, the global formulation of the model doesn't allow its implementation in a two-fluid model.

- *Virtual mass* This force arises due to an "added mass" of liquid that has to be accelerated as a particle accelerates, and can be evaluated from the following expression:

$$\mathbf{F}_{vm} = C_{vm} \frac{\pi d_p^3}{6} \rho_c \left(\frac{\mathrm{d}\mathbf{u}_c}{\mathrm{d}t} - \frac{\mathrm{d}\mathbf{u}_p}{\mathrm{d}t} \right) \tag{2.64}$$

  where C_{vm} is a virtual mass coefficient. Drew and Lahey [37] invoked the frame indifference principle and concluded that C_{vm} must be equal to the lift coefficient C_l. However, later studies demonstrated that such equality holds only in the limit of weak shears and nearly steady flows. C_{vm} is usually assumed as 0.5 for inviscid flows, but lower values (even negative in some cases) have been assumed. In some cases, C_{vm} is expressed as a function of α_p [36, 44]. The virtual mass force becomes significant if the density of the particles is much smaller than that of the continuous phase [101, 161]; as a consequence, it is negligible for gas-solid flows, but fundamental for liquid-gas flows. For solid particles in a liquid, the importance of the virtual mass force is discussed. Ekambara *et al.* [41] found its contribution negligible for slurry flows in horizontal pipes.

- *History force* The history force, often referred as Basset force, comes from the acceleration of one phase relative to another, as a result of momentum being diffused

through the boundary layer. It is given by:

$$\mathbf{F}_{hi} = \frac{3d_p^2}{2}\sqrt{\pi\rho_c\mu_c}C_{hi}\int_0^t \frac{\mathrm{d}}{\mathrm{d}\tau}\left(\mathbf{u}_c - \mathbf{u}_p\right)\frac{\mathrm{d}\tau}{\sqrt{t-\tau}} \qquad (2.65)$$

where C_{hi} is a history coefficient, equal to 1 for spherical particles [26]. The history force is very time consuming, and it is usually ignored in most computations. Sommerfeld [142] estimated that the inclusion of the history force increases the computational time by a factor about 10. The history force may be significant when the particle diameter is large and the density ratio ρ_p/ρ_c is small [101]. Chung and Troutt [25] report that the history force is even smaller than the virtual mass force, the ratio between the two being of the order of $(\rho_p/\rho_c)^{-0.5}$; therefore, the latter term may be ignored for solid-liquid flows.

2.3.3   Turbulence in the two-fluid model

The modeling of turbulence in the two-fluid model is a very complex issue, since the meaning of turbulence is less established for two-phase flows, and, particularly, in solid-fluid (either gas of liquid) flows [44]. Basically, turbulence in the fluid phase is similar to that of single-phase flow, but the generation and dissipation mechanisms may differ, as they may be influenced by the presence of particles. Turbulence in the solid phase may be interpreted as the particle velocity fluctuations caused by collisions between particles and interactions with the gas phase.

In the averaged equations governing the flow of solid-liquid mixtures (Eq. 2.36-2.38), a first effect of turbulence appears in the pseudo-turbulent stress tensor $\overline{\boldsymbol{T}}_k^T$ (Eq. 2.27), even if, as already noticed, this term is virtually non zero even for laminar flow. However, the formulation of the two-fluid model consisting of Eq. 2.36-2.38 and the closured previously reported doesn't allow reproducing the *turbulent dispersion* of the particles, a mechanism related to the fluctuating part of the fluid particle interaction force which tends to flatten the solids volume fraction distribution.

To account for this effect, Ishii [70] introduced a dispersion force per unit volume $\mathbf{M}_k^{\mathrm{disp}}$ as part of the generalized drag $\mathbf{M}_k^d$:

$$\mathbf{M}_k^{\mathrm{disp}} = -C_t\rho_c k\nabla\alpha_c \qquad (2.66)$$

where: $C_t = 0.1$ is a numerical constant, and k is the turbulent kinetic energy of the fluid phase. The author reports that $\mathbf{M}_k^{\mathrm{disp}}$ is modeled in the analogy of the molecular dispersion force, but doesn't explain where does an additional term in the generalized drag come from.

A rigorous derivation of the turbulent dispersion force term is reported by Enwald *et al.* [44] who expressed in Eulerian form the equation of motion of a single sphere at high Reynolds number (neglecting all the forces but the drag), applied a Reynolds decomposition and showed that the final formulation is equivalent to that obtained from

the traditional approach provided that the generalized drag $\mathbf{M}_k^d$ is given by:

$$\mathbf{M}_p^d = \frac{\alpha_p \rho_c}{\langle \tau_p \rangle^{X_p \rho_p}} \left(\hat{\mathbf{u}}_r + \langle \mathbf{u}_c' \rangle^{X_p \rho_p} \right) \tag{2.67}$$

in which τ_p is the relaxation time of a particle (Eq. 1.4), and $\langle \mathbf{u}_c' \rangle^{X_p \rho_p}$ the drift velocity, which causes particle dispersion. The dispersion force $\mathbf{M}_k^{disp}$ added by Ishii [70] comes from the drift velocity; if $\langle \mathbf{u}_c' \rangle^{X_p \rho_p} = 0$, then Eq. 2.67 reduces to Eq. 2.48. Therefore, as mentioned previously, turbulent dispersion may be attributable to the fluctuations of the drag.

Such interpretation is confirmed by the alternative derivation of the turbulent dispersion force performed by Burns *et al.* [15], who time-averaged the averaged equations (Eq. 2.36-2.38) and appled a Favre-averaged Reynolds decomposition of the variables (Eq. 2.22 and 2.24). According to the authors, applying a second time-averaging operation makes sense if the averaged equations are derived using esamble averaging, therefore are fully time and space dependent. Following this *double-average* approach, neglecting all the forces but the drag, and introducing the variable $\mathbf{U} = \hat{\mathbf{u}}$, the generalized drag $\mathbf{M}_p^d$ becomes:

$$\mathbf{M}_p^d = \frac{\langle \alpha_p \rangle \rho_c}{\langle \tau_p \rangle} \left[\hat{\mathbf{U}}_r + \frac{\langle \alpha_p' \mathbf{U}'_p \rangle}{\langle \alpha_p \rangle} - \frac{\langle \alpha_c' \mathbf{U}'_c \rangle}{\langle \alpha_c \rangle} - \frac{\langle \alpha_p' (\mathbf{U}'_p - \mathbf{U}'_c) \rangle}{\langle \alpha_p \rangle} \right] \tag{2.68}$$

In this derivation, the dispersion force per unit volume $\mathbf{M}_k^{\text{disp}}$ whose existance had been previously argued by Ishii [70] arises from the last three terms involving turbulent mass fluctuations. The correlations $\langle \alpha_i' \mathbf{U}'_j \rangle$ are commonly modeled via the eddy diffusivity hypothesis:

$$\langle \alpha_i' \mathbf{U}'_j \rangle = -\frac{\nu_{tc}}{\sigma_\alpha} \nabla \langle \alpha_i \rangle \tag{2.69}$$

in which: ν_{tc} is the turbulent viscosity of the fluid phase, and σ_α the turbulent Schmidt number for volume fractions. Since, for dispersed two-phase flows, $\alpha_p + \alpha_c = 1$, from Eq. 2.68 it can be derived the following expression for the dispersion force per unit volume:

$$\mathbf{M}_p^d = \frac{\langle \alpha_p \rangle \rho_c}{\langle \tau_p \rangle} \frac{\nu_{tc}}{\sigma_{\alpha c}} \left(\frac{1}{\langle \alpha_p \rangle} + \frac{1}{\langle \alpha_c \rangle} \right) \nabla \langle \alpha_p \rangle \tag{2.70}$$

Rundqvist *et al.* [127] followed a similar approach, but neglected the pseudo-turbulent stress tensor $\overline{\boldsymbol{T}}_k^t$ in Eq. 2.37 and interpreted Eq. 2.36-2.38 as volume averaged instead of ensamble averaged. The authors came to Eq. 2.68 and neglected the last term.

An alternative *double-average* approach was followed by Elgobashi and Abou-Arab [43], who time-averaged the averaged equations (Eq. 2.36-2.38) (without the pseudo-turbulent stress tensor $\overline{\boldsymbol{T}}_k^t$ and interpreted as volume-averaged) applying a non-weighted Reynolds decomposition. Doing so, additional terms will come up from the correlations among the fluctuating components of the Reynolds-decomposed variables.

Assuming constant density and making reference to the above introduced variable $\mathbf{U} = \hat{\mathbf{u}}$, if as usual all the forces are neglected but the drag, the generalized drag $\mathbf{M}_p^d$

becomes:

$$\mathbf{M}_p^d = \frac{\langle\alpha_p\rangle\rho_c}{\langle\tau_p\rangle}\left[\langle\mathbf{U}_r\rangle - \langle\alpha_p'\left(\mathbf{U}_p' - \mathbf{U}_c'\right)\rangle\right] \tag{2.71}$$

Like Burns and co-workers [15], also Elgobashi and Abou-Arab [43] used the eddy viscosity hypothesis (Eq. 2.69) to model the correlations $\langle\alpha_i'\mathbf{U}_j'\rangle$. As a consquence, the latter term in Eq. 2.71 is 0 and no dispersion force is introduced in the momentum equations. However, the effect of turbulent dispersion is accounted for by the correlations arising from the convective terms of all conservations equations, including the continuity one. The mass conservation equations include correlations between the fluctuating velocity and the fluctuating volume fractions and, applying Eq. 2.69, become:

$$\frac{\partial}{\partial t}\left(\langle\alpha_k\rangle\rho_k\right) + \nabla\cdot\left(\rho_k\langle\alpha_k\rangle\langle\mathbf{U}_k\rangle\right) = \nabla\cdot\left(\rho_k\frac{\nu_{tc}}{\sigma_\alpha}\nabla\langle\alpha_k\rangle\right) \tag{2.72}$$

The momentum conservation equations have a very complex form, and they include the binary correlations $\langle\alpha_j'\mathbf{U}_j'\rangle$, $\langle\mathbf{U}_j'\mathbf{U}_j'\rangle$, $\langle\alpha_j'\nabla p'\rangle$, and the triple correlation $\langle\alpha_j'\mathbf{U}_j'\mathbf{U}_j'\rangle$, besides other correlations arising from the decomposition of the stress tensor. Both $\langle\alpha_j'\nabla p'\rangle$ and $\langle\alpha_j'\mathbf{U}_j'\mathbf{U}_j'\rangle$ are commonly ignored, even if such assumption holds only for low particle loading [16], while $\langle\mathbf{U}_j'\mathbf{U}_j'\rangle$ is modeled as discussed later in the present Subsection. The correlation $\langle\alpha_j'\mathbf{U}_j'\rangle$ is modeled by means of the eddy-viscosity hypothesis (Eq. 2.69), giving rise to phase diffusion terms of the following form:

$$\mathcal{F}_D = \nabla\cdot\left(\rho_k\langle\mathbf{U}_k\rangle\frac{\nu_{tc}}{\sigma_\alpha}\nabla\langle\alpha_k\rangle\right) \tag{2.73}$$

Later, Chen and Wood [16] followed the same approach and derived a simplified formulation of the two-fluid model applicable to dilute suspensions ($\alpha_p \to 0$).

Whatever the approach followed is, correlations between the fluctuating velocity of each phase appear in the momentum conservation equations and need proper modelling. These terms have a different physical meaning. In the traditional formulation (Eq. 2.36, 2.37 and 2.38) such correlations appear in the pseudo-turbulent stress tensor $\overline{\boldsymbol{T}}_k^T$ (Eq. 2.27). As remarked in Subsection 2.3.1, this term quantifies momentum fluxes arising from both the turbulent fluctuations within each phase and the fluctuations of the velocity of phase k due to the presence of the other phase and doesn't necessarily vanish even if the flow is laminar [61]. In double-average formulations, either Favre-averaged or not, the pseudo-turbulent stress tensor is usually neglected before averaging the equations the second time, and correlations between the fluctuating velocity of each phase comes from a Reynolds decomposition, therefore are necessarily related to turbulence. However, since in all cases the correlations are often treated in analogy to turbulent single-phase flows, for simplicity of notation the symbol $\mathbf{u}$ will refer as either $\hat{\mathbf{u}}$, $\hat{\mathbf{U}}$ or $\mathbf{U}$.

Ishii [70] reports a closure for the correlations $\langle\mathbf{u}_j'\mathbf{u}_j'\rangle$ based on a Mixing Lenght model. However, a more common choice is to make use of a standard Boussinesq approximation [44]:

$$\langle\mathbf{u}_j'\mathbf{u}_j'\rangle = -\nu_{tj}\overline{\boldsymbol{S}}_j - \frac{2}{3}\boldsymbol{I}\left[k_j + \nu_{tj}\left(\nabla\cdot\mathbf{u}_j\right)\right] \tag{2.74}$$

in which ν_{tj} is the eddy viscosity ($j = c, p$); k_j the turbulent kinetic energy; and $\overline{\boldsymbol{S}}_j$ the strain rate tensor defined in Eq. 2.40. Eq. 2.74 requires proper modeling of the terms ν_{tj} and k_j. Generally, the eddy viscosity of the fluid phase ν_{tc} is expressed as a function of the turbulent kinetic energy $k_c = k$ and the disspation rate $\epsilon_c = \epsilon$ as in single-phase flows:

$$\mu_{tc} = C_\mu \frac{k^2}{\epsilon} \tag{2.75}$$

where C_μ is a numerical constant. Transport equations for k and ϵ are needed, while k_p may be related to k by algebraic expressions. As in single-phase flows, those equations contain an unsteady term, a convective term, a diffusion term, and a source term:

$$\frac{\partial}{\partial t}(\alpha_c \rho_c k) + \nabla \cdot (\alpha_c \rho_c k \mathbf{u}_c) = \nabla \cdot \left(\alpha_c \rho_c \frac{\nu_c^t}{\sigma_k} \nabla k \right) - \alpha_c \rho_c \left(\langle \mathbf{u}'_c \mathbf{u}'_c \rangle \nabla \mathbf{u}_c - \epsilon \right) + \Pi_k \tag{2.76}$$

$$\frac{\partial}{\partial t}(\alpha_c \rho_c \epsilon) + \nabla \cdot (\alpha_c \rho_c \epsilon \mathbf{u}_c) = \nabla \cdot \left(\alpha_c \rho_c \frac{\nu_c^t}{\sigma_\epsilon} \nabla \epsilon \right) + \alpha_p \rho_c \frac{\epsilon}{k} \left(C_{1\epsilon} \langle \mathbf{u}'_c \mathbf{u}'_c \rangle \nabla \mathbf{u}_c - C_{2\epsilon} \epsilon \right) + \Pi_\epsilon \tag{2.77}$$

The terms Π_k and Π_ϵ must be consistent with the derivation of mass and momentum conservation equations. In the single-averaged formulation of Enwald *et al.* [44] ($\mathbf{u} = \hat{\mathbf{u}}$), they are functions of the drift velocity $\langle \mathbf{u}'_c \rangle^{X_p \rho_p}$. In the double-averaged formulation of Burns *et al.* [15] and Rundqvist *et al.* [127] ($\mathbf{u} = \hat{\mathbf{U}}$), they are given by:

$$\Pi_k = \frac{\langle \alpha_c \rangle \langle \alpha_p \rangle \rho_c}{\langle \tau_p \rangle} \left[-2k + \langle \mathbf{u}'_c \cdot \mathbf{u}'_p \rangle - \frac{1}{\langle \alpha_p \rangle} \langle \mathbf{u}'_c \alpha'_p \rangle (\mathbf{u}_c - \mathbf{u}_p) + (\mathbf{u}_c - \mathbf{u}_p)^2 \right] \tag{2.78}$$

$$\Pi_\epsilon = \frac{\langle \alpha_c \rangle \langle \alpha_p \rangle \rho_c}{\langle \tau_p \rangle} \left[-\epsilon + \nu \langle \nabla \mathbf{u}'_c : \nabla \mathbf{u}'_p \rangle \right] \tag{2.79}$$

in which the particle relaxation time τ_p has been already defined in Eq. 1.4. The first three terms in Eq. 2.78 are the additional dissipation owning to the particles, that is the turbulent kinetic energy transfer to the particulate phase; the latter one accounts for the additional production that larger particles can cause. The term Π_ϵ represents the influence of particles on fluid-phase dissipation.

Elgobashi and Abou-Arab [43] report the equations for k and ϵ applying their double-average method ($\mathbf{u} = \mathbf{U}$). These equations consists of 38 and 67 terms respectively, and involve correlations up to the fourth order, most of which are claimed negligible. A simplified derivation is also reported by Chen and Wood [16]. In the final form, the Authors retained the correlations between the fluctuating velocity and volume fraction of the fluid $\langle \alpha'_c \mathbf{u}'_c \rangle$, modeled according to the eddy-viscosity hypothesis (Eq. 2.69), between the fluctuating velocity of the phases $\langle \mathbf{u}'_p \cdot \mathbf{u}'_c \rangle$, and between their derivatives $\langle \nabla \mathbf{u}'_c : \nabla \mathbf{u}'_p \rangle$.

In both double-average derivations, the terms $\langle \mathbf{u}'_p \cdot \mathbf{u}'_c \rangle$ and $\langle \nabla \mathbf{u}'_c : \nabla \mathbf{u}'_p \rangle$ need to be modeled. Many closures have been developed for dilute gas-solid flows [92], among which the most commonly-used ones are those of:

- POURAHMADY and HUMPHREY(cited in [127]):

$$\langle \mathbf{u}'_p \cdot \mathbf{u}'_c \rangle = 2k \frac{\tau_{li}}{\tau_{li} + \tau_p} \tag{2.80}$$

$$\langle \nabla \mathbf{u}'_c : \nabla \mathbf{u}'_p \rangle = \frac{\epsilon}{\nu} \frac{\tau_{li}}{\tau_{li} + \tau_p} + \frac{\tau_{li}}{(\tau_{pL} + \tau_p)^2} \nabla k : \nabla \tau_{pL} \tag{2.81}$$

in which τ_{li} is the Lagrangian integral time scale of the fluid, which is not well characterized. According to Shirolkar *et al.* [138], this parameter can be viewed as the characteristic large eddy lifetime, and should be between 0.165 and 0.27 the ratio between the turbulent kinetic energy of the fluid k and its dissipation rate ϵ [16, 99, 138]. In the model of Pourahmady and Humprey, $\tau_{li} = 0.41k/\epsilon$, which Chen and Wood [16] report to be 2.5 times the time scale of the most energetic eddies.

- MOSTAFA and MONGIA [110]:

$$\langle \mathbf{u}'_p \cdot \mathbf{u}'_c \rangle = 2k \frac{\tau_{li}}{\tau_{li} + \tau_p} \tag{2.82}$$

$$\langle \nabla \mathbf{u}'_c : \nabla \mathbf{u}'_p \rangle = 2\epsilon \frac{\tau_{li}}{\tau_{li} + \tau_p} \tag{2.83}$$

in which the Lagrangian integral time scale of the fluid τ_{li} is given by $0.35k/\epsilon$.

- CHEN and WOOD [16]:

$$\langle \mathbf{u}'_p \cdot \mathbf{u}'_c \rangle = 2k \cdot \exp\left(-B_k \frac{\tau_p}{\tau_{li}}\right) \tag{2.84}$$

$$\langle \nabla \mathbf{u}'_c : \nabla \mathbf{u}'_p \rangle = 0 \tag{2.85}$$

in which: B_k is an empirical constant, assumed equal to 0.0825; and $\tau_{li} = 0.165k/\epsilon$. According to the Authors, their model is not valid for very small particles or if $\langle \tau_p \rangle$ is close to the time scale of the dissipative eddies, that is $\sqrt{\nu/\epsilon}$.

The proper modelling of the correlations $\langle \mathbf{u}'_p \mathbf{u}'_c \rangle$ and $\langle \nabla \mathbf{u}'_c : \nabla \mathbf{u}'_p \rangle$, describing the effect of particles on production and dissipation of the fluid turbulence, is a fundamental feature in the modelling of solid-gas flows [92, 127]. However, those terms are usually ignored in solid-liquid flows [17, 20, 48, 152], in which possibly the only added source in k and ϵ equations is due to phase diffusion effects, therefore associated to $\langle \alpha_p \mathbf{u}'_c \rangle$ and modeled via Eq. 2.69 [9, 65, 97, 160].

When modeling $\langle \mathbf{u}'_p \mathbf{u}'_p \rangle$ by the standard Boussinesq approximation (Eq. 2.74), proper closures for the particle eddy viscosity ν_{tp} must be given. The simplest approach is to make use of algebraic models, which express ν_{tp} as a function of the eddy viscosity of the carrier fluid phase ν_{tc}. The relation between ν_{tp} and ν_{tc} must account for the *intertia effect* [109, 138], that is the decreasing reponse of particles on the fluid turbulence if particle relaxation time τ_p is not negligible with respect to the fluid integral time scale τ_Λ. An inertial limit behavior [16, 99], i.e. $\nu_{tp} \rightarrow \nu_{tc}$ for $\tau_p \ll \tau_\Lambda$ (therefore for the inte-

gral scale Stokes number $S_\Lambda = \tau_p / \tau_\Lambda \to 0$) must be satisfied. Some studies simply use $\nu_{tp} = \nu_{tc}$, which is a good approximation for very low Stokes numbers. Several algebraic models includes a dependence of τ_p on the Stokes number:

1. WU and LIU (cited in [99]):

$$\frac{\nu_p^t}{\nu_c^t} = \frac{1}{(1 + \tau_p/\tau_{li})^2} \tag{2.86}$$

   in which τ_{li} is the lagrangian integral time scale of the fluid phase, already defined at Page 40, assumed equal to $0.27k/\epsilon$.

2. CHEN and WOOD[1] [16]:

$$\frac{\nu_p^t}{\nu_c^t} = \frac{1}{1 + \tau_p/\tau_{li}} \tag{2.87}$$

   in which $\tau_{li} = 0.165k/\epsilon$.

3. POURAHMADY and HUMPHREY (cited in [16]):

$$\frac{\nu_p^t}{\nu_c^t} = 1 - \frac{\tau_{li}^2 \epsilon / (15\nu)}{3K^2 / (K+2)} \tag{2.88}$$

   where: $\tau_{li} = 0.41k/\epsilon$ (as already noticed, Chen and Wood [16] state that such parameter is 2.5 times the lifetime of the most energetic eddies), and $K = 2\tau_p/\tau_{li}$. Chen and Wood [16] highlight doubts on this model which, despite recovering the intertial limit for $S \to 0$, yelds negative values of ν_p^t for reasonable values of $\sqrt{\nu/\epsilon}$, τ_p and τ_{li}.

4. MOLS and OLIEMANS [109]:

$$\frac{\nu_p^t}{\nu_c^t} = \gamma_{\text{inert}} \cdot \gamma_{\text{cross}} = \frac{1}{\sqrt{1 + \tau_p/\tau_{li}}} \cdot \frac{1}{\sqrt{1 + \left(\frac{g\tau_p\tau_{li}}{L}\right)^2}} \tag{2.89}$$

   in which the two coefficients γ_{inert} and γ_{cross} account for the interial and crossing trajectory effects respectively. The *crossing trajectory* effect is the phenomenon of migration of a particle from one eddy to another before the eddy decay [138], which leads to a decreased particle diffusivity. The Authors developed this model for the horizontal pipe flow case, and suggest to evaluate τ_{li} as 0.01 of the ratio between the pipe diameter and the pipe bulk-mean velocity.

All the above described models are based on the assumption of homogeneous isotropic turbulence. Anisotropic models for dispersed two-phase flows have been reported in technical literature. An anisotropic eddy-viscosity based model was developed by Loth [99]. Complex second order closures are reported by Mashayek and Pandya [102], but these models do not appear very commonly-used.

---

[1] Also attributed to Hinze [20] and Melville and Bray [138]

2.4   The model of Spalding

Among the two-fluid models available in literature, the one developed by Prof. Brian Spalding of Imperial College appears of particular interest for the complex flows addressed in the present thesis due to its stability and ease to attain convergence. The model is embedded in the general purpose, commercial CFD code PHOENICS and uses the SIMPLEST [143] and IPSA [144] algorithms of Spalding to solve the finite volume algebraic equations.

The model includes phase diffusion terms in all conservation equations to account for the effect of correlations between fluctuating velocity and fluctuating volume fractions. Originally, these terms came from intuitions of Prof. Brian Spalding on the basis of an analogy with turbulent dispersion of a passive scalar, rather than from a rigorous derivation. However, as already reported, it was later demonstrated that these terms arise if the balance equations are obtained from a double average, the latter being a non weighted time average [15].

The model solves the following mass and momentum conservation equations for both phases:

$$\frac{\partial}{\partial t}\left(\alpha_k \rho_k\right) + \nabla \cdot \left(\alpha_k \rho_k \mathbf{u}_k - \rho_k \frac{\nu_c^t}{\sigma_\alpha}\nabla \alpha_k\right) = 0 \qquad (2.90)$$

$$\frac{\partial}{\partial t}\left(\alpha_k \rho_k \mathbf{u}_k\right) + \nabla \cdot \left(\alpha_k \rho_k \mathbf{u}_k \mathbf{u}_k\right) = -\alpha_k \nabla p +$$
$$\nabla\left[\alpha_k \rho_k \left(\nu_c + \nu_c^t\right)\nabla \mathbf{u}_k\right] + \alpha_k \rho_k \mathbf{g} + \mathbf{M}_k^d + \nabla \cdot \left(\rho_k \mathbf{u}_k \frac{\nu_c^t}{\sigma_\alpha}\nabla \alpha_k\right) \qquad (2.91)$$

The generalized drag $\mathbf{M}_k^d$ accounts for drag, lift and virtual mass. The first is evaluated as for a single sphere in an infinite medium (Eq. 2.50), with the drag coefficient $C_{d,s}$ obtained from the correlation of Clift *et al.* [26] illustrated in Appendix A. Lift and virtual mass are calculated by Eq. 2.59 and Eq.2.64 respectively. The eddy viscosity of the fluid phase ν_{tc} is obtained from a two-equation model including phase-diffusion terms. In particular, the built-in k-ϵ model is given by Eq. 2.76-2.77 with $\Pi_k = \Pi_\epsilon = 0$. Free slip is applied to the particles at solid walls.

Chapter 3

Development of the two-fluid model: the horizontal pipe case

The flow of solid-liquid mixture in horizontal pipes is now investigated. Different reasons contribute to explain this choice. First of all, this benchmark case is of interest for many engineering applications. Moreover, the simplicity of the geometry leads to computationally cheap simulations, but, at the same time, the flow involves many physical mechanisms which are very complex to model. At last, the literature covering this topic is rather abundant, in terms of both the theoretical description of the physical phenomenon and the availability of experimental data, numerical results, and predictive models.

The present chapter is divided in six sections. In Section 3.1 the main features of solid-liquid flows in horizontal pipes are illustrated on the basis of the knowledge of the phenomenon inferred from technical literature. In Section 3.2 a summary of previous investigations is reported, classifying the studies according to the approach followed (experimental tests, physically-based models, numerical simulations). In Section 3.3 the performance of the model of Spalding [144] which, due to its peculiar robustness and stability, is taken as the starting point for the development of a new two-fluid model, is analyzed in detail by comparison to the experimental data. Section 3.4 describes the process of development of the new model. Afterwards, in Section 3.5 the performance of the new model is investigated by comparison to experimental data from literature over a wide range of operating conditions. At last, in Section 3.6 the applicability of the new model, together with a comparison to the existing ones, is discussed.

3.1   Flow patterns of solid-liquid flows in horizontal pipes

The turbulent flow of solid-liquid mixtures in horizontal pipes is very complex, as it is the result of the interactions between the turbulent flow and the particles, between the particles and the wall, and among the particles. According to Doron and Barnea [34], who recovered and extended earlier works, three different patterns can be identified as the slurry superficial velocity decreases:

FULLY-SUSPENDED FLOW

Pseudo-homogeneous flow

(a)

Heterogeneous flow

(b)

FLOW WITH A MOVING BED

Moving bed

(c)

FLOW WITH A STATIONARY BED

Stationary deposit

(d)

α_p

α_p

α_p

α_p
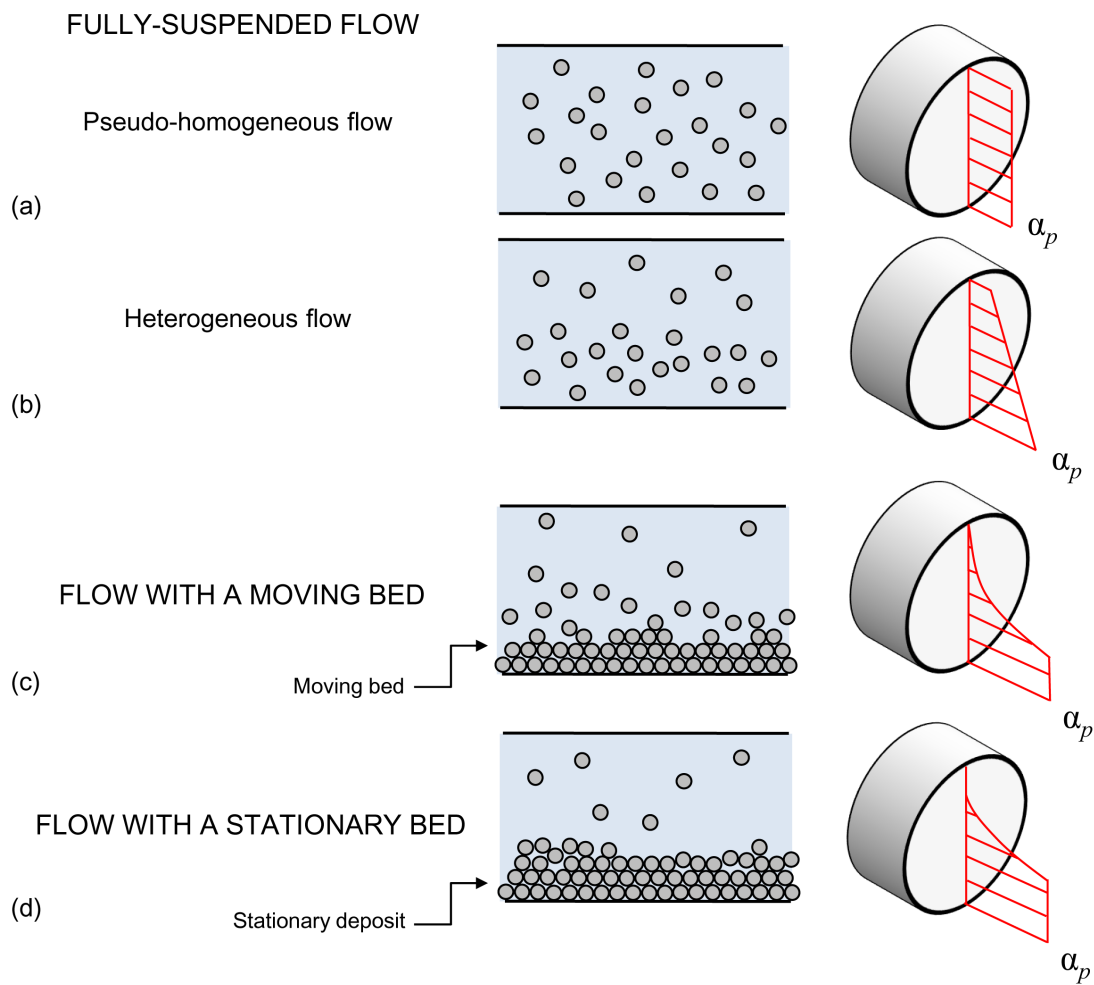
Figure 3.1: Flow patterns for solid-liquid flows in horizontal pipes, according to Doron and Barnea [34]: (a) pseudo-homogeneous flow; (b) heterogeneous flow; (c) flow with a moving bed; (d) flow with a stationary bed.

- FULLY-SUSPENDED FLOW

  At high velocity turbulence is effective in keeping all the particles suspended. This flow pattern can be further classified between *pseudo-homogeneous* flow, in which the solids are distributed nearly uniformly across the pipe cross-section (Figure 3.1(a)); and *heterogeneous* flow, where there is a concentration gradient in the direction perpendicular to the pipe axis, with more particle transported at the lower part of the pipe cross section (Figure 3.1(b)). This pattern is the most significant for the application, therefore will be the main focus in the present thesis.

- FLOW WITH A MOVING BED

  At lower velocity the solid particles accumulate and form a packed bed layer which moves along the pipe bottom. The concentration of this layer is the maximum packing one, or nearly so. A heterogeneous suspension occupies the upper part of the pipe cross-section (Figure 3.1(c)).

- FLOW WITH A STATIONARY BED

  When the mixture velocity is too low to move all the immersed particles, a stationary deposit is observed at the pipe bottom. On top of this deposit, particles tend to roll and tumble as the fluid above tends to move the solids by entrainment; therefore, they form a separate moving layer at the top of the stationary bed, often characterized by dune-like form. The rest of the flow system is filled with heterogeneous suspension flow (Figure 3.1(d)).

The identification of the flow regime of a given mixture can be made by analyzing the solids concentration distribution over the pipe cross section. Since the concentration is typically uniform along each horizontal chord, the distributed concentration field can be reduced to the profile along the vertical diameter. The trend of the solids concentration profile allows distinguishing among pseudo-homogeneous, heterogeneous and bed flows. A discrimination between moving and stationary bed flows is difficult on the basis of this parameter only, as, in both cases, the solids concentration of the bed is the maximum packing one. During experimental campaigns, it is usually performed by visual observation of the flow of the mixture through the pipe [121].

The flow regimes can be also identified by a plot of pressure gradient versus slurry superficial velocity, qualitatively depicted in Figure 3.2 on the basis of the work of Baha Albunaga [8]. Threshold values of velocity define the transition between flow patterns. To clarify these aspects, the different mechanisms of frictional losses will be discussed below.

The way in which the particles affect the dissipations is a very complex matter. Typically, the presence of a solid phase produces an increase of the losses with respect to the single-phase flow case. It is worth noticing that, under specific flow conditions, either negligible variations of even a decrease were observed [139]. However, this eventuality was not considered here, as it is pronounced only for vertical pipe flows and anyway very rare. The increase in pressure gradient is due to the additional frictional mechanisms due to the interactions between the particle with each other, the suspending liquid, and the
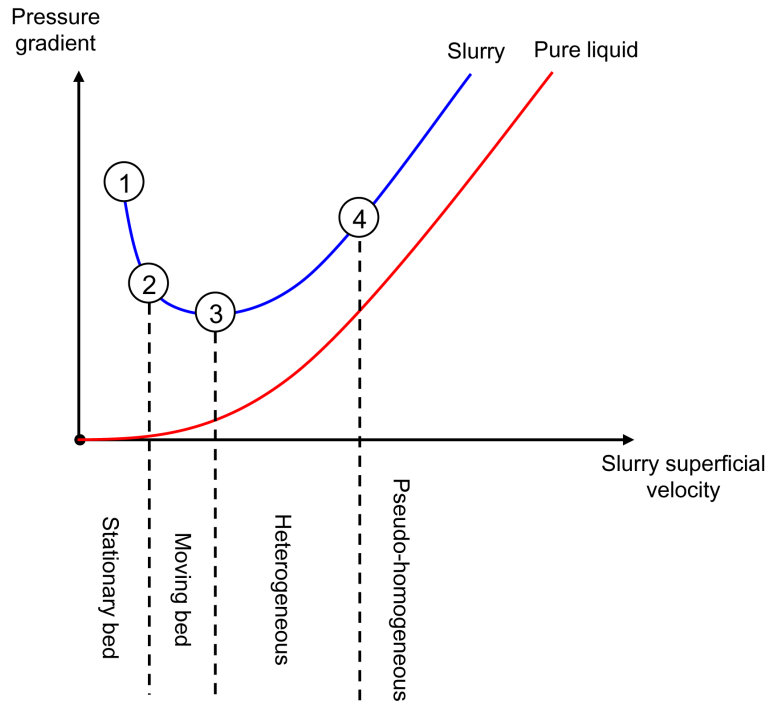
Figure 3.2: Flow patterns for solid-liquid flows in horizontal pipes identified by the plot of pressure gradient versus slurry superficial velocity. The curve for an equal flow rate of pure liquid is reported too.

pipe wall. In a fully-suspended flow, the frictional loss of the two-phase flow is commonly considered as a combination of the *viscous* friction and the *mechanical* friction [75, 105]. The former is a "liquid-like" friction, due to the liquid viscosity in the laminar sublayer over the pipe wall. If the particles are fine enough to be trapped within the laminar sublayer (which is actually not the case of the flows considered in this work), the density of the fluid in the laminar sublayer will be changed by the immersed particles.

If the particles are much larger that the thickness of the laminar sublayer, they tend to move outside the laminar sublayer to escape from the high shear force in this region, and the laminar sublayer is, theoretically speaking, formed entirely by the liquid, thus resulting in a viscous friction equal to that of the single-phase flow case. However, the real flow is much more complicated: the solid particles are subjected not only to a lift force which causes them to migrate towards the pipe center, but also to a turbulent dispersive action (turbulent eddies tend to disperse the particles in all directions) and a collisional dispersive action (collisions among the particles cause them to disperse more uniformly in the liquid), which both push the particles towards the pipe wall resulting in additional losses due to particle-wall interactions. This explains why in Figure 3.2 the blue curve which refers to the solid-liquid case is above the red one referring to the pure liquid case. The transition between the two sub-patterns of fully suspended flow, namely the pseudo-homogeneous and the heterogeneous flow, is defined in terms of a threshold velocity V_4. Some empirical correlations for its estimation are reported by

Baha-Albunaga [8].

In the case of flows with a moving bed, the contact between the bed and the wall is a significant mechanism of frictional losses. The shear stresses arising from this mechanism may be evaluated by a model developed by Wilson (reported by Matousek [105]), which assumes that there is a hydrostatic-type of distribution of the normal stresses in the vertical direction through the bed and that the normal stresses at the wall produces the solids shear stresses according to Coulomb's law. These additional Coulomb-type stresses determine the increase in pressure gradient as the bed forms, explaining why the transition to a moving bed flow corresponds to a minimum in pressure gradient versus slurry bulk-mean velocity (Figure 3.2). The threshold velocity V_3 between the two flow regimes is usually referred to as *deposition velocity*. There are several correlations - usually of empirical nature - related to the deposition velocity in literature: an overview is reported by Baha-Albunaga [8] and Pecker and Helvaci [121]. These equations appear mutually incompatible and the first impression is that they may provide only a very rough estimation of this parameter. Specific studies proved the inadequacy of some of these models for multi-sized commercial slurries [82]. By way of example, it is reported the formula of Wasp, which is one of the simplest and most frequently cited in literature:

$$V_3 = 4 \left(d_p/D_p\right)^{1/6} C^{1/5} \sqrt{2gD_p \left(\frac{\rho_p}{\rho_c} - 1\right)} \tag{3.1}$$

where: d_p is the particle size, D_p the pipe diameter, C the mean delivered solids volume fraction, g the gravitational acceleration, and ρ_p and ρ_c the density of the particles and the fluid respectively. The analysis of the performance of the Wasp model, reported in Appendix C revealed its rather poor predictive capacity. More precisely, Eq. 3.1 appears likely to underestimate the deposition velocity.

As the slurry velocity decreases, the bed stops and a stationary deposit forms at the bottom of the pipe. For this flow pattern, the pressure gradient is due to the following mechanisms: *viscous* friction and *mechanical* friction of the heterogenous flow in the upper part of the pipe; Coulomb-type stresses due to the contacts between the intermediate moving layer and the pipe wall; and the friction on the top of the stationary bed. The threshold velocity between the stationary bed and the moving bed, indicated as V_2 in Figure 3.2, is called *minimum deposition velocity*, and can be estimated by different models available in literature [105].

Actually, another threshold velocity is depicted in Figure 3.2, that is the minimum velocity below which all the particles are stuck at the bottom and therefore the system reduces to a single-phase flow over a fixed granular bed.

One final peculiar feature of the flow of solid-liquid slurries in horizontal pipes concerns the shape of the velocity profile in fully-suspended flows. In fact, unlike that of a single-phase flow, the velocity profile of a solid-liquid mixture are asymmetric with respect to the pipe axis, with the maximum velocity above it (Figure 3.3). This behaviour was interpreted by different authors considering that, due to the effect of gravity, the slurry density in the lower part of the pipe is higher than that in the upper part. As a
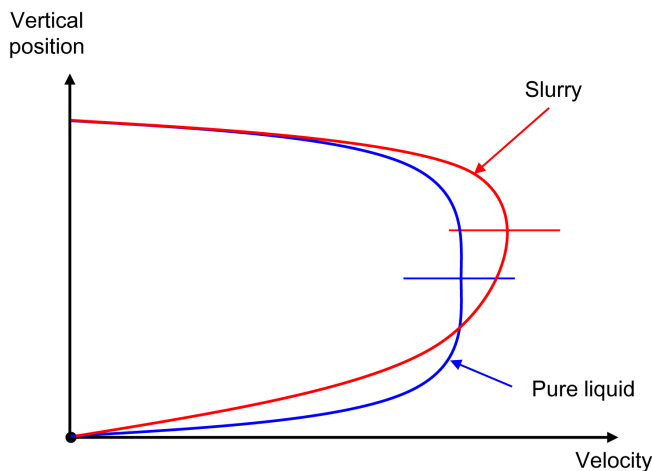
Figure 3.3: Qualitative trend of velocity profile for the single-phase and two-phase flow case

result, the fluid spends more energy to drive the particles in the lower part, resulting in a lower slurry velocity in that area. Actually, the asymmetry of the velocity profile is almost undetectable for pseudo-homogeneous flows.

From an operational point of view, the realization of a certain flow pattern depends on several parameters, such as the pipe diameter, the flow rate, the characteristics of the particles (size, shape, density), and the mean solids concentration. Flow pattern maps have been developed to help engineers predict the flow pattern for a given combination of the significant parameters [34]. Although in principle these maps may be a powerful tool for designers, in practice the great number of independent variable makes it difficult to attain an answer of general validity from them.

3.2 Previous works

As already mentioned at the beginning of the present chapter, many investigations concerning the flow of solid-liquid slurries in horizontal pipes are reported in literature. A brief summary is given below, distinguishing among experimental campaigns aimed at collecting data to understand the phenomenon, and predictive models, in turn divided between simplified physically-based models and numerical models.

3.2.1 Experimental tests

Several experimental investigations have been performed to study the behaviour of solid-liquid slurry flows in horizontal pipes. Researches are usually focused on the solids concentration profile, the pressure gradient, and, less frequently, the velocity profile and the particle deposition velocity.

In most cases, only fully suspended flows were considered, due to the importance of this pattern for many applications.

The researches of Kaushal, Tomita and co-workers are worth mentioning in this field. In first works [80, 82], the authors measured the solids concentration profile and the pressure gradient for multi-sized slurries in a 105 mm diameter pipe. The mixtures were made of zinc-tailings with different sizes ranging from about 30 to 740 μm. Particle density is 2815 kg/m^3, the specific gravity being thus 2.82. The slurry superficial velocity was between 2 and 3.5 m/s, and the mean solids concentration between 4 and 26%. Measurements of solids concentration were performed using an L-shape probe (Figure 2.3(a)). In a later investigation, Kaushal and Tomita [81] studied the flow of the same mixture of water and multi-sized zinc tailings in a 105 mm diameter pipe and a in 200 mm x 50 mm rectangular duct, comparing pressure drop and solids concentration at the bottom. They concluded that, the Reynolds number being the same, the pressure gradient is lower in the rectangular duct case because secondary flows decrease the mechanical contribution to friction, caused by the interactions between the particles and the walls. In 2005, Kaushal and co-workers [77] measured pressure gradient and solids concentration profile of a mixture a mixture of water and either mono- and bi-dispersed spherical glass beads with density of 2465 kg/m^3 and size of 125 and 440 μm for the following flow conditions: pipe diameter = 54.9 mm; slurry superficial velocity between 1 and 5 m/s; mean delivered solids concentration between 10 and 50%. An L-shape probe was used to measure local values of solids concentration. A couple of years later [79], the authors repeated the same measurements for the mono-dispersed mixtures by means of the absorption method (Figure 2.1), concluding that the former method doesn't allow evaluating correctly the solids concentration close to the pipe bottom for the bigger particles.

Kumar *et al.* [88] measured the solids concentration profile (using an L-shape probe) and the pressure gradient of mixtures of water and multi-sized ashes for the following flow conditions: pipe diameter = 150 mm; slurry superficial velocity between 0.5 m/s and about 4.5 m/s; particle density about 2090 kg/m^3; particle average size between 40 and 150 μm; mean delivered solids concentration up to about 50%. Gillies *et al.* [53] report measurements of solids concentration profile, velocity profile and pressure drop of sand-water mixtures. Two kind of monodisperse sands, with particle density of 2650 kg/m^3 and mean particle size of 90 and 280 μm, were considered. The pipe diameter is 103 mm, the slurry bulk-mean velocity between 1.3 and about 8 m/s, the mean solids concentration between 10 and 45%. Values of solids concentration are obtained using the absorption method. Skudarnov *et al.* [140] measured the pressure gradient of slurries made of water and bi-dispersed glass beads. The solid component of the slurry was 50% by 50% by volume combinations of beads with two densities (2490 and 4200 kg/m^3) and three narrow particle size distribution (mean particle size = 125, 255 and 515 μm). The bulk-mean velocity of the mixture ranged between 0.7 and 3 m/s. The mean solids concentration is 5, 10 or 15%. Shaan *et al.* [136] analyzed the effect of particle shape on solids concentration profile - measured by means of the absorption method - and pressure gradient of solid-liquid slurries. Two different sands (density = 2655 kg/m^3), namely Lane Mountain Sand and Ottawa Sand, and spherical glass beads (density =

2440 kg/m^3) were considered; in all cases, particle size is around 100 μm. The particles
are characterized by different shape, which is quantified by reference to the axis ratio
and the circularity index, already defined in Section 1.4. The following flow conditions
were tested: pipe diamter = 158.5 mm; slurry superficial velocity between 1 and 5 m/s;
and mean delivered solids concentration between 15 and 40%. Kim *et al.* [83] performed
measurements of pressure gradient of sand-water mixtures in a 200 mm diameter circular
pipe and a 200 mm side square duct. The sand particles have a density of 2645 kg/m^3
and mean size of 540 μm. The slurry superficial velocity is between about 2 and about
6.25 m/s, the mean delivered solids concentration between 5 and 22%.

Fewer authors extended the experimental research to other flow patterns. Roco and
Shook [126] performed a comprehensive investigation of the flow of sand-water mix-
tures in horizontal pipes. Four kinds of sand, with density 2650 kg/m^3 and particle
size between 165 μm and 13 mm, were flowing in pipelines with various diameters (be-
tween 50 and 500 mm), at mean delivered solids concentration up to about 40%. The
slurry superficial velocity was between 1.6 and 4.33 m/s. The authors reported several
solids concentration profiles measured by the absorption method and few velocity pro-
files. They didn't identify the flow pattern according to the more recent classification of
Doron and Barnea [34] (Figure 3.1) and didn't report plots of pressure gradient versus
slurry velocity from which this information can be inferred (Figure 3.2). However, for
the smallest particles the data suggest suspended flow, whereas for the largest diameters
the indications are for moving-bed flow. Matousek [103, 104] investigated experimentally
the flow of sand-water mixtures for fully-suspended and moving-bed flows. He reported
measurements of concentration distribution, obtained by the absorption method, and
pressure gradient. He considered mono- and bidispersed mixtures obtained from combi-
nation of three kind of sands, with narrow size distribution and average size between 120
μm and 1.85 mm, but didn't reported the value of the density. The pipe has an inner
diameter of 150 mm, the slurry superficial velocity varies between about 1 and 9 m/s,
the mean solids concentration ranged between 25 and 43%. Jiang and Zhang [75] mea-
sured the pressure gradient as a function of the bulk-mean velocity for mixtures of solid
nitrogen particles (density = kg/m^3, diameter = 1.0 mm) and liquid nitrogen (density
= 867 kg/m^3) in a 10 mm diameter pipe. The slurry superficial velocity ranges between
0.5 and 3.5 m/s, and the mean delivered solids concentration between 10 and 30%.

3.2.2   Simplified physically-based models

Simplified physically-based models have been developed to predict specific characteris-
tics of the phenomenon. These models are usually semi-theoretical, in the sense that
they have a physical bases but make use of empirical closures. Simplified models are
commonly-used to estimate the pressure gradient of the mixture; in this case, they are
based on a global formulation, obtained by integrating the mass and momentum conser-
vation equations on a control volume with finite dimension. Simplified physically-based
models have also been developed to estimate the solids concentration profile. In most
cases, these models can be used only for a specific flow condition. For completeness of
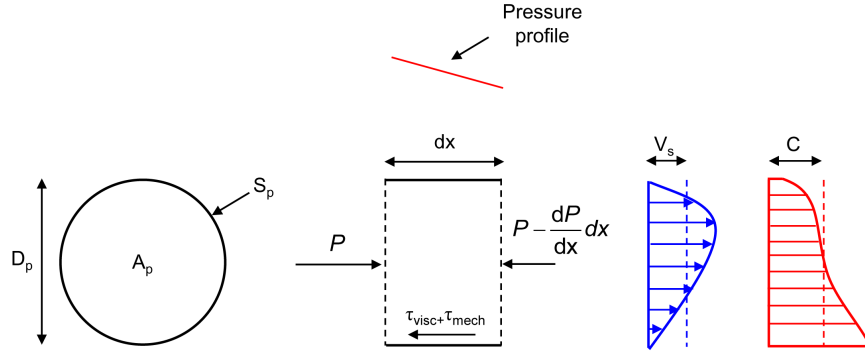
Figure 3.4: Sketch of global-formulation models for fully-suspended flows

exposition, a brief overview of the models for fully-suspended, moving-bed and stationary bed flows is provided. The main focus will be on fully-suspeded flow, as this is the flow pattern most commonly encountered in the applications to which the present thesis is addressed. Despite their importance and effectiveness for may engineering problems, these models will not be longer considered in this thesis, since they have a application-specific formulation which doesn't allow extension to more complex flows.

Models for fully-suspended flows

Physically-based models based on a global formulation are frequently used for estimating the pressure gradient in case of fully-suspended flows. With reference to Figure 3.4, showing a control volume within the pipe, a force balance along the flow direction yields:

$$A_p \frac{\mathrm{d}P}{\mathrm{d}x} = -\left(\tau_{\mathrm{visc}} + \tau_{\mathrm{mech}}\right) S_p \tag{3.2}$$

in which $\mathrm{d}P/\mathrm{d}x$ is the pressure gradient; A_p and S_p are the area of the pipe section and its perimeter; and τ_{visc} and τ_{mech} are the shear stresses due to the two contribution to friction, namely the *viscous* one and the *mechanical* one, already mentioned in Section 3.1. The effectiveness of the two contributions, and therefore the expressions for τ_{visc} and τ_{mech}, depend mainly on the size of the particles compared to that of the viscous sub-layer. If the particles are smaller than the thickness of the viscous sub-layer, the mechanical contribution to friction is negligible and the viscous stresses τ_{visc} are given by:

$$\tau_{\mathrm{visc}} = \frac{1}{2}\rho_m f_m V_s^2 \tag{3.3}$$

in which: $\rho_m = (1 - C)\rho_c + C\rho_p$ and f_m are the density and the friction factor of the mixture, respectively (C is the mean delivered solids volume fraction); and V_s is the slurry superficial velocity. The term f_m is evaluated as for single-phase Newtonian fluid, but with a different definition of the Reynolds number: Doron *et al.* [35] defined Re as $\rho_m D V_s/\mu_m$, being μ_m the viscosity of the mixture which can be calculated by any of the expressions reported in Appendix B. Wilson and co-workers [154] reported a definition

of Re based on the density and viscosity of the pure liquid, but underlined that this is valid only for moderate concentrations. In this case, the friction factor of the mixture f_m becomes equal to that of an equal flow of liquid alone (f_c). As in single-phase flows, the friction factor depends on the flow regime (either laminar or turbulent); Doron *et al.* [35] suggested the following correlations:

$$f_m = 16\mathrm{Re}^{-1} \qquad\qquad f_m = 0.046\mathrm{Re}^{-0.2} \qquad\qquad (3.4)$$

valid in the laminar and turbulent regime respectively. If the particles are bigger than the thickness of the viscous sub-layer, the particles don't affect the viscosity of the mixture. Therefore, the viscous stresses τ_v are evaluated by means of Eq. 3.3-3.4 with the Reynolds number defined in terms of the viscosity of pure liquid μ_c. However, the density usually remains that of the mixture ρ_m [35]. In this case the mechanical contribution to the pressure gradient, arising from particle-wall interactions and quantified by the stresses τ_{mech}, becomes significant. Different expressions, mainly of empirical nature, have been proposed to model τ_{mech}. The most commonly-used are those of:

1. SHOOK AND BARTOSIK [11, 139]

$$\tau_{\mathrm{mech}} = \frac{8.3018 \cdot 10^7}{\mathrm{Re}} D_p^2 \rho_p d^2 \left[\left(\frac{C}{\alpha_{\max}} \right)^{1/3} - 1 \right]^{1.5} \left(\frac{\tau_{w,c}}{\mu_c} \right)^2 \qquad (3.5)$$

   where $\mathrm{Re} = D_p V_s / \nu_c$, and $\tau_{w,c}$ is the wall shear stress of an equivalent flow rate of pure liquid. All the other symbols have been already defined. The model was calibrated with respect to the flow of sand-water slurries with three different particle sizes (1.37, 1.5 and 3.4 mm) in two narrow vertical pipes ($D = 26$ and 40 mm).

2. GILLIES AND SHOOK [54]

$$\tau_{\mathrm{mech}} = \frac{1}{2}\rho_p f_p V_s^2 = \frac{1}{2}\rho_p \left\{ 0.00002 \left[\left(\frac{C}{\alpha_{\max}} \right)^{1/3} - 1 \right]^{-2} \right\} V_s^2 \qquad (3.6)$$

   This correlation was obtained from fitting of experimental data about the flow of 175 μm sand particles in a 495 mm diameter pipe at high velocity.

3. MATOUSEK [105]

$$\tau_{\mathrm{mech}} = 0.499 \left[\left(\frac{C}{\alpha_{\max}} \right)^{1/3} - 1 \right]^{-1.36} V_s^{1.02} \qquad (3.7)$$

$$\tau_{\mathrm{mech}} = 0.991 \left[\left(\frac{C}{\alpha_{\max}} \right)^{1/3} - 1 \right]^{-0.81} V_s^{0.99} \qquad (3.8)$$

   for horizontal and vertical flow respectively. The shear stress is in Pascal, the slurry velocity in m/s; therefore, the numerical coefficient is not dimensionless.

The expressions were obtained from the flow of sand-water particle with particle size of 120 and 370 m/s, flowing in pipes with diameter of 150 mm.

Actually, the shear stress of solid-liquid flows may be affected by the presence of the wall lubrication force introduced in Sub-section 2.3.2. As previously reported, Wilson and co-workers [154, 155] gave a theoretical interpretation of the origin of this force and developed a model accounting or its effect on the pressure gradient. The model, which can be applied to both fully-suspended and moving-bed flows, starts from a theoretical basis but makes use of empirical closures. The pressure gradient of the mixture is given by:

$$\frac{\mathrm{d}P}{\mathrm{d}x} = \frac{\rho_m}{\rho_c} \left[\frac{1}{2} \frac{S}{A} \rho_c f_c V_s^2 + g \left(\rho_p - \rho_c \right) CR \right] \tag{3.9}$$

Two terms appear on the right side of Eq. 3.9. The former accounts for *viscous* friction, while the latter accounts for *mechanical* friction including the effect of the wall lubrication force. In particular, the second term is expressed as a function of the stratification ratio R, which is the ratio between the additional hydraulic gradient with respect to an equal flow rate of pure liquid and the density ratio ρ_m/ρ_c. The stratification ratio is assumed equal to the inverse between the ratio of the maximum value of the wall lubrication force ($\mathbf{F_w}$) (Eq. 2.63) to the submerged weight of a particle $\mathbf{G}_p$. The following expression for R is finally derived:

$$R = \frac{\mathbf{G}_p}{(\mathbf{F}_w)} = \frac{32}{3} \frac{g \left(\rho_p - \rho_c \right) d_p}{f_c V_s^2 C_L} \tag{3.10}$$

in which the C_L is a off-wall lift coefficient of the mixture. This term is obtained from the value C_{L0} relative to a single particle by applying several correction factors to account for the effects of particle size, pipe diameter, and mean solids concentration. These correction factors will be briefly discussed below. Since the lubrication force is effective only when the center of the particles is in the logarithmic portion of the velocity profile, the authors introduced a term Λ which is a function of the particle diameter expressed in wall units, $d^+ = \rho_c U^* d_p/\mu_c$, and goes from 0 for $d^+ \leq 9$ to 1 for $d^+ \geq 27$ (U^* is the shear velocity). Also the ratio between particle size d_p and pipe diameter D_p and that between the the mean solid concentration and the maximum packing concentration $\alpha_{\max}$ appear among the independent variables of the model because they determine the size of the turbulent scales and affect the off wall lift coefficient for highly concentrated slurries. The final formula for C_L is:

$$C_L = C_{L0} \Lambda \mathrm{sech} \left(\frac{60 d_p}{D_p} \right) \left\{ 1 - 0.02 \left[\left(\frac{C}{\alpha_{\max}} \right)^{1/3} - 1 \right]^{-1.75} \right\} \tag{3.11}$$

Due to its local characterization, the solids concentration distirbution cannot be derived from a global-formulation model. However, a simplified physically-based model have been developed for predicting this parameter in case of fully-suspended flows. This methods is based on a local formulation, and requires the solution of a differential equations. However, it is referred to as *simplified* as it relies on simplifying assumptions which avoid the need to solve the whole set of equation for the two-phase mixture. The first

assumption is that the solids concentration α_p is uniform along each horizontal chord, therefore $\alpha_p = \alpha_p(y)$, being y the height above the pipe bottom. This implies that the solids concentration distribution is fully represented by the solids concentration profile along the vertical diameter. The second assumption is that the solids concentration distribution is the results of the equilibrium between two mass fluxes: an advective flux, which is the result of the combined effect of gravitation and drag and causes the particles to move towards the bottom with velocity equal to their hindered settling velocity w'; and a dispersive flux, essentially due to the large-scale eddies which tends to make the flow isotropic. This equilibrium is represented by the following equation:

$$\epsilon_d' \frac{\partial^2 \alpha_p}{\partial y^2} + w' \frac{\partial \alpha_p}{\partial y} = 0 \tag{3.12}$$

in which ϵ_d' is the local diffusion coefficient. Assuming that mean diffusion coefficient (ϵ_d) and mean hindered terminal settling velocity (w) can be applied, integration of Eq. 3.12 yields:

$$\alpha_p(y) = \alpha_{p,0} \exp\left(-\frac{w}{\epsilon_d} y\right) \tag{3.13}$$

where $\alpha_{p,0}$ is the solids concentration at the pipe bottom. The hindered terminal settling velocity w can be evaluated from the value w_0 for a single particle by different correlations. For example, Doron *et al.* [35] report that of Richardson and Zaki:

$$w = w_0 (1 - C)^m = \sqrt{\frac{4}{3} \frac{(\rho_p - \rho_c) d_p g}{\rho_p C_d}} (1 - C)^m \tag{3.14}$$

where m is and C_d depend on the particle Reynolds number defined in terms of the terminal settling velocity w_0, that is $\mathrm{Re}_p = \rho_c w_0 d_p / \mu_c$. The mean diffusion coefficient ϵ_d is evaluated as:

$$\epsilon_d = 0.026 U^* D_h \tag{3.15}$$

in which U^* is the shear velocity. Since the mean delivered solids concentration C, that is the mean value of the solids concentration profile, is known, $\alpha_{p,0}$ can be evaluated by integration of Eq. 3.13 over the whole pipe section.

Models for flows with a moving bed

Global-formulation models for flows with a moving bed were developed by Doron *et al.* [35] and Gillies *et al.* [55]. These models are usually referred to as *two-layer* models since the pipe is divided in two layers by a horizontal separation plane. The typical configuration of a two-layer model is depicted in Figure 3.5. The lower part, referred to as "mb", is the moving bed while in the upper one, referred to as "h", a fully-suspended flow takes place. Slip is not allowed between the two phases in each layer. Mass and momentum conservation equations are integrated over the two layers, and solved together with two additional equations for the concentration in the two layers C_h, C_{mb}. Given the slurry flow rate and the mean delivered concentration, solution of these equations allow
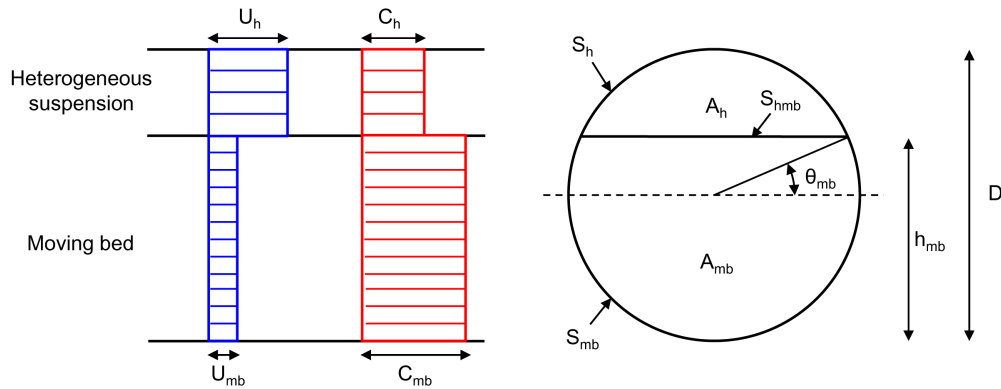
Figure 3.5: The typical configuration of a two-layer model

determining the heigh of the bed layer y_{mb}, the slurry superficial velocity $V_{s,h}$, $V_{s,mb}$ and the mean concentration C_h, C_{mb} of the two layers, and the pressure gradient.

Models for flows with a stationary bed

Global-formulation models for flows with a stationary deposit were developed by Doron and Barnea [33, 35] and Matousek [106]. In all cases the pipe section is divided in different sectors, but the characterics of such subdivision vary according to the particular model. Doron *et al.* [35] indicated a strategy to use their *two-layer* model, originally developed for moving-bed flows, also for stationary-bed flows. In particular, the pipe is divided in two-layers as in Figure 3.5, but the lower layer is a stationary bed and not a moving one. In the *three layer* model of Doron and Barnea [33] the pipe is divided in three horizontal layer, occupied by the stationary bed, a moving bed, and a heterogeneous suspension. In the model of Matousek [106], the pipe is divided between a lower layer, occupied by the stationary deposit, and an upper layer where the mixture flows, which is in turn divided between two sub-layers. An integral formulation of mass and momentum conservation equations for the two upper layers and additional closures yelds the main features of the flow.

3.2.3 Numerical investigations

All the numerical investigations about the flow of solid-liquid mixtures in horizontal pipes have been performed following the coontinuum approach based on an averaged formulation (see Sub-Section 2.2.2), since the prohibitive computational cost of methods based on the kinetic approach precludes their use for simulating dense flows. Some workers studied the problems by means of the Algebraic Slip Model (ASM) which solves the momentum equation for the mixture rather then for both phases, thereby saving computational time. As already mentioned in Sub-section 2.2.2, the ASM relies on very restrictive assumptions which limits its applicability to small particles and moderate concentrations. Ling *et al.* [95] concluded that the ASM cannot reproduce the pressure gradient in moving bed flows; however, the ASM proved inadequate to estimate the
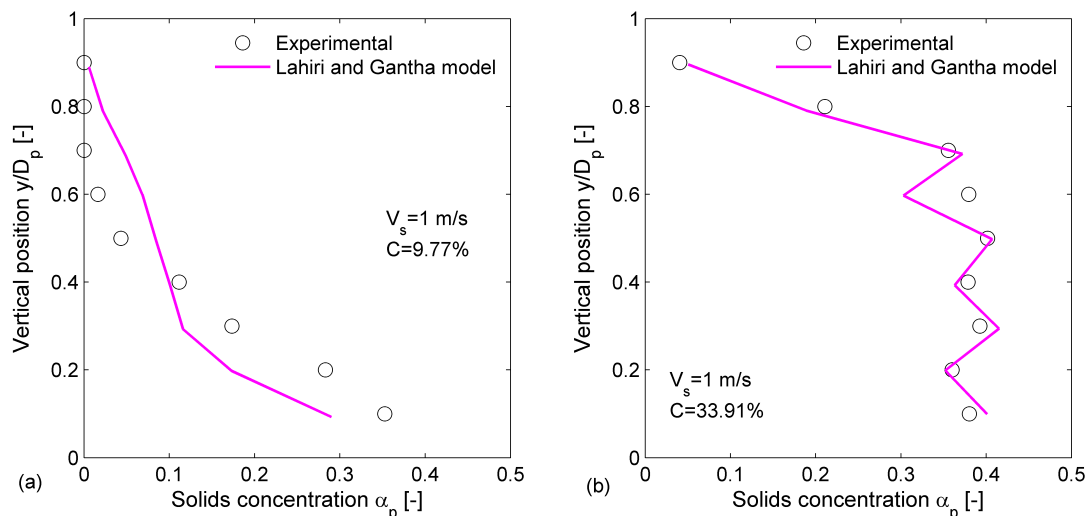
Figure 3.6: Comparison between measured (from Kaushal *et al.* [77]) and computed (from Lahiri and Gantha [89]) solids concentration profiles for the following cases: (a) Slurry superficial velocity = 1 m/s and mean solids concentration = 9.77%; (b) Slurry superficial velocity = 1 m/s and mean delivered solids concentration = 33.91%.

pressure gradient even for fully-suspended flows [78]. At last, also when applicable, the ASM appears rather inaccurate in predicting the solids concentration distribution [78, 95, 120]. Due to all these reasons, the use of the ASM seems rather limited at present.

Most authors made use of two-fluid model with closures derived either from empirical of semi-empirical equations, or, more frequently, from the Kinetic Theory of Granular Flow (KTGF). As already mentioned, the KTGF-based models have the advantage of a strong theoretical basis which aims at reproducing all the physical mechanisms governing the phenomenon. Anyway, even for pipe flows the existing two-fluid models show some limitations, most important of which are the susceptibility to numerical instability and the need of significant calculation time. Therefore, their application to more complex flows may not be straighforward. A critical analysis of the capabilities of the existing models is reported below.

Chen [19] performed numerical simulation of homogeneous slurry flow by means of a two-fluid models with closures derived from empirical or semi-empirical closures. In order to account for turbulent particle dispersion, phase diffusion terms are included only in the mass conservation equation for the solid phase. The validation reported by the author appears rather poor, being limited to a comparison between measured and computed velocity profiles for the following flow conditions: pipe diameter = 25.4 mm; liquid (iodide solution) density = 1550 kg/m^3 and viscosity = $1.145 \cdot 10^{-3}$Pa · m; particle density = 1860 kg/m^3; particle size = 40 μm; mean delivered solids concentration between 5 and 25%; slurry superficial velocity between 0.20 and 0.32 m/s.

The model of Lahiri and Gantha [89] uses closures based on the KTGF, but the incompleteness of the information provided doesn't allow a proper analysis of the equations. The model is validated with respect to the experimental data of Kaushal *et al.* [77]
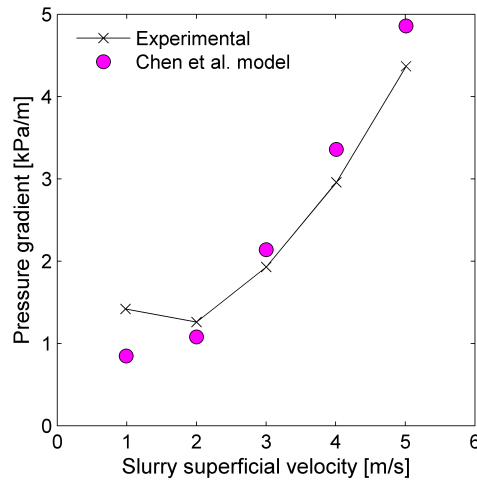
Figure 3.7: Comparison between measured (from Kaushal *et al.* [77]) and computed (from Chen *et al.* [17]) pressure gradient versus bulk-mean velocity for a slurry made of water and a binary mixture of 125 and 400 μm size glass beads at 40% total influx concentration. Straight line segments connect the experimental data to better highlight the minimum in the curve.

about the flow of water and mono-dispersed spherical glass beads with particle density equal to 2645 kg/m^3 and two values of particle diameter, namely 125 and 400 μm. The pipe diameter is 54.9 mm, the slurry superficial velocity between 1 and 5 m/s, and the mean delivered solids concentration between 10 and 50%. The predicted concentration profiles appear in rather good agreement to the experimental data for most case study but significant discrepancies can be observed under certain flow conditions, typically at low velocity and low mean solids concentration (an example is reported in Figure 3.6(a)). However, the oscillating behaviour of the solution seems to indicate strong numerical instabilities (an example is reported in Figure 3.6(b)) which may be enhanced in more complex flows. Comparison between predicting and measured pressure gradient is reported in the form of "computed pressure gradient" versus "measured pressure gradient". This method of presentation alone doesn't allow easy identification of the discrepancies between measured and predicted values, and therefore may fail to identify properly the capabilities of the model.

Chen *et al.* [17] made use of a multi-fluid model, based on KTGF, to simulate the flow of water and a binary mixture of particles. Validation is performed with respect to the experimental data from Kauhal *et al.* [77] about the flow of water and a mixture of spherical glass beads with particle diameter of 125 and 440 μm in volume ratio 50:50. The slurry superficial velocity was between 1 and 5 m/s, and the mean delivered solids volume fraction is 40%. The agreement between computed and measured solids concentration profiles seems farily good except for the case of slurry velocity equal to 1 m/s. Comparison between predicted and measured pressure gradient versus slurry velocity revealed that the model is not capable to detect the presence of a minimum pressure gradient corresponding to the transition between fully-suspended and moving-bed flow

patterns (Figure 3.7).

Also the model of Ekambara *et al.* [41] makes use of closures derived from the KTGF for evaluating the stress tensor of the solid phase. A dispersive force in the form of Eq. 2.70 is introduced to account for the effect of particle dispersion. Validation is performed with respect to the measurements of different authors over a wide range of operating conditions: pipe diameter between 50 and 500 mm; slurry superficial velocity between 1.5 and 5.5 m/s; particle size between 90 and 500 μm; and mean delivered solids concentration between 8 and 45%. The model appears accurate in predicting the solids concentration distribution, but the steady state solution was attained by performing a U-RANS simulation with a time step of 0.001 s and then averaging the solution over 100 s, leading to a significant amount of computer time. A similar procedure may not be applicable to more complex flows, since the already significant calculation time would be likely to become unaffordable. Moreover, the model seems capable to predict the pressure gradient rather accurately, but the graphical representation of "computed value" versus "measured value" alone makes it difficult to evaluate the real capabilities of the model particularly in respect to the moving-bed regime.

Jiang and Zhang [74, 75] studied the flow of solid nitrogen particles and liquid nitrogen in horizontal pipes. Closures from the KTGF are used to evaluate pressure and shear stresses of the solid phase. In order to account for particle dispersion, the drift velocity is introduced in the conservation equation for the turbulent kinetic energy and the dissipation rate of the fluid phase. In a former work [74], the computed solids concentration and velocity profiles are compared to experimental data from literature referring to different mixtures, with particle size between 125 μm and 1 mm and density ratio between 1.05 and 2.47. The agreement seems rather good, but the use of a 2D model casts doubts on the representativity of the numerical solution. Moreover, for each reference, the comparison is limited to just one or two scenarios in terms of slurry superficial velocity and mean solids concentration. In a latter work [75], the pipe is modelled in 3D, and validation is performed by comparing computed and measure pressure gradients for a mixture of solid nitrogen particles (density = kg/m^3, diameter = 1.0 mm) and liquid nitrogen (density = 867 kg/m^3) under the following flow conditions: pipe diameter equal to 10 mm, slurry bulk-mean velocity between 0.5 and 3.5 m/s, and mean solids concentration between 10 and 30%. The numerical predictions match the experimental data fairly well for fully-suspended flow, but the model proved inadequate for flows with a moving bed, confirming the results of Chen *et al.* [17].

Kaushal *et al.* [78] used a granular flow model to simulate the flow of fine particles at high concentration. The model is rather similar to that of Jiang and Zhang [74, 75]. Validation is performed with respect to experimental data about the flow of water and spherical glass beads with density of 2645 kg/m^3 and diameter of 125 μm. The pipe diameter is 54.9 mm, the slurry superficial velocity between 1 and 5 m/s, and the mean solids concentration between 30 and 50%. Unlike in the work of Ekambara *et al.* [41], the steady state solution was obtained directly by dropping the transient term in all conservation equation, and not by averaging a U-RANS solution. Anyway, the lack
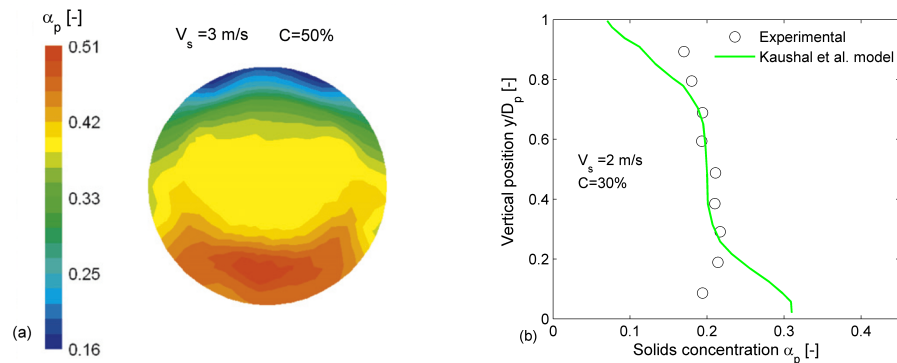
Figure 3.8: Results from Kaushal et al. [78]. (a) Solids concentration distribution for a slurry velocity of 3 m/s and a mean solids concentration of 50%. (b) Predicted and measured solids concentration profiles for a slurry velocity of 2 m/s and a mean solids concentration of 30%.

of symmetry with respect to the vertical diameter may indicate numerical instabilities (Figure 3.8(a)). The predicted concentration profiles agree to the experimental evidence in the inner part of the pipe, but considerable deviations are observed in the outer one (Figure 3.8(b)). The authors reported CFD predictions of pressure drop versus slurry velocity including comparison to experiments; as can be deduced from the figures, the agreement seems rather good, but only the results for the fully-suspended flow of a unique set of particles have been reported.

The model of Spalding [144], already described in Section 2.4, looks very simplistic compared to a KTGF-based model. Moreover, its application to solid-liquid slurry flows in horizontal pipes yelds very inaccurate predictions in terms of pressure gradient, solids concentration profile, and velocity profile. However, this model is numerically very stable and fast to procure converged solution, probably because of the presence of phase-diffusion fluxes and because of the efficiency of the SIMPLEST [143] and IPSA [144] algorithms used for the solution of the algebraic equations. This feature may appear of minor interest when simulating pipe flows, but becomes really fundamental when dealing with the complex flows of engineering interest addressed here. Therefore, the model of Spalding [144] is the starting point in this thesis. At first, it is made a detailed analysis of its performance for the case of horizontal pipe flows, underlining the advantages compared to the existing models and trying to give an explanation of its limitations (Section 3.3). This served as the basis for the development of a new two-fluid model (Section 3.4), which was validated with respect to experimental data from open literature (Section 3.5) and compared to the existing models (Section 3.6). In the next chapters, the model will be applied to more complex flows.

3.3   Performance of the model of Spalding

The performance of the model of Spalding [144] were first analyzed in detail in order to point out its advantages and limitations. Starting from the theoretical background of the phenomenon, illustrated in Section 3.1, and in view of the applications addressed in this

Table 3.1: Details of the flow conditions considered. The pipe is assumed hydraulically smooth

Case	A	B	C	D	E	F
Pipe diameter [mm]	51.5	10.27	5.07	10.27	10.27	10.27
Superficial velocity [m/s]	3.78	5.4	2.0	$2.6 \div 7$	$1.3 \div 7$	$2.6 \div 7$
Particle size [μm]	165	280	520	280	90	280
Particle density [kg/m^2]	2650	2650	2650	2650	2650	2650
Mean solids concentration [%]	9	30	25	11	28	40

thesis, the investigation focuses on the capacity of the model to predict the main features of the flow (solids concentration distribution, velocity profile, and pressure gradient) in case of fully-suspended flows at either low or high mean delivered solids concentration. Anyway, in order to define more completely the applicability of the model, the analysis will be extended to moving-bed flows. Unfortunately none of the experimenters collected measurements of solids concentration, velocity, and pressure at the same time, therefore the analysis is performed with respect to data collected by different authors and referring to different flow conditions.

As far as the solids concentration distribution and the velocity profile are concerned, reference is made to the flow conditions named as A, B, and C in Table 3.1. Case A is taken from Roco and Shook [126]. The authors measured the solids concentration profile using the absorption method and the velocity profile. Obviously, the authors didn't identify the flow pattern according to the more recent classification of Doron and Barnea [34] and, since they didn't report any value of the deposition velocity, or plots of pressure gradient versus slurry superficial velocity, it is not even possible to infer it. However, the indications from the experimental data available are for fully-suspended flow. Case B is taken from Gillies *et al.* [53]. The authors reported measurements of the solids concentration profile and the plot of pressure gradient versus slurry velocity, which indicates fully-suspended flow. Case C is again taken from Roco and Shook [126]. Here the only information available is the solids concentration profile. Due to the lack of more detailed information, the flow pattern can only be presumed. The trend of the experimental data suggests flow with a moving bed.

The capability of the model of Spalding to reproduce the pressure gradient is made with respect to case D, E, and F in Table 3.1 for fully-suspended flow at low and high concentration, and moving bed flow respectively. All the scenarios were investigated experimentally by Gillies *et al.* [53], who reported plots of pressure gradient versus slurry superficial velocity.

In all the simulations perfomed, the pipe is considered hydraulically smooth. Anyway, this assumption can be verified in the experiments of Gillies *et al.* [53], as indicated by inspection of the Moody diagram in the light of the extremely low roughness to pipe diameter ratio ($\approx 2 \cdot 10^{-5}$).

Before comparing the experimental data to the numerical predictions, preliminary tests were performed in order to define the proper numerical settings in terms of domain size, mesh resolution, and discretization scheme. Simulations were steady-state, in the
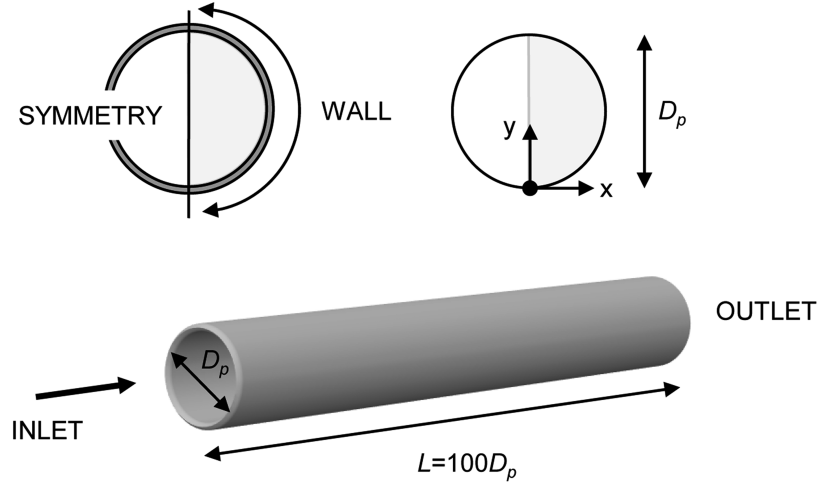
Figure 3.9: Computational domain and boundary conditions

Table 3.2: Fully developed profile at inlet. The friction factor is given by Finolenko's equation [68]

$$u_{c,z} = V_s \frac{(N+1)(2N+1)}{2N^2} \left(1 - \frac{2r}{D_p}\right)^{1/N} \quad N = \frac{1}{\sqrt{f}} \quad f = [1.82 \log(\text{Re}) - 1.64]^{-2}$$

$$k = V_s^2 \frac{f}{8} \left[1 + \frac{2}{3}\frac{2r}{D_p} + \frac{10}{3}\left(\frac{2r}{D_p}\right)^3\right]$$

$$\epsilon = 0.1643 \frac{k^{3/2}}{l_m} = 0.1643 \frac{k^{3/2}}{\frac{D_p}{2}\left[0.14 - 0.08\frac{2r}{D_p} - 0.06\left(\frac{2r}{D_p}\right)^4\right]}$$

sense that the transient term was dropped from all conservation equations. The computational domain is shown in Figure 3.9, where it is evident that the flow and geometrical symmetry of the phenomenon with respect to the vertical axis [77, 126] has been exploited by solving only over one half of the pipe section. A fully-developed turbulent flow profile is specified at the pipe inlet, with the distribution of the axial velocity, turbulent kinetic energy and dissipation rate determined from Nikuradse's boundary-layer theory [130] for single-phase flow, as reported in Table 3.2. No slip is assumed between the phases, and the inlet volume fraction of the solids is taken as uniform. At the outlet, the normal gradients of all variables and the value of the pressure are set to zero. The length of the computational domain is $100D_p$ to ensure that fully-developed flow conditions are attained, which typically occurs some $50D_p$ downstream of the inlet, which confirms the results of previous workers [93, 95]. In the model of Spalding [144] a free slip condition (i.e absence of wall shear stress) is imposed to the solid phase at the pipe wall. The equilibrium logarithmic law of Launder and Spalding [91] for smooth walls is applied to the fluid phase. This boundary condition requires that the non-dimensional distance of the cells adjacent to the wall is between 30 and about 130-180.

The general-purpose, commercial CFD code PHOENICS was employed for the numerical solution of the finite-volume equations analogue of the mathematical described in Section 2.4, which are embedded in the code. The calculations are performed following the elliptic-staggered formulation in which the scalar variables are evaluated at the cell centers and the velocity components at the cell faces. Central differencing is employed for the diffusion terms, while the convection terms are discretized using the hybrid differencing scheme of Spalding [145]. Higher order discretization schemes, like Linear Upwind or Harmonic Van Leer, proved unnecessary for the flow considered here. The numerical solution procedure requires appropriate relaxation of the field variables to achieve convergence. Inertial relaxation is applied to the momentum equations with a false-time step of 0.01 s of the order of the cell convection time. A linear relaxation factor of 0.4 is applied to all other flow variables. The PHOENICS solver was run until the sum of the absolute residual sources over the whole solution domain are less than 1 per cent of reference quantities based on the total inflow of the variable in question. An additional requirement is that the values of the monitored dependent variables at a selected location do not change by more than 0.1% between subsequent iteration cycles. As already noticed, the model appears numerical very stable and only about half of a hour was required to attain a converged steady state solution.

A cylindrical-polar structured mesh was used to discretize the domain. A grid sensitivity study was performed to determine the optimum discretization of the domain by reference to the predicted values of the parameters of interest, namely the solids concentration profile, the velocity profile and the pressure gradient. For this purpose the following flow conditions were considered: pipe diameter = 0.1027 m; slurry superficial velocity = 3.0 m/s; particle size = 90 μm; particle density ρ_p = 2650kg/m^3; mean delivered solids concentration C=19%. The pipe is assumed hydraulically smooth. Three different meshes were employed, as follows: 10 angular by 20 radial by 200 axial (Grid
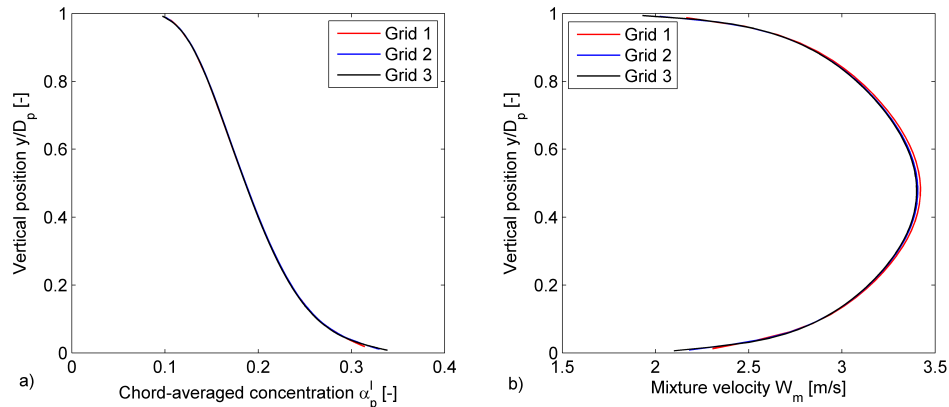
Figure 3.10: Effect on mesh resolution on: (a) solids concentration profile; (b) velocity profile

1); 15 by 30 by 300 (Grid 2); and 20 by 40 by 400 (Grid 3) cells. Since Gillies *et al.* [53] used the absorption method to measure local values of the solids concentration profile, the predicted solids concentration at a distance y from the pipe bottom is evaluated by using the chord-average value α_p^l, i.e:

$$\alpha_p^l(y) = \frac{1}{x} \int_0^x \alpha_p(\zeta, y) \, \mathrm{d}\zeta \tag{3.16}$$

The velocity profile along the vertical diameter is calculated with reference to the mass-averaged velocity field $\mathbf{u}_m$:

$$\mathbf{u}_m = \frac{\rho_c \alpha_c \mathbf{u}_c + \rho_p \alpha_p \mathbf{u}_p}{\rho_c \alpha_c + \rho_p \alpha_p} \tag{3.17}$$

The pressure gradient is evaluated from the difference between the area-averaged pressure at $60D_p$ and $80D_p$ from the inlet section, where fully-developed flow conditions are attained and therefore the pressure decreases linearly.

The predicted concentration and velocity profiles for each grid are shown in Figure 3.10. The solutions obtained on the two finest meshes (Grid 2 and 3) are very close to each other, whilst that for Grid 1 deviates slightly from the finer grid solutions. The pressure gradient on the three grid levels is 532.9 Pa/m, 529.4 Pa/m, and 528.4 Pa/m respectively. The Grid 2 solution is therefore considered adequate.

In the model of Spalding [144], the effective modeling parameters that can be managed are quite limited. In practice, they are basically the forces included in the interfacial momentum transfer term $\mathbf{M}_k^d$, the turbulence model for estimating the eddy viscosity of the fluid ν_c^t, and the turbulent Schmidt number for volume fractions σ_α (Sub-section 2.3.3). A literature review and specific tests on different flow conditions revealed that lift, virtual mass and history force are negligible for the kind of flows considered at this stage of the work. Moreover, the standard $k - \epsilon$ model proved adequate, since specific additional terms accounting for rapid strain (as in the $k - \epsilon$ RNG) are ineffective. The influence of the turbulent Schmidt number for volume fractions σ_α on the three parameters of interest was investigated.
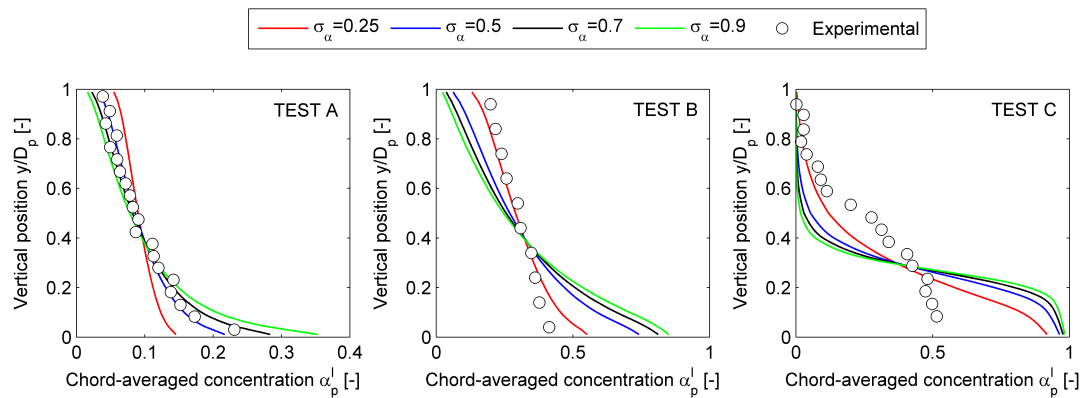
Figure 3.11: Effect on Schmidt number on the chord-averaged solids concentration profile for cases A, B and C in Table 3.1. The experimental data of cases A and C are reported in Roco and Shook [126], those of case B in Gillies *et al.* [53]
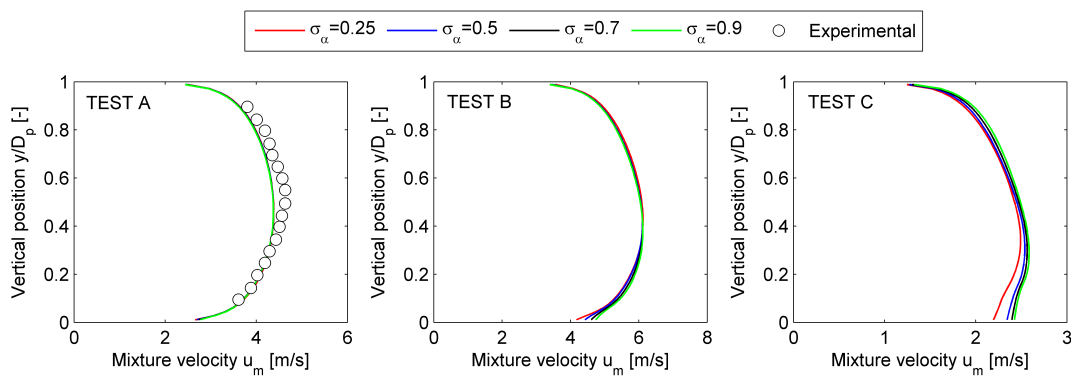
Figure 3.12: Effect on Schmidt number on the chord-averaged solids concentration profile for cases A, B and C in Table 3.1. The experimental data of case A are reported in Roco and Shook [126]
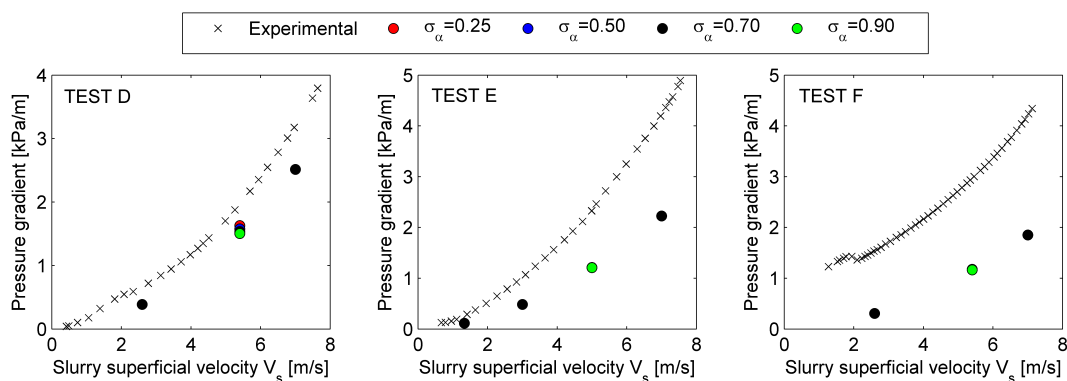
Figure 3.13: Pressure gradient versus slurry superficial velocity for the flow conditions D, E, and F in Table 3.1: comparison between the experiments of Gillies *et al.* [53] and the predictions of the model of Spalding 3.1 for different values of the turbulent Schmidt number for volume fractions

Figures 3.11 and 3.12 show the concentration and velocity profiles for the flow conditions A, B, and C in Table 3.1 when σ_α varies within the range usually considered in literature $(0.2 \div 0.9)$. The turbulent Schmidt number for volume fraction has a significant effect on the solids concentration profile, because it is associated with the turbulent dispersion of particles: in particular, a reduction of σ_α results in a flatter concentration profile as a result of the increase turbulent dispersion (Figure 3.11). The best match between computations and experiments is obtained with σ_α equal to about $0.5 \div 0.7$ and 0.25 for cases A and B respectively, while no value of that parameter is capable to produce an accurate solution for case C. For cases A and B, the velocity profile doesn't appear to be much affected by σ_α (Figure 3.12). However, a rediction of σ_α produces a shift of the velocity profile towards the symmetrical configuration characteristic of single-phase flows, probably as a conseguence of the evolution of the flow configuration towards the pseudo-homogeneous one. For case C, the velocity distribution is highly influenced by σ_α, resulting in a significant variation of the velocity profile (Figure 3.12). Conversely, the turbulent Schmidt number for volume fraction doesn't appear to have any influence the pressure gradient, as it can be inferred from Figure 3.13, which shows the pressure gradient as a function of slurry superficial velocity for the flow conditions D, E, and F in Table 3.1 when σ_α varies between 0.25 and 0.9.

The above reported analysis evidences that the model of Spalding [144] is unsuitable for simulating solid-liquid slurry flows in horizontal pipes. Despite under certain flow conditions a fairly good prediction of the solids concentration profile may be obtained by a proper choice of the turbulence Schmidt number for volume fractions (Figure 3.11, cases A and B), the numerical solution appears unconsistent with some physical features of the phenomenon. Most important, the model is not capable to reproduce the increase in pressure gradient with respect to the single-phase flow case caused by the interaction between the particles and the pipe wall (Figure 3.12). This limitation may arise from the free slip condition (i.e. zero wall shear stress) applied to the solid phase at the pipe wall. Moreover, the model doesn't account for the fact that the solids volume fraction is upper bounded by the maximum packing concentration, and cannot approach a unit value as in Figure 3.11, case C. At last, the model predicts the maximum velocity below the pipe axis instead of above it (Figure 3.12, cases B and C). This result is clearly unphysical on the grounds of what reported in Section 3.1.

3.4 A new two-fluid model

A new two-fluid model is developed. The new model has to be accurate and, at the same time, numerically stable and fast in procuring converged solutions, features all indispensable for simulating complex flows. Due to its peculiar stability and robustness, the model of Spalding [144] is taken as the starting point in this work. In order to overcome the inaccuracy or, even, the implausibility ot its predictions highlighted in the earlier section, the most significant modelling features were reconsidered. This required the development of specific subroutines and user-defined functions which were embedded

in the PHOENICS code.

The kew features of the new model are:

1. PHASE DIFFUSION

   In order to account for the turbulent dispersion of the particles, phase diffusion fluxes are present in all conservation equations. These terms come from the modeling of the correlations between fluctuating velocity and fluctuating volume fractions which arise from the double average process illustrated in Sub-section 2.3.3. The presence of phase diffusion fluxes, especially in the mass conservation equations, contributes significantly to the numerical stability of the model.

2. DRAG FORCE

   In the model of Spalding [144], the drag force per unit volume is evaluated as for a single sphere in an infinite medium. However, this assumption holds only for dilute suspensions, as it doesn't consider that the drag acting on a single particle is affected by the presence of other particles. This is one of the reasons which make the model of Spalding [144] unsuitable for simulating dense flows. As already discussed in Sub-section 2.3.2, different modeling approaches ere developed to account for the effect of multiple particles on the drag force. In the proposed model, it is followed the mixture viscosity approach, which consists in defining the particle Reynolds number with respect to the viscosity of the mixture μ_m instead of that of the fluid phase. The maximum packing concentration is introduced in the model through the correlation for μ_m.

3. PARTICLE PRESSURE

   A collisional pressure term is added in the momentum equation of the solid phase, in order to keep the particles apart and avoid their compenetration. This term, which is not present in the model of Spalding [144], is modeled in the form of Eq. 2.45, with the solids elasticity modulus G given by the empirical expressions reported in Figure 2.10. Due to the sharp variation of G with the local solids volume fraction α_p, the collisional pressure may make the model more susceptible to numerical instability.

4. PARTICLE VISCOSITY COEFFICIENT

   In almost all two-fluid models available in literature, the deviatoric stresses in the solid phase was evaluated by means of a Newtonian-like constitutive equation (Eq. 2.42) under the (a priori improper) constrain $\nabla \cdot \mathbf{u}_p = 0$. This introduces a particle viscosity coefficient ν_p, which is expressed as a function of the granular temperature for the KTGF-based models and set equal to that of the fluid phase ν_c in the model of Spalding [144]. In order to account for the effect of particle pressure on the numerical solutions, in the development of the new two-fluid model different options for ν_p were considered, namely $\nu_p = 0$, $\nu_p = \nu_c$, and ν_p evaluated by means of the formula of Ahilan and Sleath (Eq. 2.43).

5. PARTICLE EDDY VISCOSITY

The particle eddy viscosity arises when the correlations between the fluctuating components of the particle velocities $\langle \mathbf{u}'_p \mathbf{u}'_p \rangle$ were modeled by the standard Boussinesq approximation (Eq. 2.74), again under the (a priori improper) assumption of divergence-free flow field. The KTGF-based models don't include this term explicitly but, roughly speaking, account for its effect via the particle viscosity ν_p. Conversely, the other models introduce a particle eddy viscosity ν_p^t. This is also the case of the proposed model, in which ν_p^t is either set to ν_c^t (as in the model of Spalding [144]) or evaluated by the algebraic models reported in Sub-section 2.3.3.

6. WALL BOUNDARY CONDITIONS FOR THE SOLID PHASE

The wall boundary condition of the solid phase must account for the shear stress due to the interactions between the particles and the wall. The model of Spalding [144], which imposes zero shear stress (free slip condition) produces significant underestimation of the pressure gradient. Partial slip boundary conditions are obtained from the KTGF, and were implemented in some two-fluid models [17, 41]. In the new two-fluid model, in addition to the free slip conditions, the following options were considered:

- Equilibrium logarithmic law of Launder and Spalding [91] for smooth walls for the velocity of the solid phase:

$$\frac{u_p^{//}}{U^*} = \frac{1}{\kappa} \ln \left(E y^+ \right) \qquad (3.18)$$

  in which: $u_p^{//}$ is the absolute value of the solid phase velocity parallel to the wall at the first grid node; U^* is the friction velocity; $\kappa = 0.41$ is the von Karman constant; E is a roughness parameter, equal to 8.6 as suggested for hydraulically smooth walls; and y^+ is the dimensionless wall distance of the first grid point, equal to $U^* y / \nu_c$, being y the normal distance of the first grid point from the wall. This option was chosen by Kaushal and co-workers [78] who developed a KTGF-based model.

- Local formulation of the model of Shook and Bartosik [11, 139] for the wall shear stress of the solid phase $\tau_{w,p}$:

$$\tau_{\mathrm{w,p}} = \frac{8.3018 \cdot 10^7}{\mathrm{Re}} D_p^2 \rho_p d^2 \left[\left(\frac{\alpha_p}{\alpha_{\max}} \right)^{1/3} - 1 \right]^{1.5} \left(\frac{\tau_{w,c}}{\mu_c} \right)^2 \qquad (3.19)$$

  The model was originally based on a global formulation, but, in order to include it in the two-fluid model, it was necessary to derive a local formulation by replacing the mean delivered solids concentration C with the local value α_p. However, this option is not without perplexity because two bulk parameters (the pipe diameter D_p and the bulk Reynolds number Re defined with respect to D_p as well as the slurry superficial velocity V_s) still appear in Eq. 3.19, and

preclude its application for different flows.

- Fully rough logarithmic law, which is similar to the law of Launder and Spalding [91] but uses the particle size d_p as the variable to non-dimensionalize the normal distance of the first grid points y:

$$\frac{u_p^{//}}{U^*} = \frac{1}{\kappa}\ln\left(\frac{y}{d_p}\right) \qquad (3.20)$$

7. WALL LUBRICATION FORCE

The wall lubrication force, discussed in Sub-section 2.3.2, may be significant for solid-liquid slurry flows in horizontal pipes. However, a literature review reveled that a distributed model of unquestioned validity for this force doesn't exist at present. In the two-fluid model, it is added in the interfacial momentum transfer term M_k^d the wall lubrication force of Antal *et al.* [3] (Eq. 2.62). Even if it was developed for laminar gas-liquid bubbly flows, this is the only correlation which is based on a local formulation and can therefore be included in a two-fluid model. The same term is present in the KTGF-based model of Ekambara *et al.* [41].

Compared to the model of Spalding [144], additional modeling features come up in the proposed one. Besides the forces considered in the interfacial momentum transfer term $\mathbf{M}_k^d$, the turbulence model for estimating the eddy viscosity of the fluid ν_c^t, and the turbulent Schmidt number for volume fractions σ_α, it is possible to define: the mixture viscosity correlation, and the associated parameters; the wall boundary conditions for the solid phase; the solids elasticity modulus in the collisional pressure term; the particle viscosity and the particle eddy viscosity.

Actually, specific numerical simulations showed that the last three items, as well as the inclusion of the wall lubrication force of Antal *et al.* [3] (Eq. 2.62), are ineffective for the flows addressed in the present Chapter. This result was interpreted as follows. The collisional pressure term has the effect to keep the particles apart so that the concentration does not exceed the maximum value obtainable for a given kind of particles [44, 56]. As it will be discussed later, in the proposed two-fluid model the same effect is obtained by the interfacial momentum transfer term, therefore the inclusion of the collisional pressure becomes ineffective. This is particularly important because it contributes to the numerical efficiency of the model, since the inclusion of a collisional pressure terms results in enhanced susceptibility to numerical instability. In the momentum equation of the solid phase, the particle viscosity coefficient ν_p is negligible compared to the particle eddy viscosity ν_p^t, whatever the way in which ν_p is evaluated (0, ν_c, or by Eq. 2.43). Actually, in the last case ν_p may become important for moving-bed flows, but only close to the pipe bottom where the drag dominates. Therefore, ν_p could be set to 0 without significant impact on the results. According to the models of Wu and Liu (Eq. 2.86), Chen and Wood (Eq. 2.86), and Mols and Oliemans (Eq. 2.89), the ratio of the eddy viscosity of the particle phase ν_p^t to that of the fluid phase ν_c^t is given by coefficients accounting for the intertial effects and, possibly, the crossing trajectory effect. For all
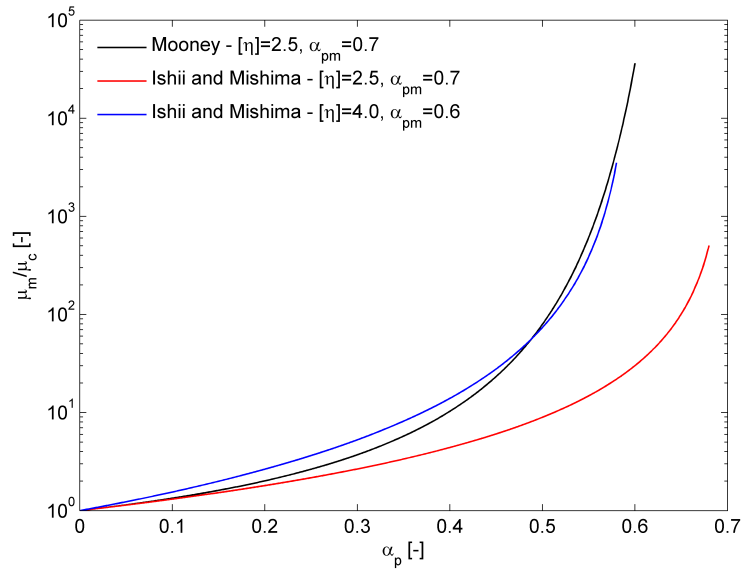
Figure 3.14: The viscosity of the mixture μ_m as obtained from the correlations of Mooney (Eq. B.7) and Ishii and Mishima (Eq. B.5) with different values of the empirical parameters $[\eta]$ and $\alpha_{\max}$

the flow conditions considered, these coefficients were found to be very close to one everywhere in the domain, therefore ν_p^t was set to ν_c^t as in the model of Spalding [144].

The three modeling features which most influence the numerical solution are the mixture viscosity correlation, the turbulent Schmidt number for volume fractions σ_α, and the wall boundary condition for the solid phase. These items are strongly coupled with each other, and, in principle, it is not possible to separate their effects. However, an attempt to identify their specific role is made, reporting the investigation in three separate Sub-sections.

The analysis is performed for the six flow conditions reported in Table 3.1, with the aim to consider: fully-suspended flows at low and high mean delivered solids concentration and, for completeness of the analysis, also flows with a moving bed.

3.4.1 Mixture viscosity correlation

The expression for the viscosity of the mixture, and the empirical parameters in it, have remarkable effect on the solids concentration profile, especially at high concentration. Among all the correlations reported in Appendix B only those covering the whole range of particle concentration have been considered, in order to ensure the widest possible applicability of the model. Except for those of Maron and Pierce (Eq. B.6) and Thomas (Eq. B.9), all the correlations depends on two empirical parameters, namely the intrinsic viscosity $[\eta]$ and the maximum packing concentration $\alpha_{\max}$, whose meaning has already been discussed. The new two-fluid model employs the formula of Mooney (Eq. B.7), which, on the grounds of several numerical simulations, proved to be the one which procures the best match to the experimental data for a unique combination of $[\eta]$ and
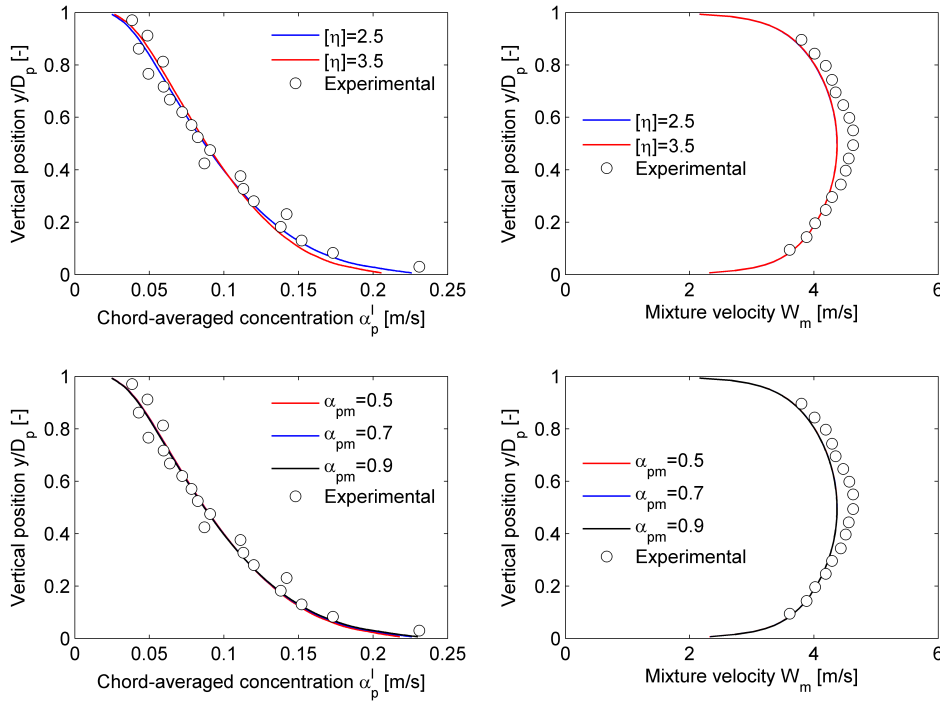
Figure 3.15: Effect of the parameters $[\eta]$ and $\alpha_{\max}$ in the mixture viscosity correlation of Mooney (Eq. B.7) on the concentration and velocity profiles for case A in Table 3.1. In all cases, the turbulent Schmidt number σ_α is 0.7 and a free slip wall boundary condition is applied to the solid phase. The dipendence on $[\eta]$ is studied for $\alpha_{\max} = 0.7$; that on $\alpha_{\max}$ for $[\eta] = 2.5$

$\alpha_{\max}$ in the range suggested by the author. However, it is worth remarking that this choice doesn't reduce the generality of the model since it seems possible to switch from a correlation to another simply by changing the values of the two empirical parameters. As an example, Figure 3.14 shows the similarity - at least for high concentration, when the effect of the multiple particles on the drag becomes important - between the correlation of Mooney (Eq. B.7) with $[\eta] = 2.5$ and $\alpha_{\max} = 0.7$ and that of Ishii and Mishima (Eq. B.5) with $[\eta] = 4.0$ and $\alpha_{\max} = 0.6$.

The viscosity of the mixture tends to infinity when the solids concentration α_p approaches the maximum packing one $\alpha_{\max}$. Therefore, the $\alpha_{\max}$ sets an upper limit to α_p, preventing the particles from over-packing. This avoids the need to need to introduce a collisional pressure term in the momentum equation of the solid phase. As already noticed, the absence of this term is important as it promotes the numerical stability of the model. The effect of $[\eta]$ and $\alpha_{\max}$ on the numerical solution one at a time is displayed in Figures 3.15 and 3.16 for cases A and C respectively. In all simulations, the turbulent Schmidt number σ_α is 0.7 and a free slip boundary condition is applied to the solid phase at the pipe wall. The results reveal that the definition of the particle Reynolds number in terms of the viscosity of the mixture rather than that of the fluid phase becomes effective if the solids concentration is high, at least somewhere in the domain. This typically
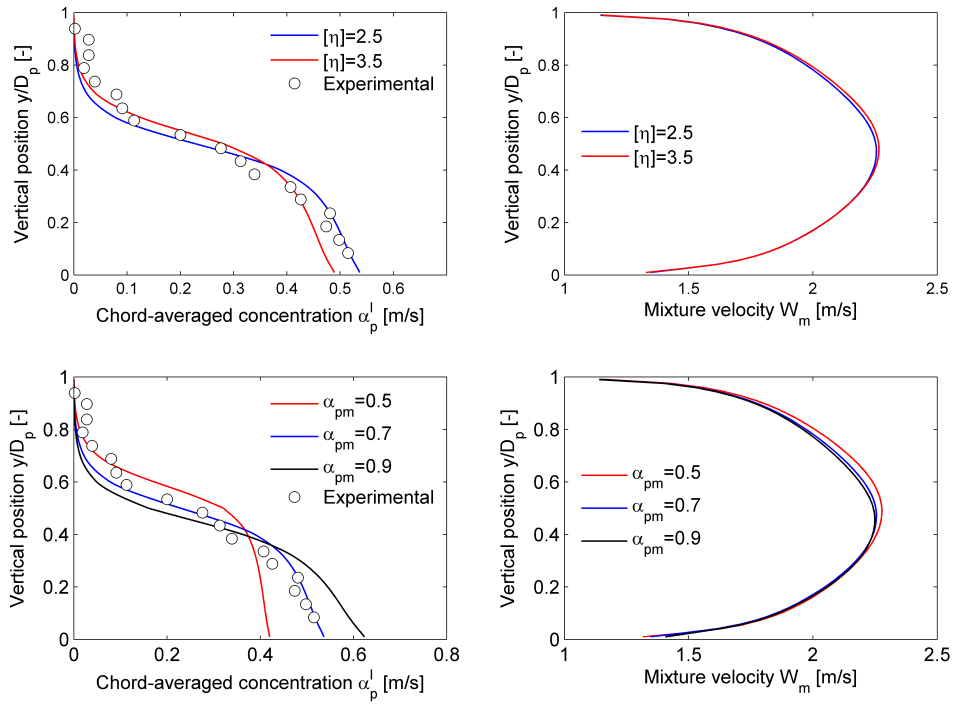
Figure 3.16: Effect of the parameters $[\eta]$ and α_{pm} in the mixture viscosity correlation of Mooney (Eq. B.7) on the concentration and velocity profiles for case C in Table 3.1. In all cases, the turbulent Schmidt number σ_α is 0.7 and a free slip wall boundary condition is applied to the solid phase. The dipendence on $[\eta]$ is studied for $\alpha_{\max} = 0.7$; that on $\alpha_{\max}$ for $[\eta] = 2.5$
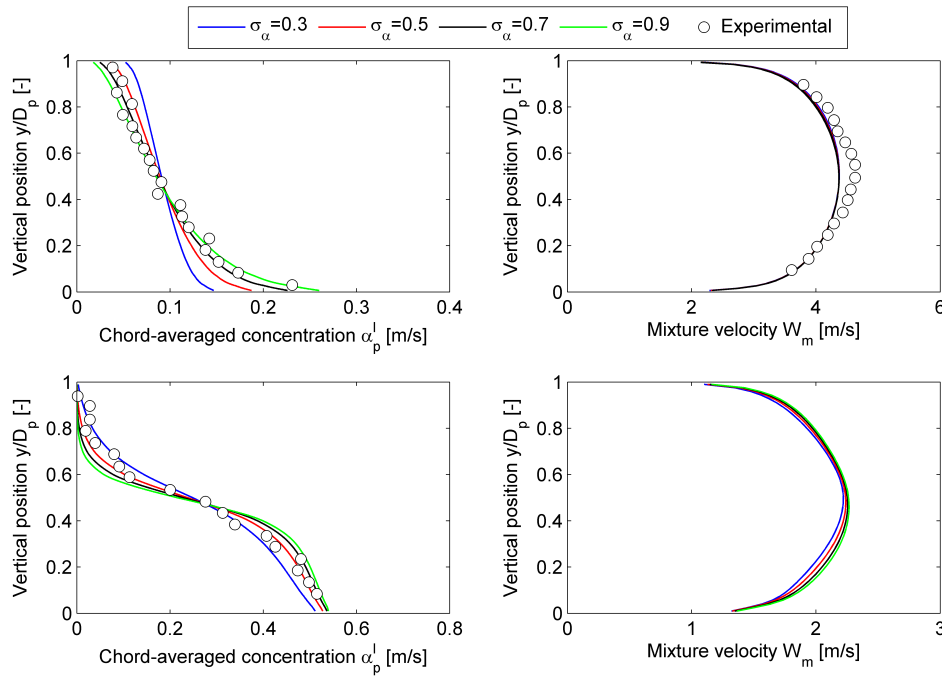
Figure 3.17: Effect of the turbulent Schmidt number σ_α on the concentration and velocity profiles for cases A and C in Table 3.1. In all cases, the viscosity of the mixture is evaluated by the correlation of Mooney (Eq. B.7) with $[\eta] = 2.5$ and $\alpha_{pm} = 0.70$. A free slip wall boundary condition is applied to the solid phase

happens for dense suspended flows and moving-bed flows. Under these condition (case C), the different definition of the particle Reynolds number improves considerably the prediction of the solids concentration profile with respect to the model of Spalding [144] (Figures 3.11 and 3.16). Conversely, no significant variation is observed for case A, in which the solids volume fraction is below 0.25 across the entire pipe section (Figures 3.11 and 3.15). The best agreement to the experimental data is obtained for $[\eta] = 2.5$ and $\alpha_{\max} = 0.70$.

Compared to the model of Spalding [144], the modification to the drag force term doesn't seem to have any influence on the mixture velocity profile in case A, whatever the values of the two parameters $[\eta]$ and $\alpha_{\max}$ are (Figures 3.12 and 3.15). Conversely, a significant change is produced in case C (Figures 3.12 and 3.16). Despite the lack of measurements doesn't allow a comparison to the experimental evidence, the new model seems to improve the prediction of the velocity profile, even if the maximum velocity remains below the pipe axis, which is unphysical.

Tests on cases D to F, whose results are not shown here, revealed that the definition of the particle Reynolds number with respect to the viscosity of the mixture doesn't procure any significant variation in the pressure gradient with respect to the predictions of the model of Spalding [144] (Figure 3.13), whatever the values of $[\eta]$ and $\alpha_{\max}$ are.

3.4.2 Turbulent Schimidt number for volume fractions

After choosing the mixture viscosity correlation (that of Mooney, Eq. B.7) and the values of the related parameters ($[\eta] = 2.5$ and $\alpha_{\max} = 0.70$), the influence of the turbulent Schmidt number for volume fractions σ_α on the numerical solution is investigated. At this stage of the work, a free slip condition is still applied to the solid phase at the pipe wall.

Figure 3.17 reports the predicted solids concentration profile and mixture velocity profile for cases A and C in Table 3.1 when different values of σ_α between 0.25 and 0.9 are employed. The definition of the particle Reynolds number with respect to the viscosity of the mixture instead of that of the fluid phase reduces the effect of σ_α on the solids concentration profile, especially in the regions characterized by high solids volume fraction (Figures 3.11 and 3.17). A possible explanation may be that, if α_p approaches $\alpha_{\max}$, the interfacial momentum transfer predominates over the phase diffusion fluxes. Unlike the model of Spalding [144], it is possible to identify a unique value of σ_α, that is 0.7, which procures good agreement between computed and measured solids volume fraction profiles. This increases significantly the robustness of the model.

The turbulent Schmidt number for volume fraction affects the mixture velocity profile only in case C, where a decrease of σ_α tends to shift the profile towards a symmetrical configuration, probably as a consequence of the enhanced turbulent dispersion. However, the solution remains unphysical, since the maximum velocity occurs below the pipe axis.

The effect of σ_α on the pressure gradient, not shown here, is minor, being the predictions essentially equal to those of the model of Spalding [144] (Figure 3.13).

3.4.3 Wall boundary condition for the solid phase

The wall boundary condition for the solid phase accounts the mechanical contribution to friction, and is therefore a key feature for correctly predicting the pressure gradient. The 5 options previously reported (including the free slip condition) were considered. In the investigation, the following other modeling features were employed: the Mooney's equation for the viscosity of the mixture (Eq. B.7) with $[\eta] = 2.5$ and $\alpha_{\max} = 0.7$, and a turbulent Schmidt number for volume fractions equal to 0.7.

When applying other options than the free slip condition, the predicted pressure gradient may be rather sensitive on the mesh resolution, mainly in terms of the disposition of the cells rather than on their overall number. Yet in the single-phase flow case, the equilibrium log law of Launder and Spalding [91] for smooth walls in conjunction with the standard k-ϵ turbulence model poses strict requirements on the dimensionless wall distance of the first grid point y^+. This law holds in the log law region, and therefore, strictly it may be applied only for y^+ in the range from 30 to about 130. As a consequence, the numerical solution (and, in particular, the computed pressure gradient), is reliable only if the above mentioned condition is satisfied; otherwise, the predictions are inconsistent. Figure 3.18 depicts the computed pressure gradient versus y^+ for the following flow condition: pipe diameter = 102.7 mm; slurry superficial velocity = 5 m/s;
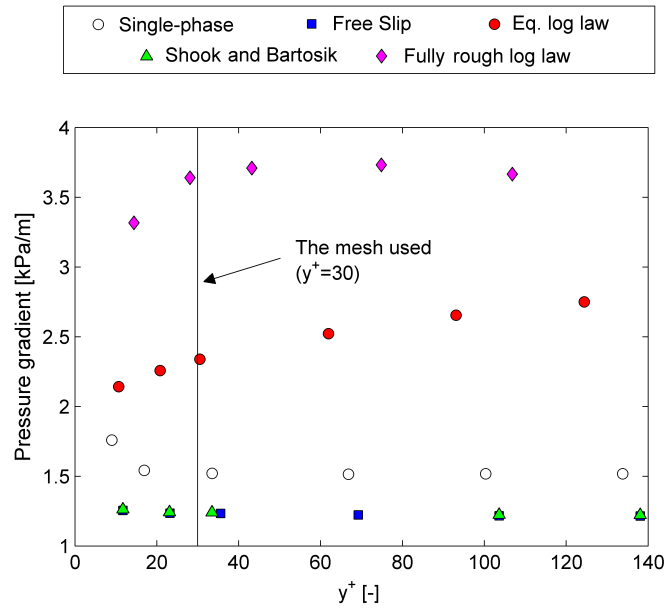
Figure 3.18: Computed pressure gradient as a function of the dimensionless distance between the centers of the near wall cells and the pipe wall for different wall boundary conditions of the solid phase. The single phase flow case is reported too

sand particles of density $= 2650$ kg/m^3 and size $= 90$ μm at a mean delivered concentration $= 28\%$. The pipe is hydraulically smooth. In the plot, the trend of the white circles, which reproduce the flow of pure liquid at the same superficial velocity, confirms that the pressure gradient is inconsistently predicted for $y^+ < 30$.

With a two-fluid model the situation is more complex because the phases are treated as coupled interpenetrating continua, and thus the dependence of the computed pressure gradient on y^+ is more difficult to interpret. With the proposed model, in which the equilibrium log law of Launder and Spalding [91] for smooth walls is applied to the fluid phase, the constrain $30 > y^+ < 130$ has still to be satisfied. In addition, the wall boundary condition of the solid phase influences significantly the dependence of pressure gradient upon y^+. Figure 3.18 indicates that, if either a free slip condition or the mechanical stress model of Shook and Bartosik [11, 139] (Eq. 3.19) is employed, the dimensionless wall distance of the first grid point has a minor effect on the computed pressure gradient. Conversely, the influence of y^+ is enhanced when either the equilibrium log law (Eq. 3.18) or the fully rough log law (Eq. 3.20) are applied to the solid phase. Hereafter, whatever the option chosen is, the mesh was designed in such a way that $y^+ = 30$, which is the smallest possible value consistent with the application of the equilibrium log law for smooth walls in the single-phase flow case. For a given y^+, further increase in the mesh resolution procured negligible changes in the numerical solution. It is worth noticing that the employment of the fully-rough log law requires the additional constrain $y > d_p$, which is fullfilled in all the simulations performed.

The effect of the wall boundary condition for the solid phase on the predicted pressure gradient is now analyzed for the flow conditions D, E, and F in Table 3.1, investigated
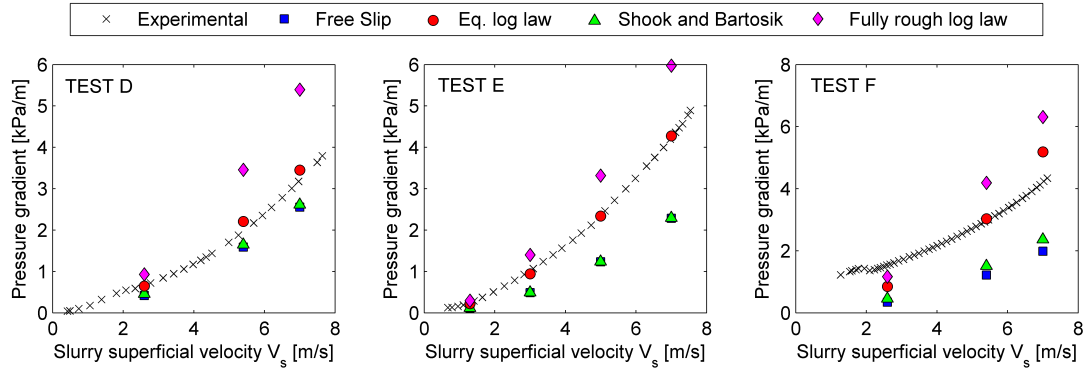
Figure 3.19: Pressure gradient versus slurry superficial velocity for the flow conditions D, E, and F in Table 3.1: comparison between the experiments of Gillies *et al.* [53] and the predictions of the new model applying different wall boundary conditions to the solid phase

experimentally by Gillies *et al.* [53]. Figure 3.19 is the analogue of Figure 3.13 for the different wall boundary conditions. The best match between computations and measurements is obtained when the equilibrium log law of Launder and Spalding [91] for smooth walls (Eq.3.18) is employed. The model of Shook and Bartosik [11, 139] (Eq. 3.19) proved inadequate for the flow conditions considered, procuring estimations of the pressure gradient which are often undistinguishable from those obtained imposing the free slip condition. This may be due to the fact, that, according to the mathematical formulation of Eq. 3.19, the wall shear stress of the solid phase becomes effective only for very dense mixtures, in which the mean solids volume fraction approaches the maximum packing value $\alpha_{\max} = 0.70$. Conversely, the fully rough logarithmic law (Eq. 3.20) results in a significant overestimation of the pressure gradient, probably due to the inadequacy of this model which is usually employed for atmospheric boundary layers. The plot on the right side in Figure 3.19, referring to case F in Table 3.1, reveals that none of the proposed boundary conditions is capable to detect the minimum in the pressure gradient versus slurry superficial velocity curve which characterizes the transition from fully suspended to moving bed flows (Figure 3.2). Moreover, for the same case F the equilibrium log law produces an overestimation of the losses at high superficial velocity. This feature will be discussed in the following section.

From Figures 3.18 and 3.19 it can be inferred a peculiar feature of the free slip and Shook and Bartosik [11, 139] (Eq. 3.5) boundary conditions, which is that they predict lower pressure gradient compared to the single-phase flow case, with such *pressure gradient defect* increasing as the mean delivered solids concentration increases. This unphysical behaviour appears evident from Figure 3.20, in which the predicted pressure gradient is depicted as a function of the mean solids concentration for a given value of superficial velocity. An interpretation of the results may be that, when applying a free slip condition to the particles, the wall shear stresses which produces the pressure gradient is uniquely attributable to the fluid phase, for which the equilibrium log law of Launder and Spalding [91] for smooth walls is used. This law is implemented in the
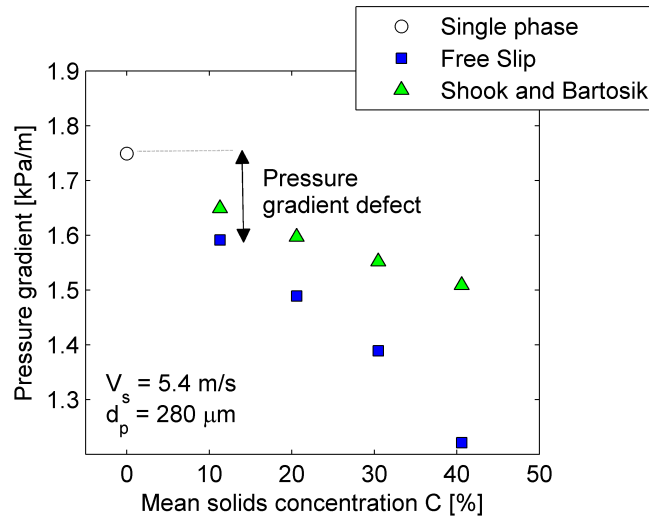
Figure 3.20: Pressure gradient versus mean delivered solids concentration for a superficial velocity of 5.4 m/s: comparison between the single phase flow case and the predictions of the two-fluid model when the free slip and the Shook and Bartosik [11, 139] boundary conditions (Eq. 3.5) are applied. Parameters non explicited are those of cases D and F in Table 3.1

momentum equations of the solid phase by way of source terms proportional to the local fluid volume fraction α_c. The fact that α_c is maximum for single-phase flow ($\alpha_c = 1$) and decreases as the mean solids concentration increases may contribute to explain the existance and the trend of the pressure gradient defect. The same considerations holds only when the model of Shook and Bartosik [11, 139] is employed, since, as already noticed, for the flow conditions simulated the application of Eq. 3.19 yelds $\tau_{w,p} \approx 0$, which is actually a free slip condition. The dependence of $\tau_{w,p}$ upon the mean delivered solids concentration C explains the lower pressure gradient defect as C increases.

The influence of the wall boundary condition for the solid phase on the solids concentration and the velocity profiles is now discussed. Reference is made to the flow conditions A and C in Table 3.1, about which the results are depicted in Figure 3.21. As far as the chord-average solids concentration profile is concerned, for both cases the effect of the wall boundary conditions seems minor. This is evident for case A (fully suspended flow), but, also for case C (moving bed flow), even if variations in the predictions are observed when using any of the other options than the free slip condition, all the solutions appear to have the same degree of agreement to the experimental evidence. A more significant influence is observed in terms of the mixture velocity profile, since the equilibrium log law for smooth walls (Eq. 3.18), the model of Shook and Bartosik [11, 139] (Eq. 3.19) and the fully rough log law (Eq. 3.20) are capable to correctly reproduce the shift of the maximum towards the upper part of the pipe.

The sensitivity analysis reported in this section allowed concluding that the most significant parameters affecting the numerical solution in the horizontal pipe case are the mixture viscosity correlation, the turbulent Schmidt number for volume fractions, and the wall boundary conditions of the solid phase. For the flow conditions chosen
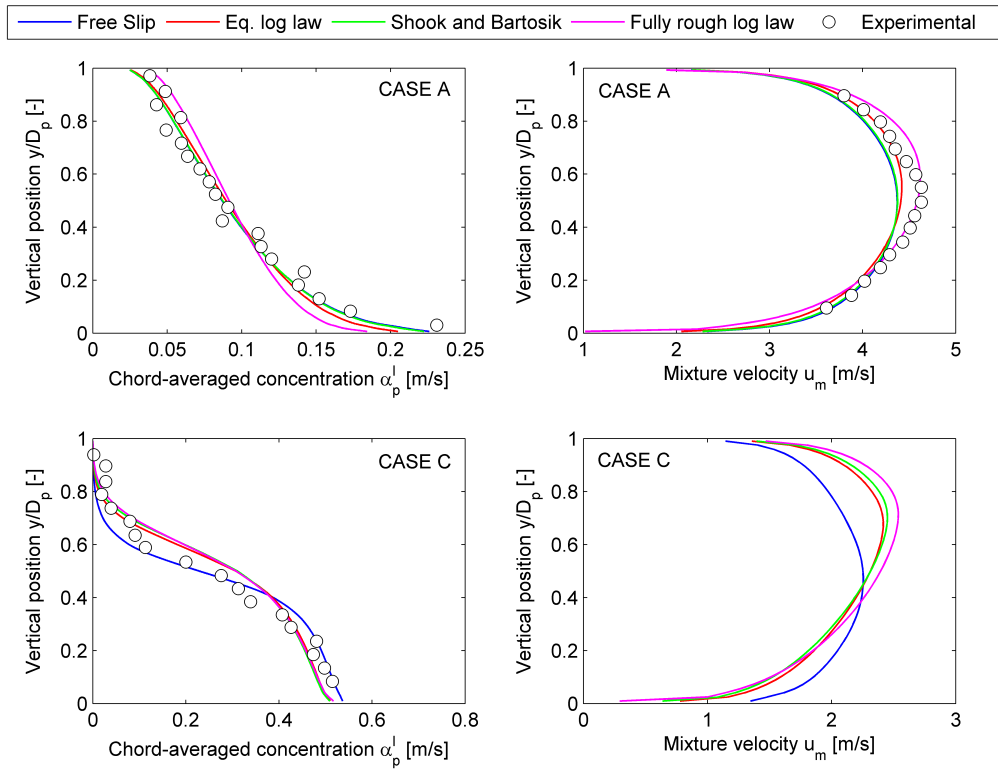
Figure 3.21: Effect of the wall boundary condition for the solid phase on the concentration and velocity profiles for cases A and C in Table 3.1. In all cases, the viscosity of the mixture is evaluated by the correlation of Mooney (Eq. B.7) with $[\eta] = 2.5$ and $\alpha_{\max} = 0.70$. The turbulent Schmidt number for volume fractions σ_{α} is 0.7

for the analysis, reported in Table 3.1 and judged representative of the phenomenon in regard to the applications addressed by this thesis, the phenomenological consistency of the solution and a good agreement to the available measurements were attained when the formula of Mooney (Eq. B.7) with $[\eta] = 2.5$ and $\alpha_{\max} = 0.7$, a turbulent Schmidt number of 0.7, and the equilibrium log law of Launder and Spalding [91] for smooth walls (Eq.3.18) are employed. The conservation equations of the proposed model as well as the closures are summarized in Appendix D. On the grounds of the above reported study, the new two-fluid model seems applicable for fully-suspended flows, since in its present form it proved uncapable to reproduce adequately the long-lasting contact stresses between the particles and the wall which determine the pressure gradient of moving bed flows (case F in Figure 3.19). In order to confirm the reliability of the model and better define its applicability, a comparison to a large dataset of experimental data from open literature over a wide range of operating conditions was performed, and illustrated in the following section.

3.5   Comparison to the experimental evidence

In order to better defining the predictive capacity of the two-fluid model, the numerical results have been compared to experimental data from open literature over a wide range of operating conditions. Details of the flow conditions simulated are summarized in Table 3.3, which indicates the measurements avaiable (concentration profile, velocity profile, pressure gradient). Most data refer to fully-suspended flows, but also some tests on moving-bed flows were considered for comparison in order to completely define the conditions of applicability of the model.

However, the experimenters rarely decleared the flow pattern. In few cases [136], it can be established rather unquestionably from measurements of the deposition velocity. More frequently, it can be evinced from plots of pressure gradient versus slurry velocity, where the identification of the minimum may be rather confusing. In other cases [126], the flow pattern can be only guessed from the shape of the concentration profile. Each dataset allows an assessment of the model's capability for reproducing the influence of specific features affecting the parameter of interest, namely the concentration distribution, the velocity profile, and the pressure gradient. The data of Roco and Shook [126] (cases P1 to P11) and Gillies *et al.* [53] (cases P12 to P36) are used to investigate the effect of particle diameter and slurry velocity on slurries with different mean concentration. The measurements of Matousek [103, 104] (cases P37 to P47) provide the opportunity to extend the validity of the model up to a pipe Reynolds number $\mathrm{Re} = D_p V_s / \nu_c$ of about 10^6. Finally, the data of Shaan *et al.* [136] (cases P48 to P69) are used to assess the performance of the model in case of solid particles with different shape of the grains. In particular, the authors compared the pressure drop when the solid phase consists of either nearly spherical glass beads or extremely irregularly shaped Lane Mountain sand. The particle shape is identified by reference to axis ratio and the circularity index introduced in Section 1.4.

Table 3.3: Flow conditions considered for the model's validation. Pattern: FS=fully suspended flow; MB=moving bed flow (*: inferred from the plot of pressure gradient versus slurry bulk-mean velocity; **: inferred from the experimental measurements of concentration and velocity). Measurements available: CP=Concentration profile; VP=Velocity profile; PG=Pressure gradient

CaseID	Reference	D_p [mm]	V_s [m/s]	$d_p[\mu m]$	$\rho_p[Kg/m^3]$	C [%]	Pattern	CP	VP	PG
P1	[126]	51.5	1.66	165	2650	8.4	-	-	X	-
P2	[126]	51.5	3.78	165	2650	9.2	FS**	X	X	-
P3	[126]	51.5	4.17	165	2650	18.9	FS**	X	-	-
P4	[126]	51.5	4.33	165	2650	28.6	FS**	X	-	-
P5	[126]	51.5	3.44	480	2650	9.2	-	X	-	-
P6	[126]	51.5	3.44	480	2650	20.3	-	X	-	-
P7	[126]	51.5	3.44	480	2650	29.6	-	X	-	-
P8	[126]	50.7	1.90	520	2650	12.1	-	X	X	-
P9	[126]	50.7	2.00	520	2650	24.7	MB**	X	-	-
P10	[126]	50.7	3.20	520	2650	11.9	-	-	X	-
P11	[126]	50.7	4.00	520	2650	11.4	-	-	X	-
P12	[53]	102.7	1.33	90	2650	19.8	FS*	X	X	X
P13	[53]	102.7	1.33	90	2650	28.3	FS*	X	-	X
P14	[53]	102.7	2.00	90	2650	19.0	FS*	-	X	X
P15	[53]	102.7	3.00	90	2650	19.0	FS*	X	X	X
P16	[53]	102.7	3.00	90	2650	23.8	FS*	X	-	X
P17	[53]	102.7	3.00	90	2650	28.4	FS*	X	-	X
P18	[53]	102.7	3.00	90	2650	33.1	FS*	X	-	X
P19	[53]	102.7	5.00	90	2650	19.4	FS*	-	-	X
P20	[53]	102.7	5.00	90	2650	28.4	FS*	-	-	X
P21	[53]	102.7	7.00	90	2650	19.4	FS*	-	-	X
P22	[53]	102.7	7.00	90	2650	23.9	FS*	-	-	X
P23	[53]	102.7	7.00	90	2650	28.4	FS*	-	-	X
P24	[53]	102.7	7.00	90	2650	32.5	FS*	-	-	X
P25	[53]	102.7	2.60	280	2650	12.0	FS*	X	-	X
P26	[53]	102.7	2.60	280	2650	20.8	-	X	-	X
P27	[53]	102.7	2.60	280	2650	31.0	MB*	X	-	X
P28	[53]	102.7	2.60	280	2650	40.7	MB*	X	-	X
P29	[53]	102.7	5.40	280	2650	10.6	FS*	X	-	X
P30	[53]	102.7	5.40	280	2650	20.3	FS*	X	-	X
P31	[53]	102.7	5.40	280	2650	30.1	FS*	X	-	X
P32	[53]	102.7	5.40	280	2650	40.5	FS*	X	-	X
P33	[53]	102.7	7.00	280	2650	11.3	FS*	-	-	X
P34	[53]	102.7	7.00	280	2650	20.6	FS*	-	-	X
P35	[53]	102.7	7.00	280	2650	30.5	FS*	-	-	X
P36	[53]	102.7	7.00	280	2650	40.6	FS*	-	-	X
P37	[103, 104]	150.0	2.00	120	-	26.0	FS*	X	-	X
P38	[103, 104]	150.0	2.00	120	-	35.0	-	X	-	-
P39	[103, 104]	150.0	3.00	120	-	26.0	FS*	-	-	X
P40	[103, 104]	150.0	4.00	120	-	26.0	FS*	-	-	X
P41	[103, 104]	150.0	6.00	120	-	34.0	-	X	-	-
P42	[103, 104]	150.0	3.00	370	-	26.0	MB*	-	-	X
P43	[103, 104]	150.0	4.00	370	-	26.0	FS*	-	-	X
P44	[103, 104]	150.0	6.00	370	-	26.0	FS*	X	-	X
P45	[103, 104]	150.0	6.00	370	-	34.0	-	X	-	X
P46	[103, 104]	150.0	6.00	370	-	43.0	MB*	X	-	X
P47	[103, 104]	150.0	8.00	370	-	26.0	FS*	X	-	X
P48	[136]	53.2	1.50	90	2655	15.0	FS	-	-	X
P49	[136]	53.2	1.50	90	2655	35.0	FS	-	-	X
P50	[136]	53.2	3.00	90	2655	15.0	FS	-	-	X
P51	[136]	53.2	3.00	90	2655	30.0	FS	-	-	X

P52	[136]	53.2	3.00	90	2655	35.0	FS	-	-	X
P53	[136]	53.2	4.00	90	2655	15.0	FS	-	-	X
P54	[136]	53.2	4.00	90	2655	35.0	FS	-	-	X
P55	[136]	158.5	1.40	90	2655	32.0	FS	X	-	X
P56	[136]	158.5	1.50	90	2655	13.9	FS	X	-	X
P57	[136]	158.5	3.00	90	2655	13.9	FS	X	-	X
P58	[136]	158.5	3.00	90	2655	32.0	FS	X	-	X
P59	[136]	158.5	3.00	90	2655	39.3	FS	-	-	X
P60	[136]	158.5	5.00	90	2655	13.9	FS	-	-	X
P61	[136]	158.5	5.00	90	2655	32.0	FS	-	-	X
P62	[136]	53.2	2.00	100	2440	15.0	FS	-	-	X
P63	[136]	53.2	2.00	100	2440	35.0	FS	-	-	X
P64	[136]	53.2	3.00	100	2440	15.0	FS	-	-	X
P65	[136]	53.2	3.00	100	2440	35.0	FS	-	-	X
P66	[136]	53.2	4.00	100	2440	15.0	FS	-	-	X
P67	[136]	53.2	4.00	100	2440	30.0	FS	-	-	X
P68	[136]	53.2	4.00	100	2440	35.0	FS	-	-	X
P69	[136]	53.2	4.00	100	2440	34.0	FS	-	-	X

In all the simulations the pipe is assumed hydraulically smooth, so that the equilibrium log law of Launder and Spalding [91] for smooth walls applies. This assumption was verified in the light of the Moody diagram for all the flow conditions in which the experimenters reported values of pipe roughness.

When comparing computations with measurements, potential sources of uncertainty were taken into account. The experimental measurements are subjected to errors which depend both on the flow condition and on the instrumentation used, previously discussed in Section 2.1. These errors will be explored when making the comparison. The sources of uncertainty in the numerical results are the mesh resolution and the empirical models employed for the interphase-transfer processes and closure of the various turbulence correlations. In a certain manner, the simulations on the whole dataset of Table 3.3 confirm and extend the results of the sensitivity analysis illustrated in Section 3.4 for few representative flow conditions. Therefore, the Mooney's correlation for the viscosity of the mixture (Eq. B.7) with $[\eta] = 2.5$ and $\alpha_{\max} = 0.7$, a turbulent Schmidt number of 0.7, and the equilibrium log law of Launder and Spalding (Eq.3.18) are employed.

The model's capability to predict the solids concentration, the velocity profile and the pressure gradient will be discussed below in separate sub-sections.

3.5.1   Solids concentration profile

For all the flow conditions summarized in Table 3.3, the absorption method is used to evaluated local values of concentration, therefore the chord-average solids concentration profile (Eq. 3.16) is used for comparison to the experiments.

Figure 3.22 compares the computed and measured solids concentration profiles for the flow conditions of Roco and Shook [126]. For the smaller particles (165 μm), the good agreement between computation and measurements reveals that, whatever the boundary condition applied is, the model is able to reproduce the effect of particle size on the concentration distribution for slurries with different in situ solids volume concentration. The agreement worsens for the larger particles (480 and 520 μm), except
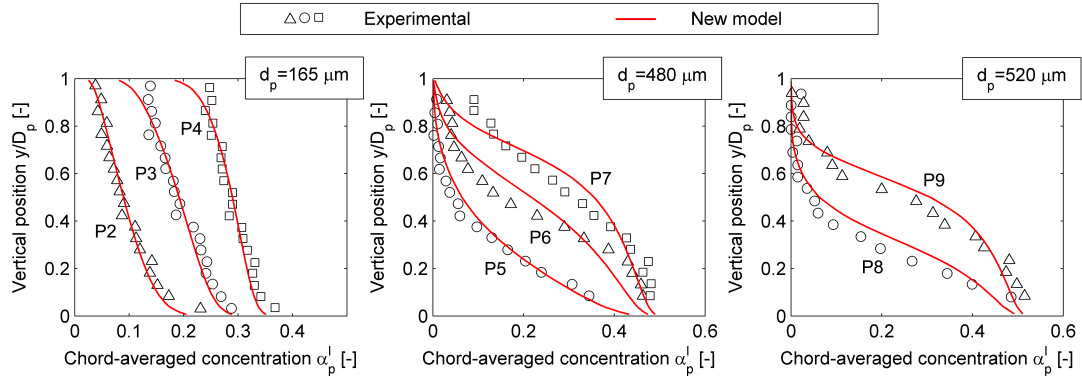
Figure 3.22: Solids concentration profile for the flow conditions of Roco and Shook [126], reported in Table 3.3

for case P5. Since the authors provide neither the values of the deposition velocity nor plots of pressure gradient versus slurry velocity, the flow pattern can be guessed only from the shape of the concentration and velocity profiles, which, for cases P5 to P9 suggests moving-bed flow. This confirms the unsuitability of the model for this flow pattern, do to the inadequate modeling of the long-lasting contact stresses among the particles and between the particles and the wall. Actually, whatever the inferred flow pattern is, for the most concentrated slurries (cases P4, P7, P9), the model seems to underestimate the solids volume fraction in the upper part of the pipe, near the pipe wall. Similar discrepancies can be detected also in the results of Ekambara *et al.* [41]. This underestimate may be due to the inadequacy of both models to catch specific features of the flow, but it is worth noting that the measurements themselves may be subject to a significant experimental error.

Figure 3.23 shows comparison of the computational and the experimental results for the chord-average distribution of the solids volume fraction with respect to the data of Gillies and co-workers [53]. From the plot of pressure gradient versus slurry velocity, it can be inferred that the flow is fully-suspended for all the flow conditions considered for comparison, even if for the larger particles ($d_p = 280\ \mu$m), the velocity $V_s = 2.6$ m/s is rather close to that corresponding to the minimum pressure gradient, which is around 2.1 m/s. Except for this flow condition (cases P25 to P28) the model produces good overall agreement with the data.

Figure 3.24 compares the computed and measured solids concentration profiles for some flow conditions investigated by Vlacav Matousek and reported in two different works [103, 104]; each set of experimental data has error bars indicating the uncertainty of 4% declared by the experimenter. Unfortunately neither the density of the solid phase nor the pipe roughness is reported in the experiments; and so the simulations were run with $\rho_p = 2650$ kg/m^3, which is the same value of Gillies *et al.* [53], and assuming the pipe hydraulically smooth. From the experimentally determined plots of pressure gradient versus slurry superficial velocity it is possible to determine the flow pattern for the flow conditions, which is fully-suspended flow for cases P37, P38, P41, and P44 and
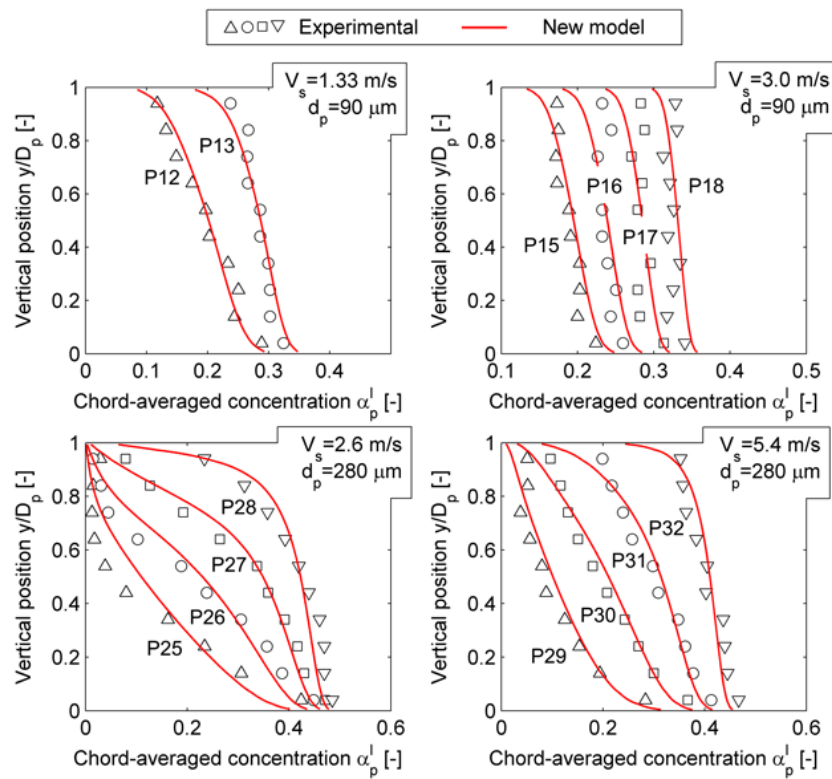
Figure 3.23: Solids concentration profile for the flow conditions of Gillies *et al.* [53], reported in Table 3.3
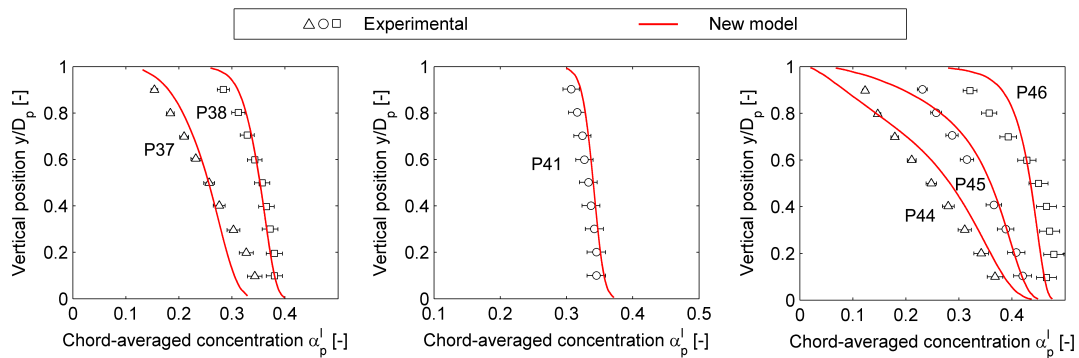
Figure 3.24: Solids concentration profile for the flow conditions of Matousek [103, 104], reported in Table 3.3
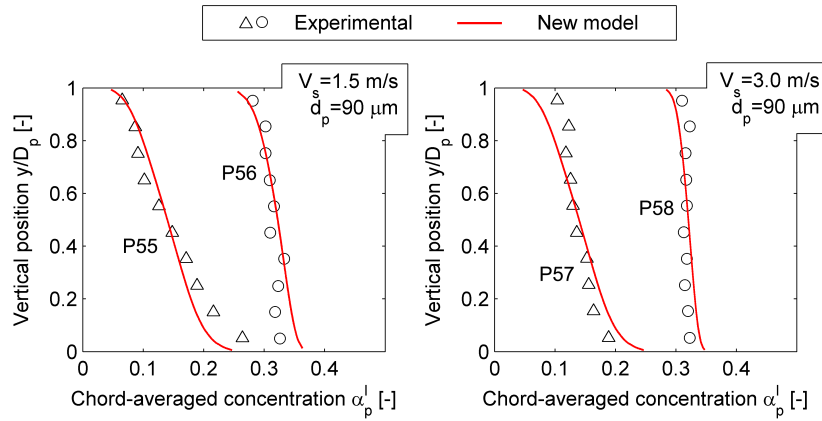
Figure 3.25: Solids concentration profile for the flow conditions of Shaan *et al.* [136], reported in Table 3.3

moving-bed flow for case P46. The identification seems instead more questionable for case P45. The rather good agreement between computations and measurements confirm the suitability of the model to provide estimation of the overall trend of the solids concentration profile for fully-suspended flows (P37, P38, P41, P44) and its unsuitability to simulate moving-bed flows (P46). The lack of complete information about the experimental conditions must be taken into account when comparing measurements and predictions, especially in regards to the deviations observed in cases P37 and P44.

The paper of Shaan *et al.* [136] focuses on the effect of particle shape on pressure gradient and deposition velocity, but the researchers also reported measurements of the solids concentration profiles. In particular, these plots are shown for mixtures of Lane Mountain sand, whose particles have a very irregular shape, as can be inferred by comparing the measured values of axis ratio (1.6) and circularity (0.62) against typical values reported in the literature for sand grains. In the simulations, the mass-median value of the particle size distribution curve is taken as the characteristic particle diameter. The numerical and experimental results are compared in Figure 3.25 for some of the flow conditions reported in Table 3.3. In all cases, the flow is fully-suspended as it can be inferred from the plot of pressure gradient versus slurry velocity. The roughly good agreement between the numerical predictions and the experimental evidence indicates that the new model is capable to predict the overall trend of the solid concentration distribution in fully-suspended flows produced by sands with a very irregular shape.

3.5.2 Velocity profile

Velocity profiles have been reported by Roco and Shook [126] and Gillies *et al.* [53]. The authors didn't specify what velocity has been reported, i.e. fluid velocity, particle velocity or mixture velocity. Actually, is it for large particles that the slip between the phases is expected to become important, resulting in non negligible difference between the three velocities. Anyway, due to the lack of information, the comparison between
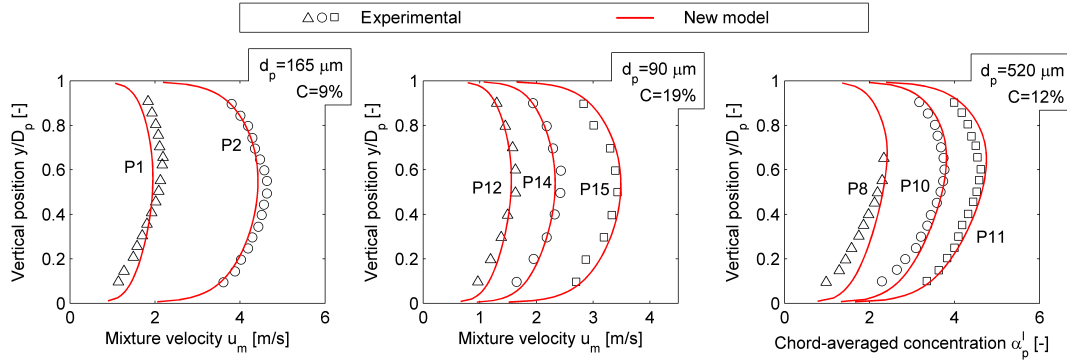
Figure 3.26: Velocity profile for the flow conditions of Roco and Shook [126] and Gillies *et al.* [53], reported in Table 3.3

computation and experiments is performed with respect to the mass averaged mixture velocity (Eq. 3.17). Figure 3.26 compares the predictions of the new model to all the measurements available among those reported in Table 3.1. For the flow conditions taken from Gillies *et al.* [53] (P12, P14, P15), the trend of pressure gradient versus superficial velocity indicates fully-suspended flow. Unfortunately, this trend is not reported by Roco and Shook [126], therefore the flow pattern for the other cases (P1, P2, P8, P10, P11) can only be inferred from the shape of the solids concentration profile, when available. Fully-suspended flow is suggested for case P1, while moving-bed flow is likely to occur for case P8. Due to the lack of specific data, a preliminar estimation of the deposition velocity was made by means of the Wasp formula (Eq. 3.1) yels 1.21 and 1.57 m/s for the flow conditions reported in the first and third plots in Figure 3.26. The analysis reported in Appendix C indicates that the Wasp formula is capable to procure a rough estimate of the deposition velocity. Therefore, the hypothesis of moving-bed flow may be plausible for cases P1 and P8, where the superficial velocity is 1.66 and 1.90 m/s respectively. At the same time, a fully-suspended flow seems likely to occur in cases P10 and P11.

The results confirm the conclusions reached up to this point. The application of the equilibrium log law of Launder and Spalding [91] to the solid phase produces physically consistent predictions of the velocity profile, in which the maximum is above the pipe axis. The numerical results show agreement to the experimental evidence for expected fully-suspended flows (P2, P10, P11, P12, P14, and P15), while a certain devitation is observed for moving-bed flows (P1 and P8).

3.5.3 Pressure gradient

Measurements of pressure gradient have been reported by Gillies *et al.* [53], Matousek [104] and Shaan *et al.* [136]. Figures 3.27 and 3.28 compare measurements and computations, in order to highlight the capability of the model to predict the effect of superficial velocity and mean delivered solids concentration one at a time on the pressure gradient. The results confirm the conclusions drawn in Section 3.4 from the analysis of few flow
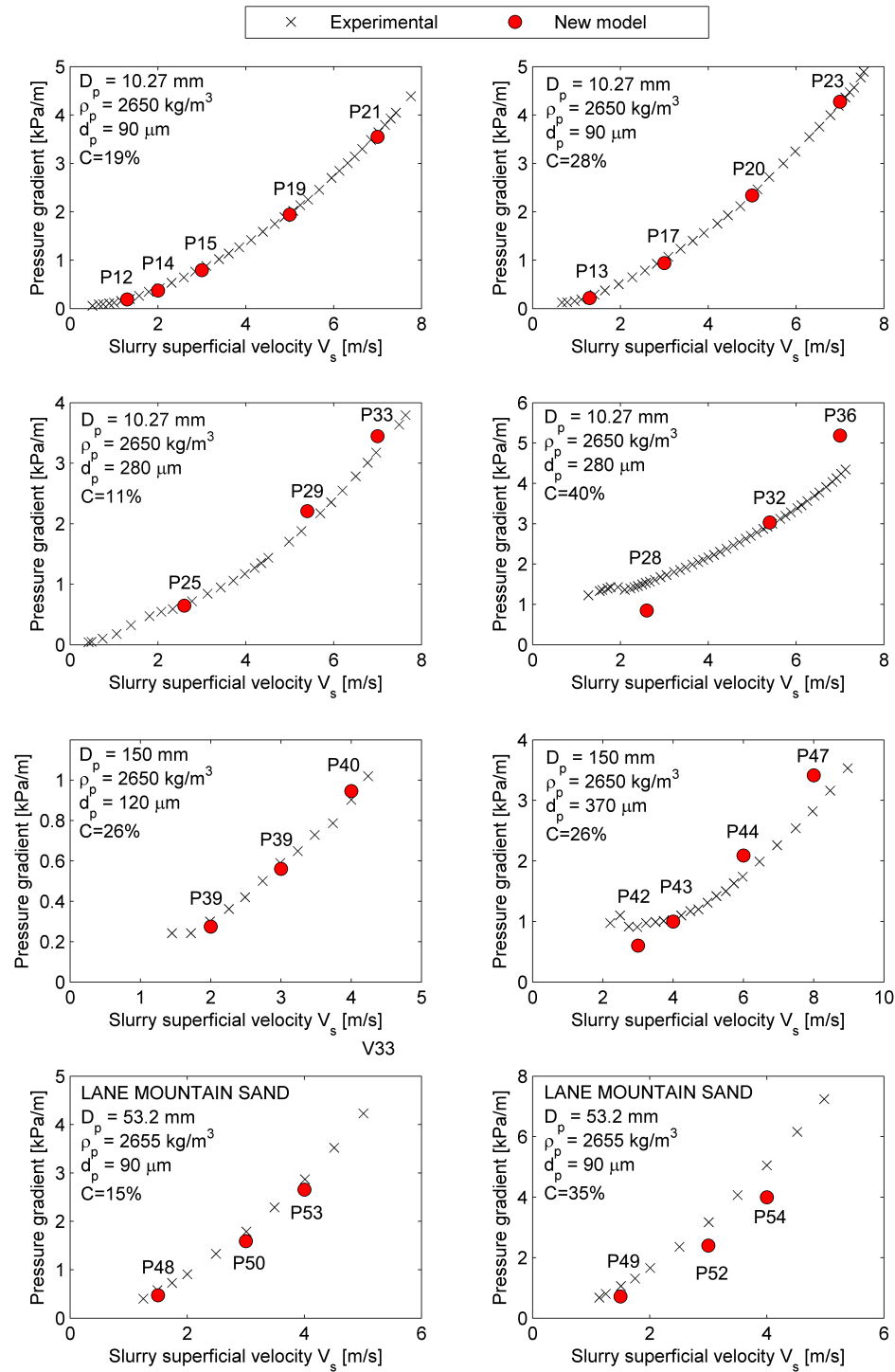
Figure 3.27: Pressure gradient versus slurry velocity: comparison between computations and experiments for the flow conditions reported in Table 3.3
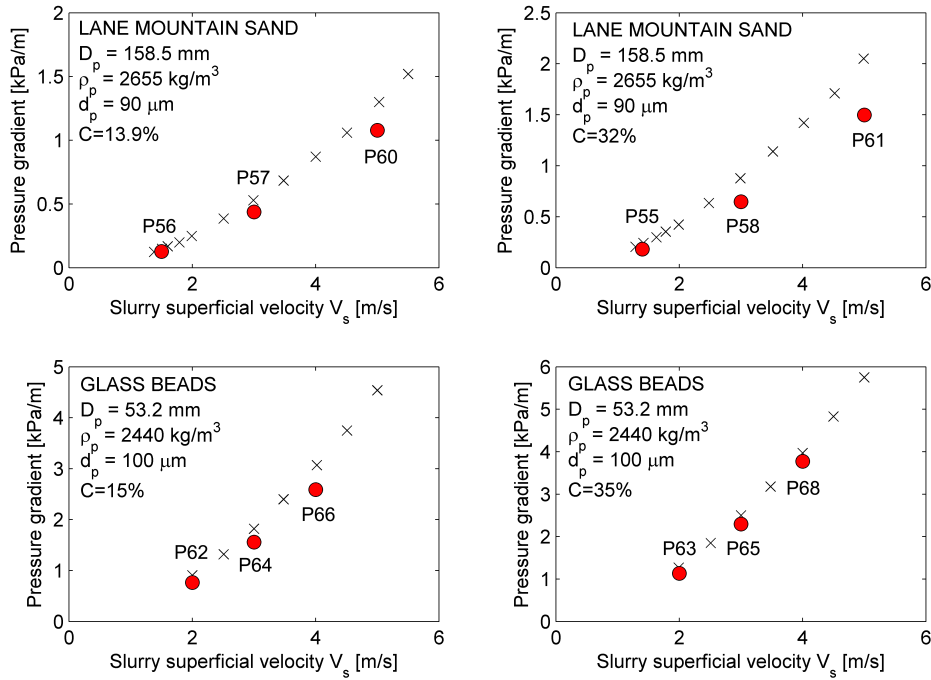
Figure 3.27: (*continued*)

conditions. The predictions are in rather good agreement with the experimental evidence for fully suspended flows, but the model is not capable to detect the presence of the minimum in the plot of pressure gradient versus slurry bulk-mean velocity which characterizes the transition to moving-bed flows (Figure 3.2). As it has been already mentioned, this limitation seems shared by all existing two-fluid models, including those based on the KTGF [17, 75]. Figure 3.29 shows the parity plot "computed pressure gradient" versus "measured pressure gradient" for all the simulations performed, excluding those referring to moving-bed flows as inferred from the experimental evidence. For the flow conditions considered, the model produces predictions of the pressure gradient within ±20% of the measured value. Despite such level of accuracy could be acceptable for many engineering applications, it is tried to investigate more deeply the results in Figure 3.29.

Figure 3.30(b) is the same plot of Figure 3.29 in which the data have been filled with different colors according to specific features of the flow. In particular, the green-filled points concern the Lane Mountain sand slurries in which the particles are charaterized by highly irregular shape (cases P48 to P61). Significant underestimations occur for this kind of slurries, especially at high solids concentration, probably because of specific friction mechanisms related to the shape of the grains. Possible developments of the work may concern the modification of the model to better accounting for the effect of particle shape. Indeed, it is worth noticing that the model appears capable to provide rather good estimation of the solids concentration profile for the same mixtures (Figure 3.25). Hereafter, these points will be excluded from the analysis, focused only on slurries made of particles with more regular shape.
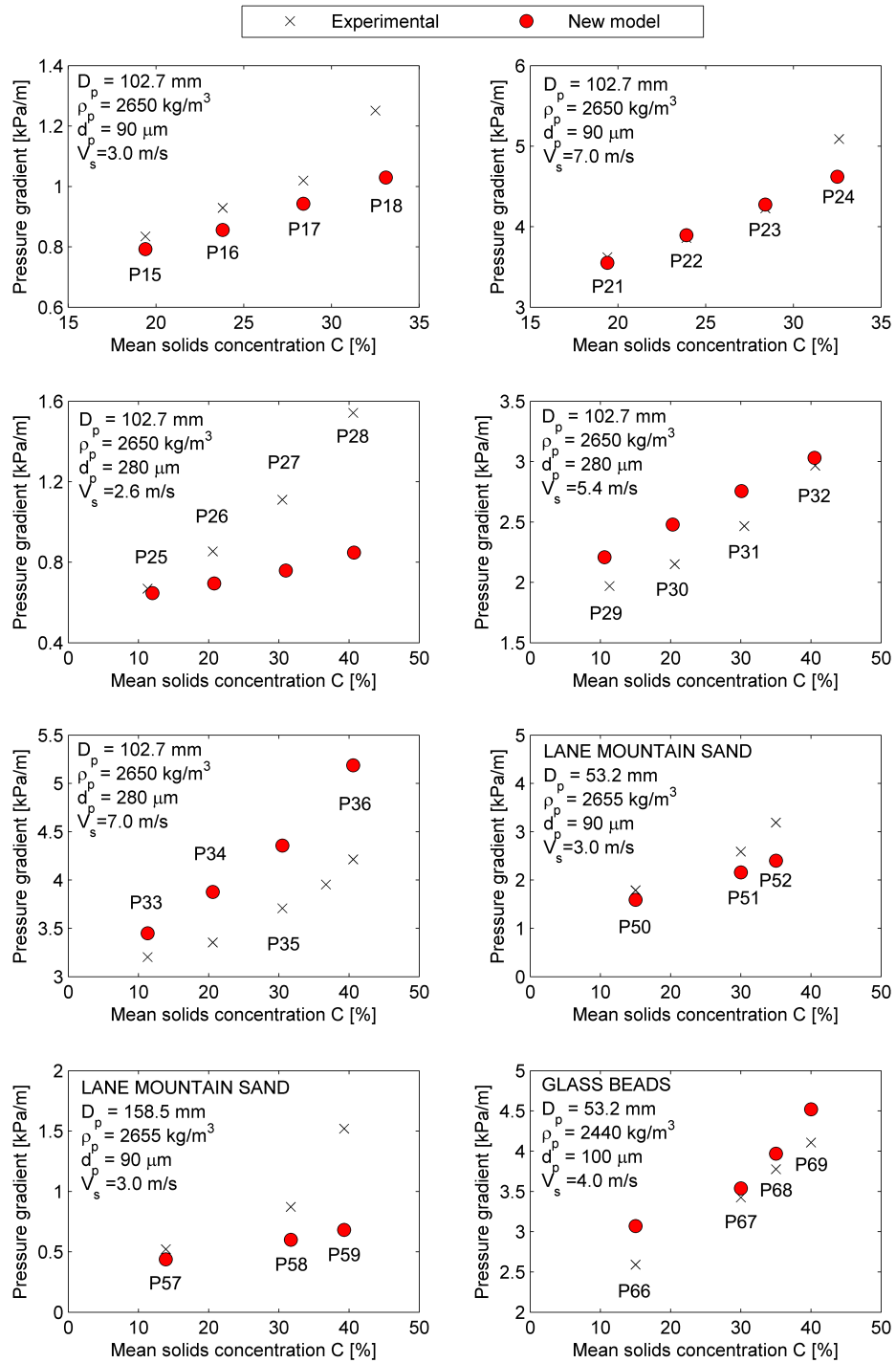
Figure 3.28: Pressure gradient versus mean delivered solids concentration: comparison between computations and experiments for the flow conditions reported in Table 3.3
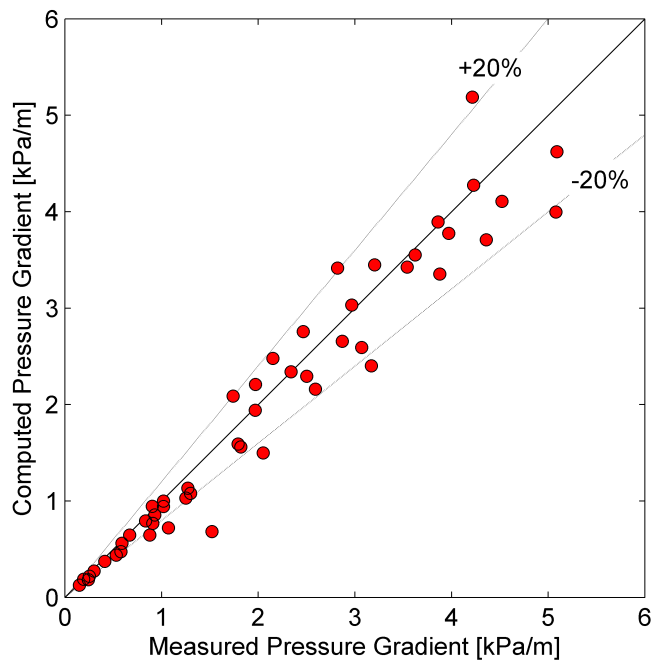
Figure 3.29: Measured versus computed pressure gradient for the flow conditions reported in Table 3.3, excluding those concerning moving-bed flows.
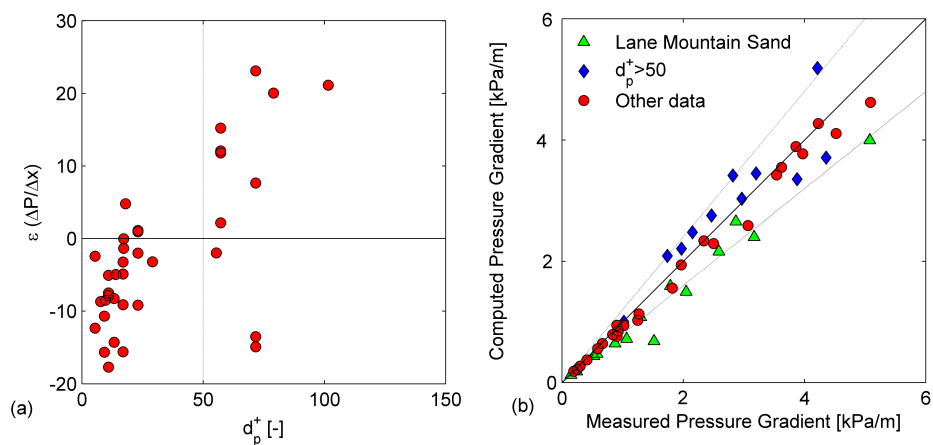
Figure 3.30: (a) Percentage deviation between measured and computed pressure gradient versus particle size in wall units for all flow conditions except those about Lane Moutain Sand (b) Measured versus computed pressure gradient for the flow conditions reported in Table 3.3, highlighting the cases of Lane Mountain Sand and those with $d_p^+ > 50$
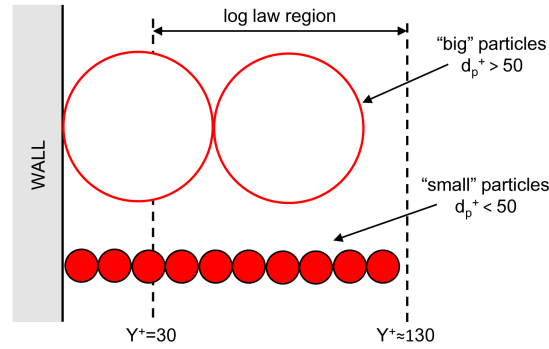
Figure 3.31: Classification between "small" and "big" particles

In order to account for the relation between the size of the grains and the thickness of the boundary layer, it is proposed a classification of the particles based on their size expressed in wall units, $d_p^+ = U^* d_p / \nu$, with the friction velocity U^* estimated by the following correlation derived for single-phase flows, $U^* = 0.1975 V_s \mathrm{Re}_D^{-0.125}$. Actually, d_p^+ could be evaluated more precisely from the value of U^* produced as output of the simulations, but no significant difference is observed in the results. Moreover, the use of the above reported correlation allows an *a priori* estimate of d_p^+. It is worth noticing that d_p^+ doesn't depend only on the particle size, but also on the flow characteristics (via U^*).

Figure 3.30(a) shows the percentage deviation between computed and measured pressure gradient $\epsilon (\Delta P / \Delta x)$ versus d_p^+ for all the flow conditions of Figure 3.29, excluding those concerning Lane Mountain sand slurries. The plot highlights that the model tends to underestimate the pressure gradient for low values of d_p^+, while an overestimation is more likely to occur for high values of this dimensionless parameter. On the grounds of these results, it is proposed a classification of the particles based on their value of d_p^+. As sketched in Figure 3.31, the particles are referred to as "small" if their size is small compared to the extension of the log law region and "big" otherwise. The threshold value $d_p^+ = 50$ separates the two classes. Actually, this value appears rather arbitrary, but not very significant in itself, because the flow conditions depicted in Figure 3.3 refer to either $d_p^+ > 50$ or $d_p^+ \ll 50$.

The parity plot in Figure 3.30(b) allows confirming the effect of d_p^+ on the accuracy of the numerical predictions, highlighting the underestimation and the overestimation which mainly characterize the "small" (red-filled points) and "big" (blue-filled points) particles according to the above reported classification. If the attention is limited to the former class, the predictions of pressure gradient essentially lie within [-15%,0] of the measured value, with significant increase of the reliability of the model. Two reasons may contribute to explain the overestimation which characterizes the "big" particles. First of all, the considerable dimension of the particles compared to the boundary layer thickness may cast doubt on the assumption that the solid phase behaves as a continuum within the log law region, with mean velocity given by 3.18. Moreover, under these con-

ditions the particles may experience a wall lubrication force (not included in the model) repelling them from the wall, resulting in losses approaching those of pure fluid [53]. This interpretation is confirmed on the grounds of the work of Wilson and Sellgren [155], who stated that the wall lubrication force is effective when the center of the particles lies in the logarithmic region of the boundary layer (or, apparently inconsistently with the theoretical derivation of their model, slightly closer to the wall), which is precisely the "big" particle case.

3.6 Applicability of the new model and comparison to the existing ones

The comparison between the prediction of the new model and the experimental evidence, illustrated in the previous section, allows establishing its applicability. The flow conditions considered for comparison, reported in Table 3.3 cover a wide range of variability of the significant parameter. The dispersed phase consists mainly of sand (particle density around $2600\,\mathrm{kg/m^3}$), but also spherical glass beads (particle density equal to $2440\,\mathrm{kg/m^3}$) have been explored briefly. The pipe diameter ranges from 50 and 158 mmm, the slurry superficial velocity from 1.3 and 8 m/s; the particle size from 90 and 520 μm; and the mean solids concentration between 8 and 43%. The data refer to either fully-suspended and moving-bed flows. It's worth noticing that for none of the existing two-fluid models such an extensive validation have been reported except for that of Ekambara *et al* [41] who focused mainly of the solids concentration distribution.

The results illustrated in Section 3.5 highlight that the new model is capable to reproduce rather accurately the solids concentration profile, the velocity profile and the pressure gradient in case of fully-suspended flows. In first approximation, and just for circular pipes, the presence of such flow pattern can be estimated by verifying that the slurry superficial velocity is sufficiently higher than the deposition velocity as estimated by any of the correlations available in literature, for example the Wasp formula (Eq. 3.1). As far as the pressure gradient is concerned, the numerical predictions are essentially within $\pm 20\%$ of the measured values (Figure 3.29). A more detailed analysis of the results allows a better definition of the accuracy by making reference to the particle size measured in wall units d_p^+. This parameter depends on the wall shear stress (via the friction velocity $U*$), which is actually an output of the simulations; however, in first approximation, d_p^+ could be evaluated from any of the available formulas for the wall shear stress in single-phase flows. If the particles are large compared to the thickness of the log law region ($d_p^+ > 50$), the model is expected to overestimate the measured pressure gradient. Conversely, if $d_p^+ < 50$, an underestimation is more likely to occur, with the predictions within [-15%,0] of the measurements (Figure 3.30(b)). Similar predictions may be judged accurate enough for many engineering applications.

Under these conditions, the accuracy of the proposed model seems comparable to that of the existing models. Moreover, it has the advantage of a remarkable numerical efficiency (in terms of numerical stability and ease to reach a converged solution). Just
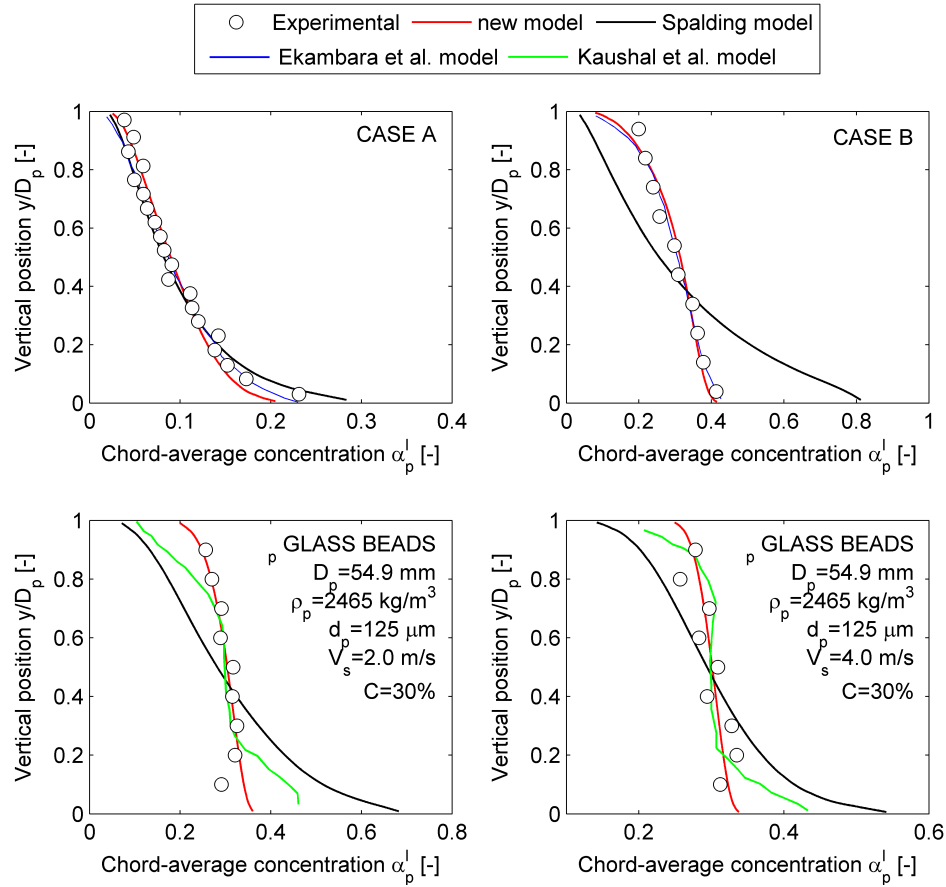
Figure 3.32: Chord-average concentration versus vertical position: comparison between experimental data [53, 78, 126] and the predictions of different models, including the new one

as a rough estimation, the simulations require about half an hour CPU time with quad core processor Intel at 2.83 GHz and 8 GB RAM. As already noticed, this feature is fundamental not so much when simulating a straight pipe flow, but mainly when dealing with more complex flows often encountered in the engineering applications.

Figure 3.32 compares the measured solids concentration profile to that predicted by the improved models and other literature models, including that of Spalding [144]. In particular, comparison to the model of Ekambara *et al.* [41] was done with respect to Cases A and B in Table 3.1; comparison to the model of Kaushal *et al.* [78] was done with respect to the following flow conditions considered by the authors: pipe diameter = 54.9 mm; particle (glass beads) density = 2465 kg/m^3; particle size = 125 μm; slurry superficial velocity = 2 or 4 m/s; and mean delivered solids concentration C=30%. The accuracy of the new model seems similar to that of the two KTGF-based models considered for comparison; indeed, the improved model seems to procure better agreement to the experimental evidence with respect to the model of Kaushal *et al.* [78] near the pipe bottom. Figure 3.32 confirms the unsuitability of the model of Spalding [144] to predict the flow of dense slurries.

A comparative analysis of the models with respect to the pressure gradient is re-
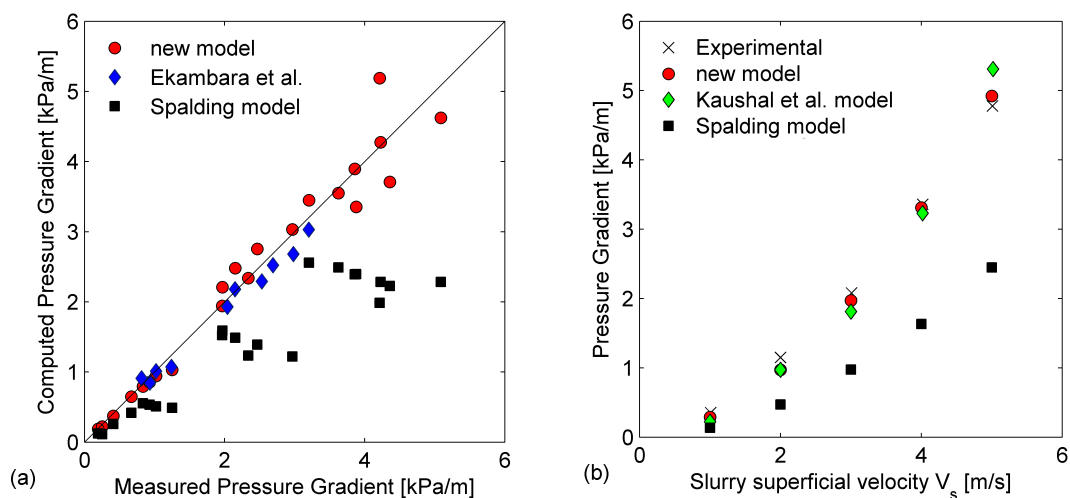
Figure 3.33: Comparative analysis between the new model and the existing models. (a) Parity plot of measured versus computed pressure gradient for the data of Gillies *et al.* [53]; (b) Pressure gradient versus slurry superficial velocity for a flow condition from Kaushal *et al.* [78], illustrated in the text.

ported in Figure 3.33. In particular, Figure 3.33 (a) shows the parity plot "measured pressure gradient" versus "predicted pressure gradient" for different flow conditions investigated experimentally by Gillies *et al.* [53]. When using the new model and that of Spalding [144], all the fully-suspended flow conditions referring to those authors among those reported in Table 3.3 were simulated, while only some of these cases are reported in the paper of Ekambara *et al.* [41] in their paper. The data shows that, when comparable, the degree of agreement to the experimental evidence is similar for the new model and that of Ekambara *et al.* [41] while the model of Spalding [144] consistently underestimate the measurements for the reasons addressed in Section 3.3. Figure 3.33(b) depicts the pressure gradient versus slurry superficial velocity for the following test case, taken from Kaushal *et al.* [78]: pipe diameter = 54.9 mm; particle (glass beads) density = 2465 kg/m^3; particle size = 125 μm; slurry bulk-mean velocity = 1 to 5 m/s; mean delivered solids concentration C=30%. The predictions of the new model and that of Kaushal *et al.* [78] are quite similar, and both agree with the experimental evidence. On the other side, the model of Spalding [144] confirms once more unsuitable for application to dense flows.

Among the possible developments of this work, a very ambitious aim may concern its extension in order to simulate moving bed flows. By the final days of writing this thesis, this matter has started to be addressed. Some preliminar results obtained are illustrated in Appendix E.

Chapter 4

Solid-liquid flow through an expansion

The present thesis involves the numerical simulation of solid-liquid flows through pipeline systems. In order to overcome the limitations which may make it difficult to apply the existing two-fluid models to more complex flows, a new model was developed and preliminarily applied to the horizontal pipe case. The model proved suitable for simulating fully-suspended flows over a wide range of operating conditions. In particular, the best performance was obtained when the shape of the particles is not extremely irregular and their size is not large compared to the boundary layer thickness ("small" particles in Figure 3.31).

Under these conditions, the two-fluid model is now applied to simulate the flow through an expansion in a rectangular duct. This geometry may be of interest for engineers since pipeline fittings involving sudden sectional area variation are often encountered in the plants. Moreover, in terms of complexity of the flow this is an intermediate step between a straight pipe and a control valve. The lack of experimental data, arising from the technical difficulties in performing the measurements, doesn't allow validating the model in the same way as for the horizontal pipe case (Section 3.5). A preliminar comparison between computations and measurements in the single-phase flow case served for defining specific settings like the turbulence model, the treatment of near-wall turbulence, and the differencing scheme for the convective fluxes. Afterwards, two-phase flow simulations were run. The modelling features found to be most effective for pipe flows were defined on the basis of the analysis described in Section 3.4: therefore, the turbulent Schmidt number for volume fraction was set to 0.7, and the Mooney's correlation (Eq. B.7) with intrinsic viscosity of 2.5 and maximum packing concentration of 0.7 was used to evaluate the viscosity of the mixture. An extended version of the log law of Launder and Spalding [91] for smooth walls was employed to better handle peculiar features of the flow. A sensitivity analysis was then performed to quantify the effect of the other modelling features, which proved to be negligible for pipe flows but could be *potentially* effective in the expansion case; basically, the lift force, the virtual mass force, and the model for the eddy viscosity of the solid phase. The phenomenological consistency of the solution was analyzed in the light of the theoretical background inferred from the technical literature.

The remainder of the chapter is divided in three sections. Section 4.1 reports a
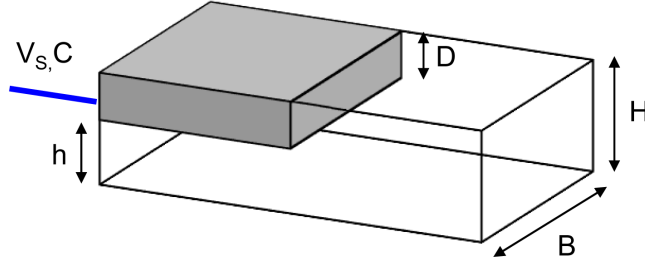
Figure 4.1: Sketch of the expansion

description of the problem and a literature background. Sections 4.2 and 4.3 describe the single-phase and two-phase flow simulations respectively.

4.1 Description of the problem and theoretical background

The geometrical configuration of the problem is sketched in Figure 4.1. A pipe with rectangular section (width B) undergoes a sudden increase in height from h to $H = h + D$. The system is subjected to the flow of a mixture of liquid and solid particles with superficial velocity V_s (upstream the expansion) and mean delivered solids concentration C. A couple of dimensionless parameters are introduced in literature, namely the expansion ratio $ER = H/h$ and the Reynolds number based on the step height $Re_D = V_s D/\nu_c$.

This geometry, often referred to as backward-facing step, has been extensively studied in the single-phase flow case, both experimentally and numerically. Variations on this theme are the planar symmetric expansion and the axisymmetric expansion in a circular pipe. A phenomenological description of the flow, as derived from the theoretical background, is given below. When a fluid flows through a backward facing-step, the flow separates and recirculation occurs downstream the step lip. The deceleration of the fluid gives rise to an increase in pressure. A qualitative sketch of the main flow variables (pressure, velocity, and turbulent kinetic energy) downstream the expansion is given in Figure 4.2. Following the nomenclature of Founti *et al.* [47], different regions can be identified, namely a core region, dominated by inertia, a shear layer region characterized by a peak in the turbulent kinetic energy, a recirculation region, and a near wall region (Figure 4.3). Two dimensionless variables are of particular interest for the kind of flow considered, namely the friction coefficient along the upper wall C_f and the pressure coefficient C_p, defined respectively as:

$$C_f = \frac{\tau_w}{0.5\rho V_0^2} \tag{4.1}$$

$$C_p = \frac{p - p_0}{0.5\rho V_0^2} \tag{4.2}$$

in which τ_w is the wall shear stress, V_0 and p_0 the reference values of velocity and pressure respectively. In the present work, V_0 is taken as the superficial velocity in the small duct.
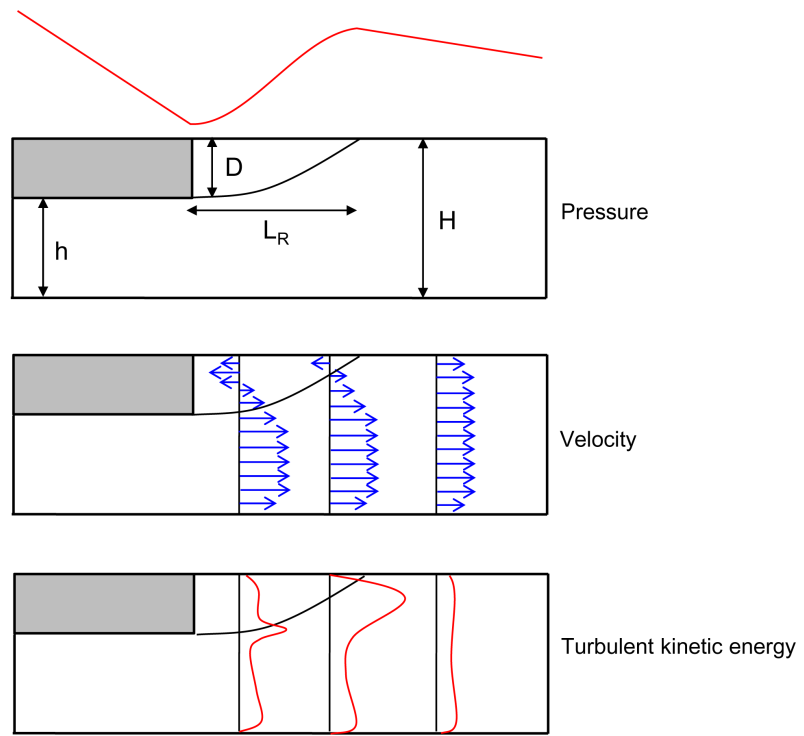
Figure 4.2: Qualitative sketch of pressure, velocity and turbulent kinetic energy downstream a backward-facing step
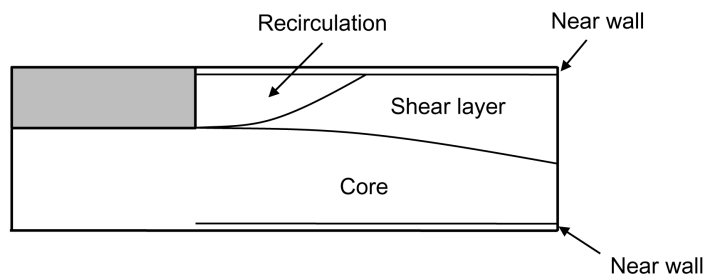
Figure 4.3: Regions downstream the step on the grounds of the work of Founti *et al.* [47]

The reattachment length L_R, which is an indicator of the size of the recirculation region, is commonly evaluated as the distance from the step where C_f (i.e. τ_w) changes its sign.

The flow of a solid-liquid mixture through an expansion is very complex, as it is the results of several physical mechanisms. The following contributions must be taken into account. Firstly, the response of the particles to the mean fluid flow, that is to what extents do the particles tend to follow the mean flow of the fluid. Secondly, turbulent dispersion, that is how the particles are affected by the turbulent fluctuations of the fluid. Turbulent dispersion causes the particles to spread throughout the fluid, entering the recirculation region. The main parameter controlling these mechanisms is the integral scale Stokes number S_Λ defined in Section 1.4. The fluid time scale τ_Λ chosen for evaluating the Stokes number is typically based on an approximate large-eddy passing frequency in the separated shear layer [12, 46]:

$$\tau_\Lambda = \frac{5D}{U_0} \tag{4.3}$$

in which U_0 is the small channel centerline velocity. Both the particle response to the mean flow and particle turbulent dispersion increase as S_Λ decreases. Two other mechanisms contribute to the development of the two-phase flow, namely gravity and inter-particle collisions and contacts. The former increases with particle mass, and contributes to keep the particles within the core region, precluding them from entering the recirculation region. In order to determine the importance of the latter, a hardly quantifiable collisional Stokes number was introduced in Section 1.4. However, roughly speaking, the effectiveness of inter particle collisions increases as the mean solids concentration increases.

The literature material about the flow of solid-liquid mixtures through sudden expansions, and, more generally, pipeline fittings, is rather poor.

Due to the technical difficulties encountered in performing the measurements, the experimental tests are essentially limited to very dilute flows. In few cases, the authors performed measurements of hydrodynamic parameters, namely the velocity of both phases and related quantities, such as the turbulent intensity. Conversely, in the majority of the campaigns the experimenters report only some derived variables which are easier to collect, besides being of significant engineering interest, like the erosion rate. Blatt *et al.* [13] studied the flow of water and spherical glass beads (size = 800 μm) in an axisymmetric sudden enlargement with expansion ratio of 1.53. The mean delivered concentration of the solid phase is 0.1%, and the step Reynolds number Re_D is 8000. The authors used LDV to measure axial and radial velocity of both phases along the pipe axis and close to the pipe wall. Nesic and Postlethwaite [115] investigated the erosion produced by a mixture of water and monodispersed solid particles of different materials (sand, glass beads) in an axisymmetric sudden enlargement with expansion ratio around 2. The mean delivered solids concentration is increased from 2 to 10%, and the step Reynolds number Re_D is around 140000. The authors didn't provide measurements of hydrodynamic quantities, but reported a parametric investigation of the erosion rate as

a function of the mean solids concentration and of the some characteristics of walls and particles. Founti and Klipfel [48] measured mean and fluctuating velocity distributions for a flow of diesel oil (density = 830 kg/m^3; viscosity = $5.21 \cdot 10^{-6}$ m^2/s) and spherical glass particles (density = 2500 kg/m^3; size = 450μm) in an axisymmetric sudden enlargement with expansion ratio of 2. The mean delivered solids concentration varies between 1 and 5%, and the step Reynolds number is around 10000.

Most of the numerical investigations focused on the erosion caused by the prolonged exposure of the pipeline fittings to the impact of solid particles dragged by the fluid. As in most engineering applications, the simulations concerned very dilute mixtures, and were usually performed following the Eulerian-Lagrangian approach (Sub-section 2.2.1) starting from which the application of erosion models is straighforward.

Nesic and Postlethwaite [114] used an Eulerian-Lagrangian model to simulate the flow conditions tested by Blatt *et al.* [13], reporting good agreement to the measured values of velocity. The authors used also their numerical solution as input for erosion models, comparing predicted and measured erosion rates. Maria Founti and co-workers [47, 48] accompanied their experimental tests by numerical simulations performed by means of an Eulerian-Lagrangian model. The mean and fluctuating axial velocity profiles were computed for mean delivered solids concentration of 3 and 5%, showing good agreement to the experimental evidence. H.M. Badr, M.A. Habib *et al.* [6, 7, 57, 58] studied the flow of sand particles and water through sudden contractions with different geometrical characteristics in vertical pipes. The authors performed a Lagrangian tracking of the particles under the hypothesis of one-way coupling with the aim to predict the erosion of the system. Validation is performed with respect to the erosion rate measurements of Nesic and Postlethwaite [115]. Mohanarangam and Tu [108] used a two-fluid model to simulate the flow of the mixture of glass particles and diesel oil tested experimentally by Founti and Klipfel [48], and analyzed the dependence of the mean and fluctuating velocities of the solid phase upon the integral scale Stokes number. Validation of the model was performed with respect to the velocity profiles reported by the experimenters. Frawley *et al.* [49] compared the performance of two-fluid and Eulerian-Lagrangian models in the simulation of the flow of the flow conditions of Founti and Klipfel [48]. The authors focused their attention on the velocity field and found that the discrepancy in the predictions of the mean velocity profiles of both phases obtained with the two models is insignificant and that the two-fluid model yields more accurate results in term of turbulent kinetic energy. Moreover, the authors applied erosion models to reproduce the erosion rate measurements of Nesic and Postlethwaite [115]. Pathak [120] used an algebraic slip model to study a solid-water slurry flow around a rectangular block at the bottom of a channel, and analyzed on the effect of particle diameter upon the mixture velocity, the volume fraction of the solid phase and the turbulence intensity. Validation is performed with respect to the solids concentration profiles measured by Kaushal *et al.* [77] about the horizontal pipe case.
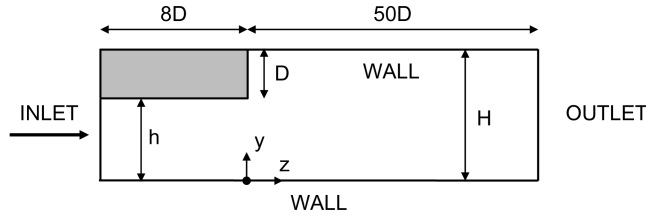
Figure 4.4: Computational domain and boundary conditions

Table 4.1: Fully developed profile at inlet. The friction factor is given by Finolenko's equation [68]

$$u_z = V\frac{(N+1)(2N+1)}{2N^2}\left(1 - \frac{2r}{h}\right)^{1/N} \quad N = \frac{1}{\sqrt{f}} \quad f = \left[1.82\log\left(\frac{2hV}{\nu}\right) - 1.64\right]^{-2}$$

$$k = V^2\frac{f}{8}\left[1 + \frac{2}{3}\frac{2r}{h} + \frac{10}{3}\left(\frac{2r}{h}\right)^3\right]$$

$$\epsilon = 0.1643\frac{k^{3/2}}{l_m} = 0.1643\frac{k^{3/2}}{\frac{h}{2}\left[0.14 - 0.08\frac{2r}{h} - 0.06\left(\frac{2r}{h}\right)^4\right]}$$

4.2   Single-phase flow study

Single-phase flow tests were first run in order to preliminary set-up the numerical model in view of the following two-phase flow simulations. In particular, they allowed defining specific settings like the domain discretization, the turbulence model, the treatment of near-wall turbulence, and the differencing scheme for the convective fluxes. The abundant experimental data available in literature were employed for validation.

The step was modeled in two-dimensions: besides reducing significantly the computer time, this configuration allows consistent comparison to the experimental data, which were typically collected in very large channels where the hypothesis of two-dimensionality of the flow is assessed. The computational domain is shown in Figure 4.4. A fully-developed turbulent flow profile is specified at the pipe inlet, employing an extension of the Nikuradse's boundary layer theory to arbitrary pipe sections for determining the distribution of axial velocity, turbulent kinetic energy and dissipation rate (Table 4.1). At the outlet, the normal gradients of all variables and the value of the pressure are set to zero. The inlet and outlet boundaries were located $8D$ and $100D$ upstream and downstream the step respectively. The latter distance, similar to those considered in previous works [84], proved to be sufficient for fully-developed flow conditions to have been achieved. No-slip conditions were imposed on the walls. In the near-wall region,
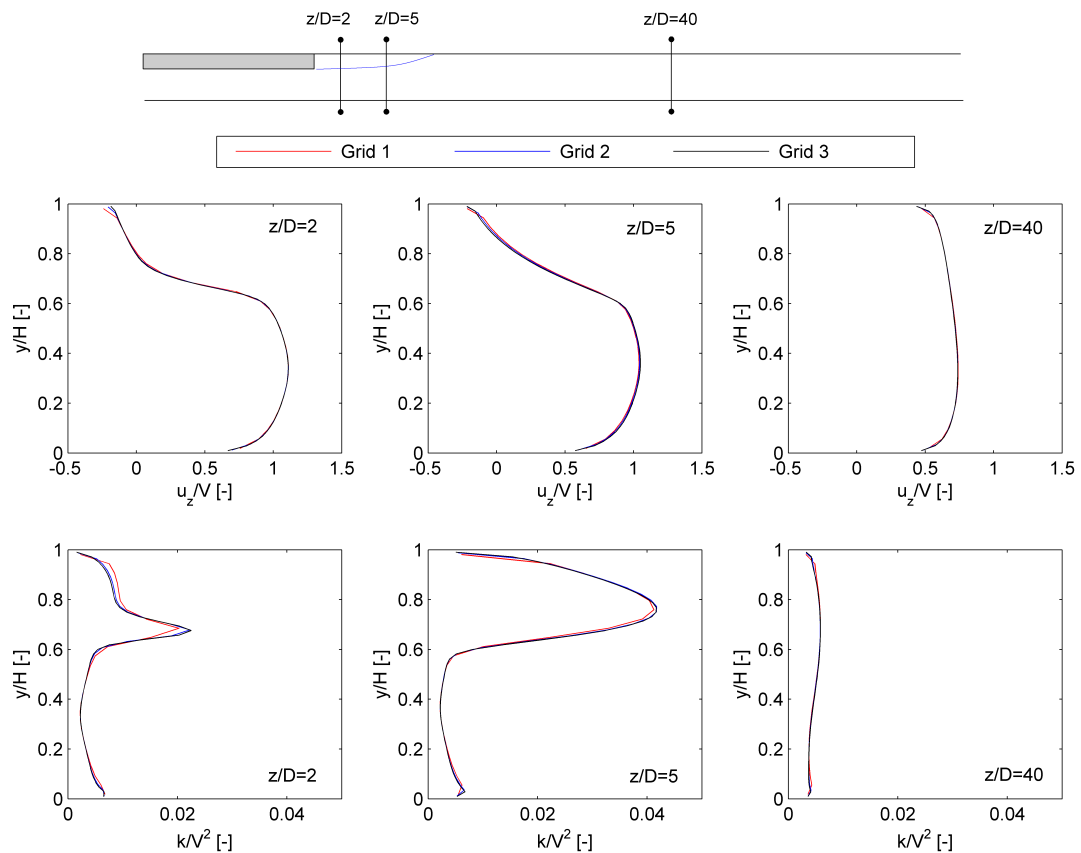
Figure 4.5: Effect of mesh resolution on the velocity and kinetic energy profiles at different locations downstream the step

the non-equilibrium log law of Launder and Spalding [91], which is an extension of the already discussed equilibrium log law, was set, as per the indications of previous workers who dealt with similar kind of flows [45, 86]. In all cases, it was checked that the application of such condition was consistent with the non-dimensional distance of the first grid points from the walls ($30 < y^+ < 130 - 180$). On the basis of the same references, the $k - \epsilon$ RNG model [150] was used.

As for the previous case, the calculations are performed following the elliptic-staggered formulation in which the scalar variables are evaluated at the cell centers and the velocity components at the cell faces. Central differencing is employed for the diffusion terms, while the convection are first discretized using the hybrid differencing scheme of Spalding [145]. The effect of higher order schemes will be discussed later in the present Section.

A cartesian mesh was used to discretize the domain. A grid sensitivity study was performed to determine the optimum discretization of the domain by reference to the predicted values of the following fluid dynamic quantities: the cross-sectional velocity and turbulent kinetic energy profiles at different locations in the streamwise direction; and the friction and pressure coefficients distributions. As far as the latter parameter is concerned, since when using an incompressible RANS model the pressure field is defined
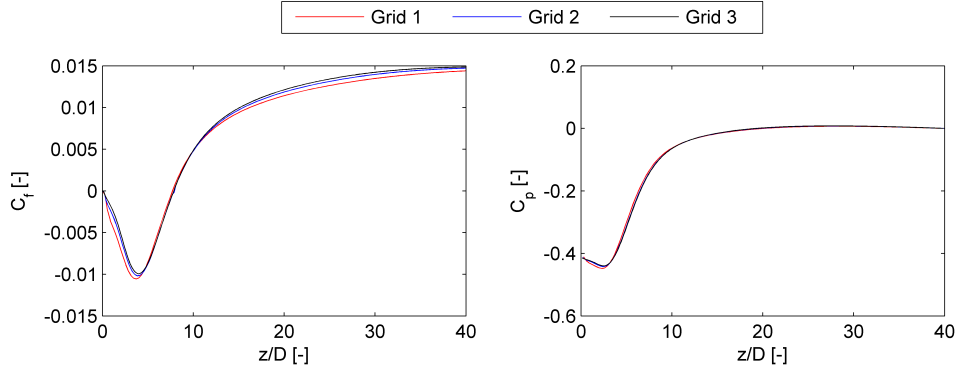
Figure 4.6: Effect of mesh resolution on the streamwise distribution of the friction and pressure coefficients

Table 4.2: Effect of mesh resolution and differencing scheme of convective fluxes on the reattachment lenght

Grid	Diff. Scheme	l_R/D
1	Hybrid	7.72
2	Hybrid	7.85
3	Hybrid	7.85
3	Harmonic Van Leer	8.00
3	Linear Upwind	8.00

up to a constant value, thus can be translated arbitrarily, the reference pressure p_0 in Eq. 4.2 was chosen in such a way that $C_p = 0$ at the outlet section. For the grid sensitivity study the following configuration was considered: $h = 26$ mm, $H = 39$ mm, $V = 4$ m/s, corresponding to an expansion ratio of 1.5 and a step Reynolds number of $5.2 \cdot 10^4$. Three different meshes were employed, as follows: 27 by 196 along the Y and Z directions respectively (Grid 1); 42 by 304 (Grid 2); and 53 by 390 (Grid 3). Figure 4.5 shows the predicted velocity and turbulent kinetic energy at distances of 2, 5 and $40D$ downstream the step computed on three different levels, whilst the effect of mesh resolution on the friction and pressure coefficient is depicted in Figure 4.6 (here the C_p distribution is evaluated in correspondence to the upper wall, but the y location of the cells used for evaluating C_p has no effect on the mesh independence analysis). From Table 4.2 it can be inferred the influence of grid discretization on the reattachment length. The solutions obtained on the two finest meshes (Grid 2 and 3) are very close to each other, whilst that for Grid 1 deviates slightly from the finer grid solutions, especially in terms of turbulent kinetic energy and friction coefficient. The Grid 3 discretization is considered adequate for comparison to the experiments.

The effect of the differencing scheme for the convective terms on the same flow parameters is investigated. Besides the hybrid scheme of Spalding [145], two higher order schemes were employed, namely the Harmonic Van Leer and the Linear Upwind. The
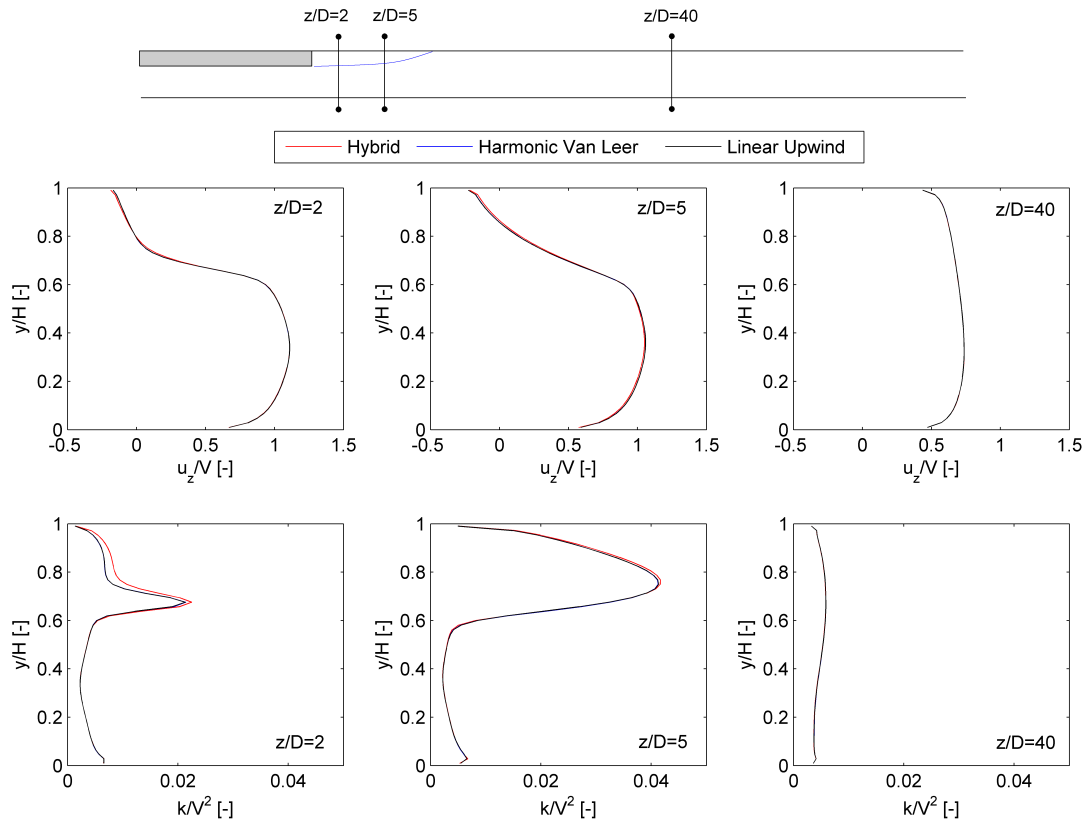
Figure 4.7: Effect of the differencing scheme for the convective terms on the velocity and kinetic energy profiles at different locations downstream the step
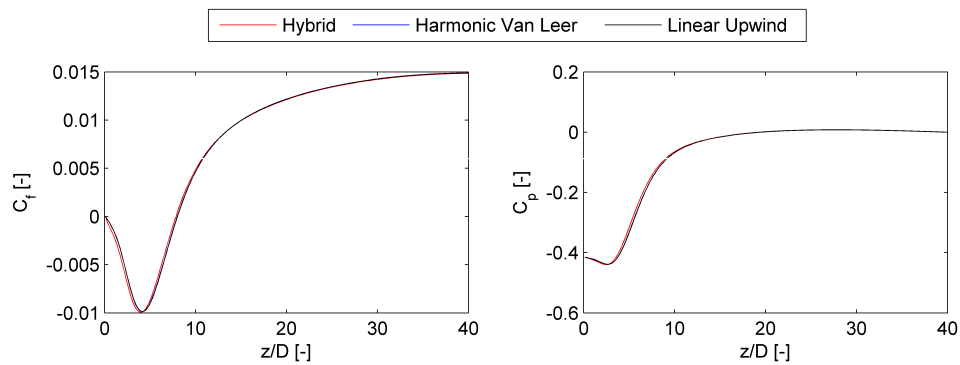
Figure 4.8: Effect of the differencing scheme for the convective terms on the streamwise distribution of the friction and pressure coefficients
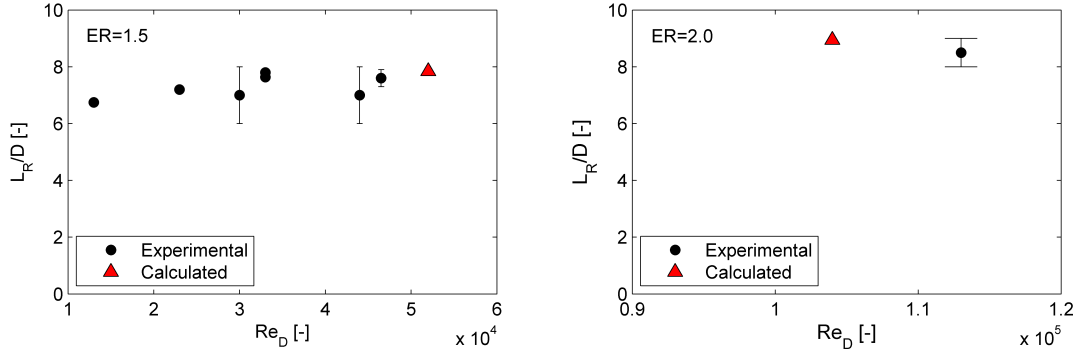
Figure 4.9: Comparison between measured and predicted reattachment length versus step Reynolds number for two different expansion ratios. The experimental data, reported in [24, 107, 111, 119, 153], have error bars indicating the uncertainty declared by the experimenters

results, reported in Figures 4.7 and 4.8 and Table 4.2, indicates that Harmonic Van Leer and Linear Upwind procure the same solution, indeed very similar to that obtained using the hybrid scheme except for the values of turbulent kinetic energy close to the step lip. The Linear Upwind scheme was used in the simulations.

A comparison to experimental data from technical literature was performed in order to check the reliability of the model in the single-phase flow case. The simulations concerned steps characterized by different expansion ratios: the number of cells along the vertical direction varied according to the expansion ratio, keeping the same aspect ratio of the cells as in Grid 3. A first validation was made with respect to the reattachment length, comparing computations and measurements from different authors [24, 107, 111, 119, 153] for expansion ratios of 1.5 and 2. Actually, the step Reynolds number of the simulations is different from the values of the experimenters. However, as already reported in literature and as suggested by the trend of the experimental data, the reattachment lenght is essentialy independent from Re_D for Re_D sufficiently high. Since this is precisely the case considered here, Figure 4.9 indicates good agreement between measurements and computations.

The model's predictions were then compared to the benchmark test case of Driver and Seegmiller [38] about the following flow conditions: expansion ratio $= 1.125$, and step Reynolds number $= 3.8 \cdot 10^4$. Figure 4.10 reveals the good agreement between measured and computed velocity profiles at different axial locations along the streamwise direction. A good match between measurements and predictions is observed also in terms of the friction and pressure coefficients, as shown in Figure 4.11. The computed dimensionless reattachment length is 5.99, rather close to the range of 6.26 ± 0.1 reported by the experimenters. Given the level of accuracy needed according to the purpose of this comparison, the model has been judged sufficiently reliable in the single-phase flow case.
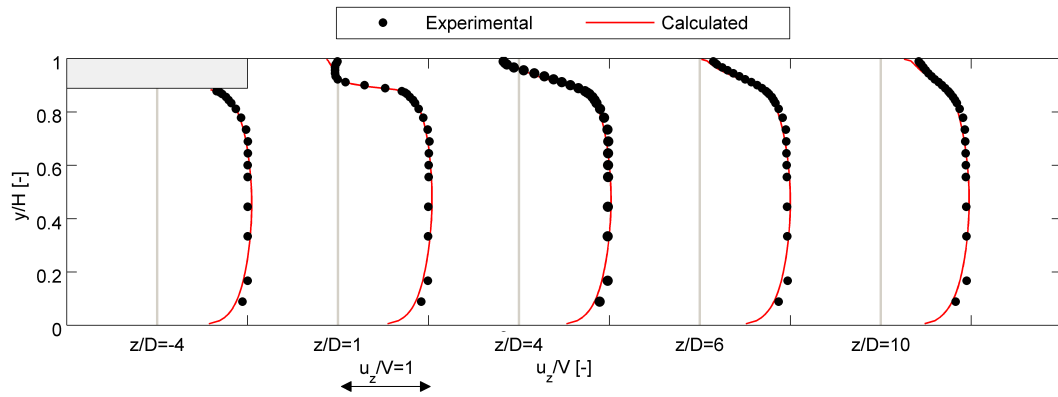
Figure 4.10: Comparison between measured and predicted velocity profiles at different locations in the streamwise direction for the benchmark test case of Driver and Seegmiller [38]
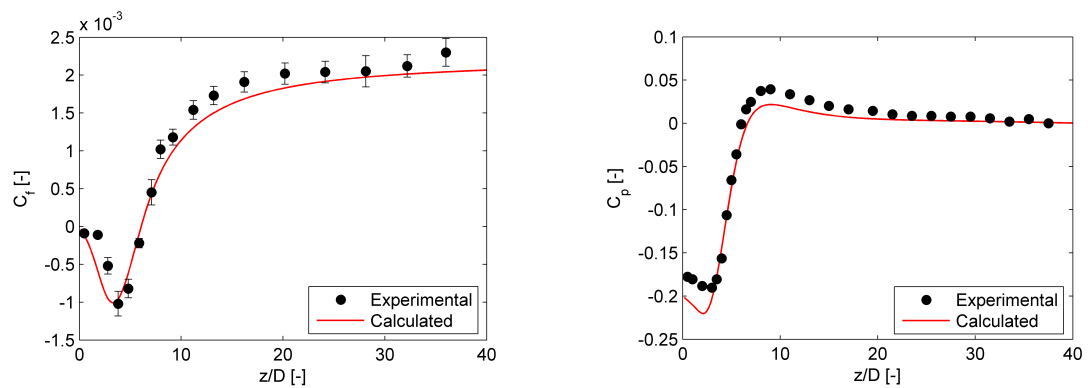
Figure 4.11: Comparison between measured and predicted friction and pressure coefficient distributions along the streamwise direction for the benchmark test case of Driver and Seegmiller [38]. The experimental data on the left plot have error bars indicating uncertainty declared by the authors

4.3   Two-phase flow study

The flow of solid-liquid mixtures through a backward-facing step is now investigated. As already noticed, the lack of experimental data about this kind of flow doesn't allow a complete validation of the two-fluid model as for the straight pipe case, implying the need to adopt alternative methods than the comparison to the experimental evidence in order to ensure the reliability of the numerical solution.

The proposed two-fluid model has a physical basis in the sense that it is obtained by a double average of the conservation equation in local instant formulation. Actually, as in other two-fluid models available in literature, many correlations arising from this process (see, for example, Elgobashi and Abou-Arab [43]) have been neglected whilst other terms have been modeled, possibly by means of empirical closures. The results reported in Chapter 3 indicates that, for fully-suspended pipe flows, either the correlations neglected are small or their effect can be fairly well represented by the closures used to model the other terms, provided that the empirical parameters upon which they depend are properly set. The effective modeling features were found to be the mixture viscosity correlation, the value of the turbulent Schmidt number for volume fractions, and the wall boundary condition for the solid phase. With a unique combination of these parameters (the correlation of Mooney with intrinsic viscosity of 2.5 and maximum packing concentration of 0.7 for the viscosity of the mixture; a turbulent Schmidt number for volume fractions of 0.7; and the equilibrium log law of Launder and Spalding [91] for the velocity of the solid phase in the near wall cells), the proposed model proved suitable to predict the flow of fully-suspended slurries in horizontal pipes. In particular, the best performance is obtained when the shape of the particles is not extremely irregular. Moreover, strickly speaking, it would be appropriate that the particle size satisfied the condition $d_p^+ < 50$ for a consitent application of the equilibrium wall function to the solid phase. The above-mentioned conditions (which imply specific contrain on particle size and density, slurry velocity, and duct size) have been essentially fulfilled in the simulations of the expansion. This may reasonably indicate that the flow field will be correctly predicted at least far from the recirculation region downstream the step (indeed, this is not straightforwardly guaranteed as the conclusions reached in Chapter 3 refer to pipe flows instead of more complex duct flows).

A sensitivity analysis is performed to investigate the influence of others "degrees of freedom" of the model which proved ineffective for pipe flows but could in principle be significant for more complex flows. Among them, the inclusion of lift and virtual mass in the generalized drag term, and the employment of more complex correlations for the particle eddy viscosity. Actually, this in itself is not enough to guarantee the reliability of the model in the expansion case, since some of the correlations arising from the double-average may become significant for such flow (or cannot be adequately represented by the closures used). As further verification step, the phenomenological consistency of the solution is analyzed critically in the light of the theoretical knowledge of the phenomenon as inferred from the open literature with mainly concerns rather dilute gas-solid flows. All

these activities contribute to establish that the two-fluid model is suitable for providing information of technical interest in case of more complex flows, consistently with the application-aimed approach of the present thesis.

At first, the step was modeled in two-dimensions in order to save computer time and primarily analyze the numerical performance of the two-fluid model for a recirculating flow. These results are reported in Sub-section 4.3.1. The two-dimensional approximation holds only for very large values of the duct width B. The effect of B on the validity of the assumption of two-dimensionality of the flow is then investigated. For low values of B, the influence of the side walls extends up to the mean section, therefore the system must be necessarily modeled in three dimensions. This part of the work is described in Sub-section 4.3.2. At last, unsteady effects are considered in Sub-section 4.3.3.

4.3.1 Two-dimensional modelling

Numerical set up and and boundary conditions

The computational domain is similar to that of the single-phase flow case, already reported in Figure 4.4; however, the length of the large duct is increased to $200D$ to investigate the development of the flow downstream the step. At the inlet, the fully developed profiles derived from the extended boundary layer theory of Nikuradse, reported in Table 4.1, were set. No slip is assumed between the phases, therefore the same velocity profile is applied to both phases. The inlet volume fraction of the solids is taken as uniform if a pseudo-homogeneous flow is likely to occurr in the small duct, otherwise the fully-developed distribution obtained from the simulation of a straight channel is imposed. At the outlet, the normal gradient of all the solved variables is set to zero. The non-equilibrium wall funcion of Launder and Spalding [91] for smooth walls is employed to model the effect of near wall turbulence, and determining the velocity for both phases, the turbulent kinetic energy, and the dissipation rate in the near wall cells. This choice is consitent with the model proposed in Chapter 3, where the equilibrium log law was used instead of the non-equilibrium log law, since the latter reduces to the former under the hypothesis of local equilibrium between production and dissipation of turbulent kinetic energy, which typically occurs in pipe flows. Similarly, a two-phase version of the $k - \epsilon$ RNG model, which includes phase diffusion fluxes, is used to model the effect of turbulence (the equations are reported in Appendix D). As usual, the calculations follows the elliptic staggered formulation, and central differencing is employed for the diffusion terms.

Mesh and differencing scheme

A cartesian mesh was used to discretize the domain. Since, in general, a discretization suitable for the single-phase case may be unsuitable for the two-phase one, the grid sensitivity analysis was conducted again.

The results reported in Figure 3.18 about the horizontal pipe case highlight the influence of the dimensionless distance between the centers of the near wall cells and the
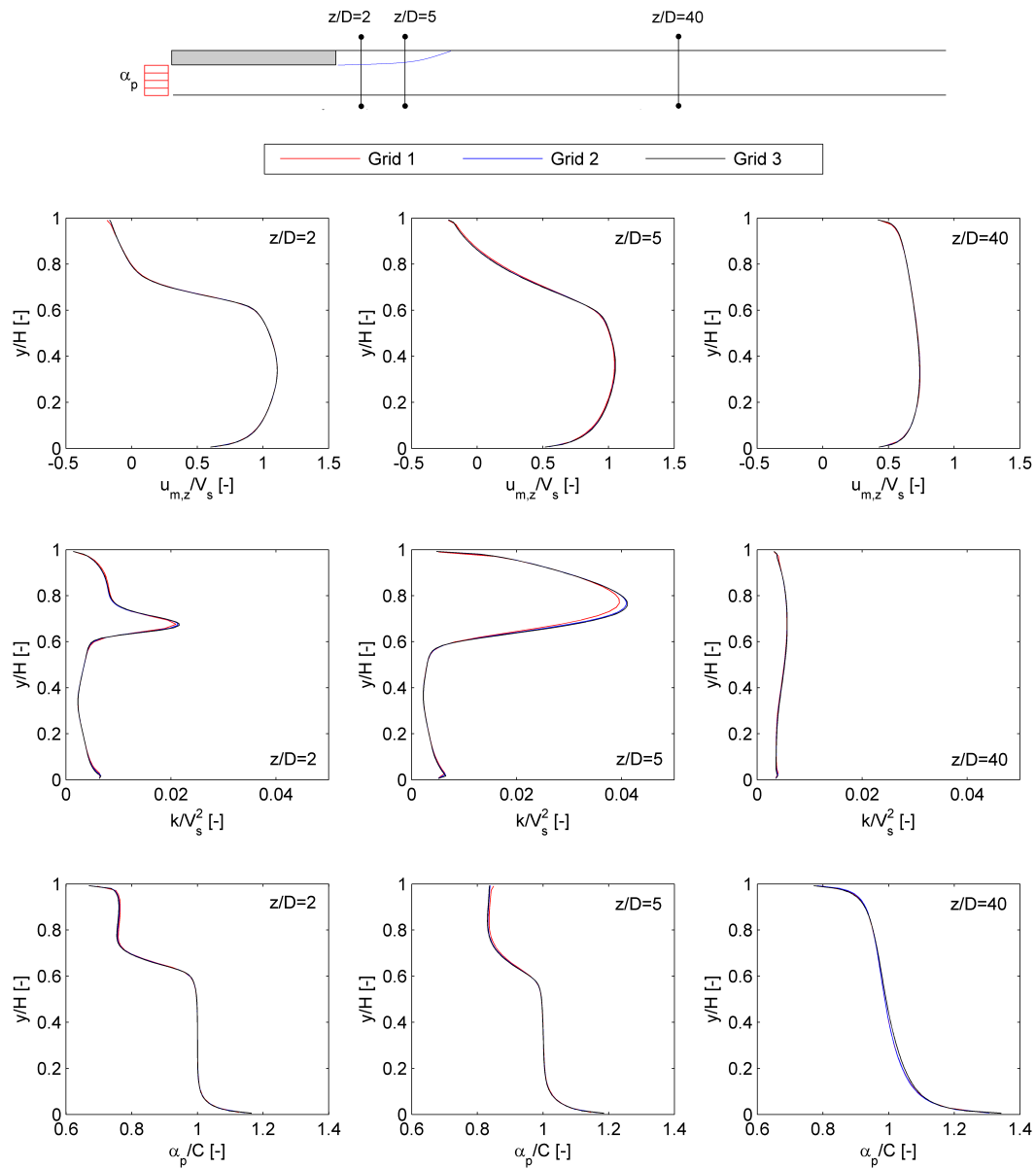
Figure 4.12: Effect of mesh resolution on the mixture velocity, kinetic energy, and solids concentration profiles at different locations downstream the step
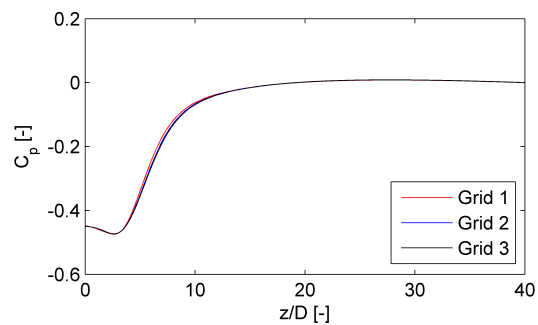
Figure 4.13: Effect of mesh resolution on the pressure coefficient

pipe wall y^+ on the wall shear stress, i.e. on the pressure gradient. For this reason, the mesh was designed in such a way that $y^+ = 30$, since this is the smallest possible value consistent with the application of the non-equilibrium log law in the single-phase flow case. Even if the simulations about the expansion case are mainly aimed at investigating the overall behaviour of the mixture (distribution of the phases, pressure recovery), which is expected to be minorly affected by y^+, it is tried to follow the same criterion in the expansion case, but a structured grid as those managed by PHOENICS forces to set the Y-size of an entire row of cells, therefore doesn't allow verifying the condition $y^+ = 30$ for the small and the large ducts at the same time. The grid was therefore designed in such a way that the condition $y^+ = 30$ is satisfied only in the portion of the large duct where fully-developed flow conditions have been re-established. The impossibility to verify the same constrain elsewhere is accepted since, confirming the initial guess, the grid sensitivity analysis showed that the computed variables of interest are essentially unaffected by further mesh refinement.

The geometrical and flow characteristics of the configuration simulated in the grid sensitivity analysis were similar to those considered for the single-phase flow case, namely $h = 26$ mm, $H = 39$ mm, $V_s = 4$ m/s, corresponding to an expansion ratio of 1.5 and a step Reynolds number $\mathrm{Re}_D = DV_s/\nu_c$ equal to $5.2 \cdot 10^4$. The mixture is made of water and sand particles with density of 2650 kg/m^3 and size of 90 μm with mean delivered solids concentration of 5%. The parameters of interest are the velocity, kinetic energy, and solids concentration profiles at different positions along the streamwise direction, and the distribution of the pressure coefficient along the streamwise direction.

Three meshes were employed, as follows: 53 by 690 cells along the Y and Z directions respectively (Grid 1); 91 by 1003 (Grid 2); and 121 by 1260 (Grid 3). The results, depicted in Figures 4.12 and 4.12, indicates the reliability of Grid 2.

As for the single-phase flow case, the effect of the differencing scheme on the numerical solution was investigated, taking the hybrid scheme of Spalding [145] and the Linear Upwind scheme as possible alternatives. The results in terms of the parameters already considered in the grid sensitivity analysis are reported in Figures 4.14 and 4.15. The use of the Linear Upwind scheme instead of the hybrid one doesn't seem to procure any effect on the velocity and concentration distribution. Detectable (but indeed minor) changes are observed with respect to the turbulent kinetic energy in the shear layer region and in the pressure coefficient distribution. Anyway, the Linear Upwind scheme was used in the simulations.

Sensitivity analysis of some terms of the two-fluid model

Due to the lack of experimental data about the flow condition considered, the results about the horizontal pipe case served as guidelines for the definition of the numerical setup. In the horizontal pipe case, the model proved adequate for application to fully-suspended flow and, strickly speaking, requires the particle size to satisfy the condition $d_p^+ < 50$. It is tried to define the simulation scenarios considered in the present chapter in such a way that these constrains were verified.
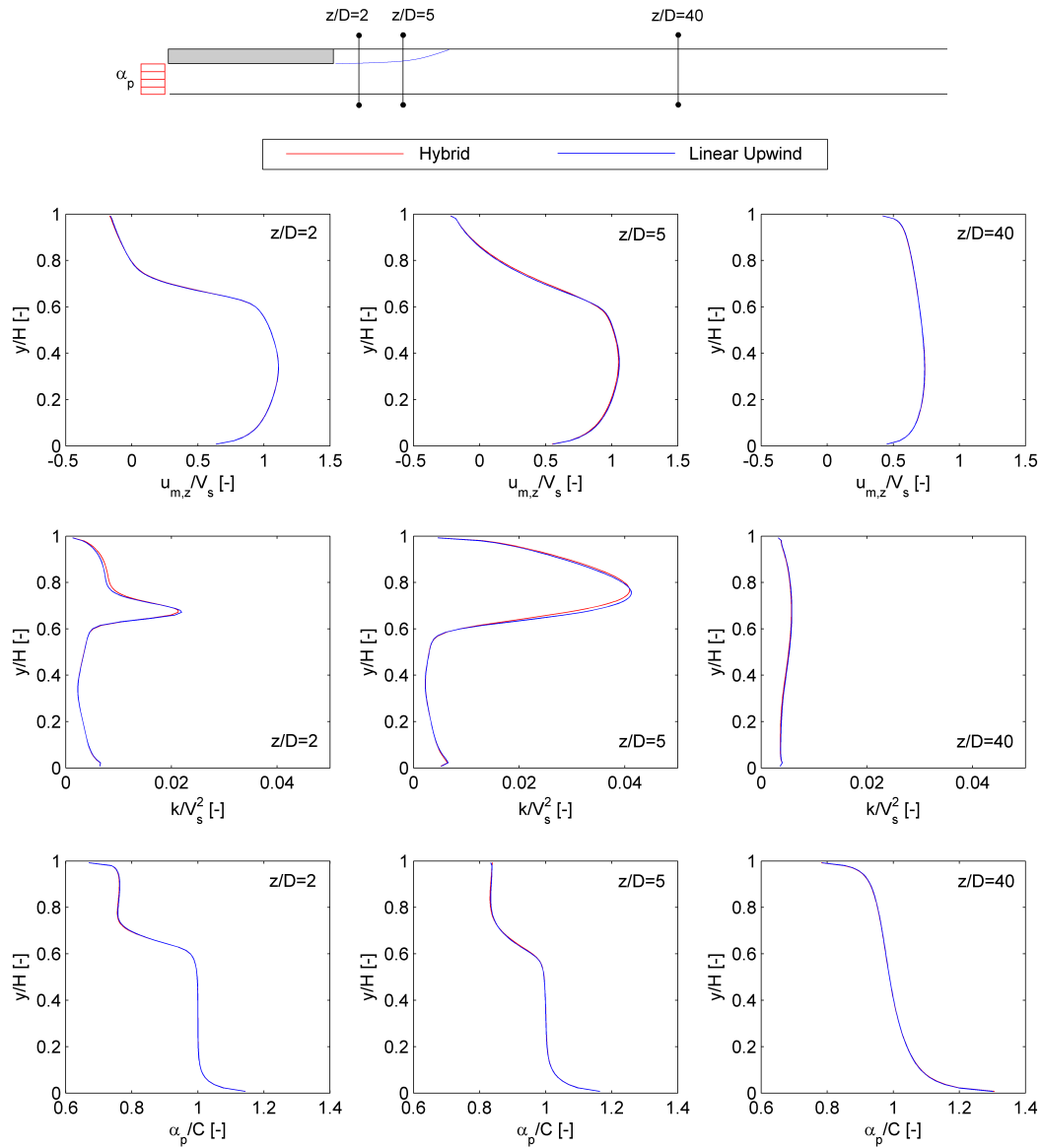
Figure 4.14: Effect of the differencing scheme for convective terms on the mixture velocity, kinetic energy, and solids concentration profiles at different locations downstream the step
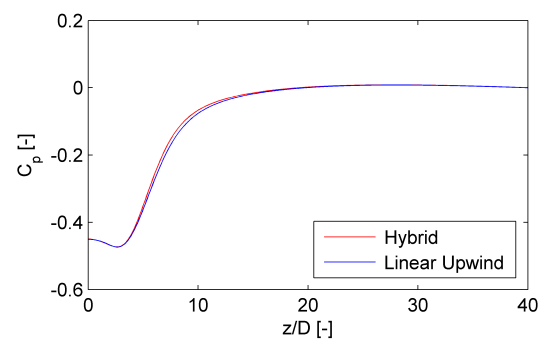
Figure 4.15: Effect of the differencing scheme for convective terms on the streamwise distribution of the pressure coefficient

Table 4.3: Case study considered in the sensitivity analysis. In all cases, $h = 26$ mm, $H = 39$ mm, and $V_s = 4$ m/s. The values of d_p^+ are calculated with respect to the bulk-mean velocity in the small duct

Case	A	B	C
Particle size [μm]	90	90	280
Particle density [kg/m^2]	2650	2650	2650
Dimensionless particle size (d_p^+) [-]	14	14	44
Mean solids concentration [%]	5	30	5

As repeatedly observed, the horizontal pipe case allows defining only some of the modelling features of the two-fluid model, that is those which are a effective for that kind of flow. In practice, they are the correlation for the viscosity of the mixture, the turbulent Schmidt number for volume fractions, and the wall boundary condition for the solid phase. Other terms proved negligible for pipe flows, but may become potentially important for expansion flows. A sensitivity analysis is performed to establish their effect on the solution.

Following the same approach of Section 3.3, three benchmark cases were considered in order to investigate the effect of mean delivered solids concentration and particle size on the flow characteristics. They are: small particles at low mean delivered solids concentration; small particles at high mean delivered solids concentration; and big particles at low mean delivered solids concentration. Details of the flow conditions for the three scenarios, referred to as A, B, and C respectively, are provided in Table 4.3. In all cases, the geometry of the step is fixed, with $h = 26$ mm and $H = 39$ mm, resulting in an expansion ratio of 1.5. The slurry superficial velocity is 4 and 2.6 m/s in the small and large ducts respectively. Actually, the slurry velocity the large duct is the bottleneck for guaranteeing fully-suspended flow, while that in the small duct is the bottleneck for the constrain $d_p^+ < 50$. However, it is worth noticing that, since the focus of the investigation is mainly the flow downstream the step, the issue which matters most is the former. For cases A and B, a pseudo-homogeneous flow (Figure 3.1(a)) occurs in the small channel, therefore the inlet volume fraction is taken as uniform. For case C, a heterogeneous flow (Figure 3.1(b)) takes place, thus the fully-developed volume fraction distribution obtained from the simulation of a straight channel is imposed.

The effect of the following modeling features is considered one at a time:

1. LIFT FORCE

   The effect of the inclusion of the lift force in the generalized drag term $\mathbf{M}_k^d$ was investigated. The lift force is evaluated by means of Eq. 2.59 with the lift coefficient C_l equal to 0.5. Figures 4.16 to 4.19 reveal that, whatever the mean delivered solids concentration is, for the small particles the influence of the lift on the numerical solution is limited to the solids volume fraction distribution within the recirculation region, and however essentially negligible. The results were interpreted in the light of the theoretical background inferred from literature. The ineffectiviness of the lift force for the small particles case is due to the low slip velocity between the phases,
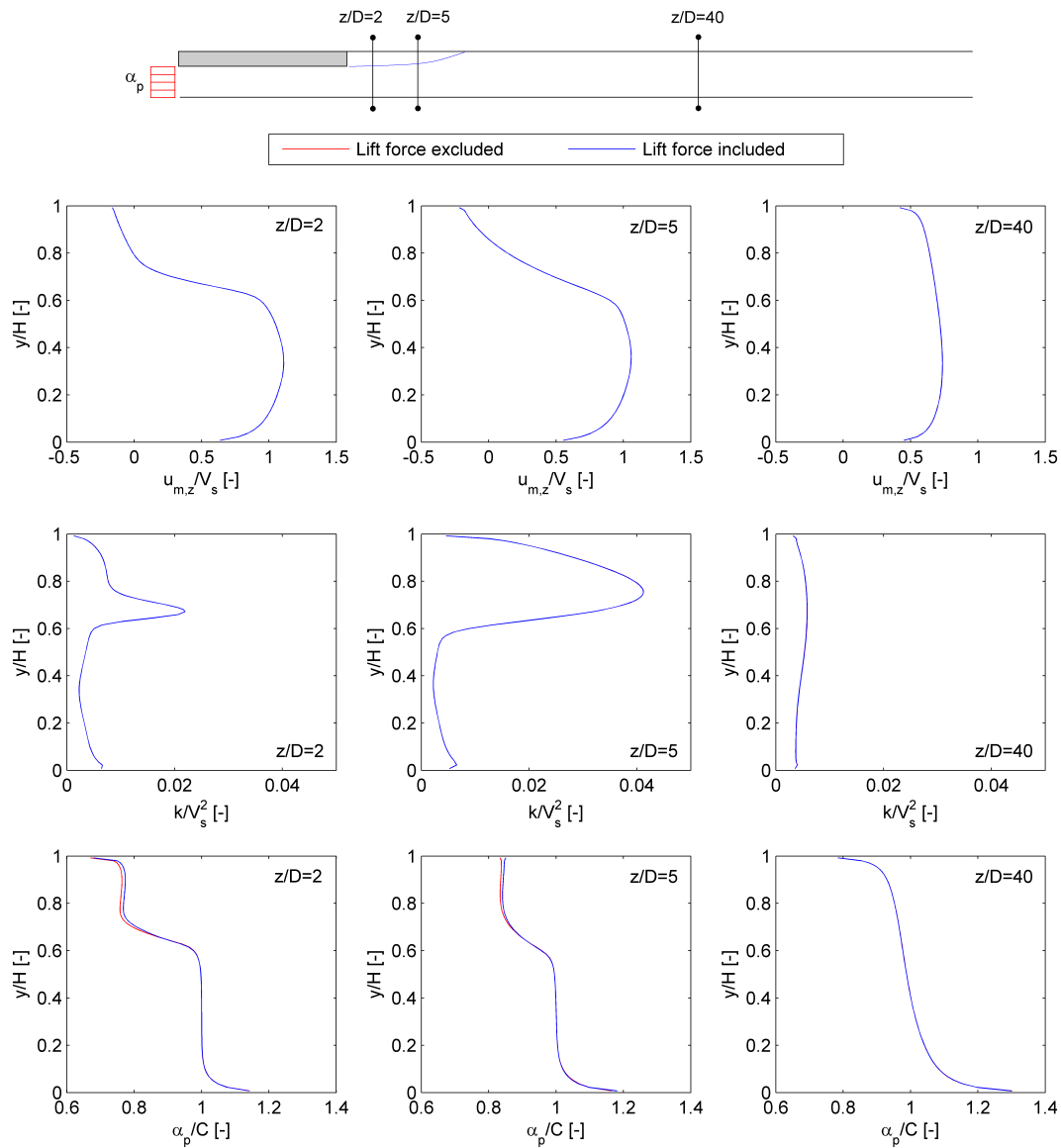
Figure 4.16: Effect of the lift force on the mixture velocity, kinetic energy, and solids concentration profiles at different locations downstream the step for Case A in Table 4.3
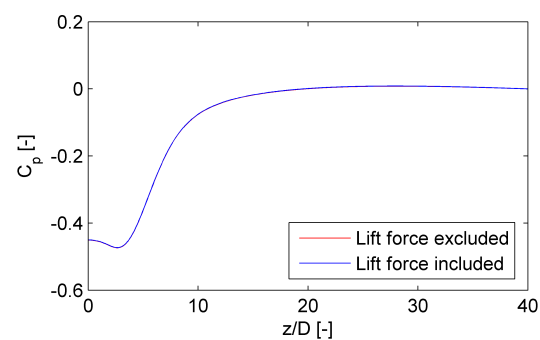
Figure 4.17: Effect of the lift force on the streamwise distribution of the pressure coefficient for Case A in Table 4.3
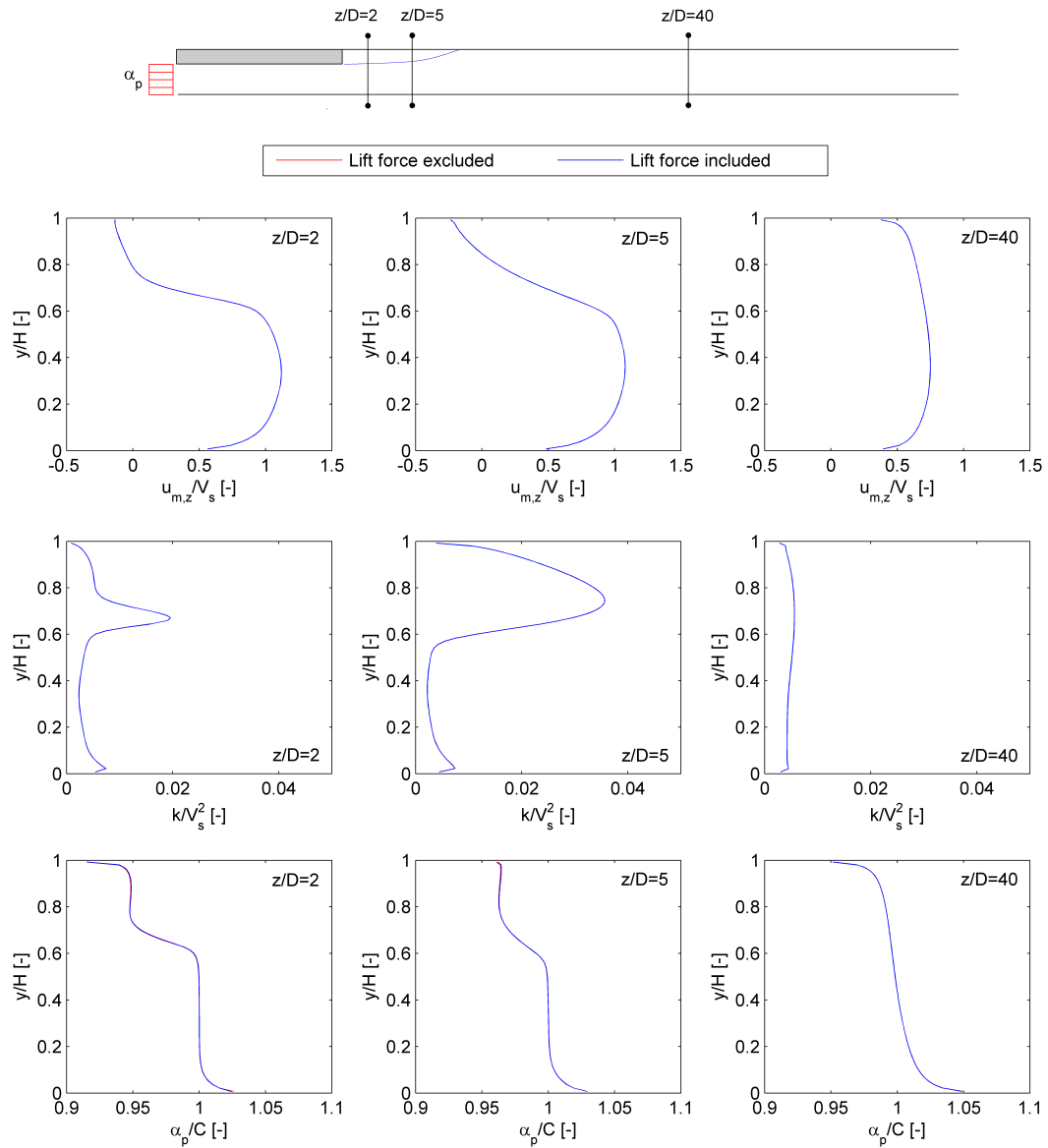
Figure 4.18: Effect of the lift force on the mixture velocity, kinetic energy, and solids concentration profiles at different locations downstream the step for Case B in Table 4.3
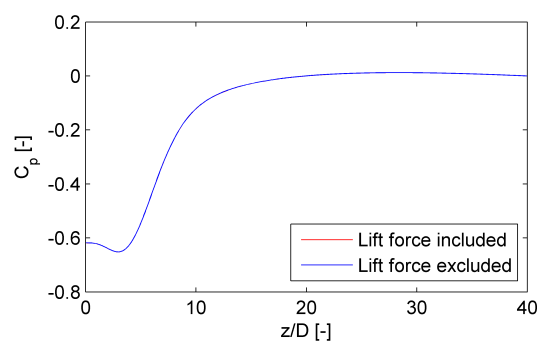
Figure 4.19: Effect of the lift force on the streamwise distribution of the pressure coefficient for Case B in Table 4.3

which varies from 0 to only about 7 mm/s within the domain. In turn, the low slip velocity can be interpreted as a consequence of the low integral scale Stokes number of the particles. For the flow conditions considered here, $\tau_\Lambda = 0.013$ s when evaluated by means of Eq. 4.3. The particle response time τ_p, evaluated by means of Eq. 1.4, is around $1.2 \cdot 10^{-3}$ s, resulting in an integral scale Stokes number of about 0.10. This means that, roughly speaking, the particles tends to "follow the fluid" resulting in a low slip velocity and therefore in the ineffectiveness of the lift force.

Figures 4.20 and 4.21 are the analog of Figures 4.18 and 4.19 for the flow conditions referred to as C is Table 4.4. As already reported, the fully-developed distribution of solids concentration obtained from the simulation of a straight duct is imposed at the inlet section. The plots indicate that, also in this case, the influence of the lift is minor and essentially limited to the solids volume fraction in the recirculation region. However, in this region the integral scale Stokes number S_Λ is about 0.92, resulting in a non-negligible slip velocity. This may in principle give rise to a detectable effect of the lift force. A possible explanation is that, due to the effect of gravity, the particles tend to remain within the core region, therefore are not likely to be dragged into the vortex through the shear layer region. In other words, the ineffectiveness of a *potentially* effective lift is due to the absence of particles in the recirculation region. As a confirmation of such interpretation, test case C was simulated again by imposing a uniform inlet solids volume fraction distribution in order to reduce the stratification induced by gravity. Figure 4.22 shows the effect of the lift force on the solids concentration profile for this alternative inflow condition. In this case, the lift force affects the solution in the shear layer region (confirming the results of Founti *et al.* [47]), pushing the particles towards the upper wall and contributing to determine a peak in solids concentration at the corner of the step lip (Figure 4.23 shows a detail of the solids volume fraction distribution in which such peak is highlighted). The prediction of solids concentration profile at the wall is a very difficult task as it is the results of the coupled effects of shear, wake phenomena and deformation on the lift force as well as the turbulence of the liquid phase. Given the scopus and the approach of the present thesis, no attempt is made for getting into this topic, which may be possibly shelved for future developments. Anyway, it is worth noticing that a peak of concentration downstream the step lip has also been observed in previous numerical works [128] concerning gas-liquid flows through an axisymmetric expansion in a vertical pipe. However, this is just a qualitative comparison since the two cases are not directly comparable, mostly because of the different orientation of the system.

2. VIRTUAL MASS

The influence of the virtual mass force on the numerical solution is analyzed by including this term in the generalized drag $\mathbf{M}_k^d$. The virtual mass force is evaluated by means of Eq. 2.64 with $C_{vm} = 0.5$. The investigation revealed that for all
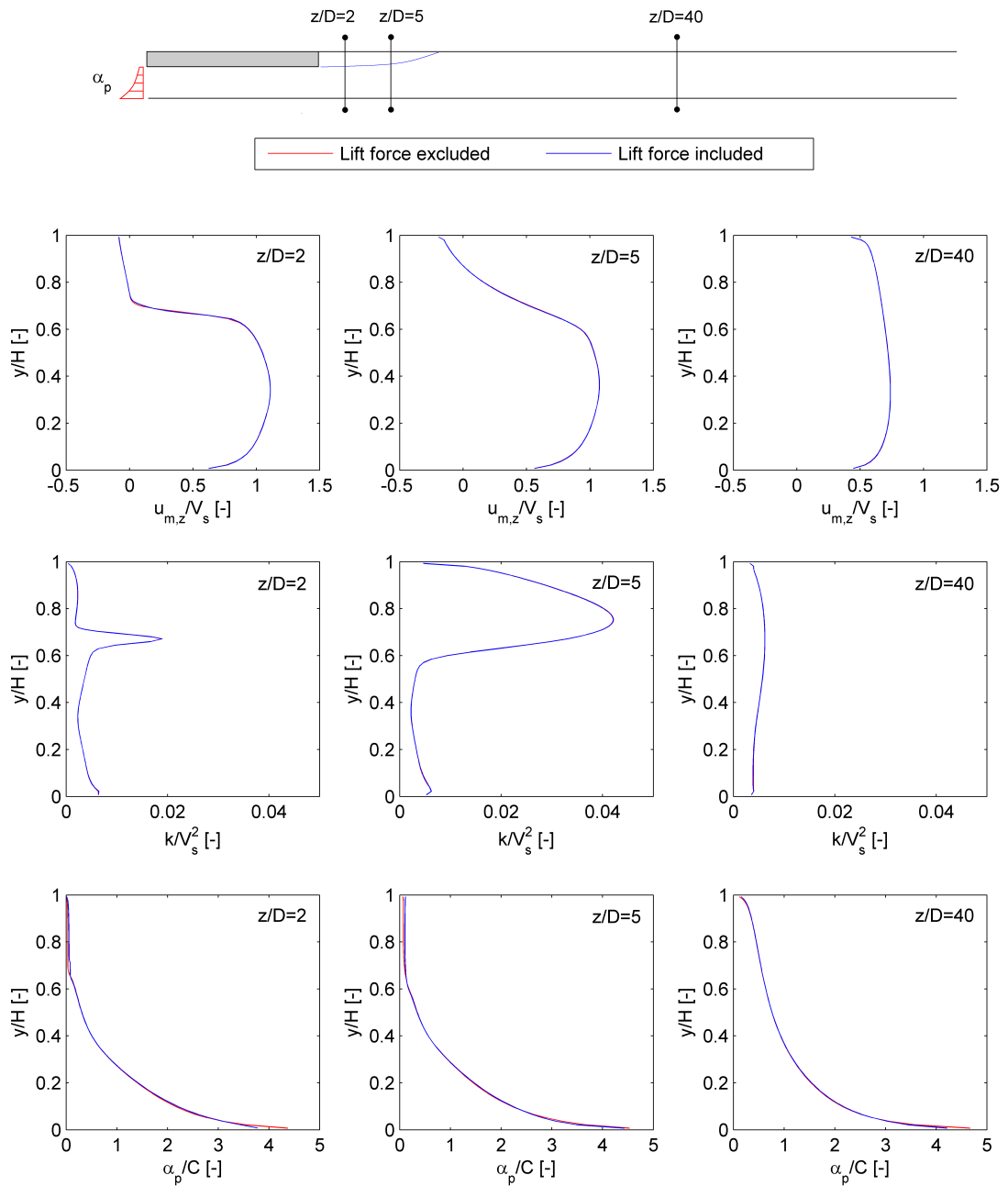
Figure 4.20: Effect of the lift force on the mixture velocity, kinetic energy, and solids concentration profiles at different locations downstream the step for Case C in Table 4.3. A fully-developed solids concentration profile is imposed at the inlet section
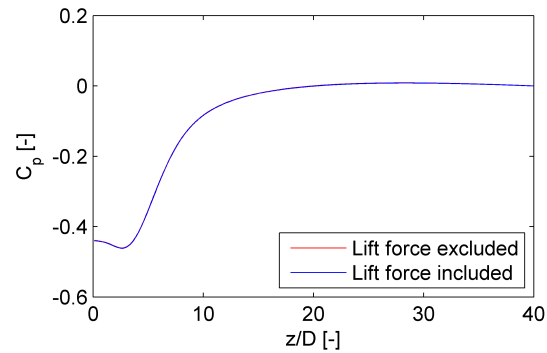
Figure 4.21: Effect of the lift force on the streamwise distribution of the pressure coefficient for Case C in Table 4.3
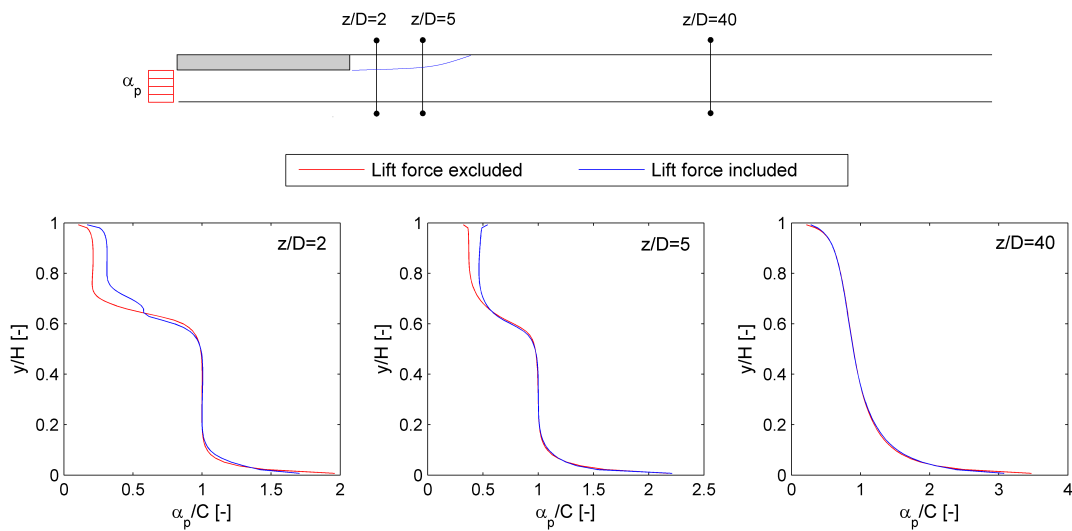
Figure 4.22: Effect of the lift force on the solids concentration profiles at different locations downstream the step for Case C in Table 4.3. A uniform solids concentration profile is imposed at the inlet section
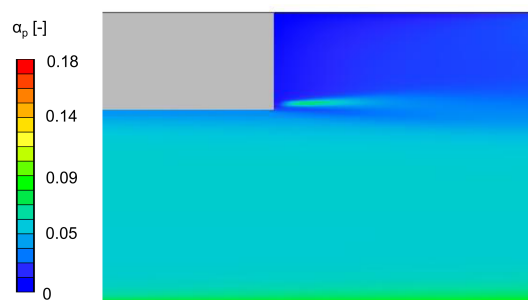
Figure 4.23: Color plot of solids concentration distribution downstream the step with a uniform solids concentration profile imposed at the inlet section. The wall peak in concentration, originated from the lift force, is highlighted
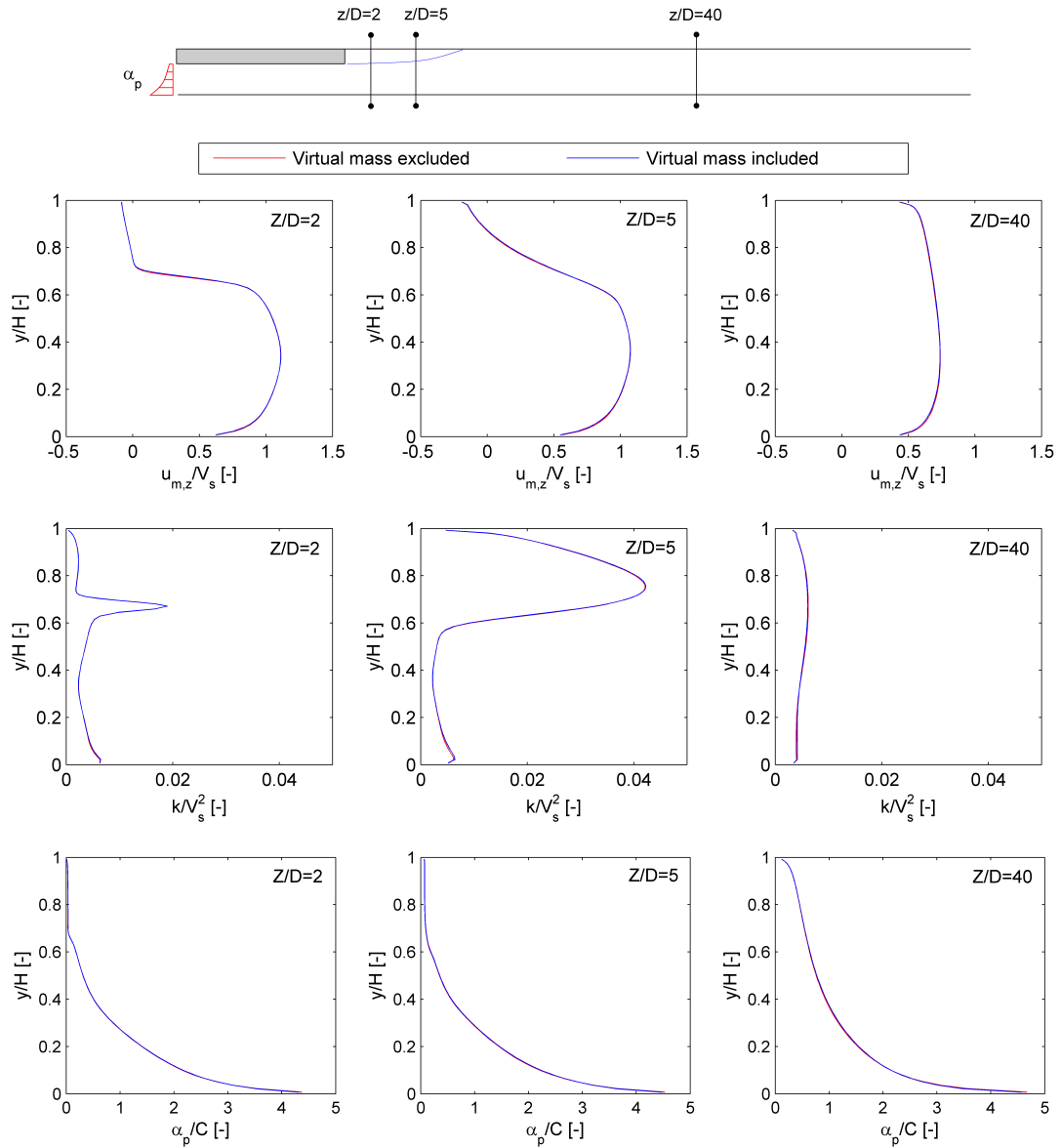
Figure 4.24: Effect of the inclusion of the virtual mass force in the generalized drag on the mixture velocity, kinetic energy, and solids concentration profiles at different locations downstream the step for Case C in Table 4.3. A fully-developed solids volume fraction profile is imposed at the inlet section
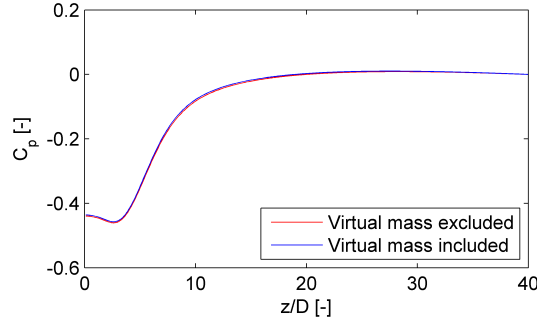
Figure 4.25: Effect of the inclusion of the virtual mass force in the generalized drag on the streamwise distribution of the pressure coefficient for Case C in Table 4.3

the three scenarios, the effect of the virtual mass is negligible, producing results essentially undistinguishable from those obtained without including this term. As an example, Figures 4.24 and 4.25 reveal the negligible influence of the virtual mass for case C in Table 4.3, which, being characterized by the higher slip between the phases, is supposed to enchance the importance of this term among the scenarios considered. Following the already adopted strategy, in order to try to attenuate the influence of gravity, case C was simulated again by imposing a uniform solids volume fraction distribution at the inlet section. Also in this way, however, the effect of virtual mass confirms absolutely negligible (Figure 4.26).

3. PARTICLE EDDY VISCOSITY

At last, the sensitivity analysis concerned the modelling of the particle eddy viscosity ν_p^t. In the horizontal pipe case, the particle eddy viscosity was set equal to that of the fluid, since the use of alternative correlations proved ineffective. Actually, many correlations avaiable in literature allows accounting for the dependence of the particle eddy viscosity on the integral scale Stokes number by means of simple algebraic expressions (Sub-section 2.3.3). An inertial limit behaviour constrain imposes that eddy viscosity of the particles approaches that of the fluid as the Stokes number tends to 0. A comparison was made between the numerical results obtained either setting $\nu_p^t = \nu_c^t$ or evaluating ν_p^t by the algebraic model of Chen and Wood (Eq. 2.87), in which the ratio τ_p/τ_{li} corresponds to the Stokes number with a local definition of the fluid time scale. The analysis highlights that the different definition of the particle eddy viscosity has a negligible influence on the numerical solution for the scenarios summarized in Table 4.3. As for the lift force, the reasons may be different. For cases A and B, the results may be interpreted considering that the very low Stokes number (≈ 0.1) produces $\nu_p^t \approx 0.9\nu_c^t$ according to Eq. 2.87. For case C, a possible explanation may be that, despite the Stokes number is considerably greater and results in $\nu_p^t \approx 0.6\nu_c^t$, gravity tends to keep the particles outside the recirculation region where the influence of the Stokes number is enhanced. In order to try to limit the influence of gravity, the analysis is per-
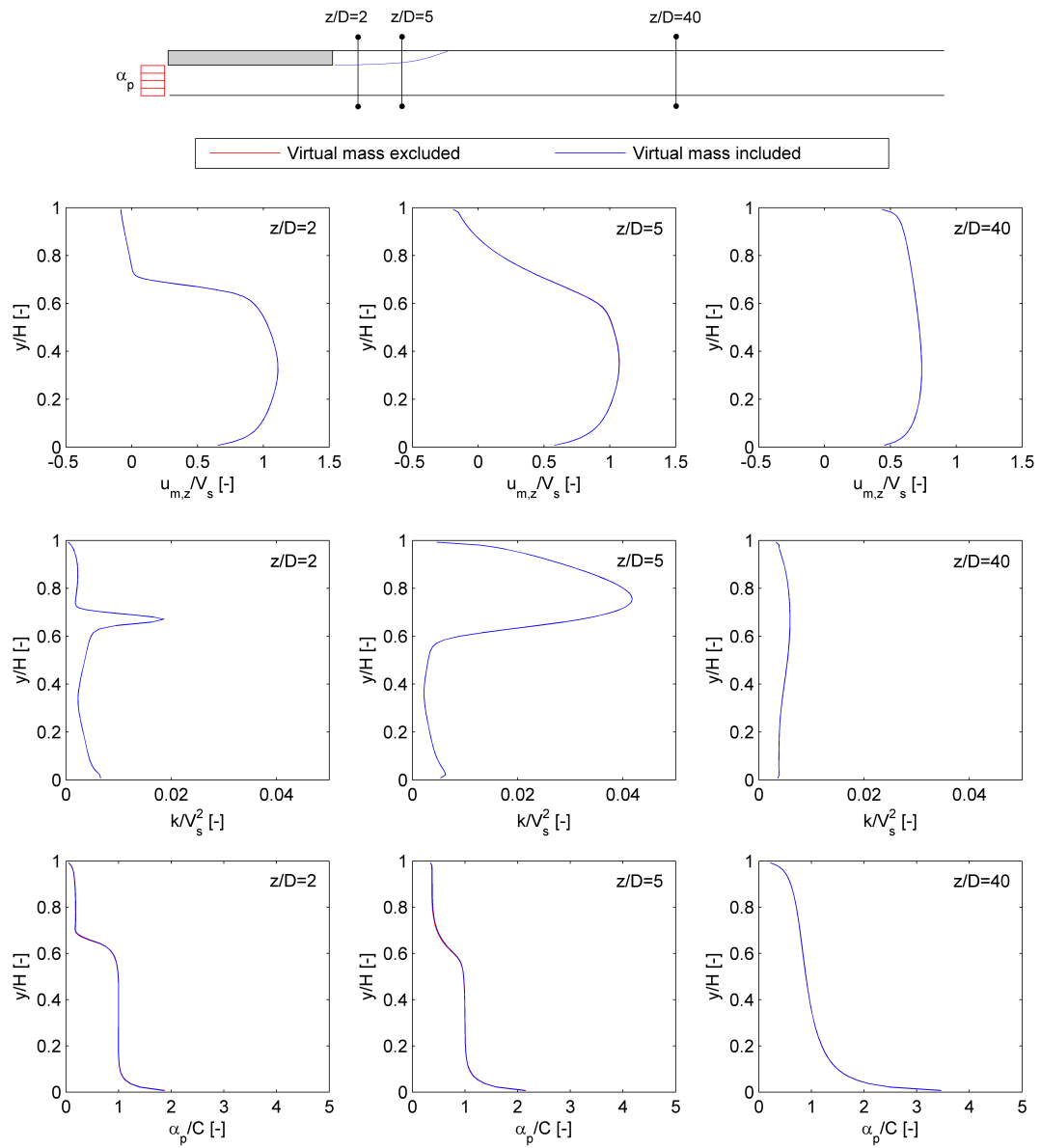
Figure 4.26: Effect of the inclusion of the virtual mass force in the generalized drag on the mixture velocity, kinetic energy, and solids concentration profiles at different locations downstream the step for Case C in Table 4.3. A uniform solids volume fraction profile is imposed at the inlet section
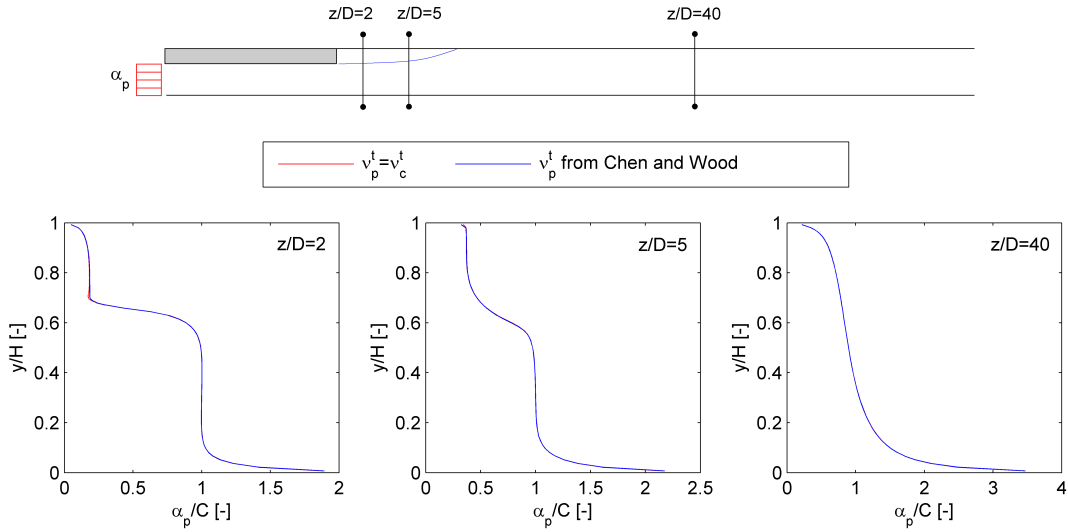
Figure 4.27: Effect of the model for the particle eddy viscosity on the concentration profile at different locations downstream the step for Case 3 in Table 4.3. A uniform solids concentration profile is imposed at the inlet section

formed also imposing a uniform volume fraction profile at the inlet section. The results, reported in Figure 4.27 for the solids volume fraction distribution, reveal the ineffectivess of the modification.

The sensitivity analysis indicates that, for the flow conditions considered, the inclusion of lift and virtual mass in the generalized drag term and the adoption of more sophisticated models for the particle eddy viscosity have essentially no influence on the numerical solution. Different reasons may contribute to this result. For the small particles, this may be due to the low integral scale Stokes number, which cause the particle to actually "follow the fluid" with low slip velocity. For the big particles, the slip between the phases isn't negligible within the recirculation region, but gravity, which opposes to the entrainment of the particles within that region, dominates. Therefore, for the flow conditions reported in Table 4.4, the *base* configuration of the model, the one illustrated in Chapter 3, could be suitable. However, in the remainder of this section the simulations will concern also other flow conditions for which it is not a priori clear how the balance between particle response to the flow and gravity will influence the solution. Moreover, since lift, virtual mass, and the expression of Chen and Wood don't affect significantly the computer time and the stability of the model, these terms will be included in the simulations.

Phenomenological consistency of the solution

As already noticed, the lack of experimental data for the flow conditions considered here doesn't allow validating the model by comparing computations with measurements. In order to guarantee the reliability of the numerical results, the sensitivity analysis described previously was followed by a critical discussion of the phenomenological con-

Table 4.4: Case study considered in the investigation. In all cases, $h = 26$ mm, $H = 39$ mm, and $V_s = 4$ m/s. The integral scale Stokes number is a value representative of the recirculation region, with the integral time scale given by Eq. 4.3

Case	E1	E2	E3	E4	E5
Particle size [μm]	90	90	90	175	280
Particle density [kg/m^2]	2650	2650	2650	2650	2650
Mean delivered solids concentration [%]	5	15	30	5	5
Integral scale Stokes number [-]	0.10	0.10	0.10	0.35	0.92

sistency of the solution in the light of the theoretical background of the phenomenon as inferred from a literature review. However, the conclusions drawn by other researchers may not be directly applicable to the flow conditions considered here, because of different features which don't procure a complete similarity. First of all, the (few) available investigations concerned flows along the vertical direction, therefore don't account for the crosswise stratification induced by gravity. Moreover, the integral scale Stokes number is higher than those considered here because previous researchers dealt with flows of rather large particles in air. Al last, the flows are very dilute, characterized by low values of mean delivered solids volume fraction, leading to a negligible effect of the interactions among the particles in almost all cases.

In this stage of the work, reference is made to the five benchmark cases illustrated in Table 4.4, in order to investigate the effect of increasing the mean delivered solids concentration for a given particle size (cases E1, E2, and E3) and that of increasing the particle size the particle loading being the same (cases E1, E4, and E5). The integral scale Stokes number is evaluated as the ratio between the particle response time (Eq. 1.4) and the characteristic fluid time scale given by Eq. 4.3. It's worth noticing that cases E1, E3, and E5 in Table 4.4 corresponds to cases A, B, and C in Table 4.3, previously considered for the sensitivity analysis.

Figure 4.28 reports the solids concentration profile (normalized by the mean delivered solids concentration C) at a distance $z/D = 5$ downstream the step, in order to investigate the dispersion of particles within the recirculation region. In particular, Figure 4.28(a) focuses on the effect of increasing the mean solids concentration from 5 to 30% for a particle size of 90 μm, while in Figure 4.28(b) the particle size is 90, 175 and 280 μm and the mean delivered solids concentration is 5%. In all cases, the particle density is 2650 kg/m^3. The numerical results highlight that the solids concentration within the recirculation region, i.e. the degree entrainment of particles within the vortex, increases with the mean solids concentration. The trend can be interpreted in the light of the works of Fessler and Eaton [46], Hardalupas *et al.* [59] and Founti *et al.* [47] who dealt with dilute gas-solid and liquid-solid flows through expansions along the vertical direction. As already reported in Section 4.1, the turbulent dispersion is mainly governed by the integral scale Stokes number S_Λ. All these authors agree that the particles are dragged into the vortex only if the Stokes number based on the large-eddy time scale (Eq. 4.3) is less than one, and that the entrainment of particles increases as the parti-
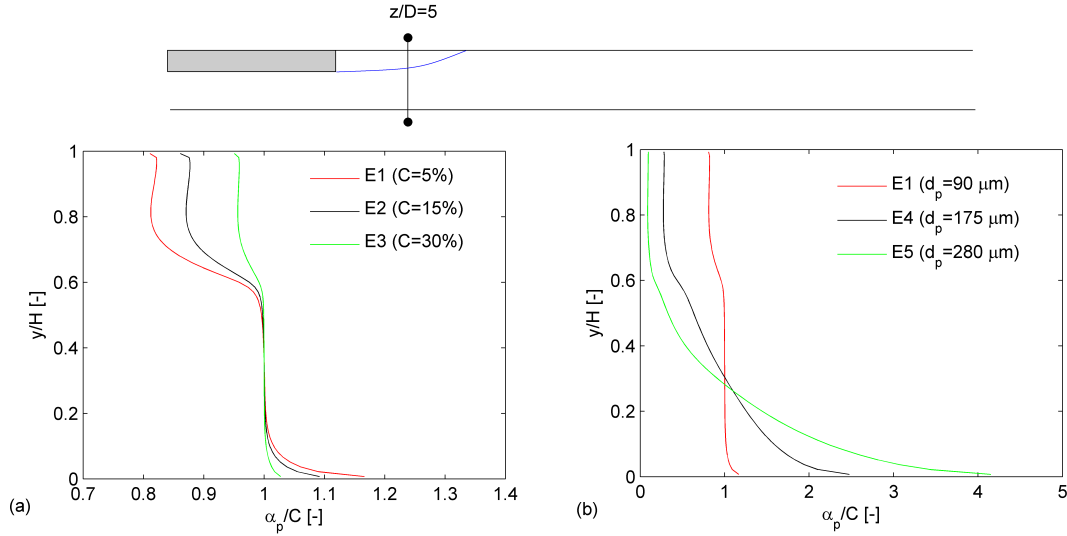
Figure 4.28: Effect of (a) mean delivered solids concentration (b) particle diameter on the solids concentration distribution at $z/D = 5$ downstream the step

cle Stokes number decreases. The Stokes numbers reported in Table 4.4 don't depend explicitly upon the mean delivered particle concentration, but the particle reponse time may be expected to decrease as the mixture becomes more and more concentrated due to the increase in the drag coefficient felt by a particle. Therefore, the numerical results in Figure 4.28(a) appear in agreement with the observations reported in literature.

Figure 4.28(b) is the analog of Figure 4.28(a) for cases E1, E5, and E5 in Table 4.4, characterized by different particle size for the same mean delivered solid concentration. The results indicate that the solids concentration within the vortex decreases as the particle size increases. For cases E1, E5, and E5 the integral scale Stokes number is less than one and, consistently with the above-mentioned references [46, 47, 59], actually some of the particles are entrained in the recirculation region. As the particle size increases, the particle response time (i.e. the inegral scale Stokes number) increases too, leading to a minor effectiveness of turbulent dispersion. Moreover, as the particle size increases, it becomes more and more enhanced the influence of gravity which tends to keep the particles in the lower core region. The latter effect was not detected in the experiments of [46, 47, 59] because of the vertical orientation of the system.

A parametric investigation of the distribution of turbulent kinetic energy downstream the step is now described. Figure 4.29 reports the vertical profile of turbulent kinetic energy at different locations along the flow direction for cases E1, E2, and E3 in Table 4.4, characterized by increasing the mean delivered solids concentration for a given particle size. The model predicts a lower turbulent kinetic in shear layer region compared to the single-phase flow case, with the turbulent kinetic energy attenuation increasing with the mean solids concentration. The similar dependence observed by Fessler and Eaton [46] may not serve as confirmation of the results of Figure 4.29, since these authors considered very dilute mixtures of particles with integral scale Stokes number around 100, very high
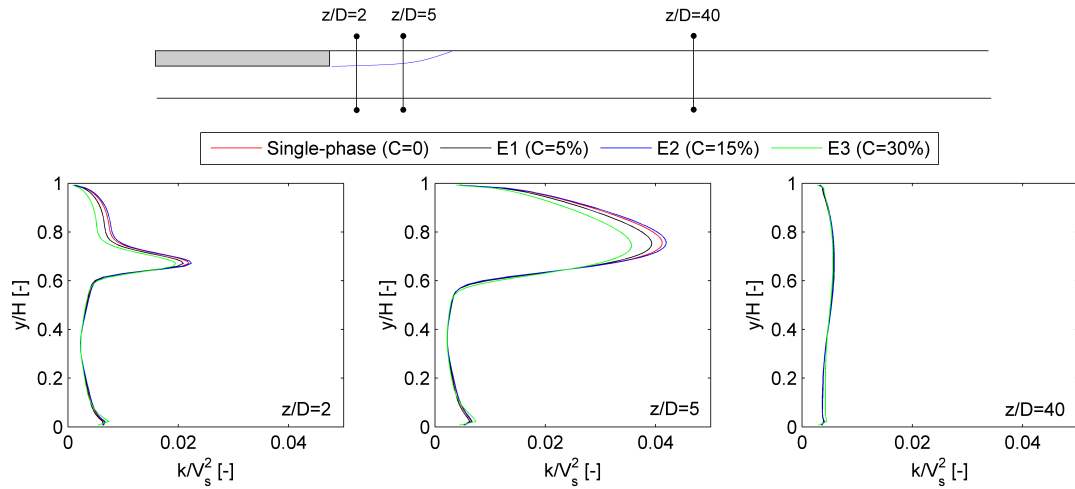
Figure 4.29: Vertical profile of turbulent kinetic energy at different locations dowstream the steps for cases E1, E2, and E3 in Table 4.4, characterized by increasing the mean delivered solids concentration for a given particle size. The single-phase flow case is reported too

compared to that considered here (which is around 0.1). A possible explanation is that, for these low values of Stokes number, the mixture tends to behave "as a whole". An increase in solids loading determines an increase in density and viscosity of the mixture, accompanied by a reduction of the turbulent kinetic energy.

At the same time, the particle size seems to have a minor effect on the turbulent kinetic energy in the shear layer region, as it can be inferred from Figure 4.30 which is the analog of Figure 4.29 for cases E1, E5, and E5 in Table 4.4, characterized by mean solids concentration of 5% and particle diameter of 90, 175, and 280 μm respectively. However, a closer inspection of Figure 4.30 reveals that the turbulent kinetic energy increase slightly with the particle size. Two reasons may contribute to explain such trend. The first, also shared by Pathak [120] who studied numerically the flow of solid-liquid mixtures through a ducted obstruction at the bottom of a rectangular horizontal channel, is that the additional momentum transfer from the particles to the fluid, increases with particle size. This transfer may be responsible for additional production of turbulence, even if the way in which the particles affect the turbulence is a very complex matter which has not been totally clarified so far. The second, peculiar for the flow condition considered here and not applicable to the setup of Pathak [120], is that, as the particle size increases, the particles tend to remain in the core region due to the enhanced effect of gravity. Therefore, the solids concentration in the shear layer region decreases and, on the grounds of the results of Figure 4.29, produces an increase in turbulent kinetic energy. The counteracting effects of mean solids concentration and particle size may produce either higher or lower turbulent kinetic energy compared to an equal flow rate of pure liquid.

The visual observation of the distribution of solids volume fraction is useful to intepret the combined effect of the most important physical mechanisms governing the flow, which
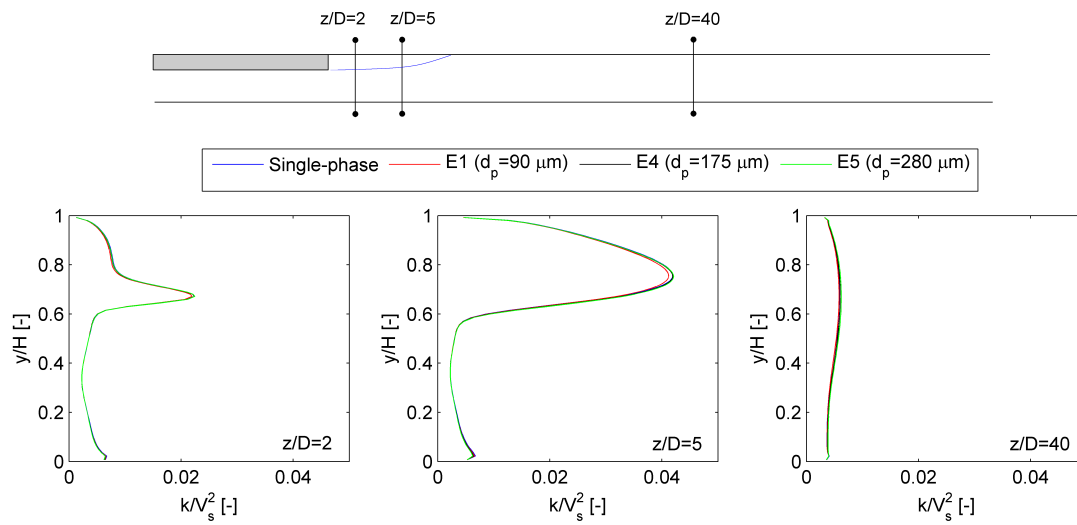
Figure 4.30: Vertical profile of turbulent kinetic energy at different locations dowstream the steps for cases E1, E4, and E5 in Table 4.4, in which the size of the particles is increased for a given mean solids concentration. The single-phase flow case is reported too
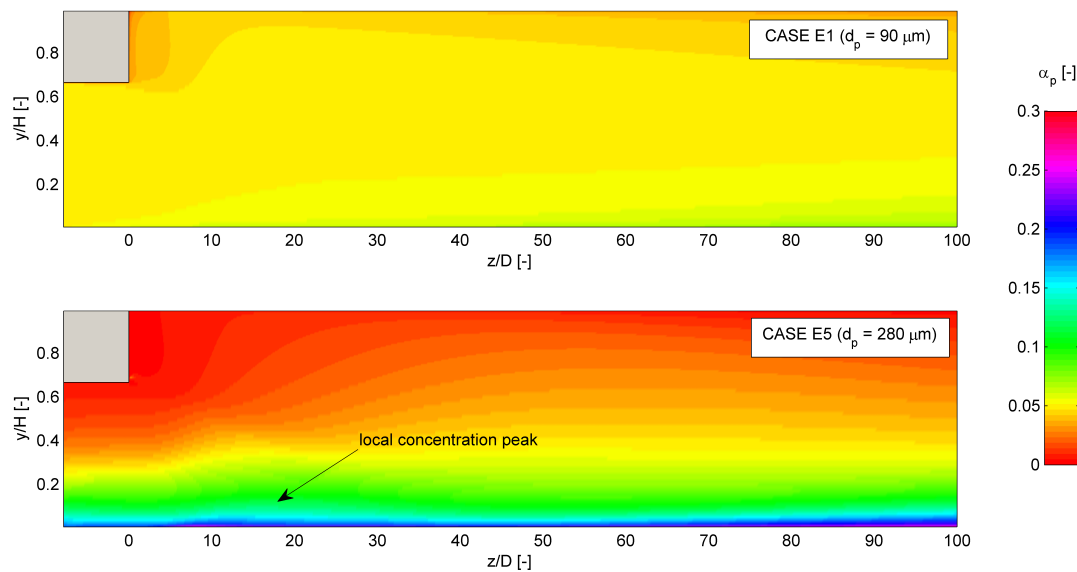
Figure 4.31: Color plot of solids volume fraction for cases E1 and E5 in Table 4.4, characterized by mean delivered solids concentration of 5% and particle diemater of 90 and 280 μm respectively

are mainly the influence exterted on the particles by the mean fluid flow, turbulent dispersion, and gravity. Each particle is subjected at the same time to counteracting forces: on one hand, gravity tends to push it downwards, towards the bottom of the channel; on the other hand, the actions due to the fluid make the particle follow the fluid and, due to turbulent dispersion, spread throughout the large duct entering the recirculation region. As the particle size increases, gravity acquires importance whilst the effect of the actions from the fluid becomes minor. This may serve to explain the results in Figure 4.31, which compares the volume fraction of particles with size of 90 and 280 μm at the same mean delivered solids concentration of 5% (cases E1 and E5 in Table 4.4). In the small particles case (E1), the effect of gravitational stratification seems minor and the particles actually "follow the fluid", immediately covering all the large duct and entering the main vortex. In the big particles case (E5), gravity tends to keep the particles within the core region, therefore they are not likely to be dragged into the recirculation region. Gravity rather then the integral scale Stokes number alone explains the behaviour of the large particles. Actually, the large particles "feel" the effect of the step in the sense that they first slow down, then they are pushed upwards by the fluid but finally, due to gravity, they fall down again unless an equilibrium between gravity, collisions and turbulence occurs. Moreover, but they are not likely to be dragged into the vortex. The deceleration of the particles induced by the step may explain the presence of a small bottom concentration peak is observed on the lower wall downstream of it.

Hints of engineering interest

As already noticed, the backward-facing step case is of particular interest because, besides being a significant benchmark from a theoretical point of view, can provide useful information also for the applications. In fact, hydraulic singularities involving sudden expansions are frequently encountered in pipeline systems, for example in correspondence to joints between pipes of different size. Being able to identify the features of a two-phase mixture which most influence the parameters of engineering interest and pointing out their specific effects, in the sense of "what affects what", is fundamental for engineers. In this context, the information provied by this simple benchmark case can be useful hints.

One of the main features for designers is the pressure profile along the system, as it dictates the selection of pump capacity. The qualitative trend of the pressure distribution for the two-phase flow case is similar to that of the single-phase flow one, depicted in Figure 4.2; essentially, an increase in pressure occurs as a consequence of the deceleration of the mixture. A parametric investigation aimed at analyzing the way in which the mean solids concentration and the size of the particles size affects the pressure recovery is performed, with reference to the pressure coefficient defined by Eq. 4.2. Figure 4.32(a) compares the results for a unique set of particles (density = 2650 kg/m^3; size = 90 μm) with mean delivered solids concentration ranging from 5 to 30%. The results highlight that the pressure recovery increases with the solids loading, possibly as a consequence of the momentum transfered from the particles to the fluid. Similar observations, as well as
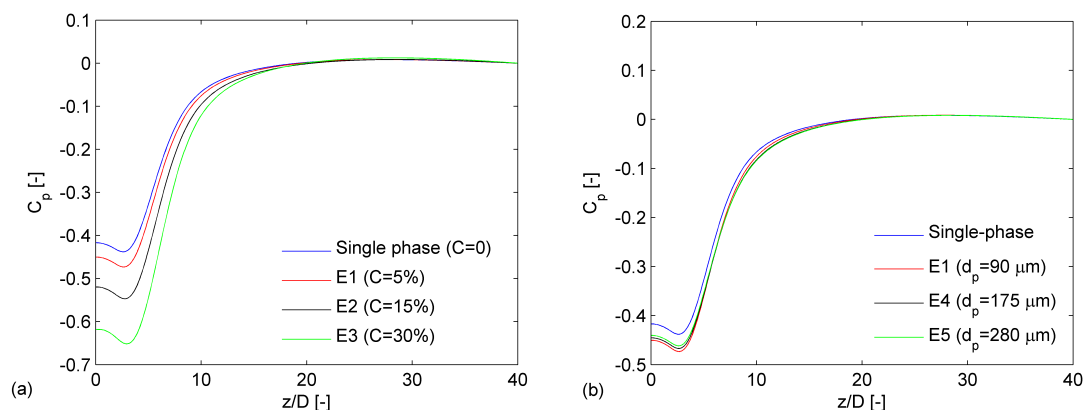
Figure 4.32: Parametric investigation of the pressure coefficient distribution downstream the step. Effect (a) increasing the mean solids concentration up to 30% for a particle size of 90 μm (cases E1, E2, and E3 in Table 4.4); (b) increasing the particle size from 90 to 280 μm for a mean solids concentration of 5% (cases E1, E4, and E5 in Table 4.4)

the interpretation given, were also reported by Tomita *et al.* [148] who investigated experimentally the flow of gas-solid mixtures in asisymmetric expansions in circular pipes. Moreover, also the pressure recovery length, which is the distance from the step at which complete recovery occurs, increases with the delivered solids concentration. Different values of particle size (90, 175 and 280 μm) are instead depicted in Figure 4.32(b), for a unique set of particle density (2650 kg/m^3) and mean solids concentration (5%). At least for the low particle loading considered, the effect of particle size on the pressure recovery appears minor. Actually, the pressure recovery slightly decreases as the particle diameter increases. This may appear in apparent contrast with the fact that, the bigger a particle is, the bigger is the momentum that it transfers to the fluid. Again, the effect of gravity may contribute to explain the trend. As the particle size increase, the particles tend to be pushed upwards and downwards but remaining into the core region, being less affected by the presence of the vortex (Figure 4.31). At the limit, if all the particles would accumulate at the bottom of the channel one would expect the pressure recovery to be close to that of pure liquid.

Another hint of interest for the applications is the evaulation of the region of influence of the step, that is the distance from the step for fully-developed flow conditions to be achieved again. The analysis is again performed following the philosophy of "what affects what", focusing on mean delivered solids concentration and particle size. Yet the results in Figure 4.32 suggest that, for the configurations considered, the distance required for the pressure recovery to be completed, therefore for the pressure profile to follow the linear trend which characterizes the fully-developed flow conditions, increases with mean particle concentration while the effect of particle size is minor. The investigation is more complex when performed with respect to the velocity and concentration fields.

A first, rough estimation of the influence of the step on the flow field is performed by considering the size of the rericulation region as inferred from the plot of the streamline
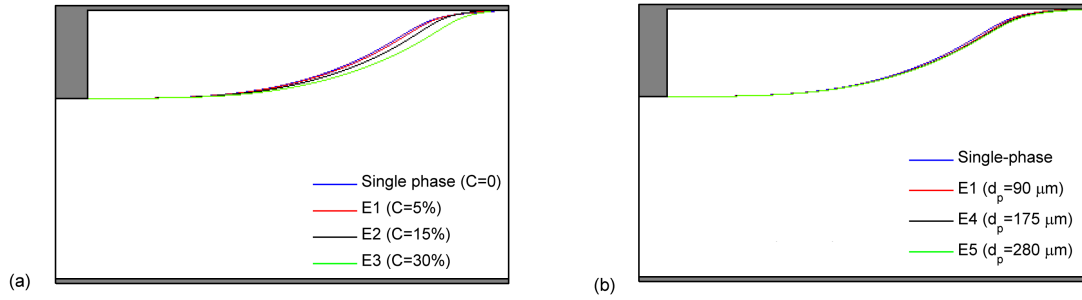
Figure 4.33: Parametric investigation of the extension of the recirculation region. Effect (a) increasing the mean delivered solids concentration up to 30% for a particle size of 90 μm (cases E1, E2, and E3 in Table 4.4); (b) increasing the particle size from 90 to 280 μm for a mean delivered solids concentration of 5% (cases E1, E4, and E5 in Table 4.4)

passing through the corner of the step. Figure 4.33(a) shows the threshold streamline for cases E1, E2, and E3 in Table 4.4, characterized by different loadings of particles with the same size. The plot indicate that the size of the recirculation region increases with the mean delivered solids concentration, even if no variation is actually detectable when C passes from 0 (single-phase) and 5%. The momentum transferred from the particles to the fluid may contribute to explain the results. The effect of particle size is analyzed in Figure 4.33(b), which depicts the streamline for three particle diameters, equal to 90, 175 and 280 μm, with the mean delivered solids concentration kept constant to 5% (cases E1, E5, and E6 in Table 4.4). The effect of particle size is minor, probably due to the already-mentioned counteracting effects of particle response to turbulence and gravity. Indeed, no difference in the size of the recirculation region is observed with respect to the single-phase flow case. It is worth noticing that for the flow conditions considered here the variation of size of the recirculation region is quite limited, therefore of little interest for applications. However, under different flow conditions (i.e. bigger particles, higher concentrations, lower velocities) the effect of mean solids concentration and particle size may be enhanced. Therefore, this analysis may be useful in the sense that it provides qualitative guidelines to engineers.

Actually, the region of influence of the step on the velocity field, that is the distance from the step at with a fully-developed velocity profile occurs, is much longer than the size of the recirculation zone, since just downstream of it the velocity still has a vertical component. The evaluation of the size of such region is not far from criticism, since the extremely low convergence to the asymptotic condition $\partial \mathbf{u}_m / \partial z$ casts doubts on the convenience to determine this parameter accurately. A gross estimation of the effect of mean solids concentration and particle size on the region of influence of the step on the velocity field may be more convenient. In the upper row, Figure 4.34 shows the mixture velocity profile at three different locations downstream the step, namely $z/D = 120$, $z/D = 170$, and $z/D = 190$ for cases E1, E3, and E5 in Table 4.4. The profiles have been normalized by the slurry superficial velocity in the large channel $V_{s,H}$, equal to 2.67 m/s.
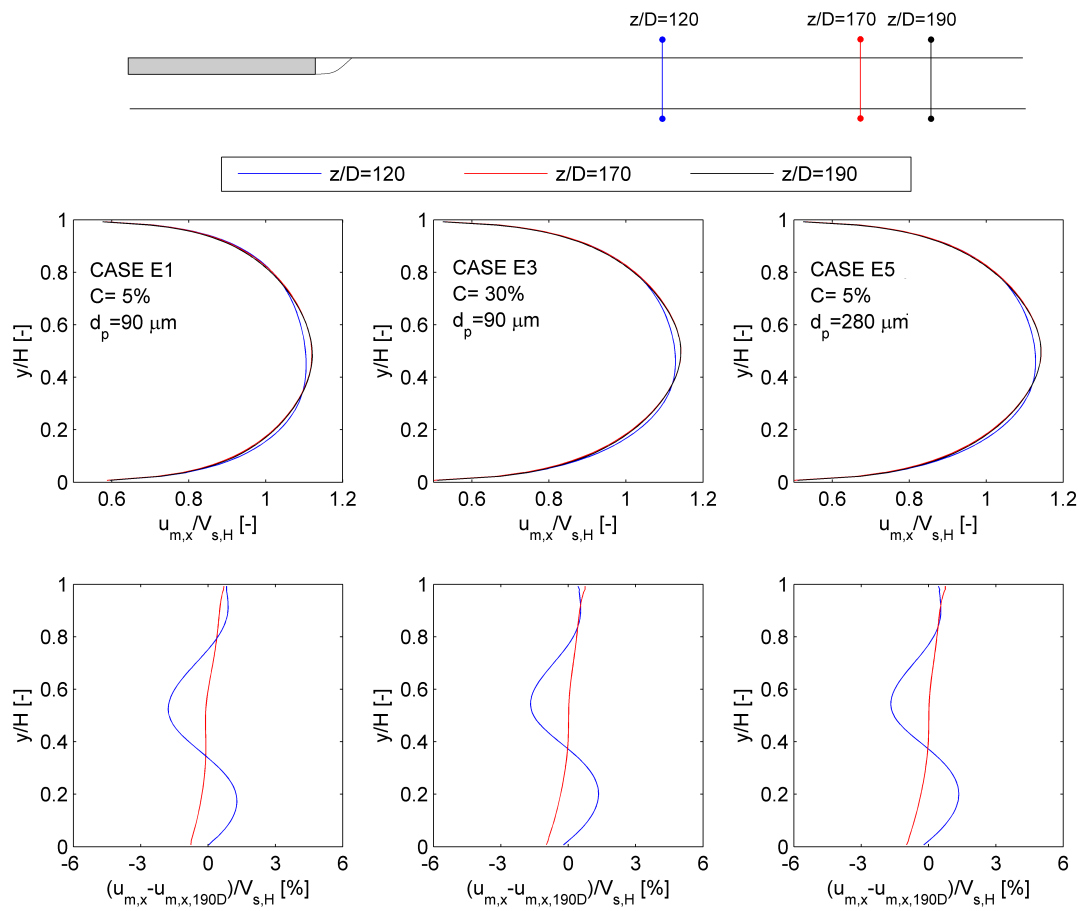
Figure 4.34: Mixture velocity profile and deviation with respect to the fully-developed one at different locations downstream the step for cases E1, E3, and E5 in Table 4.4
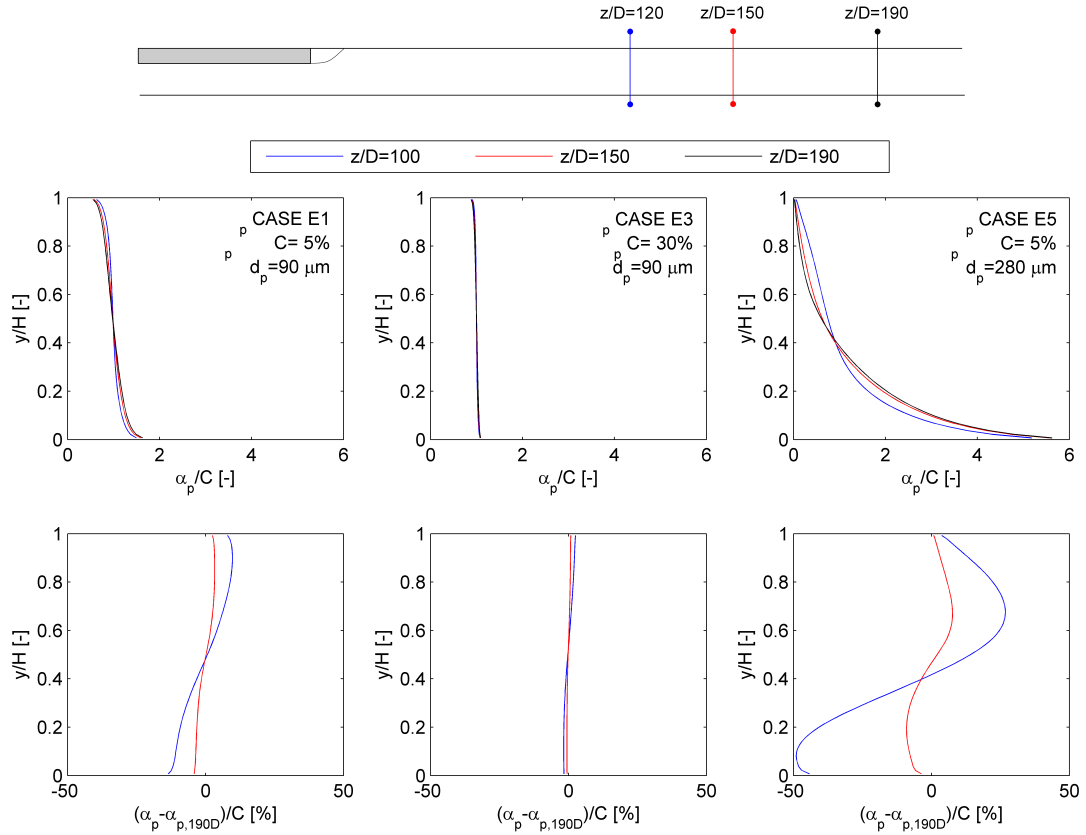
Figure 4.35: Solids concentration profile and deviation with respect to the fully-developed one at different locations downstream the step for cases E1, E3, and E5 in Table 4.4

In the low row, the percentage deviation with respect to the $z/D = 190$ profile (again divided by $V_{s,H}$) is reported. The results highlight that, for all the three flow conditions considered, the mixture velocity profile at $z/D = 170$ is almost undistinguishable from that at $z/D = 190$, suggesting a minor influence of solids loading and particle size on the recovery lenght for the mixture velocity. This may be due to the fact that the three cases are characterized by a low degree of asymmetry of the fully-developed profile, which is therefore rather close to that of the single-phase flow case. A rough guideline is that about $170D$ are required for the attainment of a fully-developed profile. For an expansion ratio of 1.5, this value corresponds to about $57H$, consistent with the $50D_p$ required in the circular pipe case starting from an inlet uniform distribution of velocity and solids volume fraction.

A similar analysis is performed to investigate the region of influence of the step on the solids concentration field. Figure 4.35 is the analog of Figure 4.34 for the solids concentration distribution, but makes reference to a different downstream section ($150D$ instead of $170D$). In the upper row, Figure 4.35 shows the solids concentration profile at the three locations downstream the step, while, in the lower row, the percentage deviation (divided by the mean solids concentration) with respect to the $z/D = 190$ profile is reported. The results highlight that, whatever the mean solids concentration is, for the
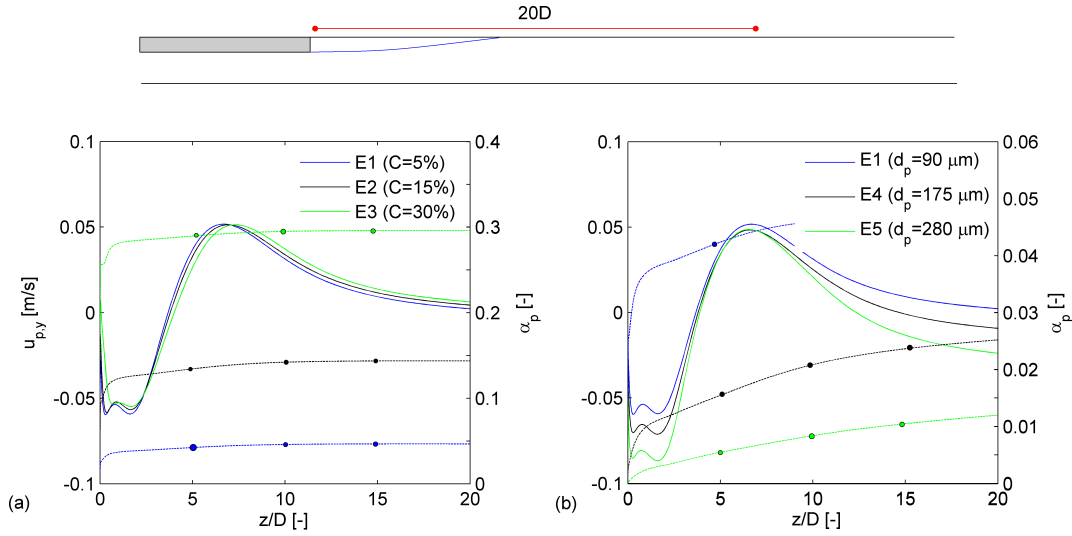
Figure 4.36: Near wall distribution of the vertical component of particle velocity (lines without markers, values on the left axis) and solids concentration (lines with circular markers, values on the right axis) along the upper wall for: (a) different solids loadings for particle size of 90 μm (b) different particle diameters for mean delivered particle concentration of 5%. In all cases, particle density is 2650 kg/m^3

small particles the volume fraction profile at $z/D = 100$ is almost undistinguishable from that at $z/D = 190$. The maximum absolute deviation from the two is about $10\% \cdot C = 0.005$ and $2\% \cdot C = 0.006$ for $C = 5\%$ and $C = 30\%$ respectively. This is due to the fact that such small particles immediately spread throughout the large duct following the fluid, therefore a short distance is required to reach a fully-developed profile. For the large particles (case E5), the solids concentration profile at $z/D = 100$ is not close to that at $z/D = 190$, resulting in maximum absolute deviations about $50\% \cdot C = 0.025$. This is due to the fact that the counteracting effects of drag, collisions and gravity made the region of influence of the step on the solids concentration field larger. As a rough guideline, whatever the solids concentration is a fully-developed concentration profile is obtained at $100D$ for the small particles (cases E1 and E3), whether for the big ones (case E5) about $150D$ are needed.

One of the most important engineering problems concerning solid-liquid mixtures is the erosion of steel goods, due to the impact of particles on a surface. Erosion is usually estimated by means of semi-empirical algebraic erosion models, which evaluate the erosion rate as a funcion of different parameters such as the impact velocity of the particles and the number of incoming particles, that is the delivered particle concentration. As already noticed in the Introduction, the application of erosion models is particularly straighforward when using Eulerian-Lagrangian models to evaluate the two-phase flow field, as the interaction between each particle and the wall can be determined as output of the simulation. Since erosion is particularly significant in systems subjected to a long lasting flow of dilute mixtures, it is generally possible to perform simulations with Eulerian-Lagrangian models. Conversely, if a two-fluid model is used (forced choice when

dealing with dense mixtures), the evaluation of the impact velocity of each particle is not immediate. The proposed model applies a zero particle velocity at the wall, while the non-equilibrium wall function of Launder and Spalding [91] for smooth walls is employed for the tangential component of particle velocity in the first row of cells. This boundary condition, or rather its simplified version under local equilibrium assumption, proved adequate for representing the mechanical contribution to friction of fully-suspended flows in horizontal pipes (Chapter 3), but doesn't seem very realistic for the backward-facing step case, where the particles are more likely to collide with the wall rather then slide along it. Therefore, the particle velocity near the wall may not be correctly predicted as it arises from a boundary condition which may be unsuitable for the particular kind of flow simulated. Under the crude assumption (actually questionable) that the particles impacting to the wall keep the same velocity within the boundary layer, the averaged impact velocity of the particles may be evaluated as the output of the improved model at a certain distance from the wall. This distance must be large enough not to be determined by the non-equilibrium wall function but, at the same time, small enough to be representative of the near wall flow field. For the flow conditions simulated, one would expect the upper wall of the large duct to be the most vulnerable part of the system to erosion risk. Figure 4.36 shows the distribution along this boundary of the flow variables which mainly affect erosion, namely the normal component of particle velocity and the solids concentration. The former variable is represented by the solid lines without markers, and the values are indicated on the vertical axis at the left side; the latter variable is indicated by the dotted lines with circular markers, and the values are reported on the vertical axis at the right side. The normal component of particle velocity was evaluated at a distance of $0.15D$ from the wall, judged adequate to fulfill the above-mentioned requirements. As in previous plots, the influence of mean solids concentration and particle size is studied once at a time in Figures 4.36(a) and (b) respectively by references to the flow conditions reported in Table 4.4. The results highlight that the highest values of normal velocity occurs across the downstream edge of the recirculation region. An increase in the mean delivered solids concentration produces a small downstream shift of the normal velocity distribution as a consequence of the increase in the size of the recirculation region (Figure 4.33(a)). However, the increase in the number of particles impinging with the wall suggests that the $C = 30\%$ case is more subjected to the risk of erosion than the $C = 5\%$ one. On the other side, Figure 4.36(b) indicates that the normal velocity of the particles slightly decreases with particle size, probably because gravity prenominates over inertia. Moreover, the decrease in particle concentration as the particle size increases seems to indicate that the maximum erosion risk occurs in the $d_p = 90$ μm case. It is worth noticing that, however, these considerations are just preliminar hints, which must be followed by a more detailed study when addressing this issue.
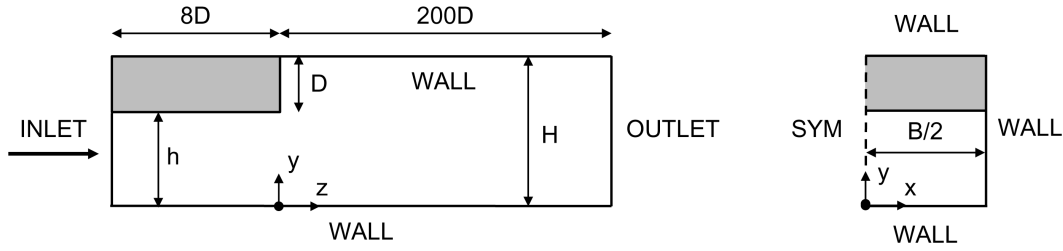
Figure 4.37: Computational domain and boundary conditions

Table 4.5: Fully developed profile at inlet. The friction factor is given by Finolenko's equation [68]

$$u_{c,z} = u_{p,z} = V_s \frac{(N+1)(2N+1)}{2N^2} \left(1 - \frac{2y}{h}\right)^{1/N} \cdot \left(1 - \frac{x}{B}\right)^{1/N}$$

$$N = \frac{1}{\sqrt{f}} \quad f = \left[1.82\log\left(\frac{RV_s}{\nu}\right) - 1.64\right]^{-2} \quad R = \frac{Bh}{2B + 2h}$$

$$k = V_s^2 \frac{f}{8} \left[1 + \frac{2}{3}\frac{2y}{h} + \frac{10}{3}\left(\frac{2y}{h}\right)^3\right] \cdot \left[1 + \frac{2}{3}\frac{x}{B} + \frac{10}{3}\left(\frac{x}{B}\right)^3\right]$$

$$\epsilon = 0.1643\frac{k^{3/2}}{l_m} = 0.1643\frac{k^{3/2}}{R\left[0.14 - 0.08\frac{2y}{h} - 0.06\left(\frac{2y}{h}\right)^4\right] \cdot \left[0.14 - 0.08\frac{x}{B} - 0.06\left(\frac{x}{B}\right)^4\right]}$$

4.3.2   Three-dimensional modelling

The dimensional simulations were carried on in order to investigate the effect of side walls on the flow.

Numerical set up and boundary conditions

The numerical set up is sketched in Figure 4.37, where it is evident that the mean flow and geometrical symmetry of the phenomenon has been exploited by solving only over one half of the duct section. $200D$ of straight duct were simulated downstream the step in order to investigate the development of the flow. At the inlet, the fully-developed profiles reported in Table 4.5, derived from an extension of the boundary layer theory of Nikuradse to rectangular ducts, were set. No slip is assumed between the phases, therefore the same velocity profile is applied to both phases. As in the 2D case, the inlet volume fraction of the solids is taken as uniform if the high bulk-mean velocity imposed is likely to produce pseudo-homogeneous flow in the small duct; otherwise, a fully-developed
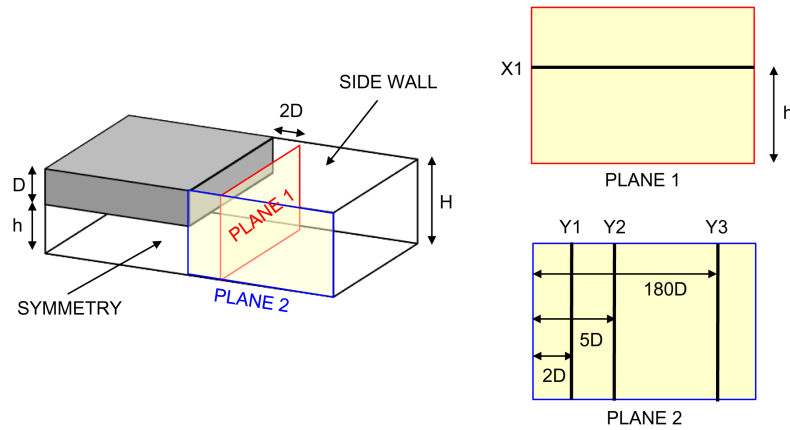
Figure 4.38: Identification of the reference sections

distribution obtained by interpolating the solution of the straigh channel is imposed. For both phases, a no slip condition is applied at all solid walls, and the non-equilibrium wall function of Launder and Spalding [91] for smooth walls is employed to model the effect of near wall turbulence. A two-phase version of the k-ϵ RNG model is used to evaluate the eddy viscosity of the fluid phase. Details of the equations and the boundary conditions are reported in Appendix D. Actually, it is well known that an eddy viscosity based turbulence model, which rely on the hypothesis of isotropicity of turbulence, may be unsuitable for simulating flows in rectangular ducts, characterized by secondary motions close to the corners. More complex Reynolds stresses models, which increase significantly the computer time and the difficulty to reach a converged solution, may be a more appropriate for these flows. However, it was decided to make use the k-ϵ RNG model since the present thesis addresses the problem from an engineering perspective, where the search for the best compromise between the computer time required and the accuracy of the model is a fundamental aspect. As usual, the calculations follow the elliptic staggered formulation, and central differencing is employed for the diffusion terms. In the light of the results about the 2D case, the Linear Upwind Scheme is used to evaluate the convective fluxes. In order to achieve convergence, it was necessary to apply strong relaxation. Inertial relaxation is applied to the momentum equations with a false-time step of 10^{-4} s. A linear relaxation factor of 0.4 is applied to all other flow variables. The two-fluid model proved numerically stable. The CPU time required to reach a converged steady-state solution varied significantly according to the mesh used and, consequently, to the width of the duct. As a rough estimate, with a mesh judged reliable and using a quad core processor Intel at 2.83 GHz and 8 GB RAM about 1-2 days computer time were needed for the case of $B/H = 1$, whilst about 20 days were required for the case of $B/H = 12$.

A cartesian mesh was used to discretize the domain. The results for the two-dimensional case served as starting point for designing the three-dimensional mesh, but the peculiarity of the flow considered here made it necessary to perform a grid sensi-
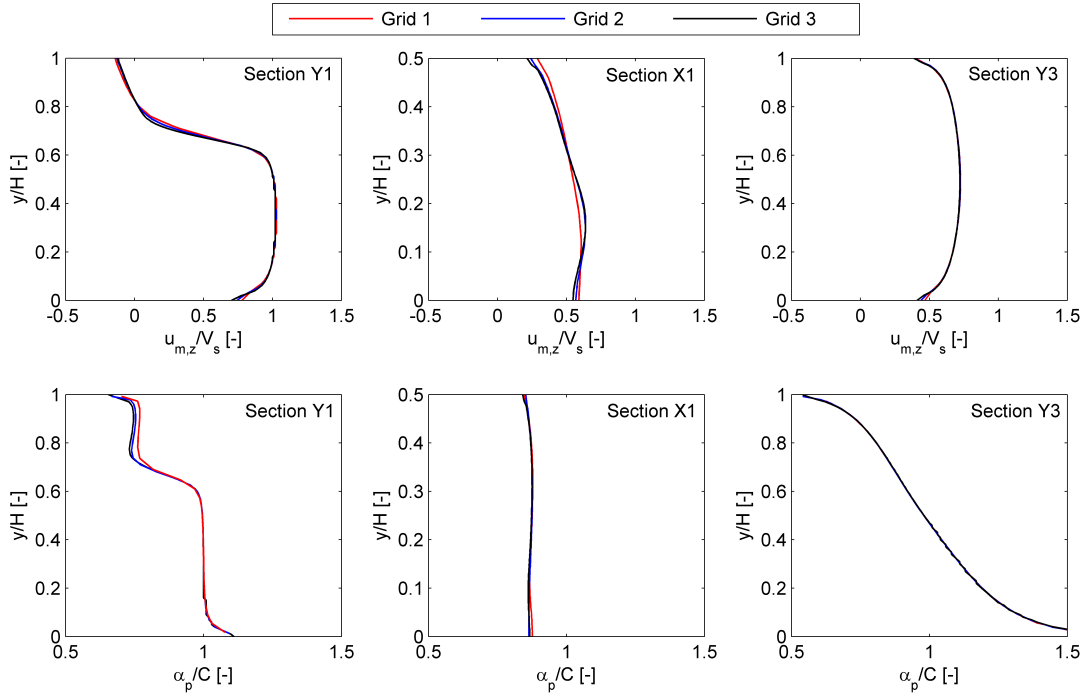
Figure 4.39: Effect of mesh resolution on the velocity and concentration profiles along different sections downstream the step

tivity analysis again. As in the two-dimensional case, the grid was designed in such a way that the condition $y_P^+ = 30$ is satisfied for all walls in the portion of the large duct where fully-developed flow conditions have been re-established. The tests were run for the following configuration, in which the low value of channel width is expected to enhance the three-dimensionality of the flow: $h = 26$ mm, $H = 39$ mm, $B = 39$ mm, and $V_s = 4$ m/s, corresponding to an expansion ratio H/h of 1.5, a large duct channel aspect ratio $B/H = 1$, and a step Reynolds number of $5.2 \cdot 10^4$. The mixture consists of water and sand particles with density of 2650 kg/m^3 and size of 90 μm with mean delivered solids concentration of 5%. The parameters of interest are the mixture velocity and solids concentration profles downstream the step, and the distribution of the pressure coefficient along the streamwise direction. Reference is made to the test Sections Y1, X1, and Y3 in Figure 4.38. Y1 and Y3 are along the vertical direction, belong to the axial slab in the streamwise direction (Plane 2), and are located at a distance from the step equal to 2 and $180D$ respectively. Section X1 belongs to Plane 1, perpendicular to the streamwise direction and distant of $2D$ from the step, and is located in correspondence to the step lip.

Three different meshes were employed, as follows: 11 by 27 by 585 cells along X, Y, and Z directions respectively (Grid 1); 16 by 39 by 795 (Grid 2); 31 by 61 by 988 (Grid 3) cells. The increase of computer time required with the number of cells is particularly significant for this three-dimensional case. On a machine with the already mentioned characteristics (quad core processor Intel at 2.83 GHz and 8 GB RAM), the simulations lasted around 15 hours, 1 day, and 20 days with the three grids. Figures 4.39 and 4.40
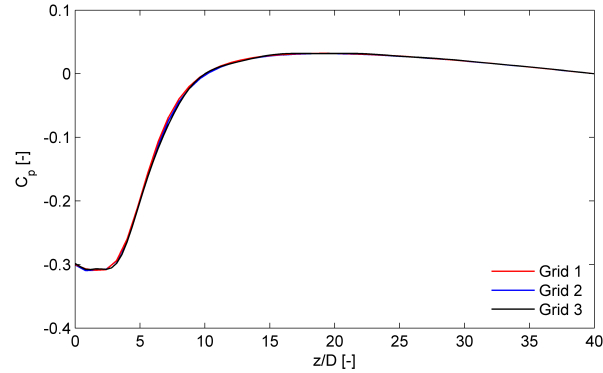
Figure 4.40: Effect of mesh resolution on the distribution of the pressure coefficient along the streamwise direction

show the mixture velocity and solids concentration profiles along Sections Y1, X1, and Y3 and the pressure coefficient along the flow direction computed on the three grid levels. The results indicate that the solutions obtained using the two finest grid are rather close to each other, whilst that for Grid 1 deviates from the finer grid solutions, especially in the recirculation region. Actually, in the same region the solutions on Grid 2 and 3 do not exactly overlap. However, the variations are essentially insignificant for the degree of accuracy required for the applications addressed by this thesis. Grid 2 was judged the best compromise between accuracy and computer time, and was therefore used for the simulations.

Sensitivity analysis of some terms of the two-fluid model

The results illustrated in the previous Sub-section highlight that, in the two-dimensional case, the inclusion of lift and virtual mass within the generalized drag term and the employment of the correlation of Chen and Wood (Eq. 2.87) for the particle eddy viscosity have substantially no effect on the solution. Such negligible influence was observed for all the three flow conditions reported in Table 4.3, corresponding to either small (cases A and B) or big (case C) particles, but the interpretation given to motivate this behaviour is different in the two cases. For the small particles, the ineffectiveness of the above mentioned terms may be due to the low Stokes number, which causes the particles to actually "follow the fluid". For the big particles, it is gravity rather than the Stokes number with most contributes to explain the results.

As it will be discussed later in the present Sub-section, a cross-wise recirculation is induced by the side walls, and consequently the flow field in the 3D simulations is more complicated compared to that in the 2D ones. Therefore, the sensitivity analysis with respect to the three modeling features was performed again. Due to the significant computer time required by three-dimensional simulations, the effect of the three terms together is studied. The numerical predictions obtained accounting for lift and virtual mass and evaluating the particle eddy viscosity via Eq. 2.87 were compared to those
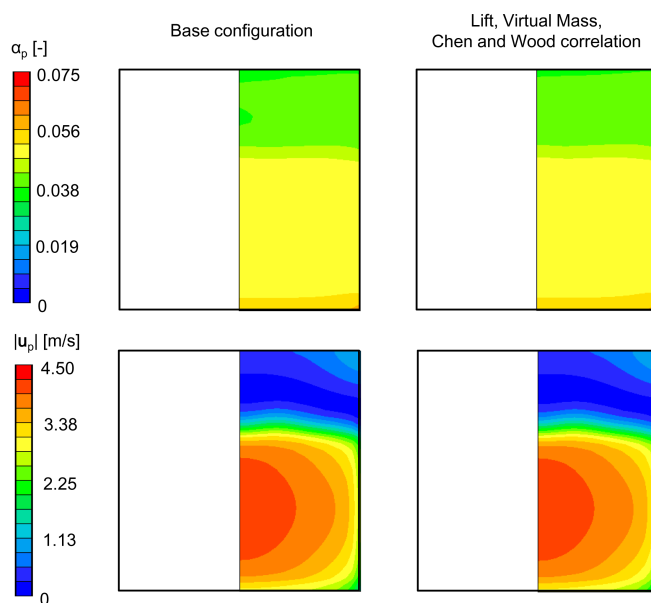
Figure 4.41: Effect of lift, virtual mass, and Chen and Wood correlation for the particle eddy viscosity on the solids concentration and particle velocity over Plane 1 in Figure 4.38 ($2D$ downstream the step) for case A in Table 4.3. The aspect ratio of the large duct is equal to 1. A uniform inlet solids volume fraction distribution is imposed.
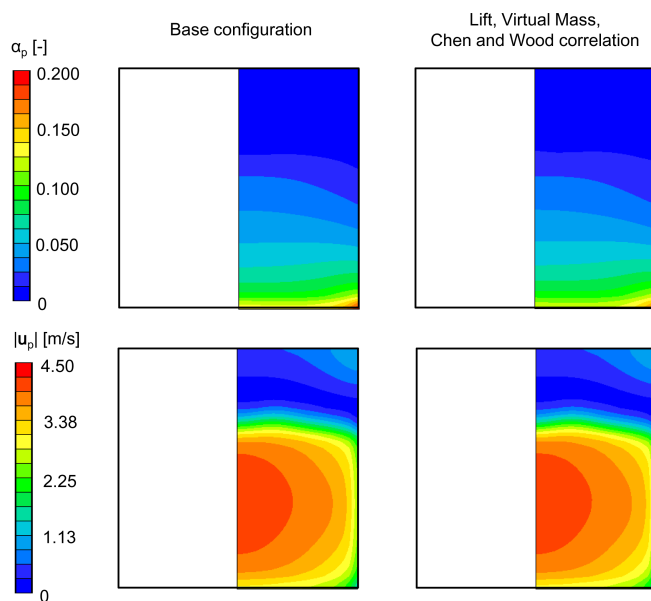
Figure 4.42: Effect of lift, virtual mass, and Chen and Wood correlation for the particle eddy viscosity on the solids concentration and particle velocity over Plane 1 in Figure 4.38 ($2D$ downstream the step). The aspect ratio of the large duct is equal to 1. A fully-developed inlet solids volume fraction distribution is imposed.
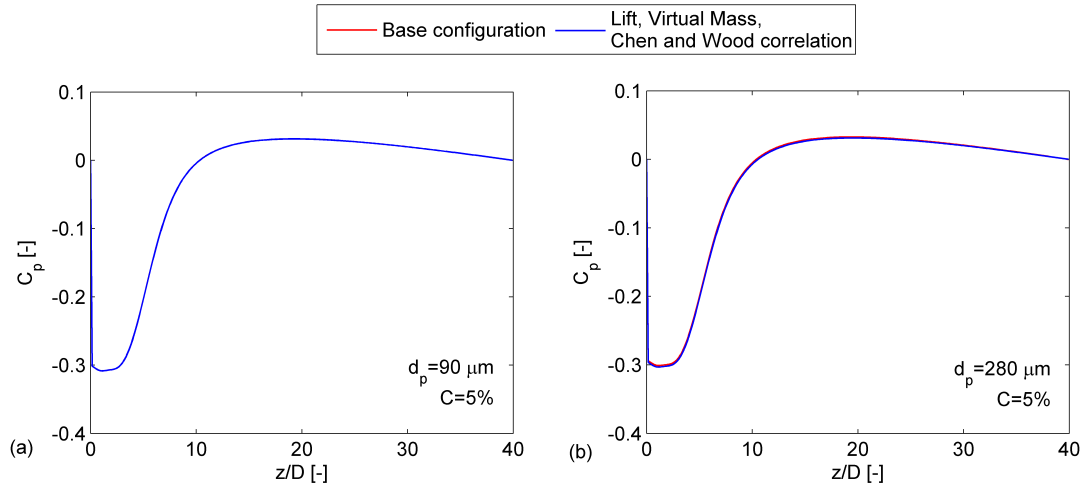
Figure 4.43: Effect of lift, virtual mass, and Chen and Wood correlation for the particle eddy viscosity on the pressure coefficient for cases A and C in Table 4.3. In both cases, the aspect ratio of the large duct is 1

corresponding to a *base* configuration of the two-fluid model, with lift and virtual mass excluded from the generalized drag, and the particle eddy viscosity equal to that of the fluid. Reference is made to the flow conditions A and C in Table 4.3 with a unit aspect ratio of the large duct. For the former case, in which a fully-suspended flow is likely to occur in the small duct, the inlet volume fraction of the solids is taken as uniform. Conversely, the distribution obtained from the simulation of a straight duct is instead imposed for case C. Figures 4.41 and 4.42 compare the solids concentration and the modulus of particle velocity over a crosswise section placed $2D$ downstream the step (referred to as "Plane 1" in Figure 4.38) computed with the two versions of the two-fluid model for both flow conditions. The choice of the reference section is due to the fact that, on the grounds of the work of Founti *et al.* [47], it is precisely at a distance of $2D$ downstream the expansion that the influence of lift is expected to be enhanced. However, for the flow conditions considered here, the comparison shows that the inclusion of lift and virtual mass, and the evaluation of the particle eddy viscosity by means of the algebraic model of Chen and Wood produce significant changes in the solution with respect to the *base* version of the model. Actually, small changes in the solids concentration distribution are observed for case C next to the corners of the duct, precisely where, as already noticed, a two-equation turbulence model may be unsuitable to reproduce the flow. Little variations - indeed almost undetectable - are observed also with respect to the pressure coefficient but only for case C (Figure 4.43). The interpretation given in the two-dimensional case may contribute to explain the results also in the three-dimensional one. The negligible effect of the modifications may be due to the fact that for case A, the particles tend to "follow the fluid" resulting in low slip velocity, while for case C gravity tend to keep the particles away from the region of higher slip.
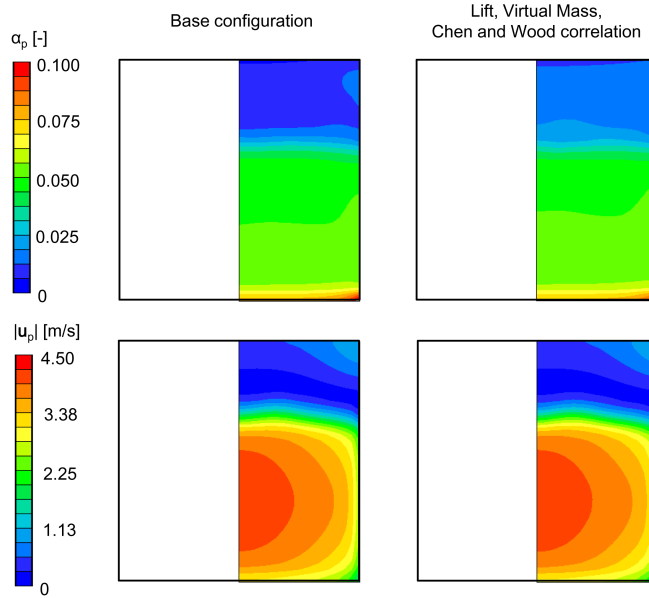
Figure 4.44: Effect of lift, virtual mass, and Chen and Wood correlation for the particle eddy viscosity on the solids concentration and particle velocity over Plane 1 in Figure 4.38 ($2D$ downstream the step) for case C in Table 4.3. The aspect ratio of the large duct is equal to 1. A uniform inlet solids volume fraction distribution is imposed.

Following the approach previously followed for the two-dimensional modeling, the sensitivity analysis for case C is performed also imposing a uniform solids volume fraction distribution at the inlet, in order to lower the influence of gravity. Figure 4.44 is the analog of Figure 4.42 for a uniform inlet solids volume fraction. As in the two-dimensional case, the inclusion of lift, virtual mass, and Chen and Wood correlation for the particle eddy viscosity seems to produce changes in the predicted solids concentration distribution. This contributes to confirm that it is the stratification induced by gravity which most determines the ineffectiveness previously observed. However, for intermediate particle sizes between 90 μm (case A) and 280 μm (case C) it is not a priori clear whether gravity will be strong enough to keep the particles in the core region. Therefore, lift and virtual mass will be included in the generalized drag, and the expression of Chen and Wood (Eq.2.87) will be used to evaluate the particle eddy viscosity.

A discussion about the effect of channel with, mean solids concentration, and particle size on the three-dimensional flow is now reported. As for the two-dimensional simulations, reference is made to the flow conditions E1 to E5 summarized in Table 4.4, which allow investigating the effect of increasing the mean solids concentration for a given particle size (cases E1, E2, and E3) and that of increasing the particle size for a given mean solids concentration (cases E1, E4, and E5). Unless otherwise specified, the aspect ratio of the large channel is 1.
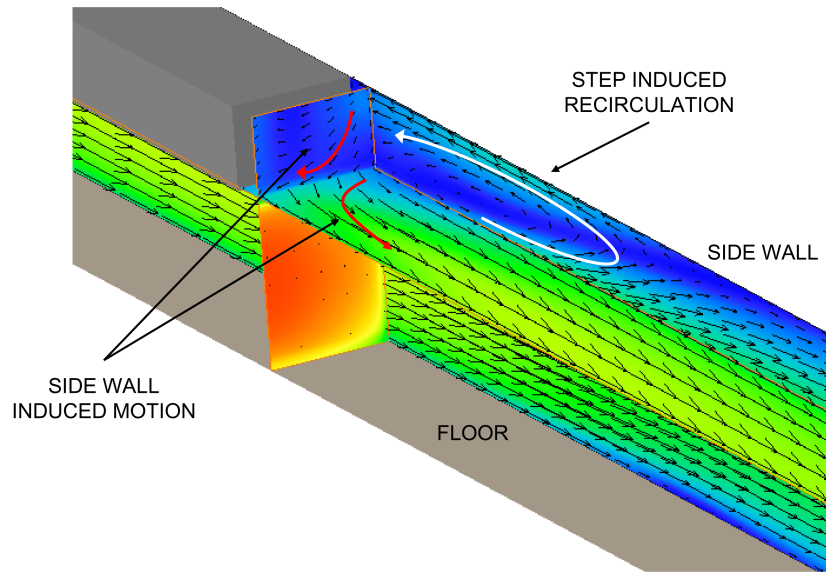
Figure 4.45: Recirculation downstream the step for test case E1 in Table 4.4

Effect of channel width

The flow field obtained as output of the three-dimensional simulations is very complex, especially in the recirculation region close to the side wall. Figure 4.45 shows the projection of the velocity vectors of the continous phase on different planes for test case E1 in Table 4.4. The picture highlights that the *main* vortex in the streamwise direction, induced by the step, is accompanied by secondary motions which tend to push the particles away from the side walls. The effect of these walls on the flow in the centerline of the duct is expected to become less significant as the duct width B, therefore the aspect ratio of the large duct B/H, increases.

In order to investigate the effect of B/H on the flow, the solutions of two simulations with B/H equal to 1 and 12 respectively were compared. Details of the flow conditions are referred to as E1 in Table 4.4. For the two values of duct width, Figure 4.46 reports the distributions of mixture axial velocity and solids volume fraction over Plane 1 in Figure 4.38 (normal to the flow direction at a distance of $2D$ downstream the step, within the recirculation region). The results highlight that, for the large aspect ratio $(B/H = 12)$, the solution is substantially uniform along the cross-wise direction in the central part of the channel, indicating that the effect of the side wall is exhausted at a relatively short distance from the wall and the flow can be regarded as essentially two-dimensional. Similar observations were also reported in previous investigations concerning single-phase flows [24, 76]. As a confirmation of such conclusion, Figure 4.47 reports the vertical mixture velocity and concentration profiles over the duct symmetry plane at different positions in the streamwise direction, indicated as Y1, Y2, and Y3 in Figure 4.38, comparing the results of the 3D simulations with different aspect ratio to those of a 2D simulation. Even if the curves are sometimes confused, the plots seem to confirm that the solution of the 3D simulations approaches those of the 2D one as B/H
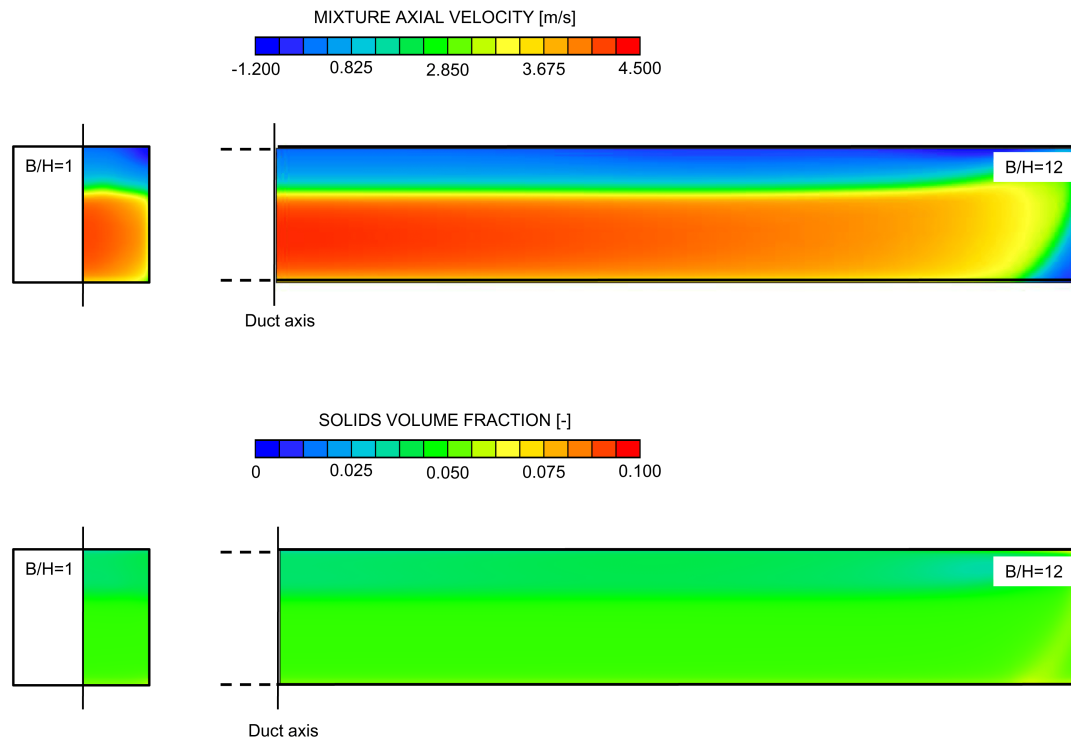
Figure 4.46: Distribution of mixture axial velocity and solids volume fraction on Plane 1 in Figure 4.38 for two values of aspect ratio of the large duct (B/H=1 and B/H=12)
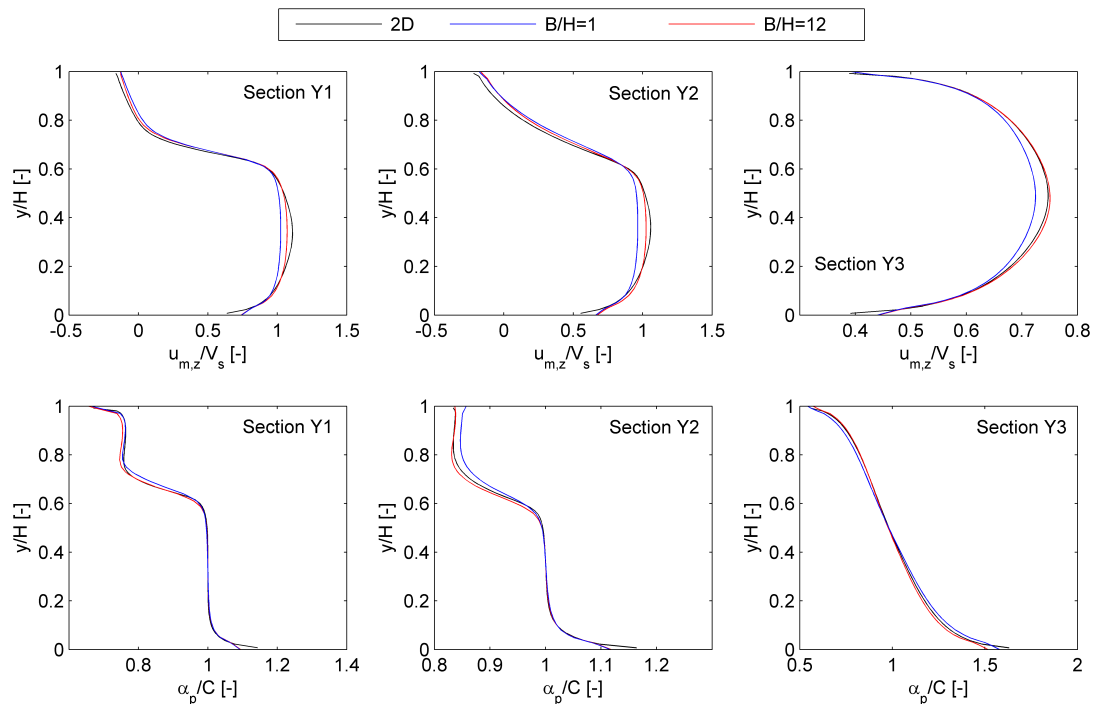
Figure 4.47: Effect of channel width, in terms of spanwise profiles of mixture velocity and solids conecntration along different different sections in the streamwise direction (depicted in Figure 4.38). Comparison between 3D and 2D simulations for the flow conditions referred to as E1 in Table 4.4

increases. Actually, for $B/H = 12$ a 2D simulation may be considered representative of the flow except close to the lateral walls.

Effect of solids loading and particle size

The effect of mean delivered solids concentration and particle size on the flow is investigated. The simulations concerned the case of a unit aspect ratio of the large duct, where the lateral motion induced by the side walls extends up to the duct axis, and therefore a two-dimensional simulation is not representative of the flow. On the other side, if the aspect ratio of the large duct is high enough (say about 12 or more), the flow can be regarded as essentially two-dimensional, therefore the conclusions drawn in Sub-section 4.3.1 apply. Simulations were run for the flow conditions summarized in Table 4.4.

Figures 4.48 and 4.49 report the color plot of the solids concentration distribution downstream the step, over the side wall and three different cross-sections. In particular, Figure 4.48 focuses on the effect of increasing the mean delivered solids concentration from 5 to 30% for a given particle size of 90 μm. The essentially uniform color of the plots appears to confirm the interpretation of the flow previously given on the grounds of the two-dimensional simulations. The small particles, characterized by a low integral scale Stokes number, are affected by drag and turbulent dispersion rather then by gravity, therefore tend to "follow the fluid", spreading throughout the large duct and entering the recirculation region. Actually, the fraction of particles within the recirculation region increases with the mean solids concentration, maybe as a consequence of the increase in the apparent viscosity of the mixture which causes a decrease in the particle relaxation time.

Conversely, three different values of particle size (90, 175, and 280 μm) are depicted in Figure 4.49, for a unique set of particle density (2650 kg/m^3) and mean solids concentration (5%). The difference in color gradation reveals the different behaviour of the systems. Gravity, which pushes the particles downwards, becomes more and more effective as the particle size increases. The degree of stratification of the particles increases with the particle size: the small sized particles (case E1 in Table 4.4) are almost uniformly distributed throughout the large duct, as already observed in Figure 4.48; the large sized particles (case E5) tend to stay in the core region, resulting in almost zero volume fraction within the recirculation region; for the medium sized particles (case E4) the counteracting effects of gravity, drag and turbulent dispersion determine an intermediate configuration, in which the volume fraction of particles within the vortex is greater than zero but lower than the mean inlet value.

Figure 4.50 is the analog of Figure 4.32 for a three-dimensional case with $B/H = 1$. The way in which the mean delivered solids concentration and the particle size affect the pressure coefficient distribution is similar to that inferred from the two-dimensional simulations. The pressure recovery increases with the mean solids concentration, probably as a consequence of the additional momentum transfer from the particles to the fluid; the effect of particle size seems instead minor.
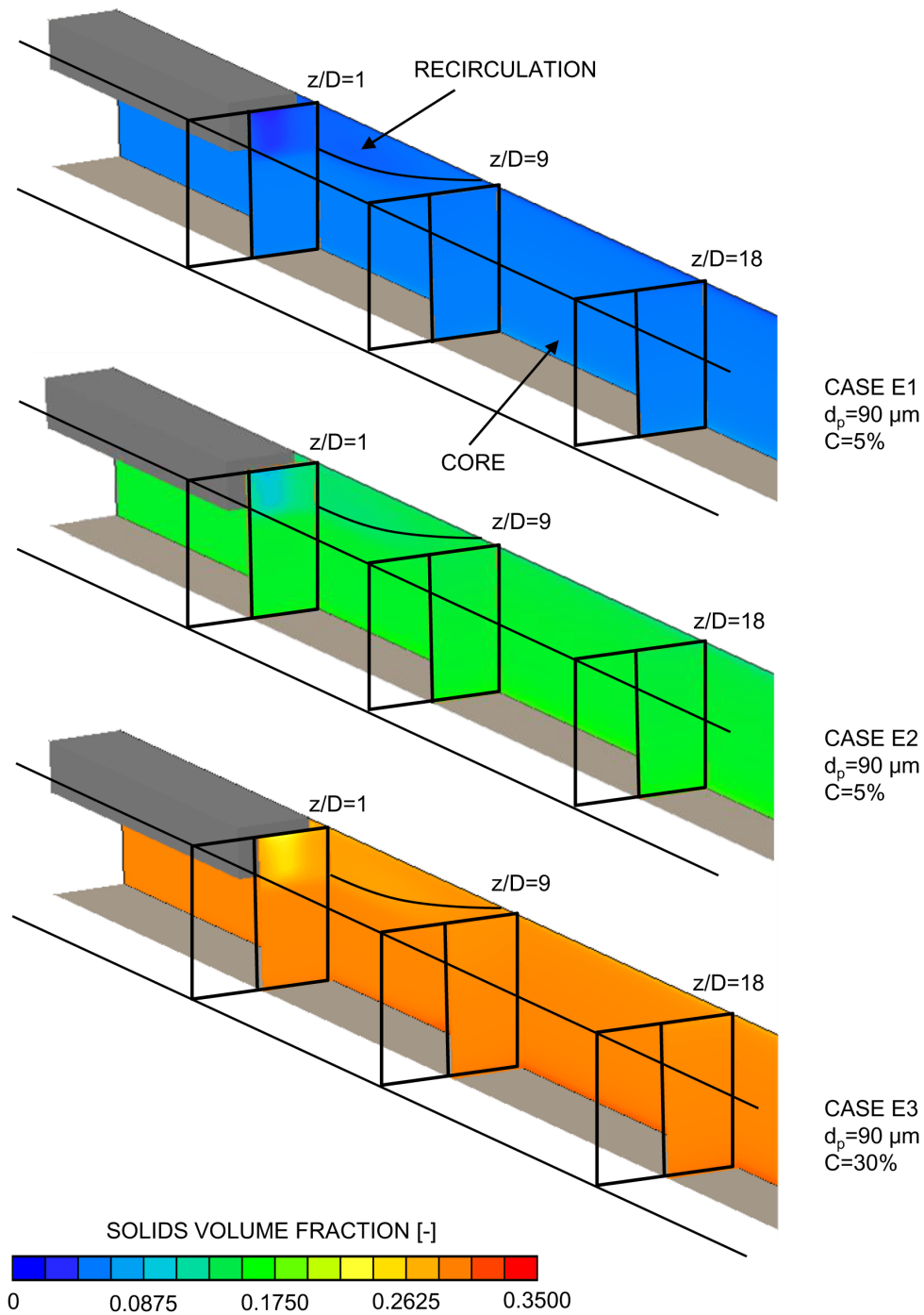
Figure 4.48: Effect of the mean solids concentration on the solids concentration distribution downstream the expansion, with reference to the flow conditions E1, E2, and E3 in Table 4.4
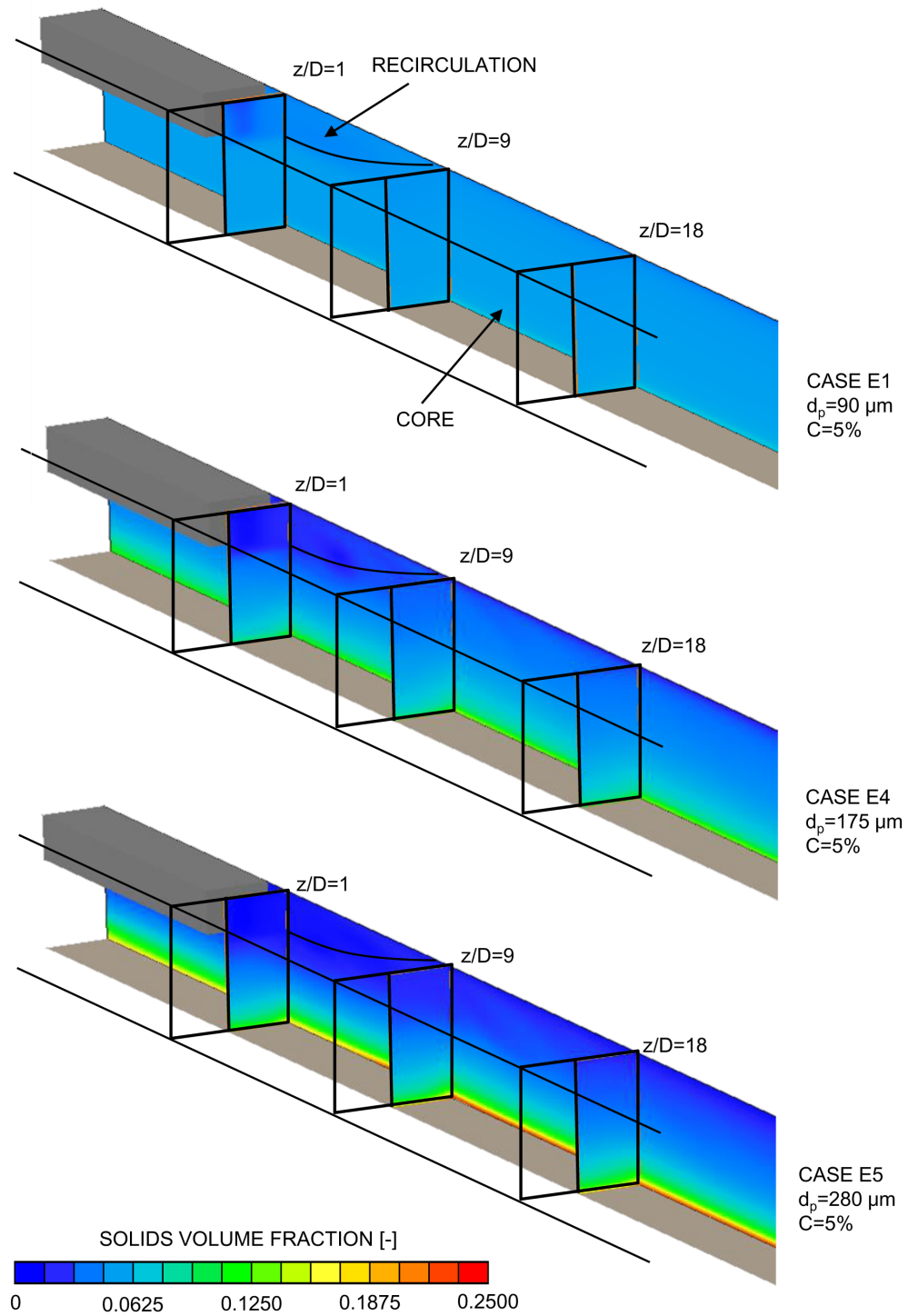
Figure 4.49: Effect of particle size on the solids concentration distribution downstream the expansion, with reference to the flow conditions E1, E4, and E5 in Table 4.4
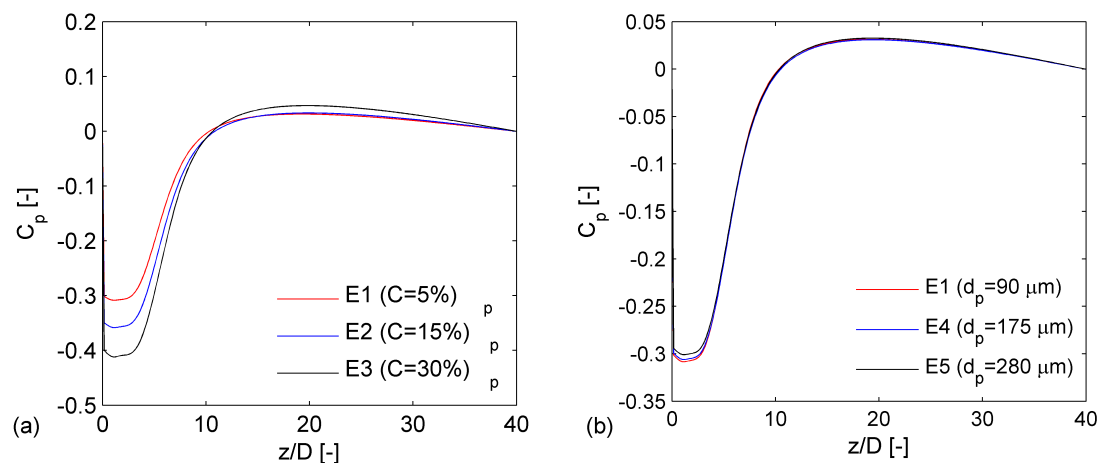
Figure 4.50: Parametric investigation of the pressure coefficient distribution downstream the step in the three-dimensional case for $B/H = 1$. Effect (a) increasing the mean solids concentration up to 30% for a particle size of 90 μm (cases E1 and E3 in Table 4.4); (b) increasing the particle size from 90 to 280 μm for a mean solids concentration of 5% (cases E1, E4, and E5 in Table 4.4)

4.3.3   Unsteady effects

Sometimes the flow of the two-phase mixture may have a strong time-dependent behaviour, therefore some issues of engineering interest may not be adequately represented by a steady-state model. For example, the typical history of a CHOPS well, sketched in Figure 1.4, is characterized by a very "noisy" trend of flow rate and solids concentration. A steady-state model is useful when the focus is on parameters concerning the averaged behaviour of the system over a time scale larger than those fluctuations, such as the mean dissipation characteristics of the plant, or the mean impact velocity of the particles on the steel goods in a certain period of life of the system. Other features of interest for designers require necessarily an unsteady-state model, being strongly related to the evolution of the inflow conditions. Among them, the evaluation of the risk of accumulation and occlusion due to the presence of particles. For example, if at a certain time instant a given amount of particles accumulate within the valve chamber, the system may react to this phenomenon, determining an increase in head losses which in turn causes the accumulation to be removed. A steady-state model doesn't allow reproducing this feature. At this stage in its development the proposed two-fluid model is applicable only to fully-suspended flows, and it is not capable to reproduce the long lasting contact stresses which characterize the specific phenomenon of accumulation addressed above. Anyway, unsteady state simulations are briefly explored in order to check the capabilities of the model and investigate the evolution of the two-phase flow.

The two-fluid model follows the U-RANS approach, in the sense that a transient term is present in all conservation equations. So far all the simulations have been performed by dropping from all conservation equations the transient term, which is now included. The unsteady state simulations are very time-consuming, and would take advantage of

a parallelization of the code to reduce the computer time. The development of a parallel version of the improved model will be shelved for future work. The unsteady-state application concerned the flow conditions referred to as E2 in Table 4.4, where the duct is modeled in two-dimensions, an approximation which proved to be acceptable for ducts with sufficiently high aspect ratio, i.e. $B/H > 12$. The dense mixture flows through the inlet section in the system which is initially subjected to the flow of fluid only. The test is aimed at investigating the evolution of the system and at estimating the time required for reaching a steady-state behaviour downstream the step.

The same structured mesh in cartesian coordinates (91273 cells) designed for the steady-state case was employed to discretized the domain. The simulation covered a time period of 2 s, which was divided in 1000 equal sub-intervals lasting 0.002 s each. The transient term is treated implicitly, while the central differencing and the Linear Upwind schemes are employed for the diffusive and convective fluxes respectively. For every time step, about 500 iterations of the SIMPLEST [143] and IPSA [144] algorithms proved sufficient to reach convergence. This resulted in approximately 10^6 iterations, corresponding about 14 days of computer time using a quad core processor Intel at 2.83 GHz and 8 GB RAM. At $t = 0$, the flow field obtained from a steady state simulation was imposed, with the volume fraction of the fluid and the particles equal to 1 and 0 respectively (only fluid). Across the whole inlet section, the volume fraction of the solid phase is set to 0.3 for every $t > 0$. The fully-developed profiles for velocity, turbulent kinetic energy and dissipation rate reported in Table 4.1 are imposed. No slip is assumed between the phases. As for the steady-state case, at the outlet the normal gradient of all the solved variables is set to zero and the non-equilibrium wall function of Launder and Spalding [91] is employed to model the effect of near wall turbulence, and determining the velocity for both phases, the turbulent kinetic energy, and the dissipation rate in the near wall cells.

Figure 4.51 shows the color plot of particle concentration at different time instants in a region around the step. Downstream the step, the particles tend to expand through the large duct, and are pushed upwards by the fluid. At the same time, the turbulent dispersion makes the border of the solids concentaration distribution smoother and causes the particles to enter the recirculation region. This is consistent with the fact that, for this flow condition, the integral scale Stokes number is very low and the influence of gravity is minor. The particles fill the recirculation region rather slowly, probably because the velocity there is low and the turbulent dispersion is the main mechanism contributing to this phenomenon. Actually, the evolution of the flow is very rapid, and after only 0.8 seconds a steady-state solution is reached.

To better understand the process the local concentration history for the first 0.8 seconds of simulation in the three monitor points named A, B, and C in Figure 4.52 is depicted in Figure 4.53(a). All the points are located downstream the step at a distance from the upper wall equal to half of the step height D. Points A and B lie within the recirculation region, at a distance from the step lip equal to 2 and $4D$, while point C is $20D$ downstream of it. Obviously, the particles reach point C later than point A and
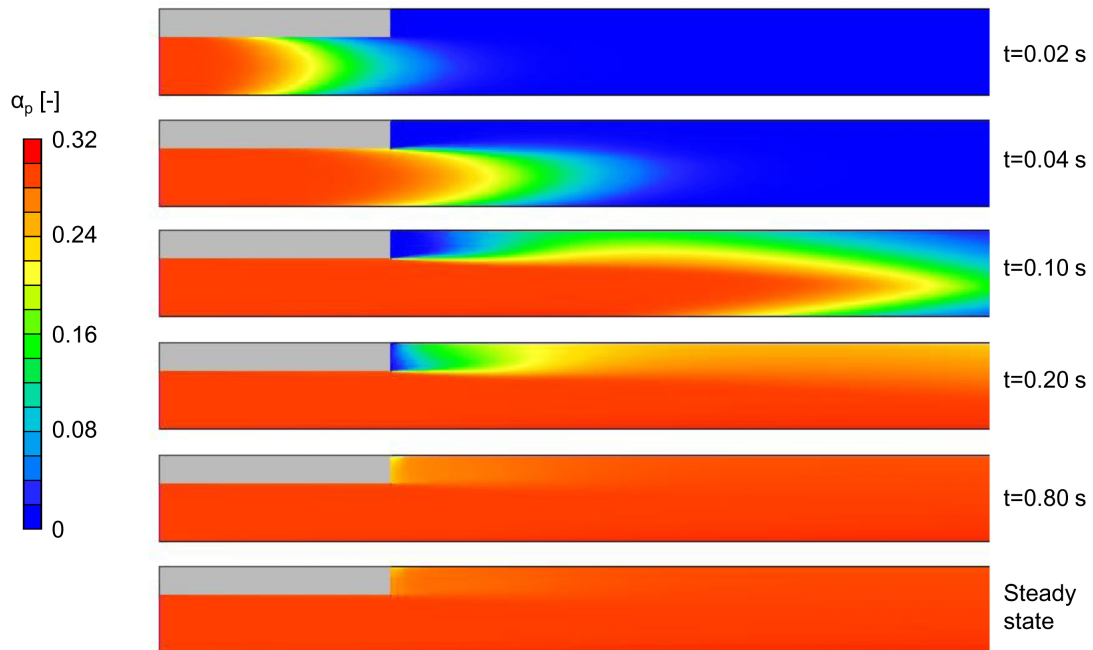
Figure 4.51: Distribution of particle concentration at different time instants and comparison to the steady-state solution
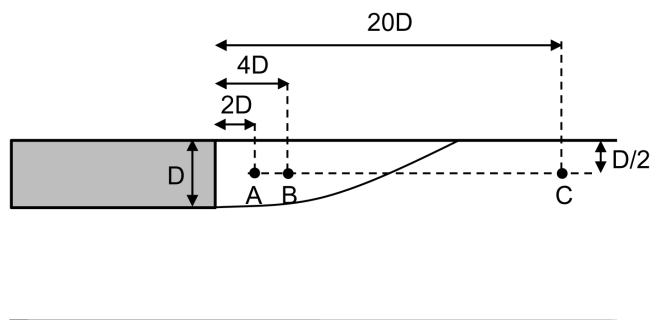
Figure 4.52: Identification of the monitor points A,B,C
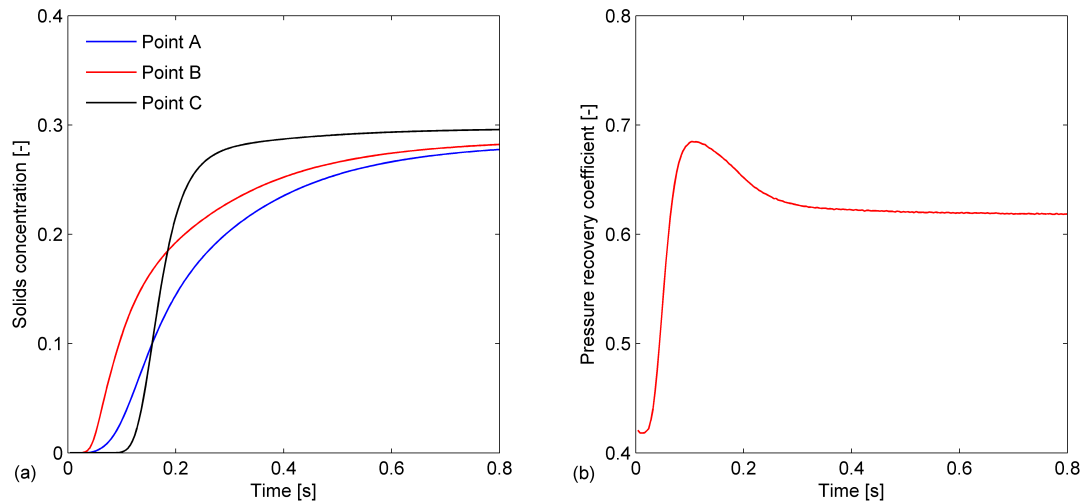
Figure 4.53: (a) Solids concentration history at the monitor points A,B,C, in Figure 4.52 (b) Pressure recovery coefficient history

B, and determine a sharp increase in the solids concentration, since convection rather then dispersion is the dominant mechanism in this part of the domain. Conversely, the increase in the solids concentration is smoother at points A and B, which are within the recirculation region, since dispersion, which is modeled by means of a diffusive term, becomes a dominant mechanism. The expansion of the solids concentration distribution in the recirculation region proceeds upstream, therefore at a given time instant the solids concentration at point B is higher than that at point A.

The evolution of the pressure recovery is then investigated by reference to the pressure recovery coefficient, which is the ratio of the pressure recovery (in turn evaluated as the difference of pressure at $z = 40D$ and $z = 0$) to the dynamic pressure in the small duct. The history of the pressure recovery coefficient in the first 0.8 seconds of simulation is depicted in Figure 4.53(b). As already observed, the additional momentum transferred from the particles to the fluid results in an increas of pressure recovery with respect to the single-phase flow case. The influx of particles determine a sharp increase in pressure recovery, followed by a plateau. Actually, a constant pressure recovery is reached after 0.4 s, regardless of the fact that the solids concentration in the recirculation region has not reached complete steadiness (Figure 4.53(a)).

Chapter 5

Solid-liquid flow through a choke valve

The investigations illustrated so far allowed testing the capabilities of the proposed two-fluid model in case of straight pipes and simple hydraulic singularities. The analysis showed that the model is suitable for application to fully-suspended flows, i.e. when turbulence is effective in keeping all the solids suspended and no particle accumulation occurs.

In this chapter the two-fluid model is applied to a geometry of engineering interest, which is a wellhead choke valve used for the flow regulation in oil & gas applications. For such complex flow, numerical stability and robustess are fundamental requirements of a numerical model. Making an average of U-RANS simulations, as done by other authors in the simulation of pipe flows [41], would lead to extremely high computer time. In the same way, performing experimental tests on control devices in the two-phase flow case is a fairly remote chance, not only for the technical difficulties in executing the measurements but also for the high economical cost of the equipment. Therefore, Computational Fluid Dynamics may become a fundamental tool for designers.

The analysis preliminarily addresses the problem of flow regulation operated by the device when solid particles are present in the flow. In order to dispose of experimental data collected in previous works [141] in the single-phase case, in this introductory analysis water is taken as the carried fluid phase, shelving for future developments the application to oil-solid flows. The delivered solids concentration reaches up to 20% by volume. Such value, together with the assumption of turbulent flow conditions within the device, may be in principle compatible with the initial stage of the CHOPS operations. However, the different characteristics of the fluids involved precludes direct exploitation of the results for this process without specific additional tests, which may represent a possibile development of this work.

This chapter is divided in four sections. Section 5.1 describes how the regulation characteristics of control valves are addresses by the most commonly referenced technical standards, whilst in Section 5.2 the geometry and the functioning of the device tested is illustrated. Afterwards, Sections 5.3 and 5.4 reports the results of the single- and two-phase flow numerical simulations respectively.

Figure 5.1: Sketch of the device

5.1   Regulation characteristics of control valves

Control valves are devices used to regulate the fluid flowing into a system. There exists
a very close relationship between the flow rate and the pressure drop through the valve.
In single-phase flow conditions, the dissipation of the device is commonly evaluated as
by means of the flow coefficient introduced in many technical standards, such as the
ISA.RP75.23-1995 [69] and the IEC 60534-2-3 [67]:

$$\text{CV} = K \frac{Q}{\sqrt{\dfrac{\Delta p}{\rho/\rho_0}}} \tag{5.1}$$

where: Q is the flow rate; ΔP is the pressure drop through the valve; ρ is the actual fluid
density; ρ_0 is the density of water at 15 °C; and K is a numerical constant depending
on the units of measurement of Q and ΔP. K assumes a unit value if Q is expressed
in gallon per minute [gpm] and ΔP is pounds per square inch [psi]. Hereafter, following
the prescriptions of the already mentioned standards [67, 69], the pressure drop ΔP
is evaluated as the difference in pressure between two reference sections located 2 pipe
diameters upstream and 6 pipe diameters downstream the device. It is worth noticing
that the flow coefficient is likely to be independent on the flow rate unless either cavitation
occurs or the flow rate is considerably low.

The flow coefficient of a valve is 0 when the device is fully closed, since $Q = 0$, and
reaches the maximum value when the device is fully opened. The *valve opening curve*,
which is the plot of flow coefficient versus valve opening is a very important technical
parameter of flow control devices.

5.2   Description of the device

The device considered is a Cage Control Choke valve type BCC produced by Breda
Energia S.p.A. The valve, sketched in Figure 5.1, is designed to provide precise flow
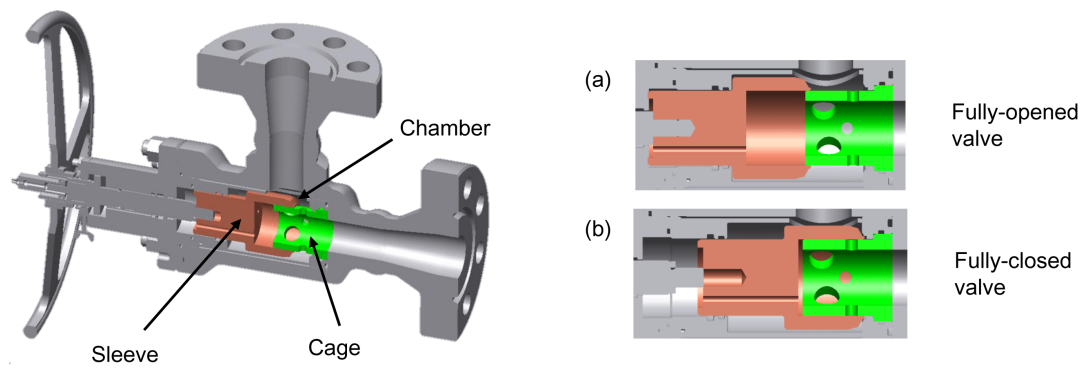
Figure 5.2: "Cage and Sleeve" functioning of the device. (a) fully-opened valve (b) fully-closed valve
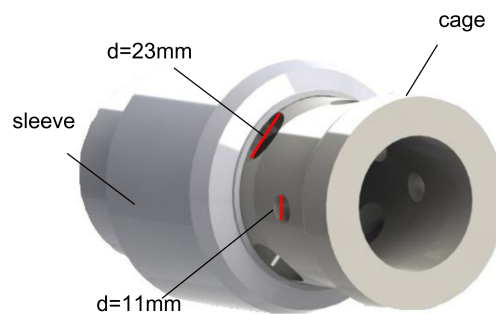
Figure 5.3: "Cage and Sleeve" assembly

control in the field of oil & gas industry, and is suitable for multiphase flow service.

The valve has a "Cage and Sleeve" functioning to control the flow rate (Figure 5.2). The fluid flows through the pipe at the top, in which the inner diameter decreases gradually from 2.5" to 2", and enters a cylindrical chamber, where there is a fixed cylindrical cage with 8 holes of different size on two levels (Figure 5.3). A sliding external sleeve determines the area open to flow by overlapping the cage. In Figure 5.2(a), the holes are entirely uncovered and the valve is fully opened. In Figure 5.2(b), the sleeve overlaps completely the cage and the valve is fully closed. The valve opening is evaluated as the relative percentage travel of the sleeve with respect to the fully-closed position (Figure 5.2(b)). Since there is a minimum travel rate at which the fluid starts flowing, the valve is actually closed until a valve opening of 19% is reached (Figure 5.4).

The fluid enters the cage in the form of several jets, then flows through the divergent outlet pipe, at the end of which the inner diameter slowly increases to its original value of 2.5".
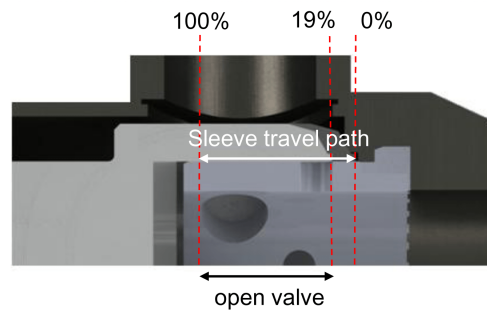
Figure 5.4: Travel rate and valve opening
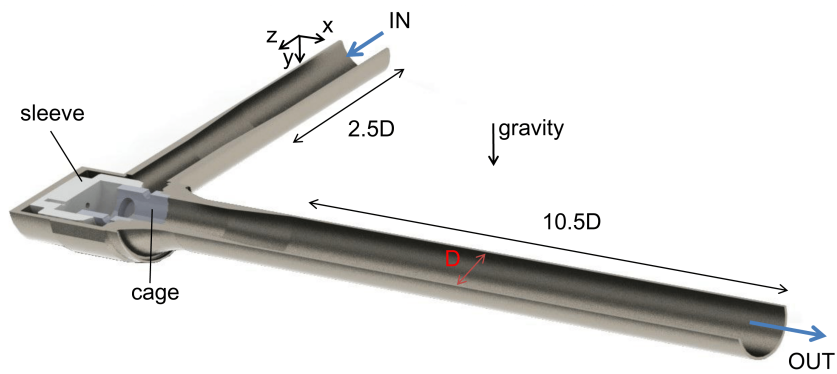
Figure 5.5: Sketch of the domain

Table 5.1: Effect of mesh resolution, turbulence model, and differencing scheme of convective fluxes on the predicted flow coefficient

Grid	Turbulence Model	Diff. Scheme	CV[gpm/$\sqrt{\text{psi}}$]
1	$k - \epsilon$ standard	Hybrid	61.6
2	$k - \epsilon$ standard	Hybrid	59.9
3	$k - \epsilon$ standard	Hybrid	61.4
3	$k - \epsilon$ RNG	Hybrid	61.2
3	$k - \epsilon$ standard	Harmonic Van Leer	63.6

5.3 Single-phase flow analysis

Af first, the flow of pure water through the device is simulated to define the numerical setup and check the performance of the model by comparison to experimental data collected in previous works [141].

A steady formulation of the incompressible Reynolds Averaged Navier-Stokes (RANS) equation is solved with the Reynolds stress tensor evaluated by means of the $k - \epsilon$ standard turbulence model as in previous numerical investigations about choke valves [60]. The working fluid is water at 20 ℃.

In order to reduce the computer time, the geometry of the valve was simplified by removing all the parts ineffective for the fluid-dynamics calculations. The computational domain, sketched in Figure 5.5, is a rectangular box circumscribing the valve and the adjacent pipes.

At the pipe inlet, a uniform distribution is set for the axial velocity, while the distributions of the turbulent kinetic energy and of its dissipation rate were derived from a turbulent intensity of 5% and an inlet mixing length equal to 7% of the pipe diameter. This choice was considered after verifying that the imposition of a fully developed profile, with the distribution of axial velocity, turbulent kinetic energy and dissipation rate determined from the Nikuradse's boundary-layer theory [68], has substantially no effect on the predicted flow coefficient and the flow field within the valve. At the outlet, the normal gradient of all the solved variables is set to zero. About 2.3 and 10.5 diameters of straight pipe were simulated upstream and downstream the body of the valve respectively, in order to guarantee the consistent application of the inlet and outlet boundary conditions. No-slip conditions are imposed on solid walls, and the equilibrium wall function of Launder and Spalding [91] for smooth walls is employed to model the effect of near-wall turbulence. The immersed boundary method, called PARSOL, employed to detect the solid borders of the valve makes hard, and virtually meaningless, to evaluate the non-dimensional distance of the first row of cells y^+ in order to verify the condition $30 < y^+ < 130 - 180$ for the consistent application of the equilibrium wall function. Anyway, the grid independence study illustrated in the following indicates that the possible misapplication of the wall function is not expected to significantly alter the numerical predictions.

The code PHOENICS was employed for the numerical solution of the finite-volume analogue of the RANS model. This was done by using a parallel version of the SIM-

PLEST algorithm of Spalding [143]. The calculations are performed following the elliptic-staggered formulation in which the scalar variables are evaluated at the cell centers and the velocity components at the cell faces. Central differencing is employed for the diffusion terms, while the convection terms are firstly discretized using the hybrid scheme of Spalding [145]. The calculation procedure is organized in a slab-by-slab manner, in which all the dependent variables are solved at the current slab before the solver routine moves to the next slab. The numerical solution procedure requires appropriate relaxation of the field variables to achieve convergence.

A structured mesh in cartesian coordinates is used to discretize the domain. Due to the peculiar way in which PHOENICS works, the mesh had to be defined over the whole domain, and the cells covered entirely by fluid, entirely by solid, and by both fluid and solid were automatically discriminated by the code by means of the already mentioned PARSOL method. A grid independence study was performed to select the optimum discretization of the domain. The tests were performed for the valve fully-opened and a flow rate of 8.4 L/s. The different meshes were employed, consisting of 201 by 118 by 161 control volumes along the X, Y, and Z directions respectively (Grid 1); 243 by 142 by 195 (Grid 2); and 267 by 156 by 215 (Grid 3). The low influence of the mesh on the predicted flow coefficient (Table 5.1) justifies the use of Grid 3. The flow coefficient is evaluated by means of Eq. 5.1. Consistently with the prescriptions of the technical standards [67, 69], the pressure drop is evaluated as the different between the average values of pressure over two cross sections placed 2 pipe diameters upstream and 6 pipe diameters downstream the valve. The flow rate is calculated with respect to the bulk-mean velocity in the downstream reference section. Since, as already mentioned, the working fluid is water at 20 °C, the ratio ρ/ρ_0 was set to a unit value, being 0.999 the actual one.

The PHOENICS solver was run until the sum of the absolute residual sources over the whole solution domain are less than 1 per cent of reference quantities based on the total inflow of the variable in question. An additional requirement is that the values of the monitored dependent variables at a selected location do not change by more than 0.1% between subsequent iteration cycles. This requires about 2 days of computer time with quad core processor Intel at 3.60 GHz and 8 GB RAM.

Additional tests were also performed to investigate the effect of the turbulence model and the differencing scheme for the convective fluxes on the numerical solution. The use of the $k-\epsilon$ RNG model instead of the $k-\epsilon$ standard one procured small variations on the predicted flow coefficient (Table 5.1). Similar results were found by previous authors who simulated the flow through a globe valve [31]. In the same way, the higher computer time required by the Harmonic Van Leer scheme was judged unnecessary, being the variations in the predicted flow coefficient only about 3.5%.

In order to verify the performance of the numerical model, different values of valve opening were simulated. The valve opening curve was then addressed by comparing the numerical predictions to experimental data collected previously in the Hydraulic Laboratory of Politecnico di Milano University. For completeness of exposition, the
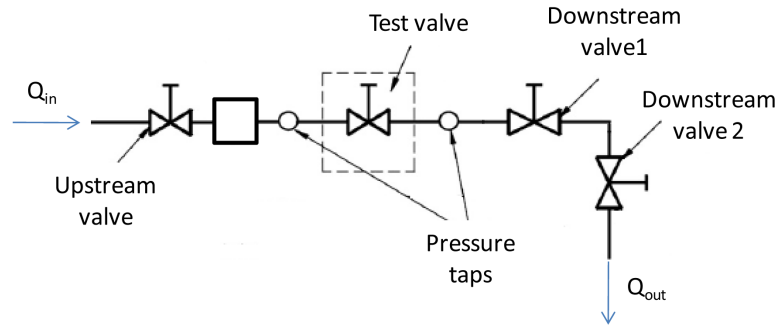
Figure 5.6: Experimental setup at the Hydraulic Laboratory of Politecnico di Milano University

experimental setup and the procedures for data acquisition will be briefly discusses in the following, referring the reader to other references [141] for more details.

The pilot plant, sketched in Figure 5.6, consists of 4" (main line) and 2.5" (test line) stainless steel AISI 304 pipes, supplied by either a gravity reservoir or a parallel pressure boost system, capable to guarantee pressure up to 10 bar upstream the valve. The maximum reachable flow rate is 80 L/s. Control valves placed upstream and downstream the test section allow setting the proper fluid-dynamic conditions in each experimental test. The pressure drop through the valve was measured with a series of absolute and differential pressure transducers in reference sections located 2 pipe diameters upstream and 6 pipe diameters downstream the device. Flow rate was measured by a 4" electromagnetic flow-meter, placed several diameters upstream the test section. During the tests, the water temperature was measured in order to monitor values of viscosity, vapor pressure, and density in order to properly evaluate the ρ/ρ_0 ratio.

The tests have been performed maintaining constant pressure at the upstream reference section and decreasing the downstream pressure, in order to increase the flow rate. As required by the IEC 6054-2-3 standard [67], it was verified that the maximum uncertainty on pressure and flow rate measurements was below 2%. For each set of measurements, the relative error on the flow coefficient, determined with respect to the International Organization of Standardization-GUM [72], was found to be lower than 2.1%. The characteristic flow coefficient at each valve opening is the average among the values in the range of self-similarity with respect to the flow rate. As prescribed in the IEC 6054-2-3 standard [67], it was verified that, within that range, the maximum deviation between two data does not exceed 4%.

In the numerical simulations, the flow rate is within the self-similarity range inferred from the experimental points. Preliminary tests were performed to verify that the existance of such range was correctly predicted by the numerical model. The good agreement between computations and experiments, as shown in Figure 5.7, reveals the reliability of the numerical model in the single-phase flow case.
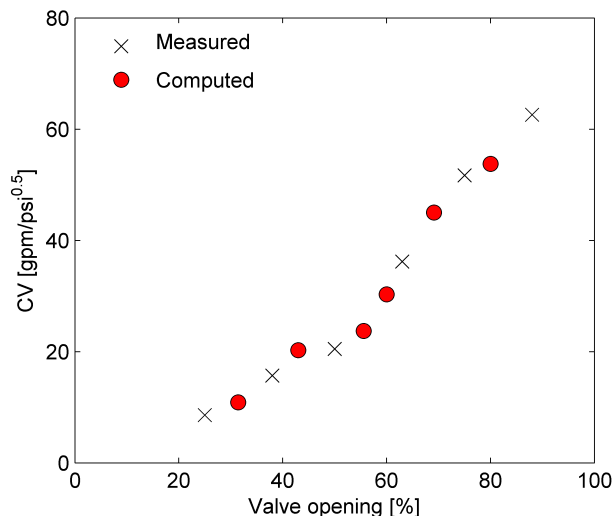
Figure 5.7: Valve opening curve: comparison between computations and experiments performed in previous works [141]

5.4   Two-phase flow analysis

The effect of the presence of a solid phase in the flow is now investigated by means of the proposed two-fluid model. As usual, the turbulent Schmidt number for volume fraction is set to 0.7, and the mixture viscosity correlation of Mooney (Eq. B.7) with intrinsic viscosity of 2.5 and maximum packing concentration of 0.7 was used to evaluate the viscosity of the mixture. In this perliminary application of the model to a complex geometry, the generalized drag term includes the drag force only, shelving for future developments the inclusion of lift and virtual mass. The extended version of the $k - \epsilon$ standard model for two-phase flow previously previously applied to the horizontal pipe case is used for evaluating the eddy viscosity. The correlation of Chen and Wood (Eq. 2.87) is used to evaluate the particle eddy viscosity.

The size of the domain and the mesh configuration are those used for the single-phase flow case, illustrated in the previous section and sketched in Figure 5.5. The carrier fluid is water and the disperse phase consists of solid particles with the characteristic density of sand (2650 kg/m^3). At the inlet, the same uniform distribution is set for the axial velocity of both phases (therefore, it is assumed no slip between the fluid and the particles), while the distributions of the turbulent kinetic energy and of its dissipation rate were derived from a turbulent intensity of 5% and an inlet mixing length equal to 7% of the pipe diameter. Also the inlet volume fraction of the solids is taken as uniform, since the flow conditions simulated are likely to produce pseudo-homogeneous flow in a straight pipe. For the same reason, gravity, which is directed along the Y direction (Figure 5.5), is expected to be of minor importance. At the outlet, the normal gradients of all variables and the value of the pressure are set to zero. At the pipe wall, no slip conditions are imposed to the fluid phase, and the equilibrium wall function of Launder

Table 5.2: Case study considered in the investigation. The valve opening is 80%.

Case	V1	V2	V3	V4	V5
Slurry superficial velocity [m/s]	3.5	3.5	3.5	3.5	3.5
Particle size [μm]	90	90	90	125	200
Particle density [kg/m^2]	2650	2650	2650	2650	2650
Mean solids concentration [%]	5	10	30	10	10

and Spalding [91] for smooth walls is used to reproduce the effect of near-wall turbulence.

As usual, the code PHOENICS is employed for the numerical solution of the finite-volume analogue of the mathematical described above. The other numerical settings (differencing schemes, mesh configuration, relaxation factors, and convergence criteria) are set as in the single-phase flow case. However, for the solution of the equations, a serial version of the SIMPLEST algorithm of Spalding [143] was employed. Approximately, about 8 days of computer time are required with quad core processor Intel at 3.60 GHz and 8 GB RAM. The compilation of a parallel version of the solver is being completed in the final days of writing this thesis.

Reference is made to the five benchmark cases illustrated in Table 5.2, in order to provide some preliminar indications about the effect of increasing the mean solids concentration for a given particle size (cases V1, V2, and V3) and that of increasing the particle size for a given mean solids concentration (cases V1, V4, and V5). Consistently with the well established condition of applicability of the two-fluid model, special attention was paid to guarantee that the combinations of volumetric flow rate Q, mean delivered solids concentration C and particle size d_p were suitable to keep all the solids in suspension. The experimental data regarding the single-phase case [141] indicates that, for a valve opening of 80%, the flow rate $Q = 12$ L/s lies within the range of self-similarity of the flow coefficient with respect to Q. The existance of a similar range doesn't seem to have been reported in the two-phase flow case, and, at this stage in the development of the work, can only be presumed. Surely tests regarding different values of superficial velocity as well as valve opening are required to confirm the observations made for these few cases only, and will be shelved as development of this thesis.

The way in which the presence of solid particles affect the dissipation characteristics of the device is considered. The particles in the flow are expected to produce a higher pressure drop with respect to the single-phase flow case, due to the additional momentum transfer from the particles to the fluid. However, a quantification appears difficult since the definition of the flow coefficient for the solid-liquid case is not straighforward, and no indication is given in the standards [67, 69].

Initially the flow coefficient, referred to as CV_0, is evaluated by means of Eq. 5.1 where the density ρ was set to that of the carrier fluid ρ_c. Since the simulation fluid is water at 20 °C, the ratio $\rho/\rho_0 \approx 0.999$ was assumed unitary. Figure 5.8 shows the percentage reduction of CV_0 with respect to the single-phase value as a function of delivered solids concentration for three values of particle size. The computed single-phase flow coefficient relative to 80% of travel rate is 53.0 gpm/$\sqrt{\text{psi}}$. The results seem
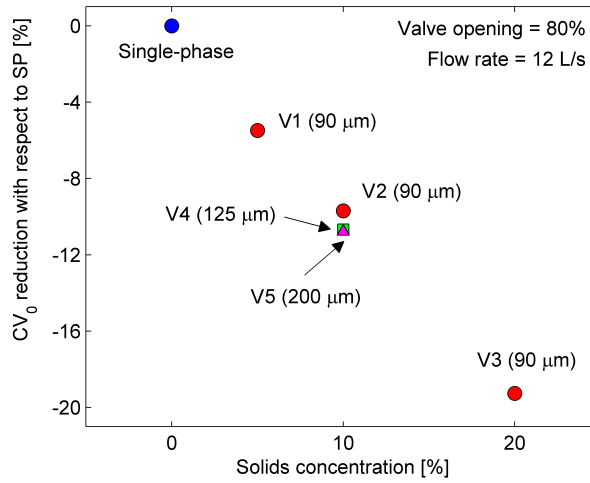
Figure 5.8: Reduction of the flow coefficient CV_0 with respect to the single-phase flow case as a function of delivered solids concentration for different particle sizes

to confirm that the presence of solid particles in the flow may increase signifcantly the pressure drop through the valve, the reduction of CV_0 being more than 20% of the single phase flow value if the delivered solids concentration if the flow is 20% (case V3). For a mean delivered solids concentration of 10%, an increase of the particle size from 90 to 200 μm (cases V1, V4, and V5 in Table 5.2) doesn't seem to affect significantly the value of CV_0. However, these tests alone are not sufficient to draw any conclusion about the influence of particle size.

Afterwards, reference is made to an alternative definition of the two-phase flow coefficient (referred to as CV_m), which is Eq. 5.1 with ρ equal to the density of the mixture ρ_m given by:

$$\rho_m = \rho_c \left(1 - C\right) + \rho_p C \tag{5.2}$$

On the grounds of what previously discussed, ρ_c and ρ_0 were assumed equal. When expressed in terms of CV_m instead of CV_0, Figure 5.8 becomes Figure 5.9, in which the deviations with respect to the single-phase flow case are significantly lower, being less than about 6%.

This consideration may be of interest for designers, because it indicates that, in a very first approximation, the pressure drop produced by the two-phase mixture can be evaluated from the equality $CV_m = \text{cost} = CV_{SP}$, being CV_{SP} the flow coefficient of an equal flow rate of pure liquid. Combination of Eqs. 5.1 and 5.2 yields:

$$\Delta p = CV_{SP}^2 Q^2 \left[\left(1 - C\right) + C \frac{\rho_p}{\rho_c}\right] \tag{5.3}$$

Eq. 5.3 is particularly useful because it allows estimating the pressure drop in the two-phase case from the composition of the mixture (C,ρ_c,ρ_p), the fluid-dynamic conditions (Q), and the flow coefficient in the single-phase case CV_{SP}. This formula implicitly relies
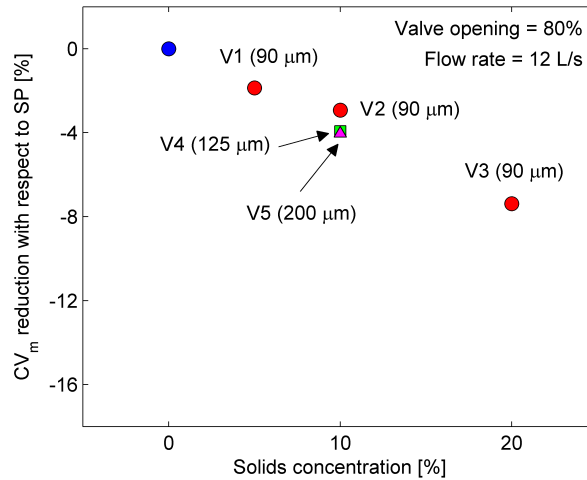
Figure 5.9: Reduction of the flow coefficient CV_m with respect to the single-phase flow case as a function of delivered solids concentration for different particle sizes

on the assumption that the mixture of fluid and particles behaves like an incompressible fluid with density ρ_m. This assumption may be acceptable for small particles at low concentration, but may be unacceptable for dense flow. Future work will be aimed at establishing in a more complete way the range of validity of Eq. 5.3 with respect to delivered particle concentration and size.

The distributions of velocity and solids concentration within the valve are very important to understand the behaviour of the mixture. Moreover, they may be used to predict secondary effects like the risk of erosion, abrasion, and occlusion of the chamber. Actually, at this stage in its development the model may not be suitable to deal with these features unless in a very rough way. The prediction of erosion requires the coupling with a suitable erosion model and basically the evaluation of the impact velocity of the particles with the solids walls. Anyway, providing such information is not straightforward with a two-fluid model whose output are the mean flow quantities. The evaluation of the particle velocity at a certain distance from the wall, briefly explored in Sub-section 4.3.1, may be a good way to overcome the problem, but specific tests are required to properly define the procedure to be followed. This may be a challenging development of this work. Moreover, the proposed model doesn't allow accounting for particle accumulation because, as already noticed, it is not suitable to reproduce the long-lasting contact stresses among the particles. It is worth also noticing that, anyway, the evaluation of the occlusion of the chamber would probably require an unsteady model, due to the time-dependent characterization of such process.

In the flow conditions summarized in Table 5.2 these contact stresses are not likely to be effective, guaranteeing the reliability of our computations. Following an application-aimed approach, the results illustrated in the remainder of this paper may be exploited to identify the most critical areas inside the valve. Precisely these areas are those to
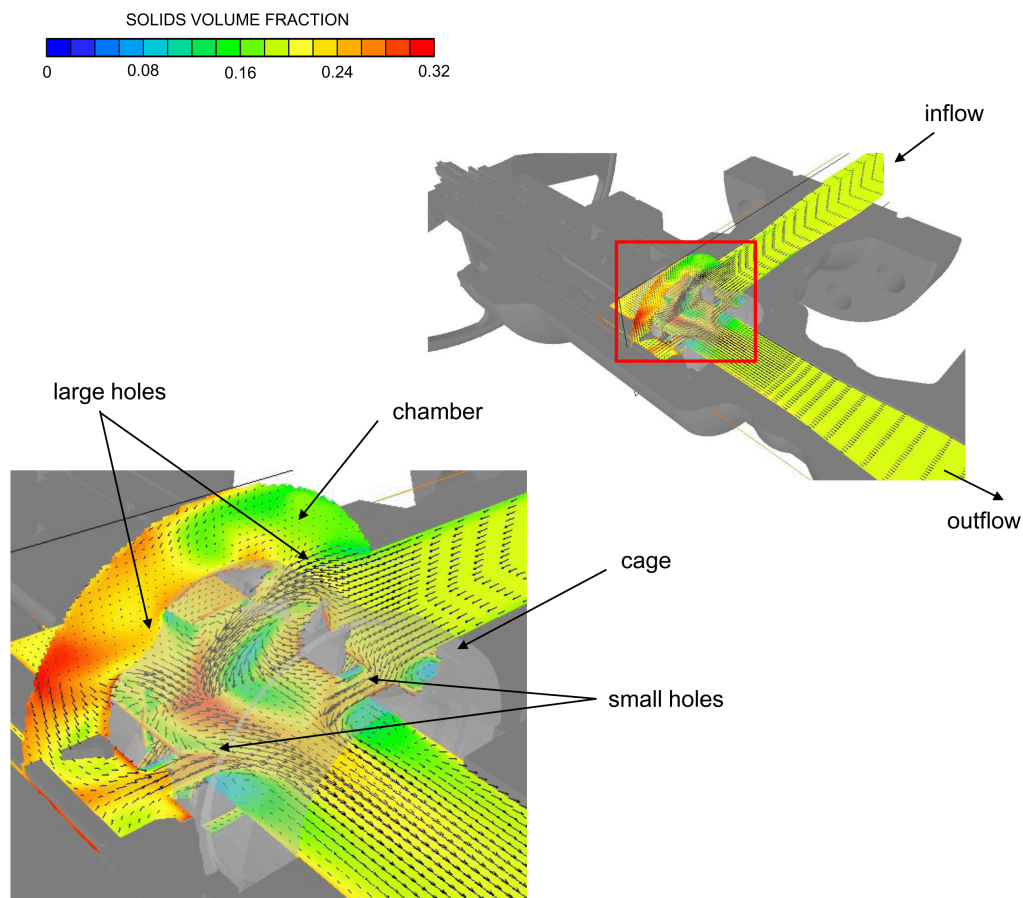
Figure 5.10: Solids volume fraction distribution and velocity vectors of the solid phase within the valve body for the flow condition V3 in Table 5.2

which the designer ought to pay more attention in view of the risks due to high solids loading.

The flow inside the valve is very complex, being the results of different interacting jets. Figure 5.10 shows the color plot of the solids volume fraction distribution within the valve body for the flow condition V3 in Table 5.2. The velocity vectors of the solid phase are depicted too. The extreme difficulty to evaluate a characteristic integral time scale in this system doesn't allow calculating the integral scale Stokes number as done in Chaptere 4. Anyway, the small size of the particles seems to indicate that they are likely to "follow the fluid" being affected by turbulent dispersion. The numerical solution seems to confirm this interpretation; the jets, in fact, are characterized by high volume fraction, which reaches the maximum values where they collide, namely within the cage and in the part of the chamber opposite to the inflow.

To better highlight the behaviour of the mixture, a projection of the solution on the two slices sketched in Figure 5.11 is reported; both slices are perpendicular to the cage axis, and located in correspondence to the big (slice A-A) and small (slice B-B) holes respectively. The effect of mean delivered solids concentration is highlighted in
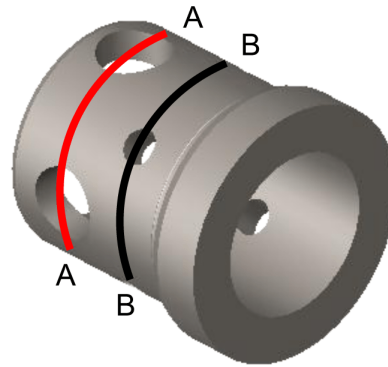
Figure 5.11: Identification of the two reference slices along the cage
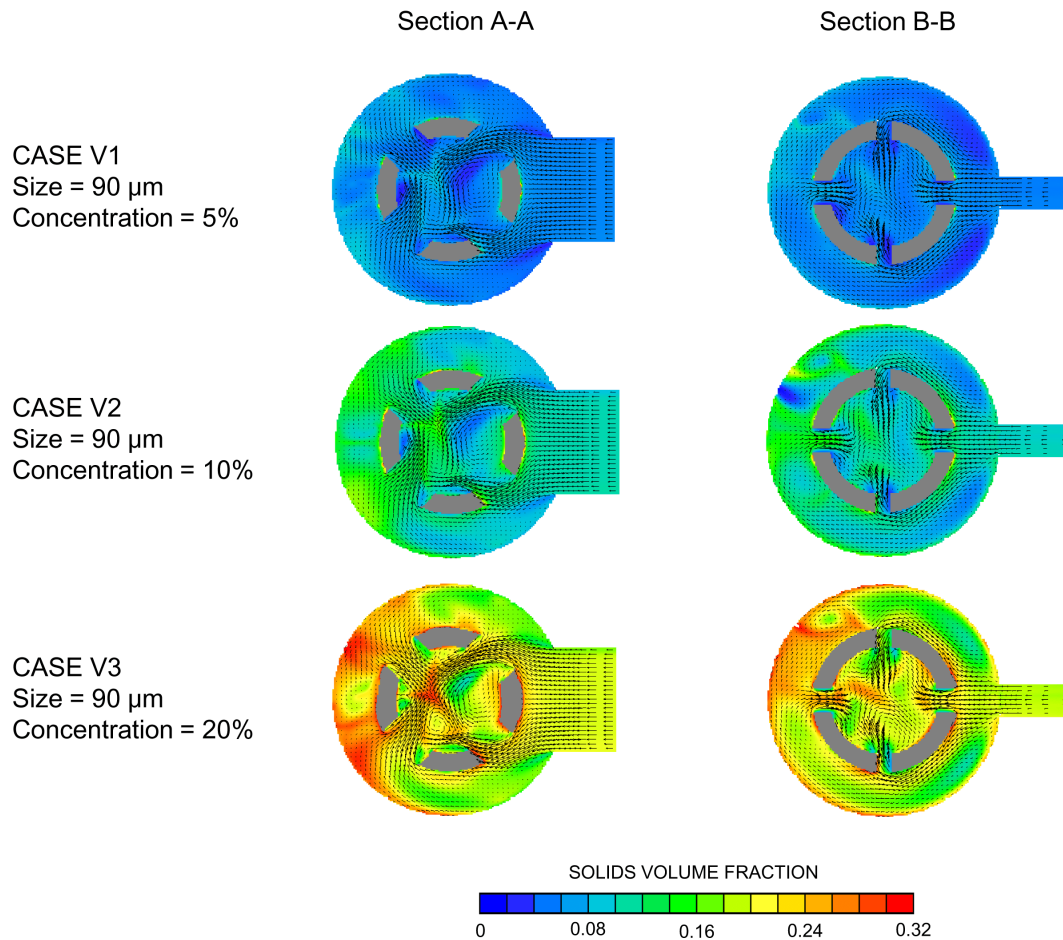
Figure 5.12: Solids volume fraction distribution and velocity vectors of the solid phase along slices A-A and B-B in Figure 5.11. Effect of the mean delivered solids concentration for the same kind of particles (cases V1 to V3 in Table 5.2)
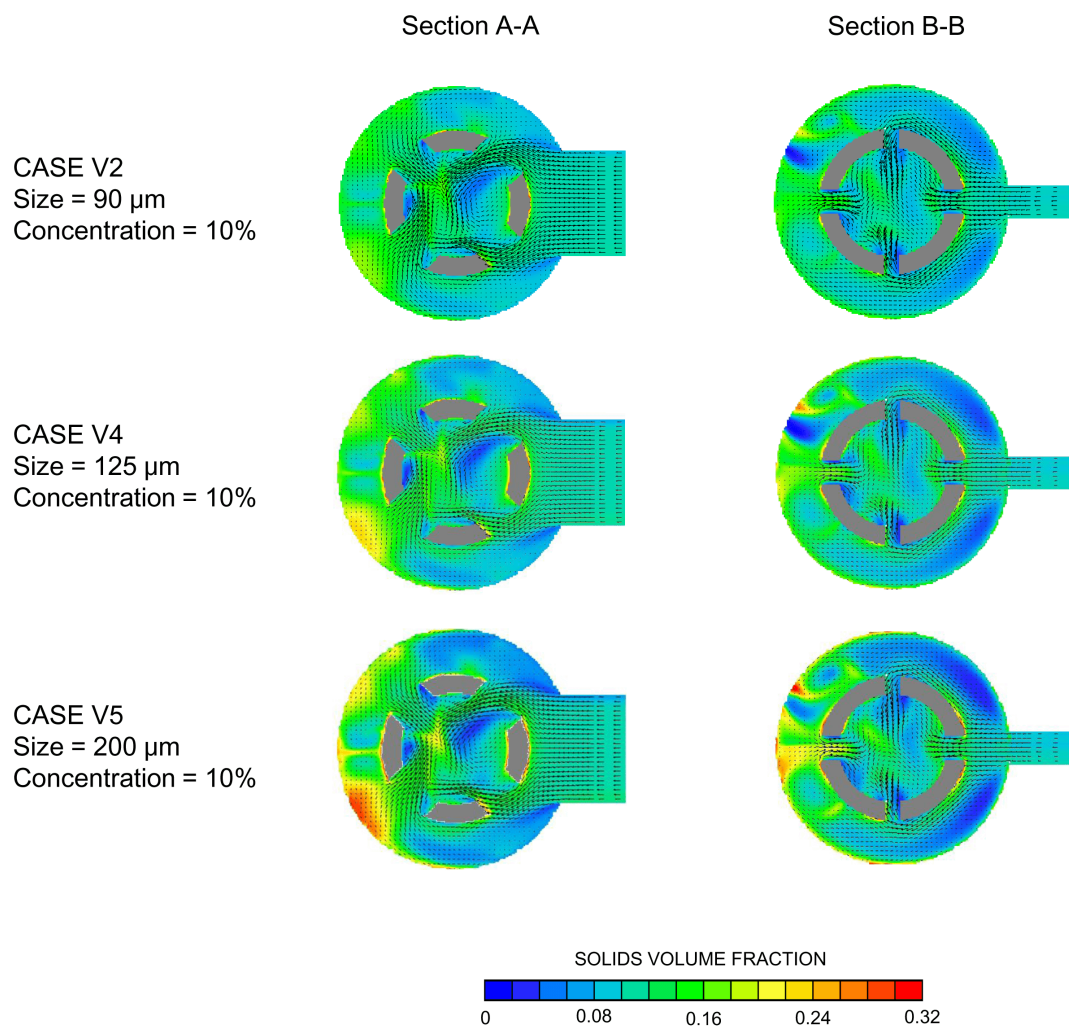
Figure 5.13: Solids volume fraction distribution and velocity vectors of the solid phase along slices A-A and B-B in Figure 5.11. Effect of particle size for the same solids loading (cases V1, V4, and V5 in Table 5.2)

Figure 5.12, which shows the solids volume fraction distribution and the velocity vectors of the solids phase on the two slices for the same particles (size = 90 μm) at different mean delivered concentration (5%, 10%, and 20%). Despite the fact that a two-dimensional plot may not be fully representative of a highly three-dimensional flow, the results seem to confirm that these small sized particle are likely to follow the jets but, being affected by turbulent dispersion, enter also the recirculation regions. As already noticed, the highest solids volume fraction occurs in the regions where the jets collide, both within the cage, and within the chamber surrounding it. The effect of particle size at a given solids loading is analyzed in Figure 5.13, which displays the the solids volume fraction distribution and the velocity vectors of the solids phase on the two slices for different particle size (90, 125, and 200 μm) at mean delivered solids concentration of 5%. Due to their higher inertia, the bigger particles appear less affected by turbulent dispersion which tends to produce a uniform solids concentration distribution. As a consequence, higher gradients are observed as the particle size increases.

Chapter 6

Conclusion and future developments

In this thesis a mathematical model for the simulation of turbulent solid-liquid flows in internal systems is proposed. This thesis is mainly addressed to the oil industry, with particular reference to the problems of flow regulation by the wellhead choke valves when a large amount of solids is present in the flow. However, turbulent solid-liquid internal flows and encountered in other engineering fields, such as mining and chemical, in which the proposed model could be applied. Slurry pipelines, fluidized beds, stirred tanks, and the systems for the production of hydrogen and nitrogen are worth mentioning in this context.

The need for a new model arises from the observation that the traditional approaches to the investigation of solid-liquid flows are not easily applicable to the complex flows addressed by this thesis. Despite being very expensive, experimental tests can encounter considerable technical difficulties, especially in determining local values of solids concentration and velocity. For dense mixtures they are essentially limited to straight pipe flows, while simple hydraulic singularities have been tested only for very low particle loading. Simplified physically-based models are a powerful tool for estimating some parameters in simple flows, but their application-specific formulation renders them unsuitable for use in case of more complex flows. Due to its versatility, Computational Fluid Dynamics (CFD) has been a commonly-used approach in recent years. The CFD models are classified in two main groups, which rely either on tracking each single particle or interpreting both phases as interpenetrating continua. Models of the former group require considerable computer time and are essentially limited to rather dilute flows; those of the latter, often referred to as *two-fluid* models, are actually the only possible way to simulate dense flows. However, even for pipe flows, the existing two-fluid models appear to be unstable numerically and computationally expensive. These features may not preclude their use for specific applications (like pipe flows) but makes really difficult, and even impossible, their employment for simulating complex geometries.

The mathematical model proposed in this thesis is a *two-fluid* one. The model solves a double-averaged formulation of the mass and momentum conservation equations for both phases, coupled by means of interfacial momentum transfer terms. The model is robust and numerically stable, and requires rather low computer time to procure converged solution. These features, which make it particularly attractive for the applications, arise

from the peculiar way in which the key physical mechanisms governing solid-liquid flows are modeled. To account for turbulent dispersion of particles, phase diffusion terms have been included in the phase continuity equations, together with all the conservation equations. To model the effect of multiple particles, an expression for the mixture viscosity is used to define the particle Reynolds number, which in turn appears in the drag coefficient correlation. The asymptotic behaviour of the mixture viscosity sets an upper limit to the solids concentration, preventing the particles from over-packing. This avoids the need to introduce a collisional pressure term in the momentum equation of the solid phase, further contributing to the stability of the model. Turbulence in the fluid phase is represented by means of eddy-viscosity based models specifically derived for two-phase flows.

The development of the model is divided in three steps. At first, the turbulent flow of solid-liquid mixtures in horizontal pipes is considered (Chapter 3). Besides of being of interest for the applications, this benchmark case allows verifying the performance of the model by comparison to both a large dataset of experimental measurements from open literature and the predictions of the existing two-fluid models. The new model proved suitable for predicting the main features of the flow under fully-suspended flow conditions over a wide range of variability of the significant parameters involved. Compared to the existing models, the proposed one appears capable to provide results with the same accuracy requiring low computer time.

Afterwards, the model is applied to a simple hydraulic singularity, which is a sudden expansion in a horizontal rectangular duct (Chapter 4). The lack of experimental data for this benchmark case, due to the technical difficulties in performing the measurements, doesn't allow comparing computations with measurements. A sensitivity analysis revealed that some of the terms which proved ineffective for pipe flows, such as the lift force, could be significant for this more complex flow. The literature available about analogous flows, even if not in complete similarity with the specific benchmark considered, allows verifying the phenomenological consistency of the numerical solution. A parameteric analysis, focused on the effect of increasing the solids loading and the particle size, allowed investigating the way in which the particle response to the flow and gravity combine in determining the development of the flow. After establishing the conditions under which the flow can be regarded as essentially two-dimensional, the temporal evolution of the system was briefly explored by running unsteady simulations.

At last, the model is applied to a complex geometry of engineering interest, which is a wellhead choke valve for oil & gas applications (Chapter 5). In order to dispose of experimental measurements collected in previous campaigns, at this stage of the work water is taken as the carrier fluid and the flow within the valve is assumed turbulent. Starting from the single-phase flow case, validated with respect to the experimental data, the effect of the presence of sand particles is studied, focusing on the influence of delivered solids concentration and particle size on the dissipation and regulation characteristics of the device, and providing useful guidelines to designers. The model proved robust and stable also for the valve case in which these features are really fundamental.

Future research may include both modeling and application enhancements. The implementation of alternative closures, for example those derived from the Kinetic Theory of Granular Flows, may improve the quality of the model, making it capable to described all the physical mechanisms governing turbulent solid-liquid flows separately in the light of a more sophisticated theoretical background. A very ambitious aim could be the development of equations to model the contact stresses which characterize bed flows, in order to reproduce the accumulation of solid particles. Anyway, developments of the two-fluid model must preserve its peculiar stability and ease to attain a converged solution. In this context, the extension of the model to laminar flows is expected to be a not straighforward task, as it implies the removal of the phase diffusion fluxes which contributes significantly to the stability of the model. The temporal evolution of the flow, explored briefly in this thesis, could be addressed more deeply in future works, due to its significancy for a better understanding of the behavior of the system and for many engineering processes. Application-aimed development concern the use of the two-fluid model in conjunction with erosion models, in order to predict the erosion rate in pipeline fittings and other devices, like stirred tanks. Moreover, the model could be employed to better handle the CHOPS processes starting from the brief exploration provided in this thesis, as well as be applied to devices of engineering interest, like control valves for slurry flows.

Appendix A

The drag coefficient on a sphere in an infinite medium

The drag coefficient on a single sphere in an infinite medium is expressed as a function of the particle Reynolds number $\mathrm{Re}_p = \rho_c |\mathbf{u}_r| d_p / \mu_c$, being ρ_c the density of the fluid, $\mathbf{u}_r$ the relative velocity between the particle and the surrounding fluid, d_p the particle size, and μ_c the viscosity of the fluid.

As Re_p increases, different regimes can be identified [26]: a Stokes regime ($\mathrm{Re}_p \to 0$), in which $C_{d,s} = 24/\mathrm{Re}_p$; an intermediate regime; a constant drag coefficient regime ($700 < \mathrm{Re}_p < 2 \cdot 10^5$). At $\mathrm{Re}_p \approx 3.5 \cdot 10^5$ separation occurs, causing a sudden drop of $C_{d,s}$. The trend of $C_{d,s}$ as a function of Re_p is usually referred as *standard drag curve* [26]. Different empirical or semiempirical expressions have been proposed to approximate this curve [21, 26, 44]. A selection of the most commonly-used is reported below.

1. SCHILLER and NAUMANN

$$C_{d,s} = \begin{cases} 24 \left(1 + 0.15 \mathrm{Re}_p^{0.687}\right)/\mathrm{Re}_p & \text{if } \mathrm{Re}_p \leq 1000 \\ 0.44 & \text{if } \mathrm{Re}_p > 1000 \end{cases} \tag{A.1}$$

2. ABRAHAM $\left[\mathrm{Re}_p < 6 \cdot 10^3\right]$:

$$C_{d,s} = 0.2924 \left(1 + \frac{9.06}{\mathrm{Re}_p^{1/2}}\right)^2 \tag{A.2}$$

3. BRAUER $\left[\mathrm{Re}_p < 3 \cdot 10^5\right]$:

$$C_{d,s} = 0.40 + \frac{4}{\mathrm{Re}_p^2} + \frac{24}{\mathrm{Re}_p} \tag{A.3}$$

4. CHENG [21] $\left[\mathrm{Re}_p < 2 \cdot 10^5\right]$:

$$C_{d,s} = \frac{24}{\mathrm{Re}_p} \left(1 + 0.27 \mathrm{Re}_p\right)^{0.43} + 0.47 \left[1 - \exp\left(-0.04 \mathrm{Re}_p^{0.38}\right)\right] \tag{A.4}$$
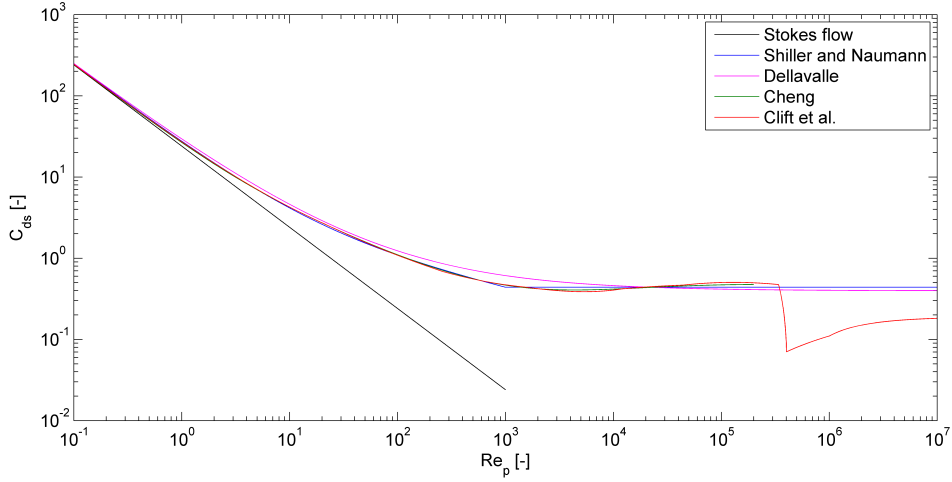
Figure A.1: Drag coefficient of a sphere as a function of the particle Reynolds number according to the correlations of Shiller and Naumann (Eq. A.1), Dellavalle (Eq. A.5), Cheng (Eq. A.4) and Clift *et al.*. The analytical solution for Stokes flow, $C_{d,s} = 24/\mathrm{Re}_p$, is depicted too

5. DELLAVALLE

$$C_{d,s} = \left(0.63 + 4.8 \sqrt{\frac{1}{\mathrm{Re}_p}} \right)^2 \tag{A.5}$$

6. IHME *et al.* $\left[\mathrm{Re}_p < 10^4 \right]$:

$$C_{d,s} = 0.36 + \frac{5.48}{\mathrm{Re}_p^{0.573}} + \frac{24}{\mathrm{Re}_p} \tag{A.6}$$

7. LAPPLE $\left[\mathrm{Re}_p < 10^3 \right]$:

$$C_{d,s} = \frac{24}{\mathrm{Re}_p} \left(1 + 0.125 \mathrm{Re}_p^{0.72} \right) \tag{A.7}$$

8. GILBERT *et al.* $\left[0.2 < \mathrm{Re}_p < 2 \cdot 10^3 \right]$:

$$C_{d,s} = 0.48 + 28 \mathrm{Re}_p^{-0.85} \tag{A.8}$$

9. KURTEN *et al.* $\left[0.1 < \mathrm{Re}_p < 4 \cdot 10^3 \right]$:

$$C_{d,s} = 0.28 + \frac{6}{\mathrm{Re}_p^{1/2}} + \frac{21}{\mathrm{Re}_p} \tag{A.9}$$

10. CLIFT *et al.* [26] developed a complex correlation in which the whole range of particle Reynolds number is divided in 10 subintervals, with a disting correlation for each interval. Their model accounts also for the sudden reduction of the drag coefficient due to separation.

The above mentioned models are reported in Figure A.1. The values of $C_{d,s}$ predicted by the correlations are rather close to each other before the occurrence of separation. The Stokes flow limit behavior, $C_{d,s} \to 24/\mathrm{Re}_p$ for $\mathrm{Re}_p \to 0$, is satisfied by all curves.

Appendix B

The apparent viscosity of a mixture

The effect of particles in a fluid is often accounted for by reference to an apparent viscosity of the whole mixture μ_m. Despite some attempts to derive theoretically the apparente viscosity of a very dilute mixture have been reported [22, 44], in most cases μ_m is evaluated by means of empirical formulas, in which the relative viscosity, i.e. the ratio of the viscosity of the mixture to that of the fluid phase μ_c is expressed as a function of the solid volume fraction α_p. Reviews of the available correlations have been reported by many Authors [10, 22, 44, 96, 101, 121, 133, 146]. The correlations, whose authorship is often uncertain, can be classified according to their range of applicability in terms of solid volume fraction α_p. The following formulas, displayed in Fig. B.1 (a), can be used only for very dilute suspensions:

1. EINSTEIN $[\alpha_p \to 0]$

$$\mu_m = \mu_c \left(1 + 2.5\alpha_p\right) \tag{B.1}$$

2. BRINKMAN [1] $[\alpha_p \to 0]$

$$\mu_m = \mu_c \left(1 - \alpha_p\right)^{-2.5} \tag{B.2}$$

3. GUTH and SIMHA $[0 \le \alpha_p \le 0.08]$

$$\mu_m = \mu_c \left(\frac{1 + 0.5\alpha_p - 0.5\alpha_p^2}{1 - 2\alpha_p - 9.6\alpha_p^2}\right) \tag{B.3}$$

Other correlations, depicted in Fig. B.1 (b), covers the whole range of particle concentrations:

1. EILERS [2] $[2.5 \le [\eta] \le 3.0, 0.58 \le \alpha_{\max} \le 0.60]$

$$\mu_m = \mu_c \left[1 + \frac{[\eta]\,\alpha_p}{2\left(1 - \alpha_p/\alpha_{\max}\right)}\right]^2 \tag{B.4}$$

---

[1] Also attributed to Roscoe

[2] Also attributed to Chong *et al.*, Leighton and Acrivos, and Wildemuth and Williams
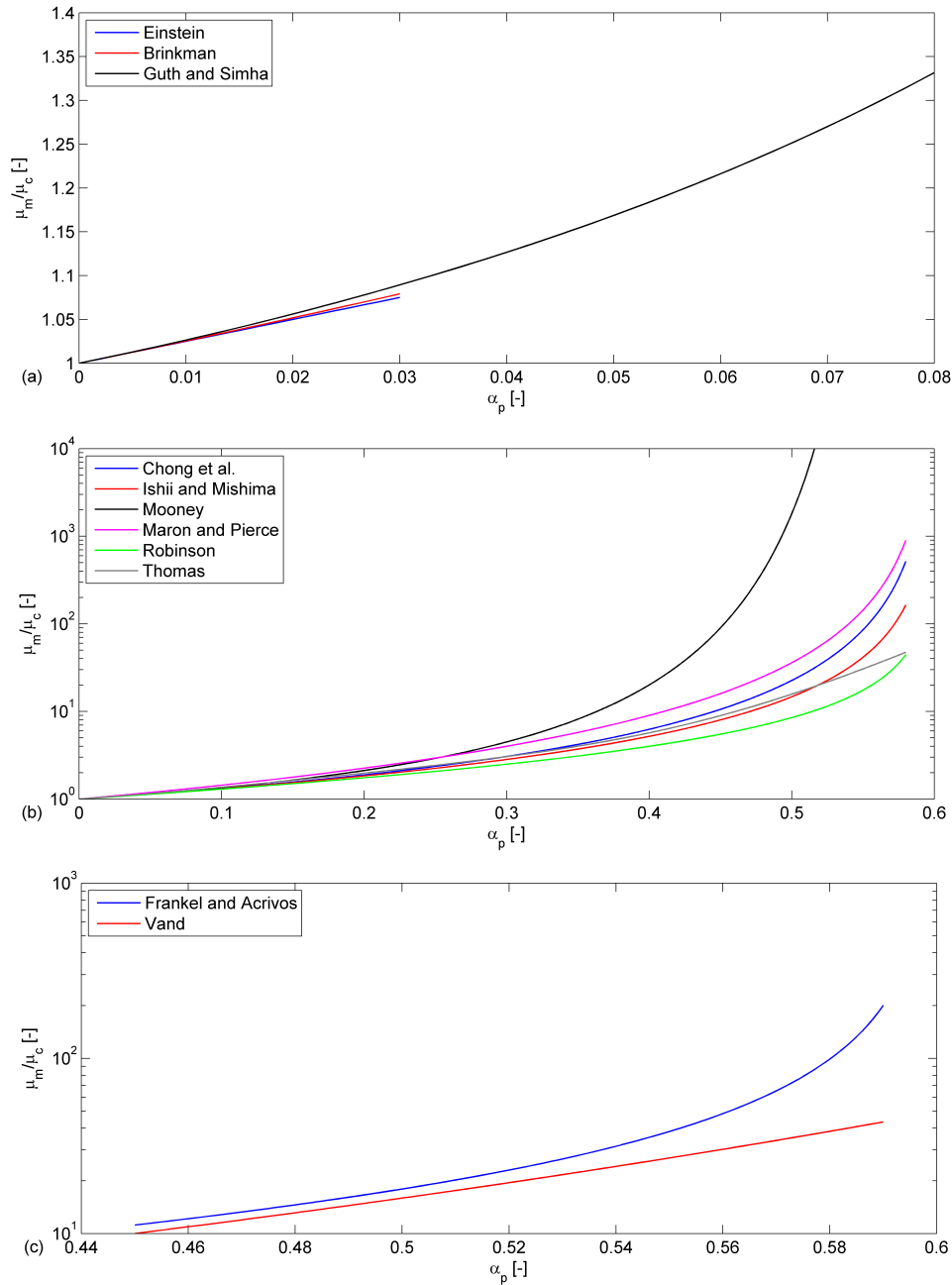
Figure B.1: Relative viscosity μ_m/μ_c as a function of the solid volume fraction α_p according to different literature correlations with maximum packing concentration $\alpha_{\max}$ and intrinsic viscosity $[\eta]$ equal to 2.5 and 0.60 respectively. Correlations for: (a) dilute suspensions (b) the entire range of particle concentrations (c) dense suspensions

2. ISHII and MISHIMA [3] $[2.50 \leq [\eta] \leq 3.13, 0.62 \leq \alpha_{\max} \leq 0.71]$

$$\mu_m = \mu_c \left(1 - \frac{\alpha_p}{\alpha_{\max}} \right)^{-[\eta]\alpha_{\max}} \tag{B.5}$$

3. MARON and PIERCE [4]

$$\mu_m = \mu_c \left(1 - \frac{\alpha_p}{\alpha_{\max}} \right)^{-2} \tag{B.6}$$

4. MOONEY $[[\eta] = 2.5, 0.52 \leq \alpha_{\max} \leq 0.74]$

$$\mu_m = \mu_c \exp \left(\frac{[\eta]\,\alpha_p}{1 - \alpha_p/\alpha_{\max}} \right) \tag{B.7}$$

5. ROBINSON

$$\mu_m = \mu_c \left(1 + \frac{[\eta]\,\alpha_p}{1 - \alpha_p/\alpha_{\max}} \right) \tag{B.8}$$

6. THOMAS

$$\mu_m = \mu_c \left[1 + 2.5\alpha_p + 10.05\alpha_p^2 + 0.00273\exp\left(16.6\alpha_p \right) \right] \tag{B.9}$$

At last, some Authors focused on very dense suspensions only, developing the following formulas, shown in Fig. B.1 (c):

1. FRANKEL and ACRIVOS

$$\mu_m = \mu_c \frac{9}{8} \left[\frac{(\alpha_p/\alpha_{\max})^{1/3}}{1 - (\alpha_p/\alpha_{\max})^{1/3}} \right] \tag{B.10}$$

2. VAND

$$\mu_m = \mu_c \exp \left(\frac{2.5\alpha_p + 2.7\alpha_p^2}{1 - 0.609\alpha_p} \right) \tag{B.11}$$

Most expressions depend upon empirical constants often treated as calibration parameters, like the maximum packing concentration $\alpha_{\max}$ and the intrinsic viscosity $[\eta]$. The former accounts for shape and size distributions of the particles as well as shear rate [121]; it usually lies in the range $0.60 \div 0.75$, but lower values have been considered for either small [96] or highly irregularly shaped [136] particles. Liu [96] developed a method for the experimental estimation of the maximum packing concentration for ceramic suspensions. The intrinsic viscosity $[\eta]$ accounts for particle shapes. A value of 2.5 has been well documented in literature for spherical particles [122], but higher values have been considered for natural sands [123]. Penko *et al.* [122] performed a sensitivity analysis of sandy bedform dynamics upon $[\eta]$ in the range $2.5 \div 5.0$. It is worth notice

---

[3]Also attributed to Barnes *et al.*, and Krieger and Dougherty
[4]Also attributed to Quemada

that, despite the differences in the analytical formulation of the correlations reported in Fig. B.1 (b) , it seems actually possible to switch from one to another simply by changing the calibration parameters $[\eta]$ and α_{max}. Starting from this consideration, Cheng and Law [22] managed to approximate many of them by a formula depending on a single calibration parameter.

Appendix C

Performance of the Wasp model

In slurry pipes, the transition from fully-suspended to moving-bed flows is identified by a minimum in the curve of pressure gradient versus superficial velocity (Figure 3.2), which corresponds to a threshold value of superficial velocity, referred to as *deposition velocity*. The formula of Wasp, reported below, gives an a priori estimate of the deposition velocity.

$$V_3 = 4 \, (d_p/D_p)^{1/6} \, C^{1/5} \sqrt{2gD_p \left(\frac{\rho_p}{\rho_c} - 1 \right)}$$

where:
V_3	=	deposition velocity
d_p	=	particle size
D_p	=	pipe diameter
C	=	mean solids concentration
g	=	gravitational acceleration
ρ_c	=	fluid density
ρ_p	=	particle density

In order to check the predictive capacity of the Wasp model, the values of the deposition velocity obtained by the earlier equation are superimposed to the experimentally determined pressure gradient versus superficial velocity curves obtained by different authors [53, 103, 104, 135, 136]. Although the minimum in the experimental curve is not always clearly detectable, the results, reported below, indicate that the Wasp formula can provide rough estimate of the deposition velocity. In particular, the model appears likely to underestimate the deposition velocity.
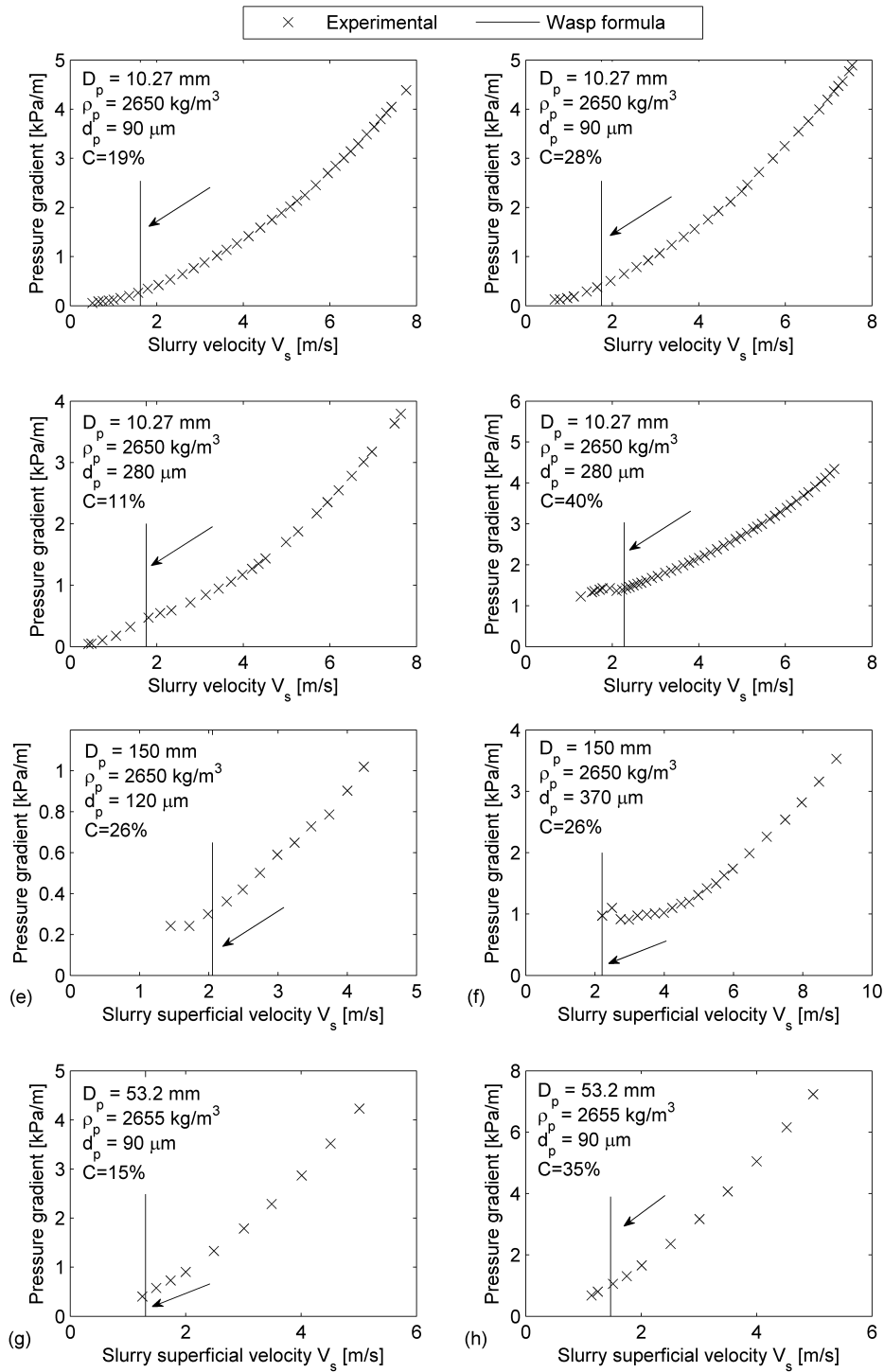
Figure C.1: Experimentally determined curves of pressure gradient versus slurry superficial velocity and predicted deposition velocity according to the model of Wasp
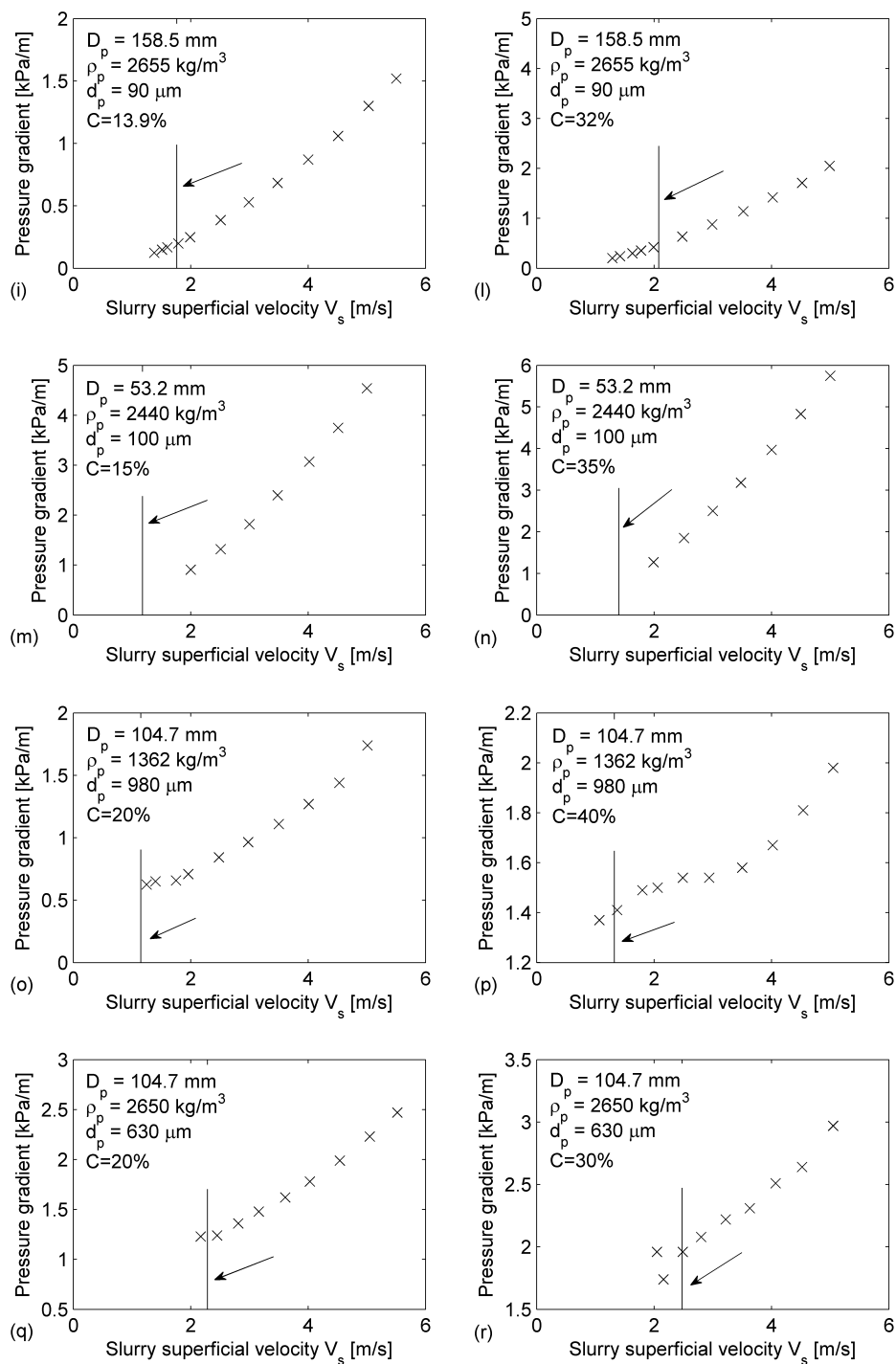
Figure C.1: (*continued*)

Appendix D

The equations of the proposed model

This appendix reports all the equations of the new two-fluid model.

1. MASS CONSERVATION FOR PHASE k ($k = c, p$)

$$\frac{\partial}{\partial t}\left(\alpha_k \rho_k\right) + \nabla \cdot \left(\alpha_k \rho_k \mathbf{u}_k - \rho_k \frac{\nu_c^t}{\sigma_\alpha} \nabla \alpha_k\right) = 0$$

where: $\begin{aligned}
\alpha_k &= \text{volume fraction} \\
\rho_k &= \text{density} \\
\mathbf{u}_k &= \text{velocity} \\
\nu_c^t &= \text{eddy viscosity of the fluid} \\
\sigma_\alpha &= \text{turbulent Schmidt number for volume fractions}
\end{aligned}$

2. FLUID PHASE MOMENTUM EQUATION

$$\frac{\partial}{\partial t}\left(\alpha_c \rho_c \mathbf{u}_c\right) + \nabla \cdot \left(\alpha_c \rho_c \mathbf{u}_c \mathbf{u}_c\right) = -\alpha_c \nabla p +$$

$$+ \nabla \cdot \left[\alpha_c \left(\boldsymbol{T}_c + \boldsymbol{T}_c^t\right)\right] + \alpha_c \rho_c \mathbf{g} + \mathbf{M}_c^d + \nabla \cdot \left(\rho_c \mathbf{u}_c \frac{\nu_c^t}{\sigma_\alpha} \nabla \alpha_c\right)$$

where: $\begin{aligned}
p &= \text{pressure} \\
\boldsymbol{T}_c &= \text{viscous stress tensor } (= 2\rho_c \nu_c \boldsymbol{D}_c) \\
\boldsymbol{T}_c^t &= \text{pseudo-turbulent stress tensor } (= 2\rho_c \nu_c^t \boldsymbol{D}_c) \\
\nu_c &= \text{kinematic viscosity coefficient of the fluid} \\
\boldsymbol{D}_c &= \text{deformation tensor of the fluid } (= 0.5\left[\nabla \mathbf{u}_c + (\nabla \mathbf{u}_c)^+\right]) \\
g &= \text{gravitational acceleration} \\
\mathbf{M}_c^d &= \text{generalized drag}
\end{aligned}$

3. SOLID PHASE MOMENTUM EQUATION

$$\frac{\partial}{\partial t}\left(\alpha_p \rho_p \mathbf{u}_p\right) + \nabla \cdot \left(\alpha_p \rho_p \mathbf{u}_p \mathbf{u}_p\right) = -\alpha_p \nabla p +$$

$$+ \nabla \cdot \left(\alpha_c \boldsymbol{T}_c^t\right) + \nabla \left(\alpha_p \rho_p \nu_p^t \nabla \mathbf{u}_p\right) + \alpha_p \rho_p \mathbf{g} - \mathbf{M}_c^d + \nabla \cdot \left(\rho_p \mathbf{u}_p \frac{\nu_c^t}{\sigma_\alpha} \nabla \alpha_c\right)$$

where: $\boldsymbol{T}_p^t$ =   pseudo-turbulent stress tensor $(= 2\rho_p \nu_p^t \boldsymbol{D}_p)$

         ν_p^t =   particle eddy viscosity

         $\boldsymbol{D}_p$ =   deformation tensor of the fluid $(= 0.5 \left[\nabla \mathbf{u}_p + (\nabla \mathbf{u}_p)^+\right])$

4. EDDY VISCOSITY OF THE FLUID

- Standard $k - \epsilon$ model

$$\nu_c^t = C_\mu \frac{k}{\epsilon}$$

$$\frac{\partial}{\partial t}\left(\alpha_c \rho_c k\right) + \nabla \cdot \left(\alpha_c \rho_c k \mathbf{u}_c\right) = \nabla \cdot \left[\alpha_c \rho_c \left(\nu_c + \frac{\nu_c^t}{\sigma_k}\right) \nabla k\right] +$$

$$+ \nabla \cdot \left(\rho_c \frac{\nu_c^t}{\sigma_\alpha} k \nabla \alpha_c\right) + \alpha_c \rho_c \left(P_k - \epsilon\right)$$

$$\frac{\partial}{\partial t}\left(\alpha_c \rho_c \epsilon\right) + \nabla \cdot \left(\alpha_c \rho_c \epsilon \mathbf{u}_c\right) = \nabla \cdot \left[\alpha_c \rho_c \left(\nu_c + \frac{\nu_c^t}{\sigma_\epsilon}\right) \nabla \epsilon\right] +$$

$$\nabla \cdot \left(\rho_c \frac{\nu_c^t}{\sigma_\alpha} \epsilon \nabla \alpha_c\right) + \alpha_c \rho_c \frac{\epsilon}{k} \left(C_{1\epsilon} P_k - C_{2\epsilon} \epsilon\right)$$

where: k =   turbulent kinetic energy

        ϵ =   turbulence dissipation rate

        P_k =   volumetric production of turbulence $(= 2\nu_c^t \boldsymbol{D}_c : \nabla \mathbf{u}_c)$

        C_μ =   model constant $(= 0.09)$

        σ_k =   model constant $(= 1.0)$

        σ_ϵ =   model constant $(= 1.314)$

        $C_{1\epsilon}$ =   model constant $(= 1.44)$

        $C_{2\epsilon}$ =   model constant $(= 1.92)$

- $k - \epsilon$ RNG model

$$\nu_c^t = C_\mu \frac{k}{\epsilon}$$

$$\frac{\partial}{\partial t}\left(\alpha_c \rho_c k\right) + \nabla \cdot \left(\alpha_c \rho_c k \mathbf{u}_c\right) = \nabla \cdot \left[\alpha_c \rho_c \left(\nu_c + \frac{\nu_c^t}{\sigma_k}\right) \nabla k\right] +$$

$$+ \nabla \cdot \left(\rho_c \frac{\nu_c^t}{\sigma_\alpha} k \nabla \alpha_c\right) + \alpha_c \rho_c \left(P_k - \epsilon\right)$$

$$\frac{\partial}{\partial t}\left(\alpha_c\rho_c\epsilon\right) + \nabla \cdot \left(\alpha_c\rho_c\epsilon\mathbf{u}_c\right) = \nabla \cdot \left[\alpha_c\rho_c\left(\nu_c + \frac{\nu_c^t}{\sigma_\epsilon}\right)\nabla\epsilon\right] +$$

$$\nabla \cdot \left(\rho_c\frac{\nu_c^t}{\sigma_\alpha}\epsilon\nabla\alpha_c\right) + \alpha_c\rho_c\frac{\epsilon}{k}\left[C_{1\epsilon}P_k - C_{2\epsilon}\epsilon - \frac{C_\mu\eta^3\left(1 - \eta/\eta_0\right)}{1 + \beta\eta^3}\epsilon\right]$$

where:
σ_k	$=$	model constant ($= 0.7194$)
σ_ϵ	$=$	model constant ($= 0.7194$)
$C_{1\epsilon}$	$=$	model constant ($= 1.44$)
$C_{2\epsilon}$	$=$	model constant ($= 1.92$)
η	$=$	Sk/ϵ
S	$=$	$\sqrt{2\boldsymbol{D}_c : \boldsymbol{D}_c}$
η_0	$=$	model constant ($= 4.38$)
β	$=$	model constant ($= 0.012$)

5. PARTICLE EDDY VISCOSITY

- Base model

$$\nu_p^t = \nu_c^t$$

- Chen and Wood model

$$\nu_p^t = \nu_c^t\left(1 + \frac{\tau_p}{\tau_{li}}\right)^{-1}$$

where:
τ_p	$=$	particle response time $\left(= \dfrac{\left(\rho_p + C_{vm}\rho_c\right)d_p^2}{18\rho_c\nu_c\left(1 + 0.15\mathrm{Re}_p^{0.687}\right)}\right)$
C_{vm}	$=$	virtual mass coefficient ($= 0.5$)
Re_p	$=$	particle Reynolds number ($= \rho_p d_p|\mathbf{u}_p - \mathbf{u}_c|\mu_m$)
d_p	$=$	particle size
μ_m	$=$	viscosity of the mixture $\left(= \rho_c\nu_c\exp\left(\dfrac{[\eta]\,\alpha_p}{1 - \alpha_p/\alpha_{\max}}\right)\right)$
$[\eta]$	$=$	intrinsic viscosity ($= 2.5$)
$\alpha_{\max}$	$=$	maximum packing concentration ($= 0.7$)
τ_{li}	$=$	lagrangian integral time scale ($= 0.165k/\epsilon$)

6. GENERALIZED DRAG

$$\mathbf{M}_c^d = \frac{6\alpha_p}{\pi d_p^3}\left(\mathbf{F}_d + \mathbf{F}_l + \mathbf{F}_{vm}\right)$$

- Drag force

$$\mathbf{F}_d = \frac{1}{2}\left(\pi\frac{d_p^2}{4}\right)C_d\rho_c|\mathbf{u}_p - \mathbf{u}_c|\left(\mathbf{u}_p - \mathbf{u}_c\right)$$

$$C_d = \begin{cases} 24\left(1 + 0.15\mathrm{Re}_p^{0.687}\right)/\mathrm{Re}_p & \text{if } \mathrm{Re}_p \leq 1000 \\ 0.44 & \text{if } \mathrm{Re}_p > 1000 \end{cases}$$

- Lift force

$$\mathbf{F}_l = C_l\rho_c d_p^3\left(\mathbf{u}_p - \mathbf{u}_c\right)\times\left(\nabla\times\mathbf{u}_c\right)$$

where: C_l =   lift coefficient $(= 0.5)$

- Virtual mass force

$$\mathbf{F}_{vm} = \left(\frac{4}{3}\pi\frac{d_p^3}{8}\right)C_{vm}\rho_c\left(\frac{\mathrm{d}\mathbf{u}_c}{\mathrm{d}t} - \frac{\mathrm{d}\mathbf{u}_p}{\mathrm{d}t}\right)$$

7. WALL BOUNADRY CONDITIONS

- Equilibrium log law for smooth walls

$$\frac{u_{c,P}}{\sqrt{\tau_{w,c}/\rho_c}} = \frac{1}{\kappa}\ln\left[Ey_P\frac{\sqrt{\tau_{w,c}/\rho_c}}{\nu_c}\right]$$

$$\frac{u_{p,P}}{\sqrt{\tau_{w,p}/\rho_p}} = \frac{1}{\kappa}\ln\left[Ey_P\frac{\sqrt{\tau_{w,p}/\rho_p}}{\nu_c}\right]$$

$$k_P = \frac{\tau_{w,c}/\rho_c}{\sqrt{C_\mu}}$$

$$\epsilon_P = C_\mu^{3/4}\frac{k_P^{3/2}}{\kappa y_P}$$

where: $u_{k,P}$ =   absolute velocity of phase k parallel to the wall at the first
                          grid node
          $\tau_{w,k}$ =   wall shear stress of phase k
          k_P =   turbulent kinetic energy at the first grid node
          κ =   von Karman constant $(= 0.41)$
          E =   roughness parameter $(= 8.6$ for smooth walls$)$
          y_P =   normal distance of the first grid point from the wall
          ϵ_P =   turbulence dissipation rate at the first grid node

- Non-equilibrium log law for smooth walls

$$\frac{u_{c,P}\sqrt{k_P}}{\tau_{w,c}/\rho_c} = \frac{1}{\kappa C_\mu^{1/4}}\ln\left(EC_\mu^{1/4}\frac{y_P}{\nu_c}\right)$$

$$\frac{u_{p,P}\sqrt{k_P}}{\tau_{w,p}/\rho_p} = \frac{1}{\kappa C_\mu^{1/4}}\ln\left(EC_\mu^{1/4}\frac{y_P}{\nu_c}\right)$$

$$\epsilon_P = C_\mu^{3/4}k_P^{3/2}\frac{\ln\left(EC_\mu^{1/4}\sqrt{k_P}y_P/\nu_c\right)}{2\kappa y_P}$$

The turbulent kinetic energy k_P is obtained from its own transport equation with the diffusion of energy to the wall being set to zero. This transport equation contains the production rate P_k and the dissipation rate ϵ, and the average rates of these two terms for the near-wall cell are determined by making an analytical integration over the control volume and assuming that the shear stress and k The mean value of turbulence energy production over the near-wall cell is represented as:

$$P_{k,P} = \frac{\tau_{w,c}u_{c,P}}{2\rho_c y_P}$$

Appendix E

Early developments of the model

The proposed two-fluid model, whose equations are summarized in Appendix D, proved suitable for application to fully-suspended flows, i.e. when turbulence is effective in keeping all the solids suspended. On the other side, the model cannot reproduce the long-lasting contact stresses which characterize particle accumulation, therefore it is not capable to simulate bed flows. The development of a proper description of these stresses is a significant task of researchers, since none of the existing two-fluid models proved to have unquestionably managed this issue [17, 75]. The few models available are either based on a global formulation [105, 121], therefore unsuitable for implementation in a CFD code, or very application-specific [126].

In order to preliminarily address this matter from an engineering-applicative point of view, and focusing on horizontal pipe flows, it may be considered that different some physically-based models based on a global formulation [33, 35, 55, 106] allow estimating the pressure gradient under either fully-suspended or bed flow conditions with sufficient accuracy for many applications. Even if these models require the solution of several nonlinear algebraic equations, which is not always simple to perform, they are mathematically much simpler compared to a CFD model. Anyway, their global formulation makes them unsuitable for predicting the solids concentration distribution, which requires the development and validation of distributed models.

It is precisely this feature which has been the focus of the earlier developments of the two-fluid model. The sensitivity analysis described in Section 3.4 allows concluding that the free slip boundary condition to the solid phase yelds consistent underestimation of the pressure gradient and an unphysical prediction of the mixture velocity profile. The equilibrium log law of Launder and Spalding [91] for smooth walls allowed overcoming this limiation, and proved suitable for estimating the mechanical contribution to friction in case of fully-suspended flows. However, the comparison of the numerical predictions to the experimental data for the large dataset of flow conditions reported in Table 3.3 revealed that the imposition of the free slip condition has a positive effect on the predicted solids concentration profile, which seems better estimated in case of moving-bed flows while no variation is observed in case of fully-suspended flow. The effect of the interfacial momentum transfer term, with the mixture viscosity that goes to infinity as the maximum packing concentration is approached, and the absence of the
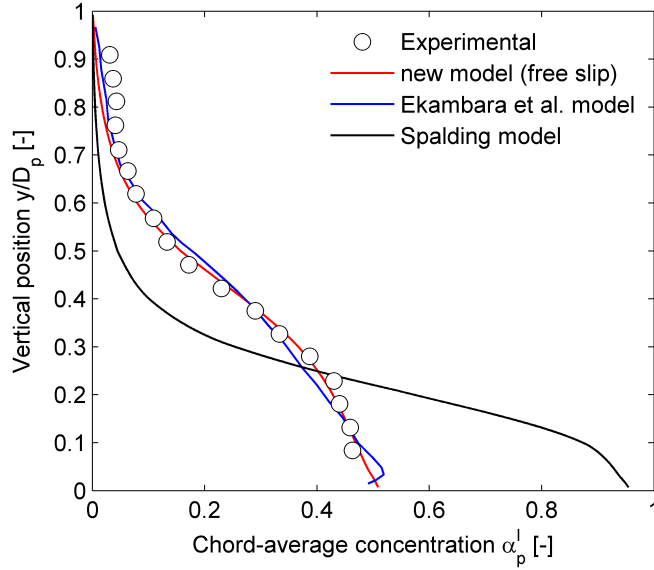
Figure E.1: Chord-average concentration versus vertical position: comparison between experimental data and the predictions of the proposed model (with the free slip boundary condition imposed to the solid phase at the pipe wall) and other two-fluid models for case P6 in Table 3.3

solution in the near wall region forcedly imposed by the equilibrium log law results in a better prediction of the solids concentration profile for moving-bed flows. Therefore, if the goal of the investigation is the estimation of the solids concentration profile only, it may be better to impose a free slip wall boundary condition to the solid phase, since this options procures a rather accurate prediction of this parameter over a wider range of operating conditions. Obviously, doing so, the model could not be used to predict the velocity profile and the pressure gradient.

An example of the performance of this *concentration-aimed* formulation of the two-fluid model is reported in Figure E.1, which compares the experimentally determined solids concentration profile for Case P6 in Table 3.3, reported by Roco and Shook[126], to the numerical predictions obtained by different two-fluid models, namely the KTGF-based model of Ekambara *et al.* [41], the model of Spalding [144], and the proposed model with the free slip condition applied to the solid phase. As already noticed in Section 3.5, for this specific case the flow pattern can only be inferred from shape of the solids concentration profile, which suggests flow with a moving bed. The degree of agreement to the experimental evidence is similar for the proposed model and that of Ekambara *et al.* [41], whilst that of Spalding [144] appears very inaccurate due to the absence of a drag correction for dense flows.

At this stage, the *concentration-aimed* two-fluid model may be used by designers to evaluate the solids concentration profile of slurries in horizontal pipes, under either fully-suspended or moving-bed flo conditions. At the same time, simplified physically-based models may be employed for the evaluation of the pressure gradient, until a suitable model for its numerical prediction will be developed.

Bibliography

[1] G. Ahmadi and Q. Chen. Dispersion and deposition of particles in a turbulent pipe flow with sudden expansion. *Journal of Aerosol Science*, 29:1097–1116, 1998.

[2] W.H. Ahmed, C.Y. Ching, and M. Shoukri. Pressure recovery of two-phase flow across sudden expansions. *International Journal of Multiphase Flow*, 33:575–594, 2007.

[3] S. P. Antal, R. T. Lahey, and J. E. Flaherty. Analysis of phase distribution in fully-developed laminar bubbly two-phase flow. *International Journal of Multiphase Flow*, 17:635–652, 1991.

[4] V. Armenio, U. Piomelli, and V. Fiorotto. Effect of the subgrid scales on particle motion. *Physics of Fluids*, 11:3030, 1999.

[5] A. Attou and L. Bolle. A New Correlation for the Two-Phase Pressure Recovery Downstream from a Sudden Enlargement. *Chemical Engineering and Technology*, 419-423:419–423, 1997.

[6] H.M. Badr, M.A. Habib, R. Ben-Mansour, and S.A.M. Said. Numerical investigation of erosion threshold velocity in a pipewith sudden contraction. *Computers & Fluids*, 34:721–742, 2005.

[7] H.M. Badr, M.A. Habib, R. Ben-Mansour, and S.A.M. Said. Erosion and penetration rates of apipeprotruded in a sudden contraction. *Computers & Fluids*, 37:146–160, 2008.

[8] D. Baha Albunaga. *Slurry systems handbook*. McGraw-Hill, 2002.

[9] R. Bakhtyar, D. A. Barry, A. Yeganeh-Bakhtiary, L. Li, J. Y. Parlange, and G. C. Sander. Numerical simulation of two-phase flow for sediment transport in the inner-surf and swash zones. *Advances in Water Resources*, 33:277–290, 2010.

[10] E. Barnea and J. Mizrahi. A Generalized Approach to the Fluid Dynamics of Particulate Systems Part 1. General Correlation for Fluidization and Sedimentation in Solid Multiparticle Systems. *The Chemical Engineering Journal*, 5:171–189, 1973.

[11] A.S. Bartosik. Influence of coarse-dispersive solid-phase on the "particle-wall" shear stress in turbulent slurry flow with high solid concentration. *The Archive of Mechanical Engineering*, 57:45–68, 2010.

[12] A. Benavides and B. van Wachem. Eulerian-eulerian prediction of dilute turbulent gas-particle flow in a backward-facing step. *International Journal of Heat and Fluid Flow*, 30:452–461, 2009.

[13] W. Blatt, T. Kohley, U. Lotz, and E. Heitz. The Influence of Hydrodynamics on Erosion-Corrosion in Two-Phase Liquid-Particle Flow. *Corrosion*, 45:793–804, 1989.

[14] C. E. Brennen. *Fundamentals of Multiphase Flow.* Cambridge University Press, 2005.

[15] A. D. Burns, T. Frank, I. Hamill, and J. M. Shi. The Favre Averaged Drag Model for Turbulent Dispersion in Eulerian Multi-Phase Flows. In *Proceedings of the 5th International Conference on Multiphase Flow ICMF 2004*, 2004.

[16] C. P. Chen and P. E. Wood. A Turbulence Closure Model for Dilute Gas-Particle Flows. *The Canadian Journal of Chemical Engineering*, 63:349–360, 1985.

[17] L. Chen, Y. Duan, W. Pu, and C. Zhao. CFD simulation of coal-water slurry flowing in horizontal pipelines. *Korean Journal of Chemical Engineering*, 26:1144–1154, 2009.

[18] R. C. Chen. *Experimental and numerical studied of solid-liquid multiphase flow in pipes.* PhD thesis, Case Western Reserve University, 1991.

[19] R. C. Chen. Analysis of homogeneous slurry pipe flow. *Journal of Marine Science and Technology*, 1:37–45, 1994.

[20] X. Chen, Y. Li, X. Niu, M. Li, D. Chen, and X. Yu. A general two-phase turbulent flow model applied to the study of sediment transport in open channels. *International Journal of Multiphase Flow*, 37:1099–1108, 2011.

[21] N. S. Cheng. Comparison of formulas for drag coefficient and settling velocity of spherical particles. *Powder Technology*, 189:395–398, 2009.

[22] N. S. Cheng and A. W. K. Law. Exponential formula for computing effective viscosity. *Powder Technology*, 129:156–160, 2003.

[23] D. Chisholm. *Two-phase flow in pipelines and heat exchangers.* George Godwin, 1983.

[24] K.B. Chun and H.J. Sung. Control of turbulent separated flow over a backward-facing step by local forcing. *Experiments in fluids*, 21:417–426, 1996.

[25] J. N. Chung and T. R. Troutt. Simulation of particle dispersion in an axisymmetric jet. *Journal of Fluid Mechanics*, 186:199–222, 1988.

[26] R. Clift, J. R. Grace, and M. E. Weber. *Bubbles, Drops and Particles.* Academic Press, 1978.

[27] J. M. Colwell and C. A. Shook. The Entry Lenth for Slurries in Horizontal Pipeline Flow. *Canadian Journal of Chemical Engineering*, 66:714–720, 1988.

[28] M.R. Cox and M. Budhu. A practical approach to grain shape quantification. *Engineering Geology*, 96:1–16, 2008.

[29] C. T. Crowe, J. D. Schwarzkopf, M. Sommerfeld, and Y. Tsuji. *Multiphase flows with droplets and particles*. CRC Press, 2012.

[30] C. T. Crowe, T. R. Troutt, and J. N. Chung. Numerical models for two-phase turbulent flows. *Annual Reviews of Fluid Mechanics*, 28:11–43, 1996.

[31] J.A. Davis and M. Stewart. Predicting globe control valve performance. part i: Cfd modeling. *ASME Journal of Fluids Engineering*, 124:772–777, 2002.

[32] R. Di Felice and M. Rotondi. A very simple relationship for the voidage function in binary-solid suspensions. In *Proceedings of the 7th International Conference on Multiphase Flow ICMF 2010*, 2010.

[33] P. Doron and D. Barnea. A three-layer model for solid-liquid flow in horizontal pipes. *International Journal of Multiphase Flow*, 19:1029–1043, 1993.

[34] P. Doron and D. Barnea. Flow pattern maps for solid-liquid flows in pipes. *International Journal of Multiphase Flow*, 22:273–283, 1996.

[35] P. Doron, D. Granica, and D. Barnea. Slurry flow in horizontal pipes - experimental and modeling. *International Journal of Multiphase Flow*, 13:535–547, 1987.

[36] D. A. Drew. Mathematical modeling of two-phase flow. *Annual Reviews of Fluid Mechanics*, 15:261–291, 1983.

[37] D. A. Drew and R. T. Lahey. The virtual mass and lift force on a sphere in rotating and straining inviscid flow. *International Journal of Multiphase Flow*, 13:113–121, 1987.

[38] D.M. Driver and H.M. Seegmiller. Features of reattaching turbulent shear layer in divergent channel flow. *AIAA Journal*, 26:163–171, 1985.

[39] M. B. Dusseault. CHOPS: Cold Heavy Oil Production with Sand in the Canadian Heavy Oil Industry. Technical report, MBDC Inc., Waterloo, Ontario, Canada, 2002.

[40] M. B. Dusseault, M. B. Geilikman, and Spanos T. J. T. Mechanisms of Massive Sand Production in Heavy Oils. In *Proceedings of the 7th International Conference on Heavy Oils and Tar Sands UNITAR 2007*, 2007.

[41] K. Ekambara, R. S. Sanders, and J. H. Nandakumar, K. Masliyah. Hydrodynamic simulation of horizontal slurry pipeline flow using ANSYS-CFX. *Industrial & Engineering Chemistry Research*, 48:8159–8171, 2009.

[42] K. Ekambara, R. S. Sanders, K. Nandakumar, and J. H. Masliyah. CFD Modeling of Gas-Liquid Bubbly Flow in Horizontal Pipes: Infuence of Bubble Coalescence and Breakup. *International Journal of Chemical Engineering*, 2012:620463, 2012.

[43] S. E. Elgobashi and T. W. Abou-Arab. A two-equation turbulence model for two-phase flows. *Physics of Fluids*, 26:931–938, 1983.

[44] H. Enwald, E. Peirano, and A. E. Enwald. Eulerian two-phase flow theory applied to fluidization. *International Journal of Multiphase Flow*, 22:21–66, 1996.

[45] A. Erdal and H.I. Anderssont. Numerical aspects of flow computation through orifices. *Flow Measurement and Instrumentation*, 8:27–37, 1997.

[46] J.R. Fessler and J.K. Eaton. Turbulence modification by particles in a backward-facing step flow. *Journal of Fluid Mechanics*, 394:97–117, 1999.

[47] M. Founti, T. Achimastos, and A. Klipfel. Effects of Increasing Particle Loading in an Axisymmetric, Vertical, Liquid-Solid Sudden Expansion Flow. *ASME Journal of Fluids Engineering*, 121:171, 1999.

[48] M. Founti and A. Klipfel. Experimental and computational investigations of nearly dense two-phase sudden expansion flows. *Experimental Thermal and Fluid Science*, 17:27–36, 1998.

[49] P. Frawley, A. P. O'Mahony, and M. Geron. Comparison of Lagrangian and Eulerian Simulations of Slurry Flows in a Sudden Expansion. *ASME Journal of Fluids Engineering*, 132:091301, 2010.

[50] I. K. Gamwo, Y. Soong, and R. W. Lyczkowski. Numerical simulation and experimental validation of solids flows in a bubbling fluidized bed. *Powder Technology*, 133:117–129, 1999.

[51] M. B. Geilikman and M. B. Dusseault. Fluid rate enhancement from massive sand production in heavy-oil reservoirs. *Journal of Petroleum Science and Engineering*, 17:5–18, 1997.

[52] R. Gillies. *Pipeline flow of coarse particle slurries*. PhD thesis, University of Saskatchewan, 1993.

[53] R. G. Gillies, C. A. Shook, and J. Xu. Modelling Heterogeneous Slurry Flow at High Velocities. *The Canadian Journal of Chemical Engineering*, 82:1060–1065, 2004.

[54] R.G. Gillies and C.A. Shook. Modelling High Concentration Settling Slurry Flows. *Canadian Journal of Chemical Engineering*, 78:709–716, 2000.

[55] R.G. Gillies, C.A. Shook, and K.C. Wilson. An Improved Two Layer Model for Horizontal Slurry Pipeline Flow. *Canadian Journal of Chemical Engineering*, 69:173–178, 1991.

[56] L. C. Gomez and F. E. Milioli. Collisional solid's pressure impact on numerical results from a traditional two-fluid model. *Powder Technology*, 149:78–83, 2005.

[57] M.A. Habib, H.M. Badr, R. Ben-Mansour, and M.E. Kabir. Erosion rate correlations of a pipe protruded in an abrupt pipe contraction. *International Journal of Impact Engineering*, 34:1350–1369, 2007.

[58] M.A. Habib, H.M. Badr, R. Ben-Mansour, and S.A.M. Said. Numerical calculations of erosion in an abrupt pipe contraction of different contraction ratios. *International Journal for Numerical Methods in Fluids*, 46:19–35, 2004.

[59] Y. Hardalupas, A.M.K.P. Taylor, and J.H. Whitelaw. Particle dispersion in a vertical round sudden-expansion flow. *Philosophical Transaction of the Royal Society of London*, 341:411–442, 1992.

[60] K. Haugen, O. Kvernvold, A. Ronold, and R. Sandberg. Sand erosion of wear-resistant materials: Erosion in choke valves. *Wear*, 186-187:179–188, 1995.

[61] K. Hiltunen, A. Jasberg, S. Kallio, H. Karema, M. Kataja, A. Koponen, M. Manninen, and V. Taivassalo. *Multiphase Flow Dynamics - Theory and Numerics.* Number 722 in VTT Publications. VTT, 2009.

[62] A. Hossain and J. Naser. CFD investigation of particle deposition around bends in a turbulent flow. In *Proceedings of the 15th Australian Fluid Mechanics Conference*, 2004.

[63] A. Hossain, J. Naser, K. McManus, and G. Ryan. CFD investigation of particle deposition and distribution in a horizontal pipe. In *Proceedings of the Third International Conference on CFD in the Minerals and Process Industries CSIRO*, 2003.

[64] A. Hossein, J. Naser, and A. Imteaz. CFD investigation of particle deposition in a horizontal looped turbulent pipe flow. *Earth and Environmental Science*, 16:359–367, 2011.

[65] T. W Hsu, H.K. Cheng, and C. M. Hsieh. A two-phase flow model of wave-induced sheet flow. *Journal of Hydraulic Research*, 41:299–310, 2003.

[66] A. Huser and O. Kvernvold. Prediction of Sand Erosion in Process and Pipe Components. In *Proceedings of the 1st North American Conference on Multiphase Technology*, 1998.

[67] IEC 60534-2-3. *Industrial-process control valves - Flow capacity - Test procedures.* Geneva, Switzerland, 1997.

[68] F.P. Incropera and D.P. DeWitt. *Fundamentals of Heat and Mass Transfer.* Wiley, 1990.

[69] ISA.RP75.23-1995. *Considerations for Evaluating Control Valve Cavitation.* Research Triangle Park, Durham, NC, 1995.

[70] M. Ishii. *Thermo-fluid Dynamic Theory of Two-phase Flow.* Eyrolles, 1975.

[71] M. Ishii and K. Mishima. Two-Fluid model and hydrodynamic constitutive relations. *Nuclear Engineering and Design*, 82:107–126, 1984.

[72] ISO - GUM. *Guide to the Expression of Uncertainty in Measurements.* Geneva, Switzerland, 1993.

[73] H. A. Jakobsen. *Chemical Reactor Modelling - Multiphase Reactive Flows.* Springer, 2007.

[74] Y.Y. Jiang and P. Zhang. Numerical investigation of slush nitrogen flow in a horizontal pipe. *Chemical Engineering Science*, 73:169–180, 2012.

[75] Y.Y. Jiang and P. Zhang. Pressure drop and flow pattern of slush nitrogen in a horizontal pipe. *AIChE Journal*, doi: 10.002/aic.13927, 2012.

[76] S. Jovic. An Experimental Study of a Separated/Reattached Flow Behing a Backward-Facing Step. $Re_h = 37000$. Technical report, Eloret Institute, Ames Research Center, Moffet Field, California, USA, 1996.

[77] D. R. Kaushal, K. Sato, T. Toyota, K. Funatsu, and Y. Tomita. Effect of particle size distribution on pressure drop and concentration profile in pipeline flow of highly concentrated slurry. *International Journal of Multiphase Flow*, 31:809–823, 2005.

[78] D. R. Kaushal, T. Thinglas, Y. Tomita, S. Kuchii, and H. Tsukamoto. CFD modeling for pipeline flow of fine particles at high concentration. *International Journal of Multiphase Flow*, 43:85–100, 2012.

[79] D. R. Kaushal and Y. Tomita. Experimental investigation for near-wall lift of coarser particles in slurry pipeline using γ-ray densiometer. *Powder Technology*, 172:177–187, 2007.

[80] D.R. Kaushal and Y. Tomita. Solids concentration profiles and pressure drop in pipeline flow of multisized particulate slurries. *International Journal of Multiphase Flow*, 28:1697–1717, 2002.

[81] D.R. Kaushal and Y. Tomita. Comparative study of pressure drop in multisized particulate slurry through pipe and rectangular duct. *International Journal of Multiphase Flow*, 29:1473–2487, 2003.

[82] D.R. Kaushal, Y. Tomita, and R.R. Dighade. Concentration at the pipe bottom at deposition velocity for transportation of commercial slurries through pipeline. *Powder Technology*, 125:89–101, 2002.

[83] C. Kim, M. Lee, and C. Han. Hydraulic transport of sand-water mixtures in pipelines. part i. experiment. *Journal of Mechanical Science and Technology*, 22:2534–2541, 2008.

[84] J.Y. Kim, A.J. Ghajar, C. Tang, and G.L. Foutch. Comparison of near-wall treatment methods for high reynolds number backward-facing step flow. *International Journal of Computational Fluid Dynamics*, 19:493–500, 2005.

[85] J. F. Klausner, F. Fu, and R. Mei. A Conductance Based Solids Concentration Sensor for Large Diameter Slurry Pipelines. *Journal of Fluids Engineering*, 122:819–824, 2000.

[86] E.D. Koronaki, H.H. Liakos, M.A. Founti, and N.C. Markatos. Numerical study of turbulent diesel flow in a pipe with sudden expansion. *Applied Mathematical Modelling*, 25:319–333, 2001.

[87] S. Kumar, M. P. Dudukovic, and B. A. Toseland. Measurement Techniques for Local and Global Fluid Dynamic Quantities in Two and Three Phase Systems. Technical report, Federal Energy Technology Center, Morgantown, West Virginia, 1998.

[88] U. Kumar, R. Mishra, S.N. Singh, and V. Seshadri. Effect of particle gradation on flow characteristics of ash disposal pipelines. *Powder Technology*, 132:39–51, 2003.

[89] S. K. Lahiri and K. C. Gantha. Slurry flow modelling by CFD. *Chemical Industry & Chemical Engineering Quaterly*, 16:295–308, 2010.

[90] S. Lain and M. Sommerfeld. Euler/Lagrange computations of pneumatic conveying in a horizontal channel with different wall roughness. *Powder Technology*, 184:76–88, 2008.

[91] B.E. Launder and D.B. Spalding. *Mathematical models of turbulence*. Academic Press, 1972.

[92] M. F. Lightstone and S. M. Hodgson. Turbulence Modulation in Gas-Particle Flows: A Comparison of Selected Models. *The Canadian Journal of Chemical Engineering*, 82:209–219, 2004.

[93] C. X. Lin and M. A. Ebadian. A numerical study of developing slurry flow in the entrance region of a horizontal pipe. *Computers and Fluids*, 37:965–974, 2008.

[94] Z.H. Lin. Two-phase flow measurements with sharp-edged orifices. *International Journal of Multiphase Flow*, 8:683–693, 1982.

[95] J. Ling, P. V. Skudarnov, and M. A. Ebadian. Numerical investigations of liquid-solid slurry flows in a fully developed turbulent flow region. *International Journal of Heat and Fluid Flow*, 24:389–398, 2003.

[96] D. M. Liu. Particle packing and rehological property of highly concentrated ceramic suspensions: ϕ_m determination and viscosity prediction. *Journal of Materials Science*, 35:5503–5507, 2000.

[97] S. Longo. Two-Phase Flow Modeling of Sediment Motion in Sheet-Flows above Plane Beds. *Journal of Hydraulic Engineering*, 31:366–379, 2005.

[98] E. Loth. Numerical approaches for motion of dispersed particles, droplets and bubbles. *Progress in Energy and Combustion Science*, 26:161–223, 2000.

[99] E. Loth. An Eulerian turbulent diffusion model for particles and bubbles. *International Journal of Multiphase Flow*, 27:1051–1063, 2001.

[100] E. Loth. *Particles, drops and bubbles: fluid dynamics and numerical methods.* Cambridge University Press, 2011. (in preparation, provided free and online).

[101] M. Manninen, V. Taivassalo, and S. Kallio. *On the mixture model for multiphase flow.* Number 288 in VTT Publications. VTT, 1996.

[102] F. Mashayek and R.V.R. Pandya. Analytical description of particle/droplet-laden turbulent flows. *Progress in Energy and Combustion Science*, 29:329–378, 2003.

[103] V. Matousek. Concentration distribution in pipeline flow of sand-water mixtures. *Journal of Hydrology and Hydromechanics*, 48:180–196, 2000.

[104] V. Matousek. Pressure drop and flow patterns in sand-mixture pipes. *Experimental Thermal and Fluid Science*, 26:693–702, 2002.

[105] V. Matousek. Research developments in pipeline transport of settling slurries. *Powder Technology*, 156:43–51, 2005.

[106] V. Matousek. Predictive model for frictional pressure drop in settling-slurry pipe with stationary deposit. *Powder Technology*, 192:367–374, 2009.

[107] Z. Mehrez, M. Bouterra, A. El Cafsi, A. Belghith, and P. Le Qur. Active control of flow behind a backward-facing step by using a periodic perturbation. *ARPN Journal of Engineering and Applied Sciences*, 5:21–29, 2010.

[108] K. Mohanarangam and J.Y. Tu. Numerical Study of Particle Turbulence Interaction in Liquid-Particle Flows. *AIChE Journal*, 55:1298–1302, 2009.

[109] B. Mols and R. Oliemans. A turbulent diffusion model for particle dispersion and deposition in horizontal tube flow. *International Journal of Multiphase Flow*, 24:55–75, 1998.

[110] A. A. Mostafa and H. C. Mongia. On the interaction of particles and turbulent fluid flow. *International Journal of Heat and Mass Trasnfer*, 31:2063–2075, 1988.

[111] M. Nallasamy and C.P. Chen. Studies on Effects of Boundary Conditions in Confined Turbulent Flow Predictions. Technical report, Universities Space Research Association, Columbia, Maryland, USA, 1985.

[112] H. Nasr-El-Din, C. A. Shook, and M. N. Esmail. Isokinetic Probe Sampling From Slurry Pipelines. *Canadian Journal of Chemical Engineering*, 62:179–185, 1984.

[113] H. Nasr-El-Din, C. A. Shook, and M. N. Esmail. Wall Sampling in Slurry Systems. *Canadian Journal of Chemical Engineering*, 63:746–753, 1985.

[114] S. Nesic and J. Postlethwaite. Hydrodynamics of disturbed flow and erosion-corrosion. part II - two-phase flow study. *Canadian Journal of Chemical Engineering*, 69:704–710, 1991.

[115] S. Nesic and J. Postlethwaite. Erosion in Disturbed Liquid/Particle Pipe Flow: Effects of Flow Geometry and Particle Surface Roughness. *Corrosion*, 49:850–857, 1993.

[116] L. Nøkleberg and T. Søntvedt. Erosion of oil&gas industry choke valves using computational fluid dynamics and experiment. *International Journal of Heat and Fluid Flow*, 19:636–643, 1998.

[117] S. Ookawara, D. Street, and K. Ogawa. Numerical study on development of particle concentration profiles in a curved microchannel. *Chemical Engineering Science*, 61:3714–3724, 2006.

[118] R. Pankajakshan, B. J. Mitchell, and L. K. Taylor. Simulation of unsteady two-phase flows using a parallel Eulerian-Lagrangian approach. *Computers and Fluids*, 41:20–26, 2011.

[119] T.S. Park and H.J. Sung. A new low-reynolds-number $k - \epsilon - f_\mu$ model for predictions involving multiple surfaces. *Fluid Dynamics Research*, 20:97–113, 1997.

[120] M. Pathak. Computational investigations of solid-liquid particle interaction in a two-phase flow around a ducted obstruction. *Journal of Hydraulic Research*, 49:96–104, 2011.

[121] S. M. Pecker and S. S. Helvaci. *Solid-Liquid Two-Phase Flow*. Elsevier, 2008.

[122] A. M. Penko, J. Calantoni, and D. N. Slinn. Mixture theory model sensitivity to effective viscosity in simulations of sandy bedform dynamics. In *Proceedings of Oceans 2009 MTS/IEEE Biloxi-Marine Technology for Our Future: Global and Local Challenges*, 2009.

[123] A. M. Penko, D. N. Slinn, and J. Calantoni. Model for Mixture Theory Simulation of Vortex Sand Ripple Dynamics. *Journal of Waterway, Port, Coastal, and Ocean Engineering*, 137:225–233, 2011.

[124] L. M. Portela and R. V. A. Oliemans. Eulerian-Lagrangian DNS/LES of particle-turbulence interactions in wall-bounded flows. *International Journal of Numerical Methods in Fluids*, 43:1045–1065, 2003.

[125] A. Prosperetti and G. Tryggvason. *Computational methods for multiphase flow.* Cambridge University Press, 2007.

[126] M. C. Roco and C. A. Shook. Modeling of Slurry Flow: The Effect of Particle Size. *Canadian Journal of Chemical Engineering*, 61:494–503, 1983.

[127] R. Rundqvist, C. Ljus, and B. van Wachem. Experimental and Numerical Investigation of Particle Transport in a Horizontal Pipe. *AIChE Journal*, 51:3101–3108, 2005.

[128] H. Rusche. *Computational Fluid Dynamics of Dispersed Two-Phase Flows at High Phase Fractions.* PhD thesis, Imperial College, 2002.

[129] H. Rusche and R. I. Issa. The effect of voidage on the drag force on particles, droplets and bubbles in dispersed two-phase flow. In *Proceedings of the 2nd Japanese-European Two-Phase Flow Group Meeting*, 2000.

[130] H. Schlichting. *Boundary Layer Theory.* McGraw-Hill, 1960.

[131] J. Schmidt and L. Friedel. Two-phase flow pressure change across sudden expansions in duct areas. *Chemical Engineering Communications*, 141-142:175–190, 1996.

[132] J. Schmidt and L. Friedel. Two-phase flow pressure drop across sudden contractions in duct areas. *International Journal of Multiphase Flow*, 23:283–299, 1997.

[133] P. K. Senapati, D. Panda, and A. Parida. Predicting Viscosity of Limestone-Water Slurry. *Journal of Minerals and Materials Characterization and Engineering*, 8:203–221, 2009.

[134] W. T. Sha and S. L. Soo. Multidomain multiphase fluid mechanics. *International Journal of Heat and Mass Transfer*, 21:1581–1595, 1978.

[135] R. J. Shaan and C. A. Shook. Anomalous Friction in Slurry Flows. *Canadian Journal of Chemical Engineering*, 78:726–730, 2000.

[136] R. J. Shaan, R. J. Sumner, R. G. Gillies, and C. A. Shook. The Effect of Particle Shape on Pipeline Friction for Newtonian Slurries of Fine Particles. *Canadian Journal of Chemical Engineering*, 78:717–725, 2000.

[137] B.B. Shannak, L. Friedel, and M. Alhusein. Prediction of Single- and Two-Phase Flow Contraction through a Sharp-Edged Short Orifice. *Chemical Engineering and Technology*, 22:865–870, 1999.

[138] J. S. Shirolkar, C. F. M. Coimbra, and M Queiroz McQuay. Fundamental aspects of modeling turbulent particle dispersion in dilute flows. *Progress in Energy and Combustion Science*, 22:363–399, 1996.

[139] C.A. Shook and A.S. Bartosik. Particle-wall stresses in vertical slurry flows. *Powder Technology*, 81:117–124, 1994.

[140] P.V. Skudarnov, C.X. Lin, and M.A. Ebadian. Double-Species Slurry Flow in a Horizontal Pipeline. *ASME Journal of Fluids Engineering*, 126:125–132, 2004.

[141] C. Somaschi. Ottimizzazione fluidodinamica di valvole chokes. Master's thesis, Politecnico di Milano University, 2011.

[142] M. Sommerfeld, B. van Wachem, and R. V. A. Oliemans (eds). *Best practice guidelines for computational fluid dynamics of dispersed multiphase flows*. ER-COFTAC/SIAMUF, 2008.

[143] D. B. Spalding. Heat-transfer and Chemical-reaction Processes. Technical report, Imperial College, London, UK, 1980.

[144] D. B. Spalding. *Numerical computation of multi-phase fluid flow and heat transfer*, volume 1 of *Recent Advances in Numerical Methods in Fluids*, chapter 5. Pineridge Press Limited, 1980.

[145] D.B. Spalding. A novel finite-difference formulation for differential expressions involving both first and second derivatives. *International Journal of Numerical Methods in Engineering*, 4:551–559, 1972.

[146] J. J. Stickel and R. L. Powel. Fluid Mechanics and Rheology of Concentrated Suspsensions. *Annual Reviews of Fluid Mechanics*, 37:129–149, 2005.

[147] H. Tashiro and Y. Tomita. Influence of Diameter Ratio on a Sudden Expansion of a Circular Pipe in Gas-Solid Two-Phase Flow. *Powder Technology*, 48:227–231, 1986.

[148] Y. Tomita, H. Tashiro, K. Deguchi, and T. Jotaki. Sudden expansion of gas-solid two-phase flow in a pipe. *Physics of Fluids*, 23:663–666, 1980.

[149] B. Van Wachem and A. E. Almstedt. Methods for multiphase computational fluid dynamics. *Chemical Engineering Journal*, 96:81–98, 2003.

[150] H.K. Versteeg and W. Malalakesera. *An Introduction to Computational Fluid Dynamics. The Finite Volume Method*. Pearson Prentice Hall, 2007.

[151] M.S. Wallace, W. M. Dempster, T. Scanlon, J. Peters, and S. McCulloch. Prediction of impact erosion in valve geometries. *Wear*, 256:927–936, 2004.

[152] L. Wang, Y. Zhang, X. Li, and Y. Zhang. Experimental investigation and CFD simulation of liquidsolidsolid dispersion in a stirred reactor. *Chemical Engineering Science*, 65:5559–5572, 2010.

[153] X.H. Wang, Z.F. Liu, and X.X. Lu. Derivation of a second-order model for reynolds stress using renormalization group analysis and the two-scale expansion technique. *Acta Mechanica Sinica*, 27:649–659, 2011.

[154] K. C. Wilson, R. S. Sanders, R. G. Gillies, and C. A Shook. Interaction of Particles and Near-Wall Lift in Slurry Pipelines. *Powder Technology*, 197:247–253, 2010.

[155] K. C. Wilson and A. Sellgren. Interaction of Particles and Near-Wall Lift in Slurry Pipelines. *Journal of Hydraulic Engineering*, 129:73–76, 2003.

[156] R. J. K. Wood, T. F. Jones, J. Ganeshalingam, and N. J. Miles. Comparison of predicted and experimental erosion estimates in slurry ducts. *Wear*, 256:937–947, 2004.

[157] R. J. K. Wood, T. F. Jones, N. J. Miles, and J. Ganeshalingam. Upstream swirl-induction for reduction of erosion damage from slurries in pipeline bends. *Wear*, 250:770–778, 2001.

[158] H. Xiaowei and G. Liejin. Numerical investigations of catalyst-liquid slurry flow in the photocatalytic reactor for hydrogen production based on algebraic slip model. *International Journal of Hydrogen Energy*, 35:7065–7072, 2010.

[159] J. Xu, A. Rouelle, K.M. Smith, D. Celik, M.Y. Hussaini, and S.W. Van Sciver. Two-phase flow of solid hydrogen particles and liquid helium. *Cryogenics*, 44:459–466, 2004.

[160] A. Yeganeh-Bakhtiary, M. H. Kazeminezhadb, A. Etemad-Shahidi, J. H. Baas, and L. Cheng. EulerEuler two-phase flow simulation of tunnel erosion beneath marine pipelines. *Applied Ocean Research*, 33:137–146, 2011.

[161] F. Yilmaz and M. Y. Gundogdu. Analysis of conventional drag and lift models for multiphase CFD modeling of blood flow. *Korea-Australia Rheology Journal*, 21:161–173, 2009.

[162] K. F. Yu, K. S. Lau, and K. C. Chan. Numerical simulation of gas-particle flow in a single-side backward-facing step flow. *Journal of Computational and Applied Mathematics*, 163:319–331, 2004.